Experimental and numerical investigation of particle-fluid systems in geotechnical engineering

Vom Promotionsausschuss der
Technischen Universität Hamburg

zur Erlangung des akademischen Grades

Doktor-Ingenieurin (Dr.-Ing.)

genehmigte Dissertation

von
Manuela Kanitz

aus
Bochum

2020

1. Gutachter: Univ.-Prof. Dr.-Ing. Jürgen Grabe
2. Gutachter: Univ.-Prof. Dr.-Ing. habil. Dr. h.c. Stefan Heinrich
3. Gutachter: Univ.-Prof. Dr.-Ing. habil. Ivo Herle

Tag der mündlichen Prüfung: 07.12.2020

Experimental and numerical investigation of particle-fluid systems in geotechnical engineering

von

Manuela Kanitz

Herausgegeben von

J. Grabe

Technische Universität Hamburg
Institut für Geotechnik und Baubetrieb

Veröffentlichungen des Instituts für
Geotechnik und Baubetrieb

48

Herausgeber:

Univ.-Prof. Dr.-Ing. Jürgen Grabe
Technische Universität Hamburg
Institut für Geotechnik und Baubetrieb
Harburger Schloßstraße 20
D – 21079 Hamburg
e-mail: *grabe@tuhh.de*

ISBN-13: 3-936310-50-4 (Erstausgabe)

Druckerei

Druckzentrum Neumünster GmbH
Rungestraße 4
24537 Neumünster

In derselben Reihe erschienen:

1. J. Grabe (Hrsg.), 2000: Verbrennungsrückstände. Tagungsband, ISBN 3-936310-00-9

2. J. Grabe (Hrsg.), 2001: Schaden- und Risikomanagement im Tiefbau. Tagungsband, ISBN 3-936310-01-7

3. J. Grabe, 2003. Bodenmechanik und Grundbau. ISBN 3-936310-03-3

4. J. Grabe (Hrsg.), 2003: Euronormen in der Geotechnik – Was ändert sich? Tagungsband, ISBN 3-936310-04-1

5. J. Grabe (Hrsg.), 2003: Bodenverdichtung, Experimente - Modellierung - Geräteentwicklung - Baustellenberichte - F+E-Bedarf. Tagungsband, ISBN 3-936310-05-X

6. M. Kelm, 2004: Numerische Simulation der Verdichtung rolliger Böden mittels Vibrationswalzen. Promotion, ISBN 3-936310-06-8

7. J. Grabe (Hrsg.), 2004: Kaimauern - Messungen und Numerik. Tagungsband, ISBN 3-936310-07-6

8. J. Stein, 2005. Experimentelle und numerische Untersuchungen zum Düsenstrahlverfahren. Promotion, ISBN 3-936310-09-2

9. J. Grabe (Hrsg.), 2005: Grenzschicht Wasser und Boden - Phänomene und Ansätze. Tagungsband, ISBN 3-936310-10-6

10. J. Grabe (Hrsg.), 2005: FEM in der Geotechnik - Qualität, Prüfung, Fallbeispiele - Tagungsband, ISBN 3-936310-11-4

11. B. Mardfeldt, 2006: Zum Tragverhalten von Kaikonstruktionen im Gebrauchszustand. Promotion, ISBN 3-936310-12-2

12. J. Grabe (Hrsg.), 2006: Optimierung in der Geotechnik - Strategien und Fallbeispiele. Tagungsband, ISBN-13: 978-3-936310-13-9

13. T. Bierer, 2007: Bodenschwingungen aus Straßenverkehr auf unebener Fahrbahn im Zeitbereich - experimentelle und theoretische Untersuchungen. Promotion, ISBN-13: 978-3-936310-14-6

14. J. Grabe (Hrsg.), 2007: Bemessen mit Finite-Elemente-Methoden. Tagungsband, ISBN-13: 978-3-936310-15-3

15. K.-P. Mahutka, 2008: Zur Verdichtung von rolligen Böden infolge dynamischer Pfahleinbringung und durch Oberflächenrüttler. Promotion, ISBN-13: 978-3-936310-16-0

16. J. Grabe (Hrsg.), 2008: Seehäfen für Containerschiffe zukünftiger Generationen. Tagungsband, ISBN-13: 978-3-936310-17-7

17. F. König, 2008: Zur zeitlichen Traglastentwicklung von Pfählen und der nachträglichen Erweiterung bestehender Pfahlgründungen. Promotion, ISBN-13: 978-3-936310-18-4

18. S. Henke, 2008: Herstellungseinflüsse aus Pfahlrammung im Kaimauerbau. Promotion, ISBN-13: 978-3-936310-19-1

19. J. Grabe (Hrsg.), 2009: Spundwände – Profile, Tragverhalten, Bemessung, Einbringung und Wiedergewinnung. Tagungsband, ISBN-13: 978-3-936310-20-7

20. J. Dührkop, 2009: Zum Einfluss von Aufweitungen und zyklischen Lasten auf das Verformungsverhalten lateral beanspruchter Pfähle in Sand. Promotion, ISBN-13: 978-3-936310-21-4

21. O. Möller, 2009: Zum Langzeit-Kompressionsverhalten weicher organischer Sedimente. Promotion, ISBN-13: 978-3-936310-22-1

22. J. Grabe (Hrsg.), 2011: Ports of container ships of future generations. Tagungsband, ISBN-13: 978-3-936310-23-8

23. S. Kinzler, 2011: Zur Parameteridentifikation, Entwurfs- und Strukturoptimierung in der Geotechnik mittels numerischer Verfahren. Promotion, ISBN-13: 978-3-936310-24-5

24. G. Qiu, 2012: Coupled Eulerian Lagrangian Simulations of Selected Soil-Structure Problems. Promotion, ISBN-13: 978-3-936310-25-2

25. X. Ma, 2013: Nutzung der oberflächennahen Geothermie mittels Energiepfählen und Erdwärmesonden. Promotion, ISBN-13: 978-3-936310-26-9

26. J. Grabe (Hrsg.), 2013: Proceedings of the Conference on Maritime Energy COME 2013. Tagungsband, ISBN-13: 978-3-936310-28-3

27. J. Grabe (Hrsg.), 2013: Bemessen mit numerischen Methoden. Tagungsband, ISBN-13: 978-3-936310-29-0

28. T. Pucker, 2013: Stoffmodell zur Modellierung von stetigen Materialübergängen im Rahmen der Optimierung geotechnischer Strukturen. Promotion, ISBN-13: 978-3-936310-30-6

29. S. Henke, 2013: Untersuchungen zur Pfropfenbildung infolge der Installation offener Profile in granularen Böden. Habilitation, ISBN-13: 978-3-936310-31-3

30. J. Grabe (Hrsg.), 2014: Ports for Container Ships of Future Generations. Tagungsband, ISBN-13: 978-3-936310-32-0

31. J. Grabe (Hrsg.), 2014: Offshore Basishäfen, Tagungsband, ISBN-13: 978-3-936310-33-7

32. C. Rudolph, 2015. Untersuchungen zur Drift von Pfählen unter zyklischer, lateraler Last aus veränderlicher Richtung, Promotion, ISBN-13: 978-3-936310-34-4

33. J. Grabe (Hrsg.), 2015: Morphodynamics 2015, Tagungsband, ISBN-13: 978-3-936310-35-1

34. T. Hamann, 2015: Zur Modellierung wassergesättigter Böden unter dynamischer Belastung und großen Bodenverformungen am Beispiel der Pfahleinbringung, Promotion, ISBN-13: 978-3-936310-36-8

35. B. Schümann, 2015: Beitrag zum dynamischen Dreiphasenmodell für Boden auf Basis der Finite-Elemente-Methode, Promotion, ISBN-13: 978-3-936310-37-5

36. M. Milatz, 2015: Untersuchungen zum Einfluss der Kapillarität auf das hydraulisch-mechanische Verhalten von granularer Tragschichten für Verkehrswege, Promotion, ISBN-13: 978-3-936310-38-2

37. H. Kaya, 2016: Bodenverschleppung und Spaltbildung infolge der Einbringung von Profilen in Dichtungsschichten aus Ton, Promotion, ISBN-13: 978-3-936310-39-9

38. J. Grabe (Hrsg.), 2017: Proceedings of the Conference on Maritime Energy COME 2017. Tagungsband, ISBN-13: 978-3-936310-40-5

39. B. Kocak, 2017: Zur numerischen Modellierung von hydraulisch-mechanisch gekoppelten Prozessen in gesättigten granularen Böden mittels Smoothed Particle Hydrodynamics, Promotion, ISBN-13: 978-3-936310-41-2

40. K. Siegl, 2017: Zur Pfahldynamik von gerammten Großrohrpfählen und der daraus resultierenden Wellenausbreitung in Wasser und im Meeresboden, Promotion, ISBN-13: 978-3-936310-42-9

41. J. Grabe (Hrsg.), 2017: Numerical Methods in Geotechnics, Tagungsband, ISBN-13: 978-3-936310-43-6

42. J. Grabe (Hrsg.), 2018: Digitale Infrastruktur und Geotechnik (DIG 2018), Tagungsband, ISBN-13: 978-3-936310-44-3

43. D. Osthoff, 2018: Zur Ursache von Schlosssprengungen und zu einbringbedingten Lageabweichungen von Spundwänden, Promotion, ISBN-13: 978-3-936310-45-0

44. E. Heins, 2018: Numerical based identification of the pile-soil interaction in terms of the axial pile bearing capacity, Promotion, ISBN-13: 978-3-936310-46-7

45. K. Seitz, 2020: Zur Topologieoptimierung von geotechnischen Strukturen und zur Tragfähigkeitssteigerung des Baugrunds durch Scherfugenverfestigung, Promotion, ISBN-13: 978-3-936310-47-4

46. D. Plenker, 2020: Physical and numerical investigations of the dynamic interaction of granulates and fluid, Promotion, ISBN-13: 978-3-936310-48-1

47. J. Grabe; J. O. Backhaus; P. Vogel, 2021: Bauprojektmanagement, ISBN-13: 978-3-936310-49-8

„When in doubt, go to the library.“

Ron Weasley
- Harry Potter and the Chamber of Secrets
Joanne K. Rowling

Vorwort des Herausgebers

In der Bodenmechanik wird Boden in der Regel auf makromechanischer Skala als ein Gebiet mit bestimmten boden-mechanischen Eigenschaften beschrieben. Dabei besteht Boden bekanntlich aus vielen unregelmäßig geformten Partikeln mit dazwischen befindlichen Poren, die mit Wasser und Luft gefüllt sein können und deren Phasen mechanisch interagieren. Die Möglichkeit die Prozesse im Boden mit mikromechanischen Ansätzen mathematisch-numerisch modellieren zu können, bot den Ausgangspunkt für die vorliegende Dissertationsschrift. Wissenschaftlich relevant ist, ob die mathematisch-mechanische Methode auf die Partikel-Fluid-Struktur Interaktionen von Boden anwendbar ist, ob die Ergebnisse durch Versuche validierbar sind und welche neuen Erkenntnisse sich aus der Anwendung der mikromechanischen Modellierung ergeben können.
Frau Kanitz nutzt für ihre Arbeit die Methode der gekoppelten Diskreten Elemente und der Fluiddynamik (CFD-DEM) und verwendet dafür das Programm CFDEM®coupling, DCS Computing, Linz. Aufgrund der Größe der gewählten Randwertprobleme wählt sie eine im Porenraum nicht aufgelöste (unresolved) Diskretisierung.
Sie befasst sich exemplarisch mit der Verflüssigung von Sand, der Suffusion in gemischtkörnigen Böden, der Saugbaggerung von Unterwasserböschungen und dem Herausziehen einer Ankerplatte aus dem gesättigten Boden. Bei diesen vier Randwertproblemen treten besondere bodenmechanische Phänomene auf, wie beispielsweise der Phasenübergang von fest zu flüssig, die Kornseparierung bei Durchströmung, die Dilatanz beim Abscheren und die Bildung von Saugspannung beim schnellen Herausziehen. Die gewählte mathematisch-numerische Methode wird hierbei von ihr auf die Probe gestellt. Ziel ist es daher auch deren Grenzen herauszufinden und sofern möglich die Methode zu erweitern. Zur Validierung der numerischen Ergebnisse führt sie einfache Experimente durch.
Zielsetzung der Arbeit von Frau Kanitz ist die Beantwortung folgender übergeordneter Forschungsfragen, siehe Kapitel 1, Seite 3:

1. What conclusions can we draw by combining experimental and numerical investigations regarding the influence of the interaction between soil particles and pore water?

2. What are the opportunities concerning an improved understanding of soil behaviour using unresolved CFD-DEM?

3. Where are the limits of unresolved CFD-DEM and what must be considered?

Sie befasst sich dazu mit folgenden Randwertproblemen, siehe Kapitel 3,

1. Internal fluidisation in sand

2. Suffusion

3. Influence of suction dredging on the failure behaviour of submarine slopes

4. Extraction of plates embedded in saturated sand

und spezifiziert auf Seite 11 weitere Forschungsfragen.
Als Vormerkung zitiert sie die von ihr bereits publizierten bzw. eingereichten Fachbeiträge, die in Teilen Eingang gefunden haben in ihrer Dissertation.
In Kapitel 1 führt sie in die Thematik und Motivation ihrer Arbeit ein. Es gelingt ihr in diesem Kapitel die Aufmerksamkeit des Lesers auf die übergeordneten Themen zu lenken. Ziel ist ja nicht die detaillierte Untersuchung eines der genannten Randwertprobleme, denn das wäre jeweils eine Dissertation für sich, sondern es geht darum das Potential und die Grenzen der mikromechanischen Betrachtung für die Bodenmechanik herauszufinden.
Das Kapitel 2 gibt einen Überblick über die zur Verfügung stehenden mathematisch-numerischen Methoden zur Modellierung von Mehrphasenmaterialien auf verschiedenen Skalen.
In Kapitel 3 stellt sie die Zielsetzung für die einzelnen Randwertprobleme dar und erläutert ihren methodischen Ansatz und die Struktur ihrer Arbeit.
Die numerischen Grundlagen der von ihr genutzten unresolved CFD-DEM werden in Kapitel 4 dargestellt. Der Unterschied von resolved und unresolved CFD-DEM wird aus Abb. 4.3 deutlich. Eine wesentliche Rolle spielen bei dieser Methode, die Interaktionskräfte zwischen Partikeln und dem Fluid. Hier sind insbesondere die auf die Partikel wirkende Strömungskraft (Abschnitt 4.3.1), die auf das Fluid wirkende Schleppkraft (Abschnitt 4.3.2), die Trägheitskraft (Abschnitt 4.3.3.) und die Abhebekraft (Abschnitt 4.3.4) zu nennen.
In Kapitel 5 werden die Materialparameter des verwendeten Sands untersucht. Für deren Bestimmung werden Messmethoden aus der Partikelmechanik verwendet. Sie nutzt dazu die Ausstattung des Instituts für Partikeltechnologie der TUHH. Die Ergebnisse sind in Tabelle 5.3. aufgelistet. Des Weiteren hat sie an unserem Institut für die Beobachtung und Auswertung der Partikelbewegung in den experimentellen Versuchen die Particle-Image-Velocimetry (PIV) Methode zusammengestellt, aufgebaut und in Betrieb genommen.
Der Versuchsaufbau zur Untersuchung der Bodenverflüssigung bei vertikaler Durchströmung ist in Abb. 6.3, Kapitel 6, dargestellt. Das zugehörige numerische Modell ist in Abb. 6.4 zu sehen. Die experimentellen Ergebnisse mit zeitlicher Darstellung der Partikelbewegung zeigen die Abb. 6.5 und 6.6. Es zeigt sich bei dichter Lagerung ein seitlicher Durchbruch (oder auch kalter Vulkan genannt) gefolgt von Turbulenzen. Die Ergebnisse der numerischen Modellierung sind im Vergleich dazu in Abb. 6.7 dargestellt. Das Phänomen der Lokalisierung als kalter Vulkan tritt bei mitteldichter Lagerung vornehmlich am Rand und bei dichter Lagerung zentral auf. Der Verdacht liegt nahe, dass hier Randeffekte eine Rolle spielen. Diesem Einfluss geht sie in Abschnitt 6.5.1 nach, siehe Abb. 6.9. Mit der verwendeten numerischen Methode wird es nun möglich die Korn-zu-Korn Kräfte zu visualisieren, Abb. 6.12, 6.13. Mit Gleichung 6.10 geht sie auf den bodenmechanischen Ansatz zur Beschreibung des hydraulischen Grundbruchs ein. Es gelingt ihr mit Gleichung 6.11 und den Simulationsergebnissen (Abb. 6.15) den Druckverlust bei Erreichen der Verflüssigung dem hydraulischen Grenzgradienten nahezu gleichzusetzen. Hier passen die Ansätze der klassischen Bodenmechanik und der Partikelmechanik zusammen. Die CFD-DEM bietet also die Möglichkeiten die Prozesse im Detail zu analysieren, was bisher nicht möglich war.
Kapitel 7 behandelt das Randwertproblem der Suffusion. Frau Kanitz geht kurz auf die wesentliche Literatur ein. Der Ansatz der Schleppkraft (Dragforce) spielt bei dieser

Problemstellung eine entscheidende Rolle. Die gängigen Ansätze sind in Tabelle 7.1 gelistet. Sie stellt einen erheblichen Einfluss der einzelnen Schleppkraftansätze auf die innere Erosion fest, siehe Abb. 7.3. Ihr experimenteller Versuchsaufbau ist in Abb. 7.8 dargestellt. Sie untersucht die Suffusion an geschichteten Glaskugeln unterschiedlichen Durchmessers und beschränkt sich in der Modellierung allerdings auf ein reduziertes Schichtmodell. In den Experimenten zeigt sich der Transport der kleineren Kugeln durch den Porenraum der Schicht mit größeren Kugeln, siehe Abb. 7.12. Abb. 7.13 zeigt die aus den PIV-Daten gewonnene Geschwindigkeit im Porenraum, die über die Probenhöhe sehr schwankt. Die ausgewertete mittlere Geschwindigkeit mit 0,05 m/s passt ungefähr zur gemittelten Abstandsgeschwindigkeit von 0,068 m/s. Den Partikeltransport bei Verwendung verschiedener Schleppkraftansätze zeigt Abb. 7.15. Sie untersucht des Weiteren den Einfluss des Parameters χ in der Formel von Di Felice.

Im Kapitel 8 befasst sich Frau Kanitz mit der Saugbaggerung von Unterwasserböschungen, siehe Abb. 8.1. Hier zeigten vorhergehenden Versuche, dass in dicht gelagerten Sanden sogenannte active banks entstehen. Diese sind auf die bei Scherung auftretende Dilatanz des dicht gelagerten Sandes zurückzuführen. Es entsteht in der Scherfuge ein gewisser Porenwasserunterdruck, der vergleichbar einem teilgesättigten Sand zu einer Kapillarkohäsion führt. Der Versuchsaufbau ist in Abb. 8.2 gezeigt. Das numerische Modell ist in Abb. 8.5 dargestellt. Sie führt Versuche an Glaskugeln und an Hamburger Sand durch. Die numerischen Simulationen zeigen bei dicht gelagerten Sanden nicht den in den Versuchen beobachteten Dilatanz bedingten Effekt temporär steiler Böschungen. Das verwendete CFD-DEM Programm ist nach Frau Kanitz nicht in der Lage diese Dilatanzeffekte abzubilden, siehe Seite 121. Frau Kanitz leitet daher ein Kohäsionsmodell auf der Grundlage eines Partikels in der Strömung her, siehe Abschnitt 8.5.1 und insbesondere Abb. 8.21 sowie resultierend Gleichung 8.9 und 8.10. In Abschnitt 8.6. validiert sie ihren Ansatz.

Das Herausziehen einer Ankerplatte aus dem gesättigten Boden wird in Kapitel 9 behandelt. Die Abb. 9.2 ff zeigen den Versuchsaufbau. Das numerische Modell ist in Abb. 9.5 dargestellt. Die Versuchsergebnisse sind in guter Übereinstimmung zu den numerischen Ergebnissen, vergleiche Abb. 9.6, 9.9 und 9.12.

In Kapitel 10 stellt Frau Kanitz die wesentlichen Ergebnisse und Schlussfolgerungen dar und gibt einen Ausblick.

Frau Kanitz hat sich einem Thema im Grenzbereich von Partikeltechnologie und Bodenmechanik gewidmet. Und sie hat es geschafft, diese beiden Welten etwas zusammenzuführen. Die von ihr verwendete und in Teilen erweiterte CFD-DEM ist durch ihre Arbeit nachgewiesenermaßen in der Lage neue Einblicke in die Partikel-Fluid Struktur Interaktion von wassergesättigten Böden zu liefern. Natürlich bleibt hier noch einiges für nachfolgende Wissenschaftler zu tun, siehe dazu ihren Ausblick.

Frau Kanitz hat mit ihren experimentellen und numerischen Untersuchungen einen wesentlichen wissenschaftlichen Beitrag zum Stand der Wissenschaft an der Schnittstelle von Partikeltechnologie und Geotechnik geleistet. Durch ihre Dissertationsschrift hat Frau Kanitz ihre Befähigung zur selbstständigen wissenschaftlichen Arbeit ausdrücklich nachgewiesen.

Frau Kanitz hat bereits Teile ihrer Arbeit in qualitätsgesicherten Fachzeitschriften publiziert. Hier sind insbesondere ihre Beiträge in den Zeitschriften Computer and Geotechnics und Numerical and Analytical Methods in Geomechanics zu nennen. Des Weiteren hat sie

mehrfach auf Tagungen der OMAE vorgetragen und als Session Leitung fungiert. Sie ist dadurch inzwischen für ihre wissenschaftlichen Arbeiten bekannt.
Aktuell arbeitet sie für die Ramboll Deutschland GmbH in Hamburg und sammelt dort Erfahrungen in der Praxis. Ich würde mich freuen, wenn Frau Kanitz den Weg zurück in die Wissenschaft finden würde.
Für ihren weiteren Lebensweg wünsche ich ihr alles Gute.

Hamburg, 11.04.2021

Jürgen Grabe

Acknowledgememt

This thesis was written while I was working as a research assistant at the Institute of Geotechnical Engineering and Construction Management at the Hamburg University of Technology.
I would especially like to thank my main supervisor, Prof. Dr.-Ing. Jürgen Grabe, for his support and the many stimulating discussions during and outside coffee breaks. Further, I would like to thank Prof. Dr.-Ing. Ivo Herle and Prof. Dr.-Ing. Stefan Heinrich for their guidance and valuable comments.
Working at the Institute has been a great pleasure and I deeply thank my colleagues who always agreed to take yet another coffee with me and would never be disturbed by me rushing into their office to tell them about my research ideas - sometimes in a very enthusiastic way, sometimes a bit more hesitant.
My thesis has been part of a research project with DCS Computing GmbH. This cooperation has been the cherry on the cake! My deepest thank to the whole staff of DCS Computing, but especially to Dr. Alice Hager and Dr. Christoph Goniva for their dedicated support and the interessting and also funny meetings and discussions.
Last but not least, I would like to thank my friends and family who had to buffer all my mood changes and supported me along the whole process of completing this thesis. Without their never ending encouragmenent and the numerous invites to coffee or wine breaks, the work on this thesis would have been much worse. Thank you for your patience when I had to get stuff off my chest and cheering me up again!
By the time I'm writing this, my computer has decided that this thesis was his last accomplishment. I thank him for his passion throughout the work for this thesis and wish him a good travel to the place where old and brave computers go after passing away.

Hamburg, 13.05.2021

Manuela Kanitz

Keywords:

Particle-scale modelling, Coupled CFD-DEM, 1-g model tests, PIV, Internal Fluidisation of sand, Suffusion, Drag force models, Suction Dredging of submarine slopes, Extraction of anchor plates

List of Figures

4.1 Contact handling of colliding particles (Kanitz et al., 2017) 18
4.2 Pressure distribution $p_{\mathrm{el}}(r_k)$ in a wall-particle contact during elastic deformation, after (Antonyuk et al., 2010) 18
4.3 Discretisation scheme of resolved CFD-DEM (left) and unresolved CFD-DEM (right) (Hager, 2014) 21

5.1 Particle distribution (left) and sphericity (right) of (a) glass beads ($D = 3\,\mathrm{mm}$), (b) glass beads ($D = 1\,\mathrm{mm}$) and (c) Hamburger Sand 27
5.2 Friction coefficient μ for (a) glass beads ($D = 3\,\mathrm{mm}$), (b) glass beads ($D = 1\,\mathrm{mm}$) and (c) Hamburger Sand 28
5.3 Microscopical view of the glass beads and the Hamburger Sand 29
5.4 Schematic representation of the contact force vs time at the impact of a particle with a stiff wall, after (Antonyuk et al., 2010) 30
5.5 Restitution coefficient e_n for (a) glass beads ($D = 3\,\mathrm{mm}$), (b) glass beads ($D = 1\,\mathrm{mm}$) and (c) Hamburger Sand 31
5.6 Determination of average modulus of elasticity E^* for (a) glass beads ($D = 3\,\mathrm{mm}$), (b) glass beads ($D = 1\,\mathrm{mm}$) and (c) Hamburger Sand 33
5.7 Comparison of Hertz-Model with Force-displacement-curve for (a) glass beads ($D = 3\,\mathrm{mm}$), (b) glass beads ($D = 1\,\mathrm{mm}$) and (c) Hamburger Sand . 34
5.8 General scheme of a PIV-DIC analysis (Kanitz et al., 2019) 37

6.1 Determination of the minimum fluidisation velocity (Gidaspow, 1994) . . . 39
6.2 Experimental setup of investigation of the fluidisation behaviour Hamburger Sand 41
6.3 Sketch of the test setup for the investigation of the fluidisation behaviour of Hamburger Sand 42
6.4 Setup of the numerical investigations of internal fluidisation of Hamburger Sand with unresolved coupled CFD-DEM 43
6.5 Fluidisation behaviour of the medium dense sand at different time steps; vector representation of the movement resulting from the PIV analysis; the grey area marks the region, which is left out of the analysis (location of the ball valve) 45
6.6 Fluidisation behaviour of the very dense sand at different time steps; vector representation of the movement resulting from the PIV analysis; the grey area marks the region, which is left out of the analysis (location of the ball valve) 46
6.7 Numerical result of the fluidisation behaviour of medium dense Hamburger Sand 48
6.8 Numerical result of the fluidisation behaviour of very dense Hamburger Sand 49

6.9 Influence of the particle-wall friction coefficient on the plug creation in a very dense sand bed by seepage flow after 1 s 51
6.10 Numerical result of the fluidisation behaviour of medium dense Hamburger Sand with reduced particle-wall friction coefficient 53
6.11 Numerical result of the fluidisation behaviour of very dense Hamburger Sand with reduced particle-wall friction coefficient 54
6.12 Distribution of the normal particle contact forces during the fluidisation of medium dense soil - contact forces are scaled by their value 55
6.13 Distribution of the normal particle contact forces during the fluidisation of very dense soil - contact forces are scaled by their value 56
6.14 Development of median void fraction over time in the fluidised channels and in the whole bed for medium dense and very dense sand 58
6.15 Pressure drop over the medium dense sand bed vs. fluid velocity u 60
6.16 Particle velocities and fluidisation behaviour of the medium dense sand bed with increasing fluid velocity u 61

7.1 Initial configuration of the particles before seepage flow in a well-mixed assembly 68
7.2 Numerical results of the particle migration after 120 s of seepage flow with the drag force models of Di Felice, Gidaspow, Koch & Hill and Schiller & Naumann 69
7.3 Erosion of fines over the column height after 120 s of seepage flow 70
7.4 Composition of the fluid-particle interaction forces acting on the fines with (a) Di Felice drag, (b) Gidaspow drag, (c) Koch & Hill drag and (d) Schiller & Naumann drag 71
7.5 Pressure drop in the particle bed with (a) rearranging fines and (b) fixed fines 73
7.6 Suffusion setup with completely mixed packing using the moist tamping method by Ladd (1978) after 3 h (left) and 23 h (right) of de-aeration . . . 75
7.7 Experimental setup of investigation of suffusion in a particle bed with 5 mm and 1 mm particles with a layered setup 76
7.8 Sketch of the test setup for the investigation of suffusion 77
7.9 Pressure drop across the bed using a coarse (1.6 cm × 2.0 cm × 1.0 cm), a medium (0.8 cm × 1.0 cm × 1.0 cm) and a fine discretisation (0.8 cm × 1.0 cm × 0.5 cm) (Kanitz and Grabe, 2020) 78
7.10 Numerical setup of the suffusion investigation (left) and the mesh-to-particle ratio (right) 79
7.11 Particle positions at the beginning (left) after 1 s (middle) and after 10 s (right) in the experiment 80
7.12 Detailed view on the particle positions during seepage flow 81
7.13 Experimental analysis of the velocity field using PIVLab (Thielicke and Stamhuis, 2014); fields of investigation with respective ROI, where the immobile coarse particles are left out of the analysis and marked in red (left) and extraction of the velocity over the height (right), the dark blue line represents the moving mean of the data 82

7.14 Initial particle configuration of the layered setup for the numerical investigations of suffusion . . . 83
7.15 Particle positions after 1 s, 10 s and 40 s of simulated time using Di Felice drag, Gidaspow drag, Koch & Hill drag and Schiller & Naumann drag . . . 84
7.16 Erosion of fines into the upper coarse particle matrix over time using the drag force model of Schiller & Naumann, Koch & Hill, Di Felice and Gidaspow 86
7.17 Erosion of fines over the column height after 40 s of seepage flow using the conventional drag force models; the light green rectangle highlights the fines layer, the light blue rectangle highlights the "migration" layer into where the fines are mainly washed . . . 87
7.18 Fluid velocity over the column height at 40 s of seepage flow using the conventional drag force models; the light green rectangle highlights the fines layer, the light blue rectangle highlights the "migration" layer into where the fines are mainly washed . . . 88
7.19 (a) Fluid velocity over height of the particle column for Koch & Hill, Di Felice, Gidaspow drag and the extended drag model of Schiller & Naumann with different values for χ - (b) Re_p over height of the particle column for drag models of Di Felice . . . 89
7.20 Development of C_D over $(u - v)$ for the formulation of Schiller & Naumann and Di Felice. . . . 90
7.21 Fluid pressure, fluid velocity, void fraction and interaction force coefficient K_{pf} evolution over the soil column after 1 s for the model of Schiller & Naumann, the drag model of Di Felice and extended drag models with varying χ; the light green rectangle highlights the layer of fine particles; the light blue area highlights the "migration layer" (Kanitz and Grabe, 2020) . 91
7.22 Particle positions after 1 s of simulated time using extended Schiller & Naumann drag with increasing value of χ . . . 92
7.23 Amount of eroded fines into the upper coarse particle matrix over time with increasing value for χ . . . 94
7.24 Amount of eroded fines vs. χ after 20 s of seepage flow . . . 94
7.25 Erosion of fines into the upper coarse particle matrix after 1 s (left) and 20 s of seepage flow with increasing value for χ . . . 96
7.26 Drag force over $(u - v)$ for the drag force model of Koch & Hill, Di Felice, and Gidaspow for (a) $n = 0.3$ (b) $n = 0.35$, (c) $n = 0.4$ and (d) $n = 0.45$. 98

8.1 Subaqueous slope failure mechanisms - liquefaction slope failure (left) and breach failure (right) (Kanitz and Grabe, 2019a) . . . 102
8.2 Sketch of the experimental setup for the investigation of suction dredging - (a) acrylic test container (b) suction dredger (Kanitz and Grabe, 2019a) . . 103
8.3 Experimental setup (left) and model suction dredger (right) . . . 104
8.4 Location of the pore water pressure transducer in the slope body during suction dredging . . . 104
8.5 Numerical setup of a suction dredged submerged slope (Kanitz and Grabe, 2019a) . . . 106

8.6 Mesh sensitivity analysis with a coarse mesh (a) of 0.01 m × 0.012 m × 0.01 m and a fine mesh (b) of 0.005 m × 0.012 m × 0.005 m; failure of a very dense slope after 1.8 s of suction dredging 108
8.7 Failure of the submerged slope with 3 mm glass beads 108
8.8 Failure of the submerged slope with 1 mm glass beads 109
8.9 Failure of the submerged slope with medium densely packed Hamburger Sand (Kanitz and Grabe, 2019a) 110
8.10 Failure of the submerged slope with very densely packed Hamburger Sand (Kanitz and Grabe, 2019a) 111
8.11 Numerical results of the failure of a suction dredged submerged slope with 3 mm glass beads 111
8.12 Numerical results of the failure of a suction dredged submerged slope with 1 mm glass beads 112
8.13 Numerical results of the failure of a suction dredged submerged slope with medium dense Hamburger Sand (Kanitz and Grabe, 2019a) 113
8.14 Numerical results of the failure of a suction dredged submerged slope with very dense Hamburger Sand (Kanitz and Grabe, 2019a) 114
8.15 Pore water pressure changes in the experiments with (a) glass beads of 3 mm diameter, (b) glass beads of 1 mm diameter, (c) medium densely packed Hamburger Sand and (d) very densely packed Hamburger Sand 115
8.16 PIV measurements of material velocity of submarine slopes with 3 mm glass beads (a), 1 mm glass beads (b), medium densely packed sand (c) and very densely packed sand (d) carried out with GeoPIV-RG 117
8.17 Numerically modelled pore water pressure changes with (a) glass beads of 3 mm diameter, (b) glass beads of 1 mm diameter, (c) medium densely packed Hamburger Sand and (d) very densely packed Hamburger Sand . . 119
8.18 Computed fluid velocity at $t = 1.8$ s of simulated time for (a) glass beads of 3 mm diameter, (b) glass beads of 1 mm diameter, (c) medium densely packed Hamburger Sand and (d) very densely packed Hamburger Sand . . 120
8.19 Numerical simulation of the very densely packed slope after 1.8 s of simulated time including the time derivative of the void fraction - (a) Numerical model with ddt-Model A, (b) Numerical model with ddt-Model B 122
8.20 Rearrangement of particles in dense (top) and loose (bottom) state by applying a shear force F; solid line illustrates a change in distance; dotted line illustrates constant distance 125
8.21 Flow field around sphere according to potential flow 126
8.22 Drag coefficient vs. Particle Reynolds number of a sphere (Crowe et al., 2012) 127
8.23 Failure of submerged sand column provided by Plenker (2020) 129
8.24 Numerical results of submerged granular column collapse of very dense Hamburger Sand without an extension to model the dilatancy-induced enhanced stability 131
8.25 Numerical results of submerged granular column collapse of very dense Hamburger Sand with simplification of instantly removed wall 132

8.26 Numerical model of the submerged granular column collapse with the lubrication model (Tomac and Gutierrez, 2014), the Stokes drag model, cohesion model type A and cohesion model type B - failure stage after 0.4 s 133
8.27 Variation of the exponent χ in the cohesion model type B - failure stage after 0.4 s 134
8.28 Numerical results of submerged granular column collapse with cohesion model type B and $\chi = 5.7$ 135
8.29 Experimental result of the failure of a very dense slope after 1.8 s and 3.4 s (a) and respective numerical simulation with cohesion model type B and $\chi = 5.7$ (b) and without cohesion model (c) 137

9.1 Failure mechanism of an object embedded in saturated sand with (a) shear surface formation in dense sand and (b) shear surface formation in loose packed sand (Kanitz et al., 2019) 139
9.2 Sketch of the experimental setup for the investigation of the extraction of a plate (Kanitz et al., 2019) 140
9.3 Extracted plate - 1 g model of extracted plate (a) and location of pore water pressure transducer (b) (Kanitz et al., 2019) 141
9.4 1 g model of the extraction of a plate embedded in saturated soil (Kanitz et al., 2019) 141
9.5 Numerical model of the extraction of an anchor plate embedded in saturated sand (Kanitz et al., 2019); the soil body is cut in half to visualize the mesh refinement 143
9.6 Shear band evolution in the (a) numerical and (b) experimental setup after 0.25 s (Kanitz et al., 2019) 144
9.7 Measured pore water pressure evolution at an extraction velocity of (a) 300 mm/min and (b) 100 mm/min (Kanitz et al., 2019) 145
9.8 PIV results for the Phase I, II and III - carried out with PIVLab 146
9.9 Comparison of measured and simulated pressure underneath the anchor plate - without time extrapolation of the numerical results and comparison to "old" simulation of plate (a) - with time extrapolated numerical results and simulation with the immersed boundary method (b) (Kanitz et al., 2019) 148
9.10 Modelled pore water pressure evolution at an extraction velocity of 300 mm/min and 100 mm/min(a) without and (b) with time extrapolation (Kanitz et al., 2019) 149
9.11 Resulting pressure evolution in the soil body with an extraction velocity of 100 mm/s using the drag model of (a) Di Felice (1994), (b) Gidaspow (1994), (c) Koch and Hill (2001) and (d) Schiller and Naumann (1935) . . 150
9.12 Force onto the plate - comparison of the experiments and simulations with and without IB representation for (a) without time extrapolation and (b) with time extrapolation (Kanitz et al., 2019) 152

List of Tables

5.1 Rolling friction coefficient 29
5.2 Maximum and minimum void fraction 33
5.3 Summary of calibrated material parameters for numerical simulations with unresolved coupled CFD-DEM 35

7.1 Some frequently used drag force correlations 67

8.1 Material parameters for 1g model tests of suction dredging 105
8.2 Removed material weight during suction dredging 107
8.3 Experimental and numerical maximum peak value of the pressure measurements in the slope body 120

Contents

0 Preliminary remarks **1**

1 Introduction **3**

2 State of research **5**
2.1 Numerical modelling of multiphase problems 5
2.2 Numerical modelling of soil-water interactions at particle-scale 7

3 Objectives **10**
3.1 Methodology for the performed research work 12
3.2 Structure of this thesis 12

4 Numerical fundamentals of unresolved coupled CFD-DEM **14**
4.1 Discrete Element Method 14
4.2 Coupling of CFD and DEM 19
4.3 Fluid-particle interaction forces 21
4.4 Void fraction schemes 24
4.5 Immersed Boundary Method 25

5 Material parameter and instrumentation **26**
5.1 Calibration of material parameters 26
5.2 Particle displacement measurements 35

6 Internal Fluidisation **38**
6.1 Introduction 38
6.2 Experimental setup 40
6.3 Numerical setup 41
6.4 Experimental results 44
6.5 Numerical results 47
6.6 Summary 60

7 Suffusion **63**
7.1 Introduction 63
7.2 Drag force in particle assemblies 65
7.3 Influence of different drag force model on suffusion 68
7.4 Experimental setup 72
7.5 Numerical setup 76
7.6 Experimental results 80
7.7 Numerical results 83

7.8 Influence of the seepage velocity on the drag force models 97
7.9 Critical assessment of the investigations 99
7.10 Summary 99

8 Suction dredging **101**
8.1 Failure mechanisms of subaqueous slopes 101
8.2 Experimental setup 102
8.3 Numerical setup 105
8.4 Results 107
8.5 Approaches to model shear-dilatancy response in fluid 122
8.6 Verification of the new cohesion models 129

9 Extraction resistance of embedded objects **138**
9.1 Introduction 138
9.2 Experimental setup 139
9.3 Numerical setup 142
9.4 Results 143

10 Conclusion **155**

References **159**

Norms and standards **169**

Appendix A Notation **170**

Appendix B Material tests **175**
B.1 Shear cell test 176
B.2 Triaxial test 190
B.3 Loosest and densest packing 196
B.4 Permeability 199

Appendix C Cohesion model implementation in LIGGGHTS® **203**

0 Preliminary remarks

Some parts of this thesis have already been published in the following papers:

- Kanitz, M.; Grabe, J. (2018): *Experimental Study of the Influence of the Pore Water Pressure Evolution and the Shear Band Formation on the Extraction Resistance of Submerged Anchor Plates.* In: Volume 9: Offshore Geotechnics; Honoring Symposium for Professor Bernard Molin on Marine and Offshore Hydrodynamics. ASME 2018 37th International Conference on Ocean, Offshore and Arctic Engineering. Madrid, Spain, Sunday 17 June 2018: ASME, DOI: V009T10A004.

- Kanitz, M.; Grabe, J. (2019): *Gekoppelte CFD-DEM-Simulation zum Verflüssigungsverhalten gesättigter Sande. In: Tagungband zum BAW-Kolloquium Numerik in der Geotechnik.* Numerik in der Geotechnik. Karlsruhe, Germany, 9. - 10. October. Bundesanstalt für Wasserbau (BAW), pp. 31—36.

- Kanitz, M.; Grabe, J. (2019): *Multiscale investigation of suffusion with coupled CFD-DEM.* In: Proceedings of 2nd International Conference on the Material Point Method for Soil-Water-Structure Interaction 2019. Cambridge, UK, pp. 122–128. URL: http://mpm2019.eu/papers, accessed: 2019-05-08.

- Kanitz, M.; Hager, A.; Grabe, J.; Goniva, C. (2019): *Numerical and experimental analysis of the extraction mechanism of an anchor plate embedded in saturated sand.* In: Computers and Geotechnics 111, S. 191–201. DOI: 10.1016/j.compgeo.2019.03.014.

- Kanitz, Manuela; Grabe, Juergen (2019): *Influence of Suction Dredging on the Failure Mechanism of Sandy Submarine Slopes: Revisited With a Coupled Numerical Approach.* In: Volume 1: Offshore Technology; Offshore Geotechnics. ASME 2019 38th International Conference on Ocean, Offshore and Arctic Engineering. Glasgow, Scotland, UK, 6/9/2019 - 6/14/2019: American Society of Mechanical Engineers.

- Kanitz, M.; Grabe, J. (2020): *The influence of the void fraction on the particle migration: a coupled CFD-DEM study about drag force correlations.* In: International Journal for Numerical and Analytical Methods in Geomechanics, DOI: 10.1002/nag.3131.

1 Introduction

Particles and their effects on each other are everywhere. Maybe while reading this thesis, the food that you are eating falls down in particles and piles up onto your desk close to the angle of repose. There is a good chance that a small disturbance will exceed its critical angle and an avalanche flows to the ground. Now when accidentally spilling your coffee onto that particle assembly, a particle-fluid system lies on your desk.
Saturated soil can be classified as a particle-fluid system. The interaction of pore water and soil grains at particle-scale level specifies the behaviour of the soil at the macroscopic level. These interactions are the cause of the complex and non-linear behaviour of saturated soil compared, for example, to steel. Already Victor Hugo in his masterpiece *Les Misérables* asked the question if the patterns created by the movement of sand grains are in no small part responsible for the shape and feel of the natural world that we live in. This statement is probably a little too wide, but a better understanding of the mechanisms at the particle-scale level improves our knowledge of the complex soil behaviour in general.
While it is not easy to perform laboratory or model tests with the ability to "look inside" the soil structure and investigate what happens at particle-scale, numerical tools can be an adequate tool. Recently, due to increasing computational power, methods that map the motion of grains on particle-scale level have become more and more important. The interest in multi-scale methods, where we can investigate the micro-mechanical processes of particles subjected to fluid flow, increases continuously. One of these methods is unresolved coupled CFD-DEM, which is used in this thesis. Unresolved coupled CFD-DEM is a combination of the Computational Fluid Dynamics (CFD) with the Discrete Element Method (DEM). CFD solves the fluid flow while DEM tracks the soil grain motion.
However, before being able to use numerical methods like this for an in-depth analysis of problems at particle-scale, the tool needs to be verified if it captures the physics accurately. While considerable work has been carried out in the field of chemical engineering with unresolved coupled CFD-DEM, in geotechnical engineering, research only begins. Hence, we need to revise this method thoroughly to identify its limits. Therefore, we need an understanding of the governing physical mechanisms to formulate possible extensions or carry out improvements to meet the need of unresolved coupled CFD-DEM to be used successfully in geotechnical engineering. Experimental investigations are crucial for this purpose. Thus, in this thesis, the following key questions are examined:

1. What conclusions can we draw by combining experimental and numerical investigations regarding the influence of the interaction between soil particles and pore water?

2. What are the opportunities concerning an improved understanding of soil behaviour using unresolved CFD-DEM?

3. Where are the limits of unresolved CFD-DEM and what must be considered?

In order to specify these general key questions, the state of research of multi-scale methods and the application of different numerical methods enabling the investigation at particle-scale in geotechnical engineering are evaluated within the next chapter. Additionally, reviewing existing applications of unresolved coupled CFD-DEM in geotechnical engineering will reveal if the method is verified and applied thoroughly and if further research and developments are required. Based on the evaluation of the state of research, the scope of work and research aim will be formulated.

2 State of research

This chapter first gives a brief introduction to different approaches for the modelling of multiphase (solid-fluid) problems. Then, the state of research concerning the modelling of soil-water interaction at particle-scale is presented.

2.1 Numerical modelling of multiphase problems

The two most important approaches to solve the motion of material are the Eulerian and the Lagrangian method. Consider a flow field where one wants to solve the displacement of an observed material. In the Eulerian method, the motion of the material is regarded at a fixed location. When the observer follows the material as it moves through the observation space, this method is called Lagrangian. The investigation of multiphase problems is often favourable to realise with coupled methods, especially when it comes to the numerical simulation of fluid-solid systems. The user has the choice between a variety of methods, which are either based on Euler-Euler or Euler-Lagrange approaches. Depending on the length scales of the considered physical phenomena which are needed to compute the multiphase problem, various numerical approaches are available. The length scales can be classified into micro-, meso- and macro-scale approaches. In the following, a brief overview of the existing approaches at the micro-, meso- and macro-scale is given.

2.1.1 Micro-scale approach

The micro-scale approach applies to systems up to a size of approximately 1 mm (Sommerfeld, 2017). At this scale, Direct Numerical Simulation (DNS) is applied. The numerical grid has to be very fine, usually smaller than the Kolmogorov (dissipation) scale, to compute all the relevant flow scales, i. e. time, length and velocity to resolve the smallest scales of turbulence (Landahl et al., 1998). In this way, the particles are resolved by the numerical grid, and the flow field around them can be computed. However, the size of the computational domain is limited due to the fine mesh grid.

2.1.2 Meso-scale approach

When larger problems need to be considered, the multiphase flow can be solved at the meso level. This scale level can be applied to problems up to approximately 10 cm (Sommerfeld, 2017). At this scale, PR-DNS (Particle Resolved DNS) is used. The particle moves through a fixed Eulerian grid, and the particle's surface is treated as a no-slip wall boundary condition (the fluid will have zero velocity relative to the boundary). Another approach makes use of adaptive grids that follow the resolved particle (immersed boundary approach,

see Sec. 4.5). Amongst others, resolved CFD-DEM and LBM-DEM can be classified as PR-DNS. In resolved CFD-DEM, the fluid flow is solved using the Navier-Stokes equations with methods of CFD. The particle motion is tracked in a Lagrangian way, using DEM. The coupling between the fluid phase and the dispersed phase is realised by adding a finite and localised forcing to the Navier-Stokes equations. Using resolved CFD-DEM, no numerical grid fitted to the particle surface is necessary as a no-slip boundary condition is applied at the particle surface. LBM-DEM is a combination of the Lattice-Boltzmann method (LBM) for the computation of the fluid flow and DEM to solve the particle motion. In contrast to CFD, it is not the Navier-Stokes equations but the Lattice-Boltzman equations, which are solved. These equations describe the change of state of the fluid through a probability distribution function. LBM is numerically very efficient and easy to parallelise. The interaction between the fluid phase and the dispersed phase is realised by using a bounce-back boundary condition on the particle surface (Guo et al., 2002).

2.1.3 Macro-scale approach

The macro-scale approach can be applied to problems of approximately 10 m. In this regime, an Euler-Euler approach, namely the two-fluid method (TFM), can be used. In this method, both the fluid phase and the dispersed phase are considered as interacting continua. Both phases share the control volume of the computational domain according to their respective volume fraction. The mean properties of both phases are derived by averaging procedures (Anderson and Jackson, 1967). The conservation equations for both phases have a similar structure and are coupled by exchange terms for mass, momentum, and heat. TFM is a favourable approach for dense dispersed two-phase flows, preferably with monodisperse particles. When a particle size distribution needs to be considered, it is necessary to solve the governing equations for each size class, which increases the computational effort (Sommerfeld, 2017). Additionally, as the particle motion is not tracked directly as in DEM, accurate formulation of colliding particles and wall collisions is crucial (Fede et al., 2016). Furthermore, the drag force acting on groups of particles is difficult to derive (Loha et al., 2012).

2.1.4 Macro-meso approach

If the problems to be analysed are to be examined on different scales, multi-scale approaches can be used. For example, if the computation of the interaction between particles and their effect on the flow is required, but larger dimensions need to be mapped at the same time, a macro-meso approach is suitable. At this multi-scale level, typically, a hybrid Euler-Lagrange approach is used. The fluid flow is solved at the macro level using CFD, and DEM tracks the motion of the dispersed phase at the meso level. The particles are considered as point particles. Thus, they are smaller than the numerical grid. This results in quite large computational cells. The fluid flow is then solved employing the Reynolds-averaged Navier-Stokes equations (RANS) in connection with an appropriate turbulence model if necessary. The dispersed phase is included by local-average variables based on the TFM formulation (Anderson and Jackson, 1967). The combination of RANS-CFD and

DEM is called unresolved CFD-DEM (see Ch. 4) and was first proposed by Tsuji et al. (1993).

2.2 Numerical modelling of soil-water interactions at particle-scale

With the rising computational power and the increased interest of the mechanisms that occur at particle-scale in geotechnical engineering, the focus on numerical modelling of soil-water interactions at particle-scale has increased significantly. This section presents a literature review on analyses carried out with numerical methods, which depict the physical mechanisms at particle-scale.

2.2.1 Soil-water interactions analysed with LBM-DEM

As described in the previous section, LBM-DEM is characterised as PR-DNS as the fluid flow between the particles is resolved by lattices which are smaller than the particles modelled by DEM. This method can be used to model the fluid flow through porous media accurately but is restricted to small dimensions. However, the coupling of LBM and DEM is very efficient, and the research interest grows continuously. Kumar et al. (2012) and Kumar et al. (2017) investigated immersed granular column collapses. The permeability of the soil specimen was computed according to the Cozeny-Karman equation by reducing the radius during the LBM step. Consequently, they could study different permeabilities. Kumar et al. (2012) found that less permeable columns have a longer runout distance than columns with higher permeability. Thus, the runout distance increases with decreasing permeability while the time required for the column to start flowing increases with decreasing permeability. In a later study, Kumar et al. (2017) analysed the effect of packing density and slope angle on the granular column with 1000 disks. They compared the results of dry against immersed column collapses. They found that the runout distance for all slope angles is longer in the dry case compared to the immersed case caused by the drag force that acts on the particles in the immersed regime. Thereby, the failure plane in the failing mass increases with increasing slope angle. The analysis of the impact of the initial packing density revealed longer runout distances for loose packings compared to dense packings. Kumar et al. (2017) found that the dense packing experiences an increased drag resistance in comparison to the loose specimen. The failing of the dense packing causes this increased drag at a steeper angle due to arising negative excess pore water pressure which increases the grain-to-grain stresses. Han and Cundall (2013) quantitatively verified a three-dimensional LBM-DEM model against the pressure drop through a fixed particle bed represented by the Ergun equation (Ergun, 1952) and the seepage flow through a single column of spheres. Furthermore, they qualitatively studied sand arching inside a perforation cavity. Both the pressure drop as well as the arising pore water pressure in the case of an upward seepage flow were compared to the analytical solutions revealing good agreement. The arching of sand in a polydisperse particle packing was modelled inspired by the trap door experiment by Terzaghi (1936), where a hole is drilled at the bottom of a cylindrical specimen. Han and Cundall (2013) could observe equilibrium of the dry

sand column caused by the development of a self-sustaining arch after opening the trap door. They then performed the same test with an immersed specimen and investigated the influence of increasing the hydraulic gradient. They found that the sand arch inside the specimen remains stable until a critical gradient is reached. The developed arch collapses and a new one forms inside the sand until a higher critical gradient is reached. Ngoma et al. (2014) and Mansouri et al. (2017) investigated the fluidisation of soil with LBM-DEM. Ngoma et al. (2014) performed experimental and two-dimensional numerical tests with 5000 glass beads. They analysed the formation of localised fluidisation zones at two water injection holes in a rectangular box. The flow rate was increased gradually. They could observe that the water flow creates cavities, which interact and merge to form a single fluidised chimney. With the increasing gap between the injection holes, this merging phenomenon vanishes, and two individual fluidisation chimneys occur. The numerical results showed a similar behaviour revealing qualitative agreement. Mansouri et al. (2017) investigated the fluidisation behaviour with a three-dimensional LBM-DEM model of 100 spheres in a polydisperse packing. The model was validated against the sedimentation of two spheres. In the fluidisation tests, they investigated the behaviour of the particle packing with increasing hydraulic gradient. Therefore, they started with a hydraulic gradient i below the critical hydraulic gradient i_c and increasing it gradually until $i >> i_c$. The critical hydraulic gradient is defined as the required gradient to fluidise soil (Terzaghi, 1943). When $i << i_c$, no grain movement could be observed. However, when i is slightly less than i_c ($i \approx 0.92 i_c$), relaxing in the particle bed occurs, and the grains undergo a carrying upwards. They found that $i \approx 0.92 i_c$ indicates the minimum hydraulic gradient to trigger fluidisation. The fluidisation develops step by step. The grains start to rearrange at the bottom, which allows the creation of cavities. No pressure drop occurs in this zone, and the hydraulic gradient through the bed increases. This initiates an uprising of this zone leading to loosening of the specimen.

2.2.2 Soil-water interactions analysed with unresolved coupled CFD-DEM

Unresolved coupled CFD-DEM can be used to investigate the interaction between pore water and the soil grains in geotechnical engineering at a larger scale in comparison to LBM-DEM. This method enables us to take into account the effect of the pore water onto the soil grains and vice versa. Thus, it is not necessary to formulate additional constitutive models because the response of the soil structure on the hydrodynamic influence is computed directly. This feature is reflected in the main research carried out in geotechnical engineering using unresolved CFD-DEM. Zeghal and El Shamy (2004) and El Shamy and Zeghal (2005) investigated the liquefaction behaviour in sands due to different hydraulic gradient amplitudes and depositing. The validation was carried out by modelling seepage through a particle assembly and comparing it against Darcy flow, which led to a good agreement. H. Tao and J. Tao (2017) investigated the problem of piping in soil with unresolved CFD-DEM. The effect of the particle size distribution, specific gravity, and particle-particle, as well as particle-wall friction, was analysed. H. Tao and J. Tao (2017) determined that the critical hydraulic gradient required to initiate piping is larger than the commonly used gradient by the theory of Terzaghi. However, the model itself

was not validated against experimental data. Instead, experimental data from a spouted bed reactor by van Buijtenen et al. (2011) was used to validate the method. In general, the investigation of internal erosion in cohesionless soil is commonly carried out with the unresolved CFD-DEM. H. Tao and J. Tao (2017) and Hu et al. (2019) investigated suffusion using this multi-scale method. H. Tao and J. Tao (2017) analysed the erosion rate by varying the fine fraction content. They concluded that a higher fine fraction content leads to increased erosion. Hu et al. (2019) implemented a confined boundary condition by including a mesh on top of the investigated soil column. Hu et al. (2019) investigated the loss of stability in a soil column due to suffusion by analysing the evolution of the contact force network. Both works were not validated against experimental data. The application of unresolved coupled CFD-DEM is not restricted to erosion problems. J. Zhao and Shan (2013) investigated sandpiling in water. The validation was carried out by a sedimentation test of a single particle and a one-dimensional consolidation for different void fraction calculation. The latter was compared to the classic Terzaghi theory. The agreement of both validation cases was good. J. Zhao and Shan (2013) then modelled conical sandpiling both in wet and in dry conditions. They could find that the repose angle in wet samples is smaller than in dry samples. T. Zhao et al. (2016) investigated the creation of an impulse wave based on the Vajont dam failure. Likewise, they modelled a rockslide entering the water at a high velocity and thus creating a wave in a pseudo-two-dimensional way. The coarse-graining method (see Sec. 4.1.4) was used to model larger dimension while maintaining reasonable computational costs. To model the two different fluid phases (i. e. gas and water), they implemented the so-called Volume of Fraction method (VOF). The generated wave is modelled in a reasonable qualitative way.

3 Objectives

Chapter 2 presented some work carried out in geotechnical engineering with LBM-DEM and unresolved coupled CFD-DEM. From this, it can be deduced that these methods are still in its infancy when it comes to the application in geotechnical engineering. It is concluded that LBM-DEM can only be applied to very small problems as the largest investigated problem consisted of 5000 particles. For problems with larger dimensions, unresolved CFD-DEM should be used. However, the state of research revealed that the presented investigation using this numerical tool lack of validation with experimental data from the same problem. A comparison of the numerical results against experimental data featuring the considered phenomenon is crucial for a multiscale method (Sommerfeld, 2017). For this reason, this thesis investigates four different problems from the field of geotechnical engineering with unresolved coupled CFD-DEM with appropriate validation by small-scale model tests. For this purpose, four problems are selected, which are difficult to model with continuum mechanical approaches. These include large deformations, a significant influence of fluid-particle interaction forces and the movement of single grains in the soil structure. In this context, the following geotechnical problems are investigated:

1. Internal fluidisation in sand
2. Suffusion
3. Influence of suction dredging on the failure behaviour of submarine slopes
4. Extraction of plates embedded in saturated sand

From a numerical point of view, the fluidisation of soils represents the simplest of these four problems since numerous investigations already verified unresolved coupled CFD-DEM for modelling fluidised bed reactor (Anderson and Jackson, 1967; Peng and Fan, 1997; Tsuji et al., 1993; Koch and Hill, 2001; J. Li and Kuipers, 2003; Wang et al., 2014; Fede et al., 2016, and many others). Some investigations on suffusion with unresolved coupled CFD-DEM can be found in the literature (cf. Sec. 2.2), but they lack proper validation, especially in regards to the employed drag force model for the depiction of the interaction between soil grains and seepage flow. Suction dredging of sand and the extraction of an embedded plate are difficult to model numerically with continuum approaches. They require sophisticated constitutive models to compute on the one hand the large displacements of the soil and on the other hand, the influence of the pore water on the behaviour of the soil skeleton. Thus, numerical investigations with unresolved coupled CFD-DEM offer a chance to capture both. To the author's knowledge, no numerical investigations of suction dredging of sandy submarine slopes and the extraction of embedded plates exist with unresolved coupled CFD-DEM. These four problems are each of huge complexity so that

this thesis will only focus on some mechanisms and their analysis. Thus, the following specific questions are treated for these particular problems:

1. **Fluidisation:** Seepage flow can cause fluidisation of soil. The underlying mechanisms are complex due to the high dynamics in this multiphase regime. This thesis will investigate whether the depiction of the internal fluidisation of soil with unresolved coupled CFD-DEM is accurate enough to help assess the risk of a possible hydraulic failure in sands. Furthermore, two criteria to assess the risk of possible fluidisation are analysed: The first criterion is based on vanishing grain-to-grain stresses due to the seepage force based on Terzaghi (1943). The second criterion is deduced from fluidised bed reactors investigated in the framework of chemical engineering. The fluidisation behaviour of the soil specimen meeting these two different criteria will be investigated.

2. **Suffusion:** Many criteria to assess the possible risk of suffusion in soil can be found in the literature. These are mainly calibrated against experimental tests and may not be adequate for every kind of soil. Numerical modelling of suffusion can help to assess if the internal instability vanishes due to the erosion of fines. Unresolved coupled CFD-DEM can depict the interaction between the seepage flow and the soil particles. However, the computation of these is dependent on the used drag force model. Now the question arises, how the drag force models, which are available in the literature, influence the erosion of the fines. Are the available models suitable for modelling suffusion, and how does the drag force influence the erosion of the fines through the coarse particle matrix?

3. **Suction dredging of sandy submarine slopes:** Effects from dilatancy and contractancy mainly influence the failure behaviour of sandy submarine slopes. These occur at the particle-scale level and the resulting pore pressure changes either enhance or reduce the effective stresses in the soil skeleton. The influence of the pore water pressure on the particle displacement will be analysed. The effect of dilatant and contractant behaviour of saturated sand on the failure mechanism of the slope will be investigated experimentally and numerically. The question is whether unresolved coupled CFD-DEM captures the influence of dilatancy and contractancy onto the shear strength of sandy submarine slopes.

4. **Extraction of an embedded plate:** Complex mechanisms caused by the rearrangement of the soil grains and the interaction with the pore water define the extraction resistance. Undrained and partially drained behaviour of the surrounding soil plays a crucial role in this context. The question arises whether unresolved coupled CFD-DEM depicts undrained and partially drained behaviour to compute the extraction resistance. Furthermore, how does the motion of the soil grains contributes to the extraction resistance?

These problem-related questions help to answer the target questions posed in Ch. 1 regarding the applicability and the limits of unresolved coupled CFD-DEM. The investigation of these problems reveals what chances investigations on particle-scale, both experimentally and numerically offer.

3.1 Methodology for the performed research work

Small-scale model tests are carried out in combination with numerical models performed with unresolved coupled CFD-DEM to meet the formulated objectives. Small-scale tests are chosen because due to the particle-scale nature of DEM, computational costs limit the dimension of the investigated problems. Thus, the results obtained from the small-scale model tests cannot directly be applied to reality caused by scale effects. However, they allow studying the investigated problems in detail to analyse the interaction between soil grains and fluid flow. The numerical models have identical dimensions as the model tests to enable validation. Both qualitative and quantitative methods are employed to perform accurate validation. The combination of experimental and numerical investigation enable an extensive analysis of the governing physical mechanism.
For qualitative comparison and experimental analysis of the displacement and particle velocities, a high-speed camera tracks the motion of the particles in the small-scale model tests. The evaluation of the velocity of the particles is carried out with Particle Image Velocimetry (PIV), for which, the tools GeoPIV-RG (Stanier et al., 2016) and PIVLab (Thielicke and Stamhuis, 2014) are used. Furthermore, the pore water pressure, void fraction changes and the extraction resistance in the case of the embedded plate are measured to link these physical properties with the particle velocities. These measurements additionally allow a quantitative comparison with the numerical results.
For numerical modelling with unresolved coupled CFD-DEM the open-source software package CFDEM®coupling, which combines the discrete element code LIGGGHTS® with CFD solvers based on OpenFOAM® is chosen (Kloss et al., 2012). For the validation of the models, the standard implementation of CFDEM®coupling is used in the first step. If the investigations show that this standard implementation is not sufficient to represent the main mechanisms in the particle-fluid system, possible extensions are presented and investigated.

3.2 Structure of this thesis

This thesis commences with a brief introduction of the fundamentals of unresolved coupled CFD-DEM (cf. Ch. 4) followed by a presentation of the relevant material parameters and their calibration (cf. Ch. 5). The same chapter includes an introduction of the PIV and the employed software tools GeoPIV-RG and PIVLab (cf. Ch. 5.2). Then, the investigations on the four relevant problems are presented. Ch. 6 presents the investigations on internal fluidisation in sand and Ch. 7 the analysis on the role of the drag force in suffusion. Ch. 8 includes the analysis of suction dredging of glass beads slopes and sandy submarine slopes. Ch. 9 depicts the analysis of the extraction of a submerged anchor plate. The investigations of each problem follow the same structure:

1. Introduction of the problem including a literature review
2. Concept of the experimental and numerical setup
3. Presentation of experimental and numerical results including comparison and interpretation of the results

4. Analysis of possible or required developments and extension

5. Conclusion and assessment of the presented results

The thesis concludes in a summary of the main results aiming to answer the target questions raised at the beginning of this thesis.

4 Numerical fundamentals of unresolved coupled CFD-DEM

The combination of Computational Fluid Dynamics (CFD) and Discrete Element Method (DEM), which is used in this contribution, is an Euler-Lagrange approach and was firstly proposed by Tsuji et al. (1993). In this approach, the fluid phase is modelled with CFD, where the Reynolds-averaged Navier-Stokes equations (RANS) are solved for the fluid and pressure field, and the soil is modelled as a particulate phase with DEM.

4.1 Discrete Element Method

Soil is a granular medium composed of particles moving independently and interacting with other soil particles at contact points. The different interaction points and displacements of the soil particles during different loading states result in complex responses, which can still not be described exactly by constitutive relations. In laboratory tests, the stress can only be measured at the boundary layers. The stress path inside the soil specimen cannot be monitored. This data can be obtained using DEM.

DEM is a Lagrangian method in which the dynamic behaviour of a system formed by a large number of discrete bodies can be studied. The method depicts the movement of every particle, either translational and rotational. It enables the investigation of micro-mechanical processes in granular mediums. These processes can rarely be monitored in physical modelling and continuum methods are not suitable for this purpose as constitutive modelling merges the behaviour of the individual particles to a macro-scale level. Though, understanding the behaviour of the solid material at the microscopic scale, whether it is the interaction with other solids or the interaction with the surrounding medium (e. g. water, gas), is essential to predict the behaviour of the material at a macroscopic scale.

4.1.1 Basic principle of DEM

Cundall and Strack (1979) firstly introduced DEM for rock mechanics problems in order to analyse the behaviour of rock masses at microscale, e. g. at a particle-scale level. The movement of the individual particles is explicitly tracked in a Lagrangian way. During one time step, the velocity and acceleration of every particle is assumed to be constant. To avoid that disturbances in one time step propagate further away than its immediate neighbour, the time step has to be chosen small enough. The resultant forces are then

calculated by the interaction with all neighbours of each particle. The governing equation to determine the resultant forces is formed by Newton's second law of motion:

$$m_i \frac{\partial \boldsymbol{v}_i}{\partial t} = \sum_j \boldsymbol{F}_{ij}^c + \sum_k \boldsymbol{F}_{ik}^{nc} + \boldsymbol{F}_i^f + \boldsymbol{F}_i^g \tag{4.1}$$

$$I_i \frac{\partial \omega_i}{\partial t} = \sum_i \boldsymbol{M}_{ij} \tag{4.2}$$

where $\boldsymbol{v}_i$ and $\boldsymbol{\omega}_i$ describe the translational and angular velocity of the particle i. $\boldsymbol{F}_{ij}^c$ and $\boldsymbol{M}_{ij}$ represent the contact force between particle i and j and the torque acting on the particle i by particle j or the walls. The last two parameters in Eqn. 4.1 $\boldsymbol{F}_i^f$ and $\boldsymbol{F}_i^g$ are the particle-fluid interaction force and the gravitational force. $\boldsymbol{F}_{ik}^{nc}$ describes the non-contact forces by a particle k or other sources. This includes for example capillary forces. Once the acting forces on the particle are determined, the calculation of the displacement is easily done. Hence, the crucial point is the accurate formulation of the forces. Various models have been proposed to calculate these, which are discussed in the following sections.

4.1.2 Contact forces

Two different methods in DEM can describe the contact between the particles: The hard-sphere and the soft-sphere contact model.
In a system where the collision time between particles is not very long and does not happen often, the particles move more or less freely in the system until a new collision is happening. This means that the state variables like position and velocity are not evaluated until the next contact occurs. The velocity after the collision is calculated via the pre-collision velocity based on the momentum conversation law. This approach is the so-called hard-sphere model, and it is efficient regarding computational costs as the velocity of the particles is not updated until a collision happens. Nevertheless, this formulation implies that the time of the freely moving particles is much longer than the duration of contact and that there is only one contact at a time. Hence, for systems that are contact-dominated, e. g. dense regimes, this formulation is not suitable (Norouzi et al., 2016).
In the soft-sphere contact model developed by Cundall and Hart (1992), a slight overlap of the contacting particles is allowed to take into account the deformation of the particles at collision. Hence, the contact is not on a single point but instead on a definable area. The contact distribution over this area can be divided into a tangential and a normal part. The determination of the exact description of the distribution is very complicated as it depends on the shape of the particle, its material properties and the state of motion. Likewise, different contact models exist to meet both computational efficiency and physical accuracy. The most common contact force model is the so-called linear spring-dashpot model (LSDM) proposed by Cundall and Hart (1992). In this model, the spring is used for the elastic deformation and the dashpot accounts for the viscous dissipation. Fig. 4.1 (left) shows the arrangement of spring and dashpot for a normal displacement. In the middle the model for a tangential contact is shown. In order to account for the deformation of the particles at contact, the particles are overlapping slightly by $x_{p,n}$ in normal and $x_{p,t}$ in tangential direction. The normal and tangential forces tending to repulse the particles can

then be calculated from this spatial overlap. Hence, the normal contact force is determined through:

$$\boldsymbol{F}_n = -k_n \Delta \boldsymbol{x}_{p,n} - c_n \Delta \boldsymbol{v}_n \tag{4.3}$$

where $\Delta \boldsymbol{v}_n$ is the relative normal velocity of the particle. In a similar way, the tangential force can be determined through:

$$\boldsymbol{F}_t = -k_t \Delta \boldsymbol{x}_{p,t} + c_t \Delta \boldsymbol{v}_t \tag{4.4}$$

with $\Delta \boldsymbol{v}_n$ as the tangential velocity. $\Delta \boldsymbol{x}_{p(n,t)}$ is determined by

$$\Delta \boldsymbol{x}_{p(n,t)} = \boldsymbol{v}_{(n,t)} \Delta t \tag{4.5}$$

where Δt describes the time interval of the computation. This linear model is very simple and straightforward in its implementation which makes it attractive to use. However, there exist some issues that lead to an unrealistic behaviour, which are associated with the linearity of this viscoelastic model (Norouzi et al., 2016). Hertz (1881) firstly proposed a nonlinear viscoealstic model describing the collision between two elastic spheres in normal direction. During uniaxial loading of a spherical particle with a smooth stiff wall, the contact area deforms as a circle (cf. Fig. 4.2). Thereby, the radius of the contact area, the force and the internal pressure distribution depend on the particle radius, the stiffness and the deformation behaviour of the particle and the wall. Hertz (1881) describes the resulting parabolic pressure distribution $p_{el}(r_k)$ in the contact area with a radius $r_{k,el}$ through:

$$\left(\frac{p_{el}}{p_{\max}}\right)^2 = 1 - \left(\frac{r_k}{r_{k,el}}\right), r_k \leq r_{k,el} \tag{4.6}$$

where the maximum contact pressure in the centre of the contact area can be described by:

$$p_{\max} = \frac{3F_{el}}{2\pi r_{k,el}^2} \tag{4.7}$$

The radius $r_{k,el}$ is given as:

$$r_{k,el} = \left(\frac{3R^* F_{el}}{2E^*}\right)^{1/3} \tag{4.8}$$

The effective modulus of elasticity E^* of the contact partners is described by the following relationship between the modulus of elasticity of the wall E_w and the particle E_p:

$$E^* = 2\left(\frac{1-\nu_p^2}{E_p} + \frac{1-\nu_w^2}{E_w}\right)^{-1} \approx \frac{2}{1-\nu_2^2} E_p \tag{4.9}$$

Note that for the term on the right hand side, it is assumed that the wall is much stiffer than the particle ($E_w >> E_p, E_w \to \infty$). The radius R^* is a characteristic radius of the contact surface curvature:

$$R^* = \left(\frac{1}{r_p} + \frac{1}{r_p}\right)^{-1} \approx r_p \tag{4.10}$$

Hertz (1881) found that the relation between the elastic contact force and the displacement in normal direction is non-linear for the contact with one material:

$$F_{el} = \frac{2}{3} E^* \sqrt{R^* s^3} \approx \frac{4}{3} \frac{E_p}{1-\nu_p^2} \sqrt{\frac{d_p}{2} s^3} \tag{4.11}$$

where s is the elastic displacement:

$$s = r_{k,\mathrm{el}}^2 / R^* \tag{4.12}$$

Due to the parabolic curvature, the contact stiffness in normal direction increases with increasing displacement s and the particle diameter d_p (Tomas, 2001):

$$k_{n,el}^* = \frac{\partial F_{el}}{\partial s} = E^* \sqrt{R^* s} \approx \frac{\sqrt{2}}{1-\nu_p^2} E_p \sqrt{d_p s} \tag{4.13}$$

During the impact of the particle with the much stiffer wall, the contact stiffness $k_{n,el}$ equals the particle stiffness $k_{n,el,p}$:

$$k_{n,el}^* = \left(\frac{1}{k_{n,el,p}} + \frac{1}{k_{n,el,w}} \right)^{-1} \approx k_{n,el,p} \tag{4.14}$$

During compression with two walls, two contact areas are formed. The force-displacement relationship for compression is given analogously to Eqn. 4.11 as:

$$F_{\mathrm{el,w\text{-}p\text{-}w}} = \frac{1}{6} E^* \sqrt{d_p s^3} \approx \frac{1}{3} \frac{E_p}{\left(1-\nu_p^2\right)} \sqrt{d_p s^3} \tag{4.15}$$

The mean contact stiffness $k_{n,el,w-p-w}^*$ of this wall-particle-wall system can be determined by:

$$k_{n,el,w-p-w}^* = \frac{\partial F_{el,w-p-w}}{\partial s} \tag{4.16}$$

$$= \frac{1}{4} E^* \sqrt{d_p s} \approx \frac{1}{2\left(1-\mu_p^2\right)} E_p \sqrt{d_p s} \tag{4.17}$$

Mindlin and Deresiewicz (1953) extended the approach of Hertz (1881) to describe the elastic contact of particles in tangential direction. This model is known as the Hertz-Mindlin contact model (HMCM). This model includes a non-linear relationship between the normal force and normal displacement and a force-displacement relationship, which depends on the whole loading history and the rate of change of normal and tangential displacement. This approach gives a very accurate tangential collision force and it covers all collision regimes. Nevertheless, it is not practical as there is a great number of particles in a typical DEM simulation, which leads to a numerous amount of collisions in each time step. Hence, this model, although very accurate, is not reasonable regarding the computational costs. For this reason, simplified models based on the theory of Hertz & Mindlin have been developed. One approach is the adoption of Langston et al. (1994). Langston et al. (1994) implemented a direct force-displacement relation for the tangential force and the Hertz theory for the normal force. Due to its simplicity and the intuitive adoption, the simplified Hertz-Mindlin contact model by Langston et al. (1994) is commonly used in DEM simulations.

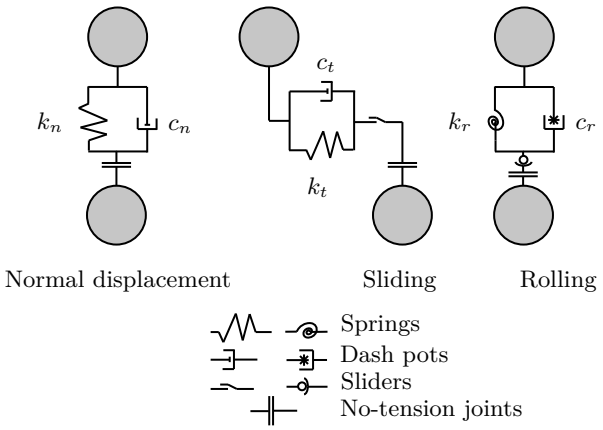


Figure 4.1: Contact handling of colliding particles (Kanitz et al., 2017)

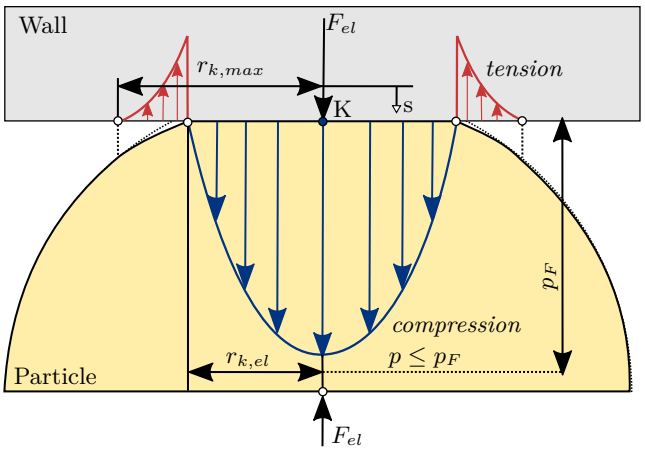


Figure 4.2: Pressure distribution $p_{\mathrm{el}}(r_k)$ in a wall-particle contact during elastic deformation, after (Antonyuk et al., 2010)

4.1.3 Rolling friction

The contact forces of colliding particles act on a contact point rather than at their mass centre, which results in a torque. The resulting torque is comprised of two components: a rotational torque caused by the interparticle contacts in the tangential direction and a rolling resistance torque. The latter arises from the unevenness of the contact pressure distribution. The rolling resistance torque causes resistance against the rotation of the particles, while the former causes the particles to rotate. The rolling resistance torque can be visualised by a particle rolling down a flat surface. The rolling resistance, dependent on the particle shape and its plastic deformation, slows down the rotation speed and finally stops it. Without the consideration of the rolling resistance, the particle rolls for a long time (Zhou et al., 1999). In order to account for the rolling friction in the numerical model, an additional set of elastic spring, dashpot, and slider is located at each contact point to deal with the torque, cf. Fig. 4.1 (right). This model was introduced by Iwashita (1998). In this concept, the elastic spring and the dashpot impose a resistance against the relative rotation from rolling. When the torque exceeds their resistance, meaning the rolling resistance, the slider starts working.

4.1.4 Coarse Graining

The higher the number of particles to model in DEM, the more expensive are the computational costs. In order to reduce these computational costs considerably, Bierwisch et al. (2009) proposed the so-called coarse-graining method. The idea is to construct an effective medium with a scaled particle size, which incorporates the same energy density and evolution of energy density as the original system with the unscaled particle. Accordingly, this one scaled particle represents a group of particles, and its physical behaviour is identical to the group of particles. Bierwisch et al. (2009) showed that the energy of the scaled system is preserved when the following parameter is identical to the unscaled system:

- particle density $\rho_s = \rho_s'$
- coefficient of restitution $e_n = e_n'$
- friction coefficient $\mu = \mu'$
- Young's modulus $E = E'$

Additionally, the force laws have to be scaled in order to obtain unchanged energy densities (Bierwisch et al., 2009). Generally, coarse-graining allows a significant reduction of the computational costs, and when correctly scaled, the bulk properties do not depend on the scaling.

4.2 Coupling of CFD and DEM

CFD is a powerful tool to analyse the flow of continuous fluid. Different discretisation techniques exist within the framework of CFD. This contribution uses the Finite Volume Method (FVM). This method decomposes the computation domain in a mesh, and solves

the governing equations in each cell of the mesh. The governing equations comply with the law of conservation of mass and momentum in terms of locally averaged variables firstly proposed by Anderson and Jackson (1967). Hence, the two governing equations are the continuity equation and the Reynolds-averaged Navier-Stokes equations (RANS). RANS are the time averaged Navier-Stokes equations through turbulence models or Reynolds stress equations. To consider the presence of particles in the description of the flow field, two variables are added: the void fraction n and the term for momentum exchange between the fluid and the particulate phase R_{pf}. The former describes the percentage of fluid in a cell and the latter stores the fluid-particle interaction forces. The conservation of mass and momentum of a fluid with presence of particles is then given by:

$$\frac{\partial}{\partial t} n + \nabla \cdot (n\boldsymbol{u}) = 0 \tag{4.18}$$

$$\begin{aligned} \frac{\partial}{\partial t}(\rho_f n\boldsymbol{u}) + \nabla \cdot (\rho_f n\boldsymbol{u}\boldsymbol{u}) = -n\nabla p + \nabla \cdot (n\tau_f) \\ + n\rho_f \boldsymbol{g} + R_{pf} \end{aligned} \tag{4.19}$$

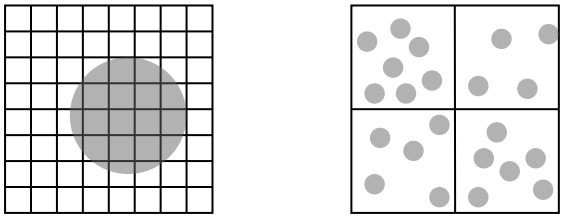
where $\boldsymbol{u}$ and p describe the fluid velocity and pressure. τ_f and ρ_f are the fluid viscous stress tensor and the density of the fluid. R_{pf} is exchanged frequently between the DEM- and the CFD-solver. It is determined through the following equation

$$R_{pf} = K_{pf}(\boldsymbol{u} - \boldsymbol{v}) \tag{4.20}$$

with the interaction force coefficient K_{pf} (Kloss et al., 2012). This coefficient is obtained by the superposition of all particle-fluid interaction forces by

$$K_{pf} = \frac{\sum_i F_i^f}{V_{\text{cell}}|\boldsymbol{u} - \boldsymbol{v}|} \tag{4.21}$$

V_{cell} is the volume of the computational cell. In addition to the interaction forces between solid (particle) and fluid phase, the scale level of the methods to be coupled have to be beard in mind. CFD computes the governing equations at a computational cell level, DEM at the individual particle level. In general, there exist two different methods in coupled CFD-DEM to connect these different scale levels: resolved and unresolved CFD-DEM. In resolved CFD-DEM, the CFD cells are significantly smaller than the particles (cf. Fig. 4.3 left). This method computes the fluid flow around the particles accurately. However, the resolved approach leads to a high number of CFD cells. When one particle is covered by e. g. 10 CFD cells, the number of required CFD cells increases dramatically with the increasing number of particles. Hence, only several particles in the order of magnitude of $\mathcal{O}^3$ can be modelled in a reasonable amount of computational time. In the unresolved CFD-DEM method, the CFD cells are notably larger than the particles (cf. Fig. 4.3 right). This method enables the computation of problems with a number of particles in the order of magnitude of $\mathcal{O}^6$. However, this method does not solve the fluid flow around the individual particles. The flow velocity is averaged in the CFD cell, and the fluid force is equally applied to the particles lying within one cell. Accordingly, one needs force models to



a) Resolved CFD-DEM b) Unresolved CFD-DEM

Figure 4.3: Discretisation scheme of resolved CFD-DEM (left) and unresolved CFD-DEM (right) (Hager, 2014)

compute the interaction forces between the particles and the fluid. In this method, the computational costs arise mainly on the DEM side.
When choosing unresolved CFD-DEM, one needs to consider some principles of volume-averaging (Crowe et al., 2012). The averaging volume, e. g. the CFD cell volume, must be sufficiently large that the average value does not depend on the mesh size. The cell size has to contain enough particles such that variations in the fluid-particle interaction forces are maintained below a minimum value. Additionally, when the particle size approaches the mesh size, the void fraction can reach zero, which leads to numerical instabilities. Pirker et al. (2011) and Marshall and Sala (2013) stated that the CFD mesh size should at least measure $\geq 3 \cdot d_p$ to avoid numerical instabilities.

4.3 Fluid-particle interaction forces

In general, when fluid flows through an assembly of particles, each particle experiences three types of forces:

1. Hydrostatic force: Buoyancy-type force due to the average pressure gradient around the particle,

2. Unsteady force: Virtual mass force and Basset history force,

3. Hydrodynamic force: Force resulting from local friction losses, which consists of the drag force and the viscous force and lift forces.

The next sections give a brief introduction to these fluid-particle interaction forces.

4.3.1 Pressure gradient force

The pressure gradient force results in buoyancy. It is caused by a pressure difference at the top and the bottom of the particle, which gives rise to a force in the direction of the pressure gradient. The pressure gradient force acting on a particle i is determined by

$$F_{p,i} = -V_p \frac{\delta p}{\delta x_i} \tag{4.22}$$

where V_p is the volume of the particle. The corresponding force caused by the hydrostatic pressure is equivalently given by:

$$F_{p,z} = \rho_f g V_p \tag{4.23}$$

It states that the force is equal to the weight of the displaced fluid, also known as the *Archimedes principle* (Crowe et al., 2012).

4.3.2 Drag force

The reaction force from particles onto fluid results in energy dissipation. As a consequence, the pressure in the fluid reduces while it passes through the bed. The most widely known theory to calculate this pressure drop is Darcy's Law:

$$-\frac{\Delta p}{L} = \frac{\mu_f}{K_f}\boldsymbol{u} \tag{4.24}$$

with the macroscopic parameter of the permeability K_f and the dynamic viscosity μ_f. It describes a linear relationship between the pressure gradient Δp and the flow field at the macroscopic level. However, it has been shown that Darcy's law is restricted to creeping flows and only valid for homogeneous, isotropic, unbounded and non-deformable porous media (Auriault, 1987). Likewise, more accurate drag force models are required to account for energy dissipation, which applies to a wider range of applications. The drag force acting on a single particle in fluid flow can be derived analytically by Newton's equation:

$$F_{D0} = C_D \pi d_p^2 |\boldsymbol{u} - \mathbf{v}|(\boldsymbol{u} - \boldsymbol{v})/8 \tag{4.25}$$

where C_D is the drag force coefficient. It is dependent on the Reynolds number Re and liquid properties. In a flow regime, three regions can be defined: the Stoke's Law region, the transition region and the Newton's Law region. For each of these regions, C_D is determined by well-established correlations (Zhu et al., 2007). However, analytical formulations of the drag force in particle assemblies are difficult to derive as an adequate model must account for the surface of every particle (Crowe et al., 2012). The presence of other particles reduces the space for the fluid to flow, which generates sharp fluid velocity gradients. As a consequence, the shear stress on the particle surface increases (Zhu et al., 2007). The drag force in particle-fluid systems strongly depends on the pore structure and the pore level physics, which generally requires it to be estimated experimentally or through the use of empirical correlations. In general, two methods have been used so far to find correlations for the drag force in particle-fluid systems:

- Based on empirical correlations for either bed pressure drop (Ergun, 1952; Wen and Y. H. Yu, 1966) or fluidisation (Davidson, 1971),
- Based on numerical simulations at microscale with DNS or LBM (Koch and Hill, 2001).

The effect of the presence of other particles is typically included by a function of the void fraction $f(n)$ and related to the particle Reynolds number Re_p (Zhu et al., 2007). Different

drag force correlations have been established. A detailed description of the most commonly used drag force models in unresolved CFD-DEM are given in Sec. 7.2. However, J. Li and Kuipers (2003) performed a systematic study to quantify the differences among these correlations. Their results indicate similar predictive capabilities of these correlations but differences in the accuracy.

4.3.3 Virtual mass force and Basset history force

The virtual mass force describes the effect that an accelerated particle in a fluid flow accelerates the fluid correspondingly. This is at the expense of the work performed by the particle (Crowe et al., 2012). The virtual mass force is expressed through:

$$F_{vm} = \frac{\rho_f V_p}{2} \left(\frac{\partial \boldsymbol{u}}{\partial t} - \frac{\partial \boldsymbol{v}}{\partial t} \right) \tag{4.26}$$

This force is called virtual mass force as the resulting force is equivalent to adding mass to the particle. The Basset history force now accounts for the viscous effects due to the acceleration. It deals with the temporal delay in the boundary layer development since the relative velocity changes with time. Because of this temporal delay, the force is called history force (Crowe et al., 2012). Basset (1888) found a formulation of this force for flow over a sphere at low Reynolds numbers, which was further developed by Reeks and McKee (1984) for the case of an initial velocity of the sphere:

$$F_{\text{Basset}} = \frac{3}{2} d_p^2 \sqrt{\pi \rho_f \mu_f} \left[\int_0^t \frac{\frac{d}{dt'} (\boldsymbol{u} - \boldsymbol{v})}{\sqrt{t - t'}} + \frac{(\boldsymbol{u} - \boldsymbol{v})_0}{\sqrt{t}} \right] \tag{4.27}$$

where t' represents the previous time step. Now it becomes obvious why this force is called history force since its value depends on the acceleration history up to the present moment. Usually, the unsteady forces (e. g. virtual mass and Basset history force) are negligible (Crowe et al., 2012).

4.3.4 Lift forces

There exist two types of lift forces when a particle is subjected to fluid flow: The Saffman lift force and the Magnus lift force. The Saffman lift force describes the lift of a particle due to a pressure gradient in the flow that is acting on the particle. The higher velocity on the top of the particle results in a lower pressure. Subsequently the lower velocity at the bottom of the particle results in a higher pressure. This pressure difference leads to an upward motion of the particle. Saffman (1965) derived a formulation for this lift force for low Reynolds numbers, which later was extended by McLaughlin (1991) and Mei (1992) for a wider range of Reynolds numbers to:

$$F_{\text{Saffman}} = C_S 1.61 d_p^2 \left(\mu_f \rho_f\right)^{0.5} |\omega_f|^{-0.5} \left[\varepsilon(\boldsymbol{u} - \boldsymbol{v}) \omega_f\right] \tag{4.28}$$

where C_S is a ratio accounting for Reynolds number effects. It is described by:

$$C_S = \begin{cases} (1 - 0.3313\beta^{0.5}) \exp(-Re/10) + 0.3314\beta^{0.5} & Re \leq 40 \\ 0.0524 (\beta Re)^{0.5} & Re > 40 \end{cases} \tag{4.29}$$

where

$$\beta = \frac{d_p}{2|\boldsymbol{u}-\boldsymbol{v}|}|\omega_f| \text{ for } 0.005 < \beta < 0.4 \tag{4.30}$$

The second lift force to mention is the so-called Magnus lift force. It develops due to the rotation of the particle in a fluid flow. The lift is then caused by a pressure difference between top and bottom of the particle as a result from the velocity differences due to the rotation. The Magnus lift force was firstly derived by Rubinow and Keller (1961) for Reynolds numbers the order of unity:

$$F_{\text{Mag}} = \frac{\pi}{8} d_p^3 \rho_f \left[\omega_p(\boldsymbol{v}-\boldsymbol{u})\right] \tag{4.31}$$

where ω_p is the particle rotation. Similar to the Saffman lift force, the lift produced by the Magnus effect can be quantified by the lift coefficient $C_{L,R}$ with:

$$F_{\text{Mag}} = \frac{1}{2}\rho_f C_{L,R} A|\boldsymbol{v}-\boldsymbol{u}|(\boldsymbol{v}-\boldsymbol{u}) \tag{4.32}$$

where A is the projected area of the particle. $C_{L,R}$ is defined based on the formulation for the lift force by Rubinow and Keller (1961) via:

$$C_{L,R} = \frac{d_p \omega_p}{|\boldsymbol{u}-\boldsymbol{v}|} = 2\Omega \tag{4.33}$$

Ω is the spin parameter. Eqn. 4.3.4 shows that the lift coefficient due to the particle rotation increases linearly with Ω. There have been numerous experiments to actually measure the spin parameter (Maccoll, 1928; Davies, 1949; Barkla and Auchterlonie, 1971; Tanaka et al., 1990). To interested readers Crowe et al. (2012) is recommended for further research.

4.4 Void fraction schemes

In an unresolved coupled CFD-DEM simulation, the void fraction in the computational cells determines the drag force acting on the particles. Thus, it is crucial to accurately determine the void fraction in the individual cells for a realistic calculation of the drag force. Thereby, a void fraction scheme should provide the following criteria (Sun and Xiao, 2015):

1. Conserve the total mass of the particulate phase,
2. Predict a grid-independent velocity field,
3. Produce a smooth void fraction field within a densely packed bed.

Several void fraction schemes exist, which are briefly summarised in the following. The simplest void fraction model is the so-called particle-centred method (PCM). Thereby, the entire particle volume is located at the centroid of the particle (Tsuji et al., 1993). However, this simplification results in large fluctuations when the particle centroid crosses

the cell boundaries (Sun and Xiao, 2015). The PCM should only be used in cases where the fluid cell is large compared to the particle size. Another void fraction scheme is the divided particle volume method (DPVM). In this scheme, the volume of the particle is subdivided into smaller volumes. The centroid of each subvolume is then used to assign the volume of the particle to the corresponding computational cell. In the framework of CFDEM®coupling, the particle is divided in 29 non-overlapping regions of equal volume (*CFDEMcoupling documentation, divided void fraction* 2020). Furthermore, statistical methods can be used in void fraction schemes. In the statistical kernel method, the solid volume fraction is determined by distributing the particle volume by a weighting function that decays away from the particle centre (Zhu and A. B. Yu, 2002). In the presented numerical simulations, the DPVM is used.

4.5 Immersed Boundary Method

When the flow around an object needs to be resolved, the Immersed Boundary Method (IBM) represents an adequate tool. IBM was firstly developed by Peskin (1973) to model flow patterns around the heart valves. Therefore, he introduced a novel procedure to simulate the effect of an immersed body in a flow: Peskin (1973) used a Cartesian grid for the flow and modelled the effect of the heart by an immersed boundary. The main feature of the IBM is the simulation of an immersed boundary on a grid that does not conform to the shape of the boundary. The represented body in the fluid field has an own surface grid, which cuts through the Cartesian grid. Likewise, only the equations in the vicinity of the boundary need to be modified. In general, this happens by adding a source term or forcing function to Eqn. 4.18 and Eqn. 4.19. Thereby, it can be distinguished between two methods: The continuous forcing and the discrete forcing (Mittal and Iaccarino, 2005). In the continuous forcing, the source term is added to the undiscretised governing equations. Consequently, this method is not dependent on the discretisation of the Cartesian grid. It is favourable for the representation of the interaction between fluids and immersed elastic boundaries (Peskin, 1973). In the discrete forcing method, the governing equations are first discretised on the Cartesian grid without regard to the immersed boundary. After this step, the discretisation in the cells near the immersed boundary is adjusted to account for its presence. This results in a strong dependence on the underlying Cartesian grid, but it allows certain control over the method in terms of accuracy and stability. A detailed discussion about these two methods can be found in Mittal and Iaccarino (2005). When treating moving boundaries, which is one main advantage of the IBM, temporal discontinuities for cells near the boundary can occur due to the sharp change between no fluid motion inside the boundary, where calculations are neglected, and fluid motion outside the cell (Mittal and Iaccarino, 2005).

5 Material parameter and instrumentation

Numerical investigations with unresolved coupled CFD-DEM need a variety of micro-mechanical material parameters that have to be investigated and calibrated before the numerical simulations to capture the behaviour of the material accurately. This chapter will give a short overview of the required material parameters, their determination, and calibration. Furthermore, the Particle Image Velocimetry (PIV) and the required technical equipment is briefly introduced. The PIV serves to capture the soil motion in the experimental investigations.

5.1 Calibration of material parameters

Three different materials are investigated in this contribution: glass beads of 3 mm and 1 mm diameter and model sand, the so-called Hamburger Sand. The latter is a coarse-grained and poorly-graded sand. Fig. 5.1 shows the particle size distribution and the sphericity of these materials.

5.1.1 Friction coefficient

For the determination of the friction coefficient, Schulze shear cell tests and triaxial tests were carried out. The Schulze shear cell is a ring shear tester for powder and bulk solids (Schulze, 2008). In general, the Schulze shear cell test is to be recommended as the setup for the simulation for calibration is simpler and requires fewer particles than a triaxial test. But since the 3 mm glass beads are too big for the shear cell test, triaxial tests had to be conducted for the 3 mm glass beads. The results of the shear cell tests and the triaxial tests for the 3 mm glass beads are displayed in Fig. 5.2. The test record of the tests can be found in the appendix B.1 and B.2.

5.1.2 Rolling friction coefficient

The rolling friction coefficient μ_r is taking into account grain shape effects. In DEM, the particles are generally modelled with perfect spheres as it saves computational time, and well-established correlations for the contact model or fluid-particle interaction forces already exist. Hence, to account for grain shape effects, the so-called rolling friction coefficient is used, cf. Sec. 4.1.3. The sphericity of the glass beads and the Hamburger Sand was measured in the laboratory with a cam-sizer. The sphericity is a measure of how closely the shape of an object resembles a perfect sphere. Wadell (1935) defined sphericity as the

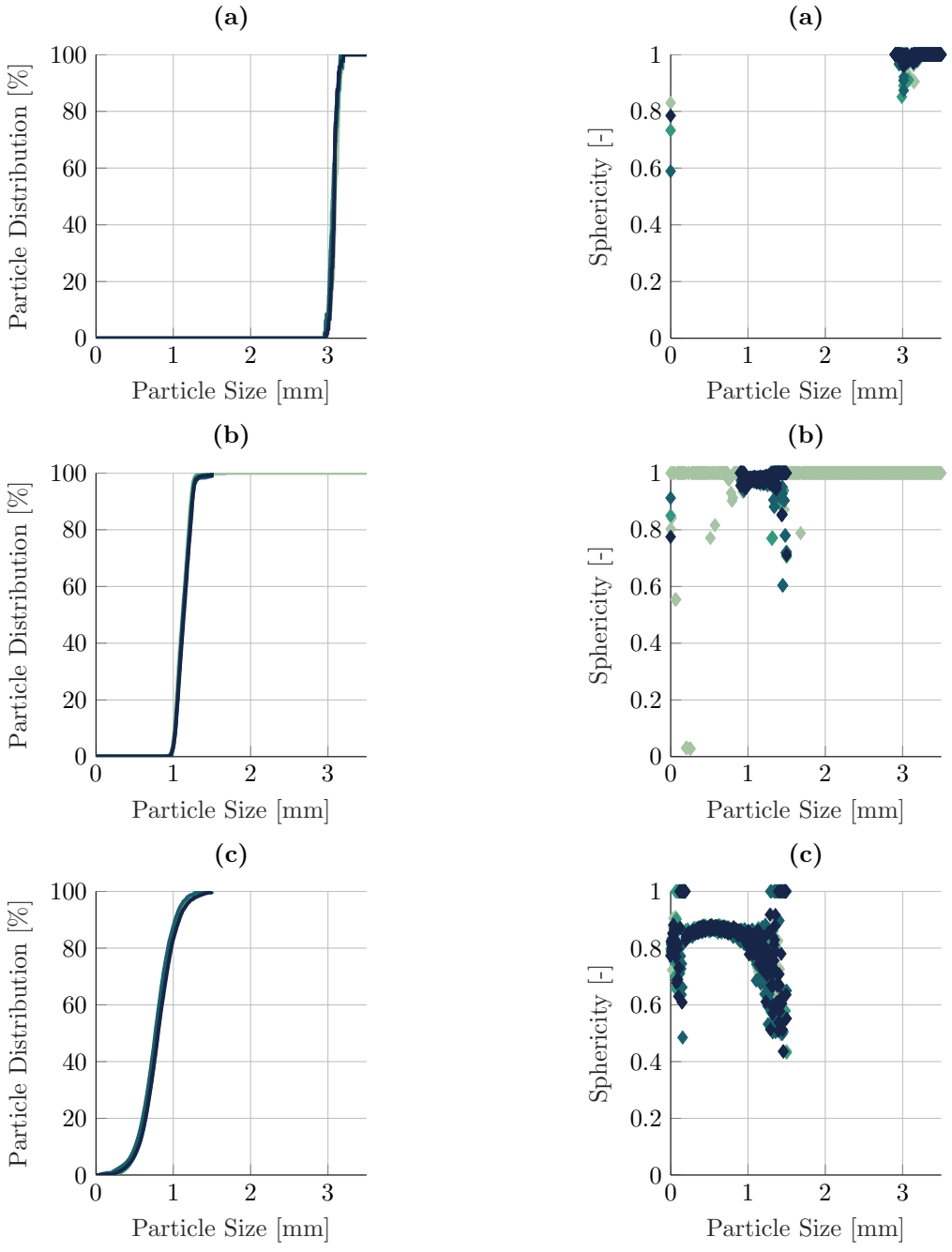


Figure 5.1: Particle distribution (left) and sphericity (right) of (a) glass beads ($D = 3\,\mathrm{mm}$), (b) glass beads ($D = 1\,\mathrm{mm}$) and (c) Hamburger Sand

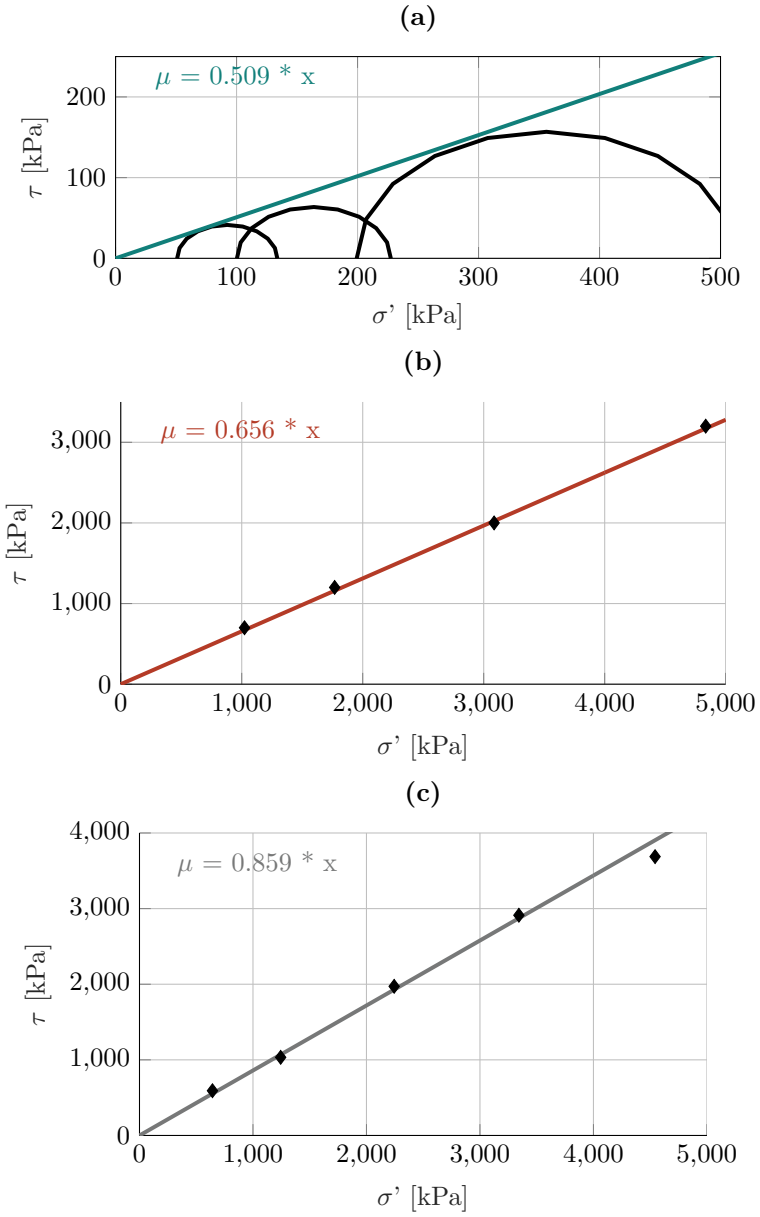


Figure 5.2: Friction coefficient μ for (a) glass beads ($D = 3\,\mathrm{mm}$), (b) glass beads ($D = 1\,\mathrm{mm}$) and (c) Hamburger Sand

ratio of the sphere surface to the particle surface, both having the same volume. Fig. 5.1 shows the results of the measured sphericity. It can be identified that the glass beads are almost perfectly spherical, while the sphericity of the Hamburger Sand is varying, but can still be considered as nearly round. Fig. 5.3 depicts a microscopical view of the particles. As the rolling friction is an artificial material parameter, it cannot be determined directly by laboratory tests but has to be calibrated with numerical simulations.

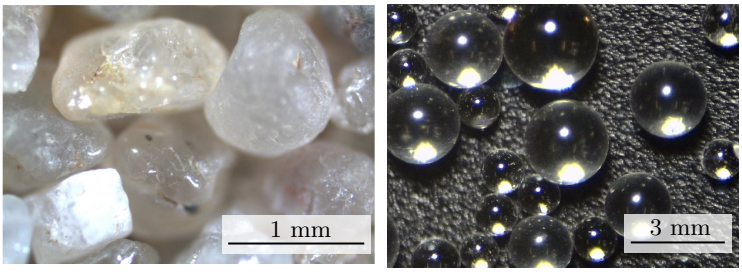


Figure 5.3: Microscopical view of the glass beads and the Hamburger Sand

The angle of repose tests calibrates the rolling friction coefficient for the numerical simulations with DEM for particle-particle contact. In this test, a cone filled with the material is lifted. The material is thus slowly flowing out, resulting in a cone with the inclination of the angle of repose φ_0. These tests are carried out experimentally and numerically, whereby the rolling friction coefficient is modified in the numerical model until the final angle of repose matches the experimental results. Tab. 5.1 lists the resulting rolling friction coefficients for particle-particle contact (p-p). The rolling friction coefficient for the contact of particle and wall is calibrated with the inclined plate test. Thereby, a plate is inclined step-wisely until the particles begin to roll. The calibrated rolling friction coefficient for particle-wall contact (p-w) is depicted in Tab. 5.1.

Table 5.1: Rolling friction coefficient

Glass beads ($D = 3\,\mathrm{mm}$)	Glass beads ($D = 1\,\mathrm{mm}$)	Hamburger Sand
0.005	0.0005	p-p: 0.057 | p-w: 0.44

5.1.3 Restitution coefficient

The restitution coefficient is an important parameter to capture the particle collisions in particle-fluid flows accurately (van Buijtenen et al., 2009). It describes the energy absorption and damping force during the collision of particles in DEM. The restitution coefficient thus models the inelastic behaviour of particles, i. e. inelastic deformation. In Fig. 5.4, the contact force vs time and displacement of a particle impacting a stiff wall is shown. In the initial impact phase, the particle is compressed, and its kinetic energy transforms into internal energy of deformation, friction and adhesion. After the compression, the restitution phase begins. In this phase, the absorbed elastic contribution of the impact energy is released and results in an elastic force separating the contact

partners. The restitution coefficient describes the change of kinetic energy into internal energy of deformation, friction and adhesion. It defines the ratio of impulse during the restitution phase of the impact to the impulse at the compression phase. It is determined through:

$$e_n = \frac{v_\mathrm{R}}{v_\mathrm{ini}} \tag{5.1}$$

where v_R is the velocity of the particle in the restitution phase and v_ini its initial velocity. In case of a fully elastic impact, the absorbed energy during compression is fully transformed into kinetic energy during the rebound of the particle. This means that the velocity of the particle is equal before and after the impact ($v_\mathrm{R} = v_\mathrm{ini} \rightarrow e_n = 1$). In the case of a perfectly plastic contact, when the kinetic energy is fully absorbed due to plastic deformation, the impacting particle does not rebound in the restitution phase ($e_n = 0$). Hence, in the case of an elastic-plastic contact, the restitution coefficient is in the range of $0 < e_n < 1$. The

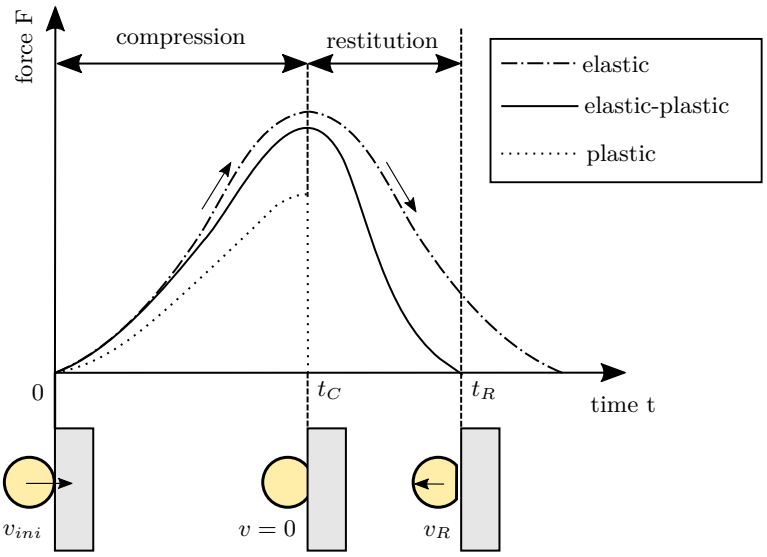


Figure 5.4: Schematic representation of the contact force vs time at the impact of a particle with a stiff wall, after (Antonyuk et al., 2010)

restitution coefficient in this contribution is measured in a free-fall test at the Institute of Solids Process Engineering and Particle Technology (TUHH). The particle is placed at a vacuum nozzle to prevent an initial rotation of the particle when released. When the vacuum is switched off, the particle falls freely onto a flat plate made of acrylic glass. A high-speed camera records the movement of the particle with a frequency of 4000 frames per second and a resolution of 512 px × 256 px. Particle tracking velocimetry is then used to determine v_ini and v_R. The test is repeated 25 times for all materials. Fig. 5.5 depicts the restitution coefficient e_n for the glass beads and the sand. As the glass beads are almost perfectly spherical, the mean variation is low. The sand particles, however, have different shapes. During the test, grains were chosen that had a similar shape and size, but a variation of e_n could not be avoided.

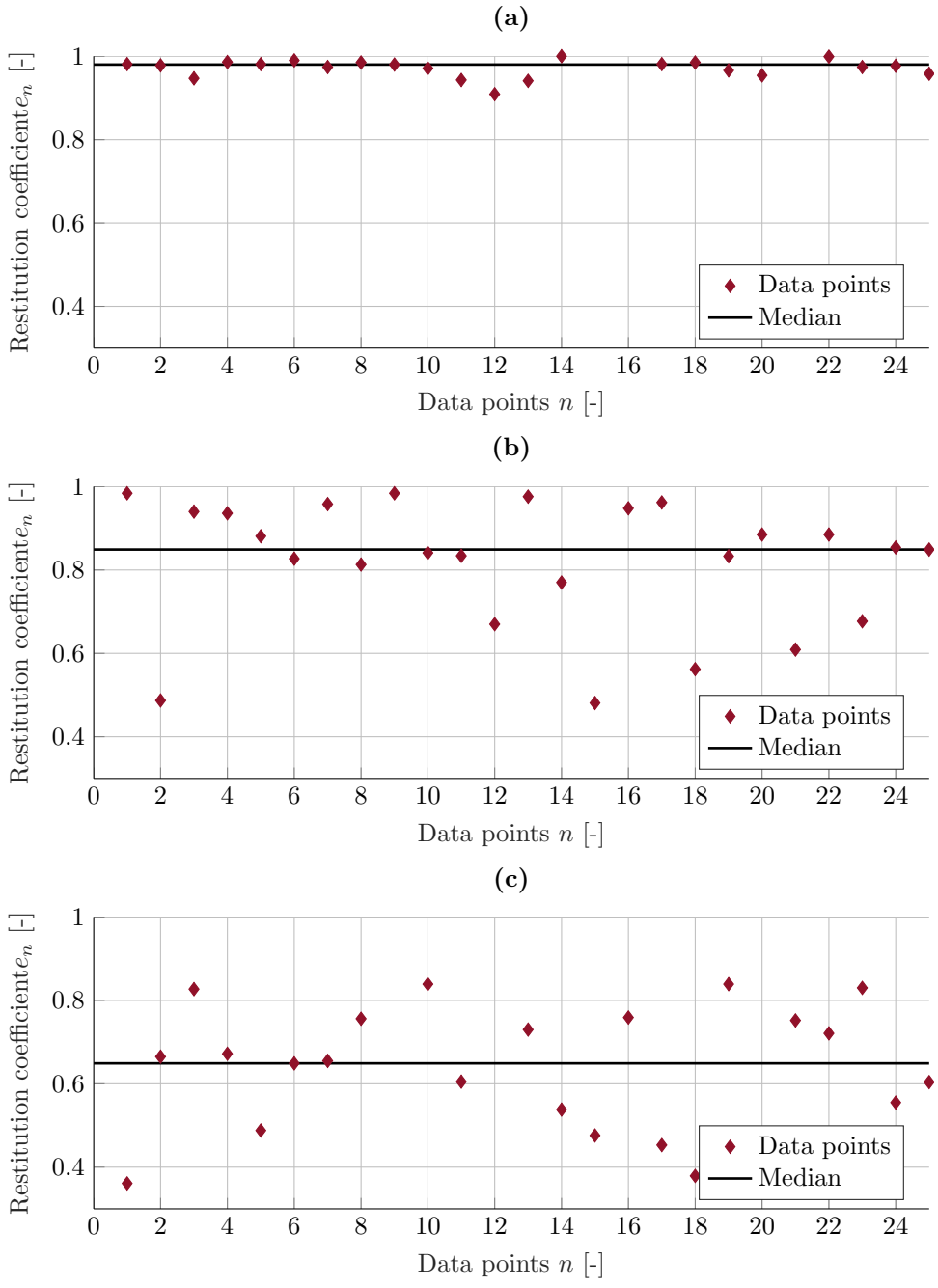


Figure 5.5: Restitution coefficient e_n for (a) glass beads ($D = 3\,\text{mm}$), (b) glass beads ($D = 1\,\text{mm}$) and (c) Hamburger Sand

5.1.4 Young's modulus

The Young's modulus of the different materials is determined in compression tests. Thereby, one particle of each material is placed between two walls, and the upper one is lowered with a constant velocity. During the compression, the displacement and the force are measured. The Young's modulus is obtained taking into account the elastic contact deformation according to Hertzian theory (Hertz, 1881), cf. Sec. 4.1.2.
The following steps determine Young's modulus:

1. Calculation of E^* using:
$$\frac{E^*}{\sqrt{s^3}} = \frac{6F}{\sqrt{d_p}} \tag{5.2}$$
where F is the applied force and s is the displacement of the stiff wall.

2. Plotting $\frac{6F}{\sqrt{d_p}}$ over $\sqrt{s^3}$ (cf. Fig. 5.6).

3. Curve-fitting in the linear region of the plot and deriving the gradient which gives E^*.

4. Determination of the Young's modulus of a single particle E_p using Hertzian theory (Hertz, 1881) with the assumption of a very stiff wall ($E_w >> E_p, E_w \to \infty$) given as:
$$E^* = 2\left(\frac{1-\nu_p^2}{E_p} + \frac{1-\nu_w^2}{E_w}\right)^{-1} \approx \frac{2}{1-\mu_2^2}E_p \tag{5.3}$$
$$\to E_p = \frac{1-\nu_p^2}{2}E^* \tag{5.4}$$
where ν is the Poisson ratio. The indices w and p are used for *wall* and *particle*.

The comparison between the force-displacement curves of the compression test with the Hertz-Model are depicted in Fig. 5.7.
The Young's modulus for glass beads with $D = 3\,\text{mm}$ is $E_{3\text{mm}} = 1241\,\text{N/mm}^2$, for glass beads with $D = 1\,\text{mm}$ is $E_{1\text{mm}} = 2319.7\,\text{N/mm}^2$ and for Hamburger Sand the Young's modulus is $E_{\text{HS}} = 3157.5\,\text{N/mm}^2$.

5.1.5 Maximum and minimum void fraction

The loosest and densest packing density of Hamburger Sand and the glass beads with 3 mm and 1 mm diameter is determined according to DIN 18126. The results are given in Tab. 5.2. The test record of the tests can be found in the appendix B.3.

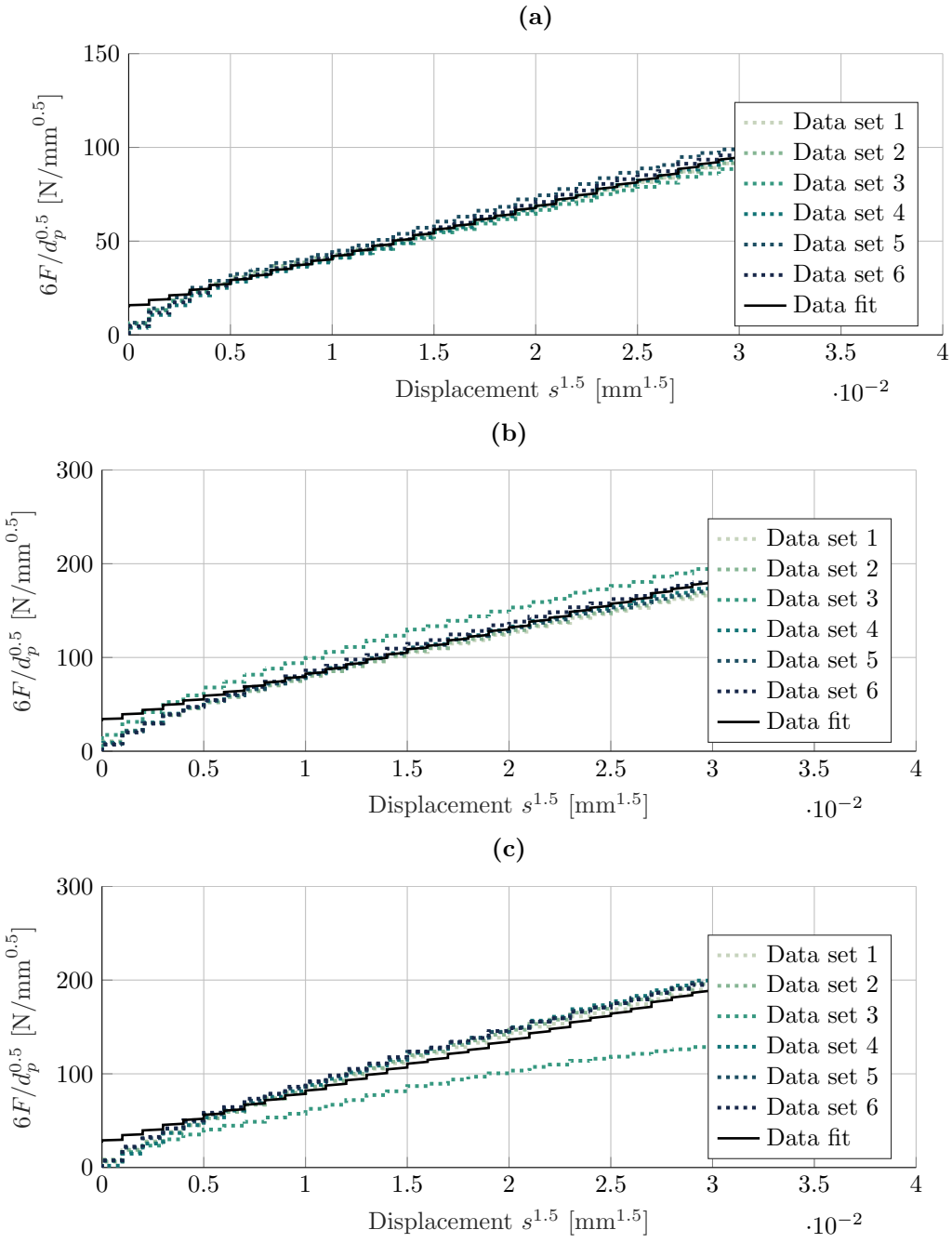


Figure 5.6: Determination of average modulus of elasticity E^* for (a) glass beads ($D = 3\,\text{mm}$), (b) glass beads ($D = 1\,\text{mm}$) and (c) Hamburger Sand

Table 5.2: Maximum and minimum void fraction

	Glass beads (D = 3 mm)	Glass beads (D = 1 mm)	Hamburger Sand
$n_{\max}$	0.385	0.441	0.446
$n_{\min}$	0.339	0.399	0.342

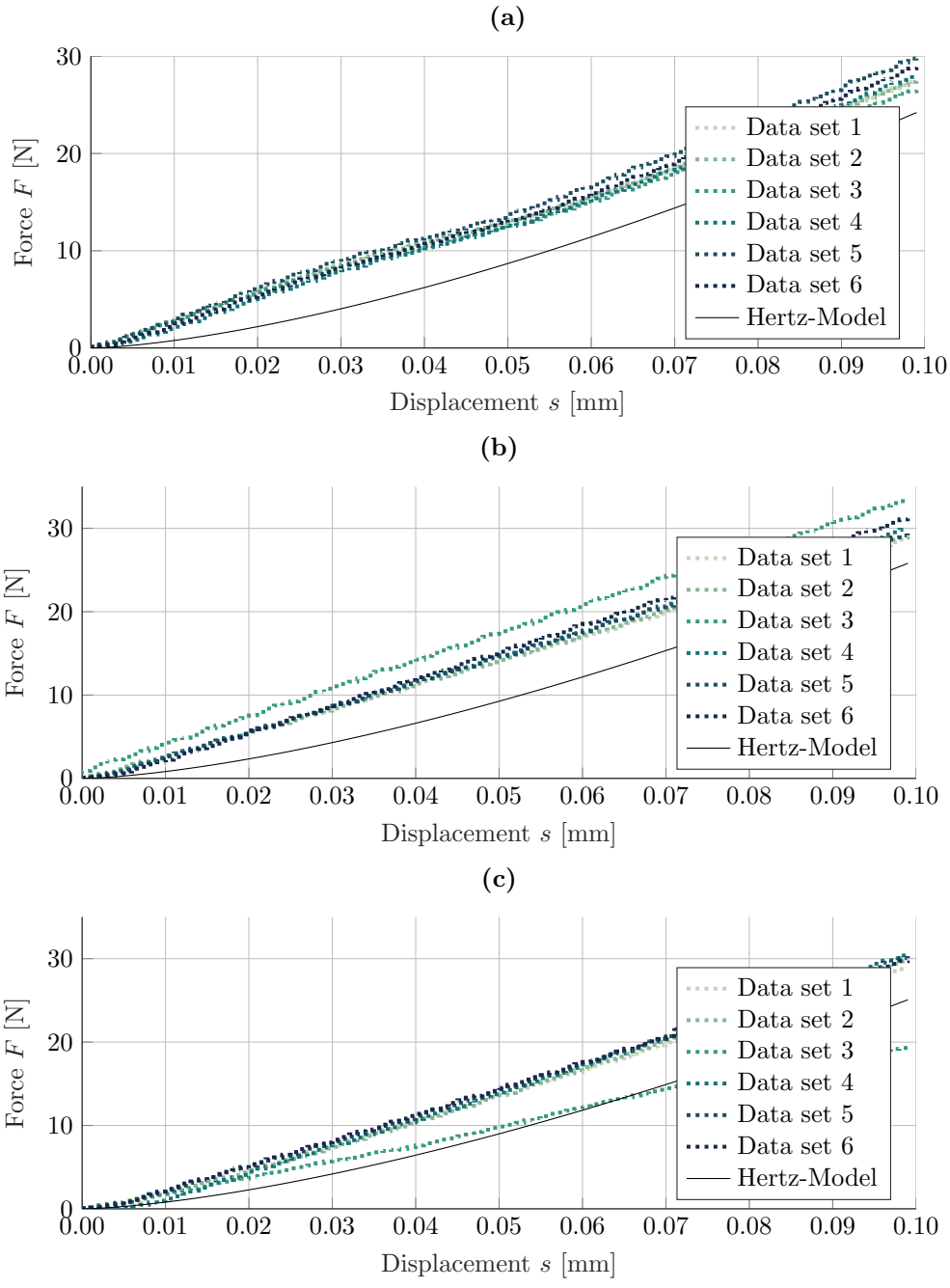


Figure 5.7: Comparison of Hertz-Model with Force-displacement-curve for (a) glass beads ($D = 3\,\mathrm{mm}$), (b) glass beads ($D = 1\,\mathrm{mm}$) and (c) Hamburger Sand

5.1.6 Material parameter for the numerical simulations with unresolved coupled CFD-DEM

In Tab. 5.3, the calibrated parameter for the glass beads with 3 mm and 1 mm diameter and the Hamburger Sand are summarised.

Table 5.3: Summary of calibrated material parameters for numerical simulations with unresolved coupled CFD-DEM

Parameter	Glass beads ($D = 3\,\mathrm{mm}$)	Glass beads ($D = 1\,\mathrm{mm}$)	Hamburger Sand
Friction coefficient μ [-]	0.509	0.656	0.859
Rolling friction coefficient μ_r [-]	0.005	0.005	p-p: 0.057 | p-w: 0.44
Young's modulus E [N/m,^{2}]	1241	2319.7	3157.5
Restitution coefficient e [-]	0.98	0.8494	0.65

5.2 Particle displacement measurements

The measurement of the particle displacement is carried out with the Particle Image Velocimetry (PIV) method. PIV is a tool for measuring deformations and displacements in a medium, whether it is a fluid or a solid. The most common method is based on a digital image correlation (DIC) technique (Sutton et al., 2000). For that purpose, the dynamic process is recorded with a camera, taking a defined quantity of photos in a definite time interval. Within the framework of PIV-DIC, a region of interest (ROI) is defined in the first (reference) image as can be seen in Fig. 5.8. This reference image is then subdivided into a mesh of subsets of user-defined size. Each of these subsets has a unique contrast pattern defined by its pixel. The contrast pattern of these subsets is searched in the subsequent (target) image using cross-correlation techniques. Thus, this integer pixel displacement of the subsets is found by locating the intensity peak of the reference and the target image in the resulting cross-correlation matrix. The highest peak gives the most probable displacement of the particles from the reference to the target image. The correlation peak is then interpolated by shape functions to obtain the sub-pixel resolution displacements to improve the quality of the analysis. Usually, zero-order shape functions are used herein, so the subsets are not allowed to deform.
Two different software tools are employed for the PIV measurements: the software GeoPIV-RG by Stanier et al. (2016) and the software PIVLab by Thielicke and Stamhuis (2014).

GeoPIV-RG GeoPIV-RG is a MatLab module that implements PIV in a manner suited to geotechnical testing. It is the further development of GeoPIV by White et al. (2003) with a reliability-guided method by Pan et al. (2012). The algorithm of White et al. (2003) uses a combination of a leapfrog scheme and a sequential scheme for the analysis of the image sequence. In the leapfrog scheme, the reference image is retained as the initial image. This method can suffer a loss of correlation in regions, where large deformations

occur. In the sequential scheme, the reference image is updated after every computation, which reduces the mismatch between the subset shape and the actual deformation, but accumulates random walk errors (White et al., 2003). By the use of the combination of these two schemes, the number of increments performed using the leapfrog scheme until updating the reference image has to be defined by the user via trial and error. The implementation of Stanier et al. (2016) avoids the necessity for trial-and-error refinements by the user through a reliability-guided method proposed by Pan et al. (2012). With this algorithm, an initial "seed" subset is analysed determining the neighbouring subset that has the highest correlation. These results are then used for the preconditioning of the subsequent computations. When the correlation coefficient for the seeds or one of the subsets violates a user-defined limit, the reference image is updated.

PIVLab PIVLab is a GUI-based open-source tool for PIV analyses in MATLAB developed by Thielicke and Stamhuis (2014). PIVLab combines the three main steps that a successful PIV analysis requires in one tool: pre-processing, image evaluation and post-processing. The image pre-processing enhances the image quality prior to the analysis to improve the image cross-correlation. In PIVLab, the user can combine different pre-processing techniques, like contrast limited adaptive histogram equalisation (CLAHE), intensity highpass filter and intensity capping filter. CLAHE enhances the contrast of the images, whereby regions with low and high exposure are optimised independently. The intensity highpass filter is useful when the lighting of the image is inhomogeneous. Intensity capping should be used to reduce the intensity of bright spots or particles. For the image evaluation, the user can choose between two techniques in PIVLab: direct cross-correlation (DCC) and discrete Fourier transform (DFT). DCC calculates the cross-correlation matrix in the spatial domain while DFT computes it in the frequency domain. DCC is more accurate than DFT but has higher computational costs. The subpixel refinement can be carried out by either using a 1D or a 2D Gaussian function, whereby the latter is required when the flow rotates. A crucial step in every PIV analysis is the post-processing of the result. In PIVLab, it can be subdivided into four steps:

1. Data validation: In this step, the outliers are removed. Either the lower and upper limits for the velocities are chosen manually or by using a local median filter. This filter evaluates the velocity fluctuations to the median.

2. Data interpolation: To interpolate the missing vectors, PIVLab uses a boundary value solver. Over larger regions with missing information, this solver tends towards the average of the boundary velocities, which prevents overshooting.

3. Data smoothing: This procedure is necessary to reduce noise in the data. Therefore, PIVLab uses an advanced smoothing method algorithm based on the penalised least square method (Garcia, 2010).

4. Data exploration: PIVLab allows - in addition to the vector map - to extract data over a region or along a path.

More information on the open-source tool PIVLab can be found in Thielicke and Stamhuis (2014).

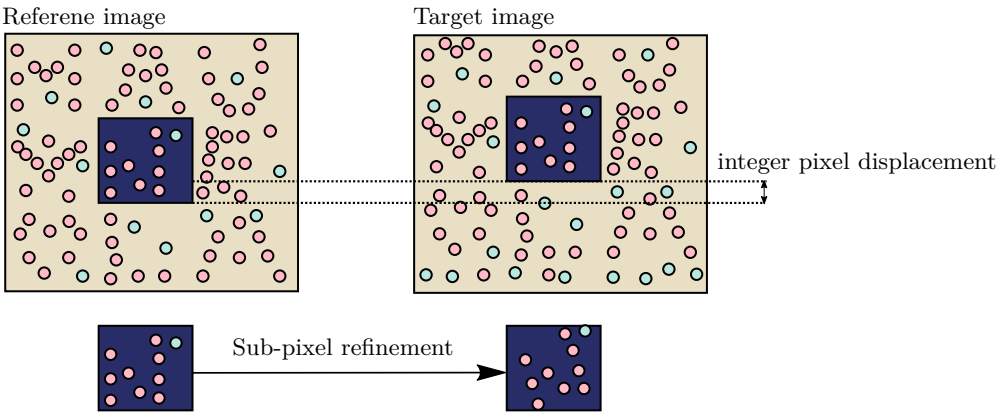


Figure 5.8: General scheme of a PIV-DIC analysis (Kanitz et al., 2019)

Technical equipment The faster a process, the more pictures need to be recorded in a definite time interval to identify the important processes. For that purpose, a high-speed camera (FastCam mini UX50) with a resolution of 1024 px × 1024 px at a maximum frame rate of 1000 Hz is used. Since the intensity of the light decreases with the increase of the frame rate, an intense lighting system has to be established. For this purpose, two LED illumination sources (ILA 5150 LPS System) with a continuous green light up to 25 W are used. The green light emitted by the LEDs has a dominant wavelength of 520 nm and a Full Width at Half Maximum (FWHM) of 34 nm. A bandpass filter is installed in the camera between the lens and the sensor to minimise the influence of other light sources and natural light. The bandpass filter has a Central Wavelength (CW) of 532 nm and a FWHM of 40 nm.

6 Internal Fluidisation

Seepage flow in saturated sand can cause material transport, which can lead to material instabilities. The interaction between the seepage flow and the individual soil particles is thereby of central importance. Hence, coupled CFD-DEM can help to understand what happens in the soil skeleton subjected to seepage flow. Hydraulic failure of soil is caused by fluidisation. The soil loses its stability which can result in severe damages on civil constructions. Therefore, it is crucial to assess the possible risk of hydraulic failure accurately and to understand what happens inside the soil. This chapter will investigate the fluidisation behaviour of sand with unresolved coupled CFD-DEM, which is validated against experimental results.

6.1 Introduction

Firstly, the term internal fluidisation requires clear definition. In geotechnical engineering, there already exists one term to define the phase transition of soil to a liquefied medium: liquefaction. The term liquefaction describes the temporary loss of stability of a saturated granular soil due to short duration loadings such as earthquakes (Alsaydalani and Clayton, 2014). This section is concerned with a mechanism, whereby the soil is transformed into a fluid-like state when exposed to seepage flow. In chemical engineering, this mechanism is called internal fluidisation. This term is used throughout this contribution for the transition of soil to a fluid-like state evoked by fluid flow. In general, a soil fluidises when the effective stresses σ' vanish (Terzaghi, 1943):

$$\sigma' = \sigma - p_w \stackrel{!}{=} 0 \tag{6.1}$$

where σ is the total stress defined by the total weight of the soil including water and p_w is the pore water pressure. The risk of hydraulic failure, which is a cause of fluidisation of the soil is assessed by the critical hydraulic gradient i_c. It is defined by the limit equilibrium between the net upward facing fluid force F_D exterted on the soil volume and the net buoyant weight of the soil $F_g = \gamma' \Delta h A$. The fluid force F_D is defined based on Darcy's law through:

$$F_D = i \gamma_w \Delta h A \tag{6.2}$$

where Δh is the height of the soil volume and A its cross-sectional area. The critical hydraulic gradient is obtained through:

$$\begin{aligned} F_D &= F_g && (6.3)\\ i_c \gamma_w \Delta h A &= \gamma' \Delta h A && (6.4)\\ i_c &= \gamma' / \gamma_w && (6.5) \end{aligned}$$

In addition to the criterion of Terzaghi (1943), the required pressure to fluidise the granular medium may be predicted by the Ergun equation (Shi et al., 1984; Peng and Fan, 1997) by:

$$\frac{\Delta p}{L} = A\frac{\mu_f}{\varphi_s^2 d_p^2}\frac{(1-n)^2}{n^3}U + B\frac{\rho_f}{\varphi_s d_p}\frac{1-n}{n^3}U^2 \tag{6.6}$$

where μ_f is the dynamic viscosity of the fluid, φ_s is the sphericity of the material and U is the superficial fluid velocity. $A = 150$ and $B = 1.75$ are constants calculated by Ergun (1952). Eqn. 6.6 thereby predicts that less spherical material fluidises at lower pressures (Alsaydalani and Clayton, 2014). The Ergun correlation is valid until the minimum fluidisation velocity (Crowe et al., 2012). Fig. 6.1 shows the pressure drop across the particle bed against the superficial velocity. The increase of the superficial velocity increases the pressure drop linearly following the Ergun equation. At minimum fluidisation velocity, the drag force acting on the particles equals their weight, and the packed bed becomes fluidised. At this point, the pressure drop remains constant as it is equal to the buoyant weight of the particles. The constant pressure drop marks the flow regime, where the criterion of Terzaghi (1943) governs. In this stage, the fluid force equals the exerted weight by the particle bed, which is used to calculate the risk of hydraulic failure.

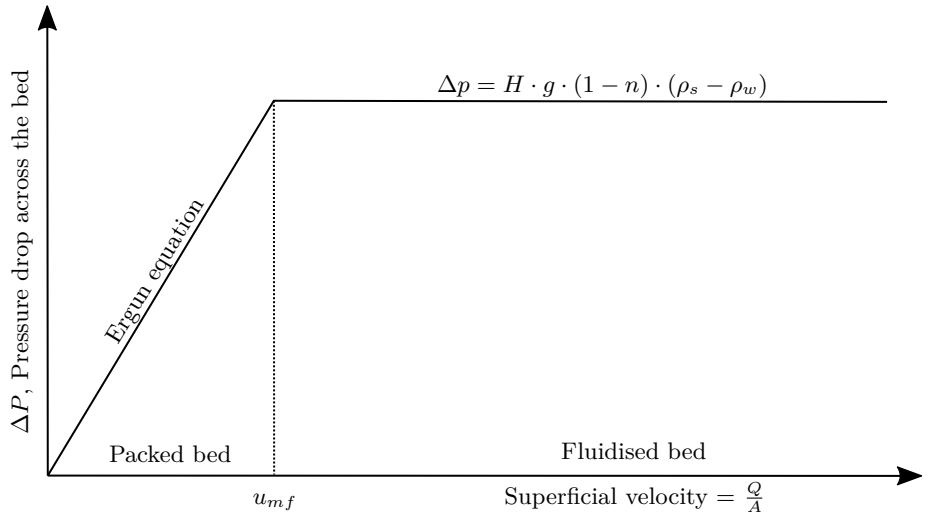


Figure 6.1: Determination of the minimum fluidisation velocity (Gidaspow, 1994)

The minimum fluidisation velocity can be estimated for spherical particles by first calculating the Archimedes number A_r through:

$$A_r = \frac{d_p^3\left(\rho_s - \rho_f\right)\rho_f g}{\mu_f^2} \tag{6.7}$$

where d_p is the mean particle diameter. Then, the Reynolds number at minimum fluidisation velocity Re_{mf} is determined according to Wen and Y. H. Yu (1966):

$$Re_{mf} = \sqrt{33.7^2 + 0.0408A_r} - 33.7 \tag{6.8}$$

Re_{mf} is defined as:

$$Re_{mf} = \frac{d_p u_{mf}\rho_f}{\mu_f} \tag{6.9}$$

Alsaydalani and Clayton (2014) performed a literature review on the subject of internal fluidisation in granular soils caused by fluid injection. They found that fluidisation initiates at the orifice/soil contact. Furthermore, Alsaydalani and Clayton (2014) concluded that increasing the water flow at the opening leads to an increase of the excess pore water pressure and the hydraulic gradient in the soil at the inlet. This increase firstly produces a Darcy flow, but with increasing flow rates, non-Darcy flow occurs. The flow increases until the fluid force equals the buoyant weight of the granular bed. At this moment, the soil starts to move away from the orifice. This outward movement, which is in the order of three times the particle diameter, allows the mobility of the granular medium. A cavity forms, where the grains are loosened by the jet and start to circulate rapidly (van Zyl et al., 2013). Outside of the flow, the grains remain fixed, or they circulate slowly around it. With progressing time, the fluidised zone enlarges, and arching of the soil is overcome. Thereby, gravity leads to the collapse of the upper side of this zone (Niven and Khalili, 1998). In summary, internal fluidisation can occur once the fluid force exceeds the buoyant weight of the soil above the inlet. The strength of the material needs to be exceeded to create space for the fluidisation to occur (Alsaydalani and Clayton, 2014).
Few studies about the topic of internal fluidisation of soil exist, cf. (van Zyl et al., 2013; Bolognin et al., 2017; Vardoulakis et al., 1998), Nevertheless, it is essential to know when soil is prone to fluidisation. Hydraulic failure can be a consequence of internal fluidisation of soil, which can damage civil structures. Consequently, to further understand the mechanisms that lead to internal fluidisation and to assess its risk, numerical investigations with unresolved coupled CFD-DEM are carried out, which are validated against experimental tests. First numerical investigations by Kanitz and Grabe (2018b) with unresolved coupled CFD-DEM of the fluidisation of glass beads showed a good agreement with the experimental results. However, the investigation of spherical material cannot directly be applied to differently shaped material. Hence, the following sections will present the investigation of internal fluidisation of Hamburger Sand.

6.2 Experimental setup

The experimental setup for the investigation of internal fluidisation in cohesionless soils is depicted in Fig. 6.2. A cylindrical acrylic glass container with a diameter of 8 cm and a height of 25 cm is used. The nozzle orifice consists of a perforated plate, with an edge distance of 1 cm (cf. Fig. 6.3). A fine-mesh filter membrane is located on this orifice. Thus the flow is constant over a width of 6 cm and depositing of the sand in the orifice inlet is prevented. The test cylinder is connected to the water conduit, and a ball valve initialises and stops the water flow. It streams from the bottom to the top of the cylinder vertically. The outflowing water is gathered in a bucket, where a scale measures the outflow. A pressure regulator is installed, which maintains a constant pressure of 6 kPa, cf. Fig. 6.3, and thus a constant water flow.
The cylinder is filled with water to prepare the test. Material is then carefully poured into the cylinder to ensure a fully saturated state. Medium dense and very dense Hamburger Sand is used for the investigation of fluidisation. A material height of 4.0 cm is realised. For a looser packing, the material is poured into the cylinder, and water is then gently

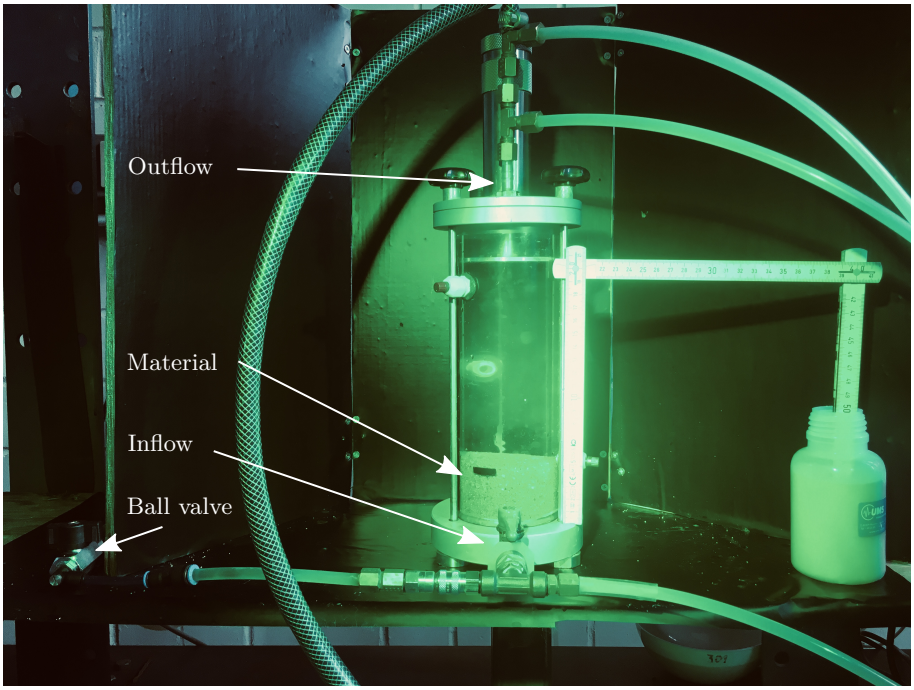


Figure 6.2: Experimental setup of investigation of the fluidisation behaviour Hamburger Sand

streaming through the particle packing. To reach a very dense state, the Hamburger Sand is compacted by vibrations after pouring the material into the cylinder. Likewise, the more loosely packed Hamburger Sand has a void fraction of $n = 0.38$, which corresponds to a medium dense packing. The dense Hamburger Sand a void fraction of $n = 0.35$ corresponding to a very dense packing. The test is started by opening the ball valve. A high-speed camera records the whole process of fluidisation at 250 fps. The water flow is constant with a velocity of 0.027 m/s over the orifice inlet of 6 cm. The fluid velocity was measured both in the filled and in the empty test cylinder by measuring the outflow with a scale. Every test was carried out three times. After 5 s the water flow is stopped and the sedimentation of the material is recorded. In this way, the void fraction after fluidisation can be analysed as well.

6.3 Numerical setup

The setup for the numerical investigations of the internal fluidisation of Hamburger Sand with unresolved coupled CFD-DEM is depicted in Fig. 6.4.

6.3.1 Geometry and initial conditions

The geometry of the numerical setup has the same dimensions as the experimental setup. The particle parameters and distribution are chosen consistent with the calibrated material for Hamburger Sand, cf. Tab. 5.3. The material height is 4.0 cm. The particles are initialised in a pure DEM computation. This technique reduces the computational costs significantly.

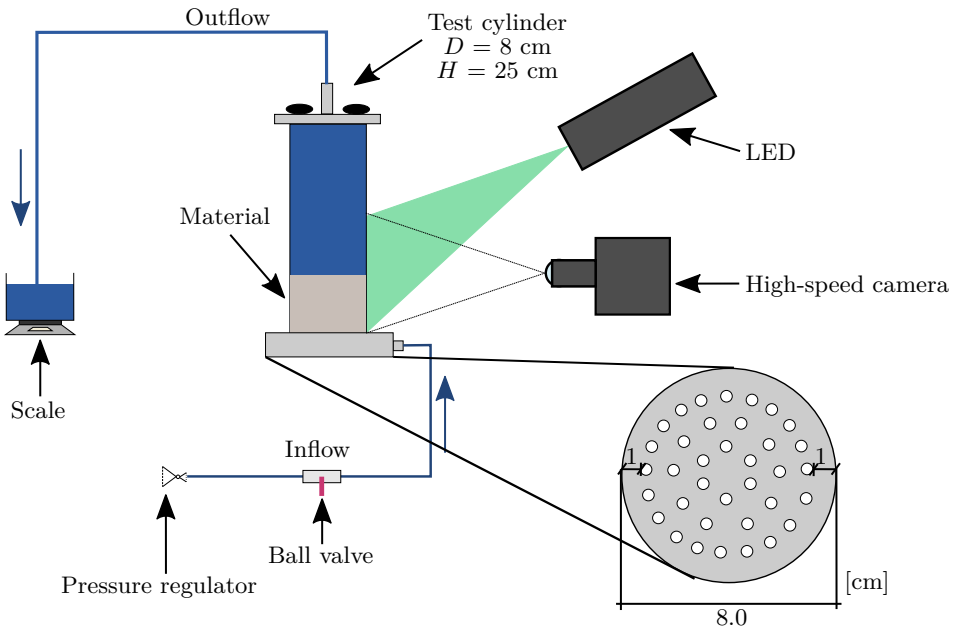


Figure 6.3: Sketch of the test setup for the investigation of the fluidisation behaviour of Hamburger Sand

The packing density is chosen following the experimental setup. The very dense state of the particles is reached by reducing the rolling friction coefficient μ_r, and the friction coefficient μ during the initialisation of the particles. No gravitation acts during the initialisation to prevent the particles from clogging. When the initialisation is finished, and all particles have the desired radius, the gravitation is activated. The material starts to settle. The final particle arrangement is reached when the kinetic energy is below a level of 5×10^{-7} J. Since a smaller time step is required in the DEM calculation with stiffening particles, the numerical simulations are performed with $E = 1 \times 10^7\,\mathrm{N/m^2}$. The simulated fluid has the properties of water at a temperature of 20 °C. Its density is $\rho_f = 1000\,\mathrm{kg/m^3}$ and the kinematic viscosity is $\nu_f = 1 \times 10^{-6}\,\mathrm{m^2/s}$.

6.3.2 Boundary conditions

The flow is initialised with a constant inlet velocity of $u = 0.027\,\mathrm{m/s}$ over a width of 6 cm. Therefore, the groovyBC-utility available in OpenFOAM is used, which allows setting non-uniform boundary conditions. The pressure is a zero-gradient boundary condition (*OpenFoam documentation, Boundary conditions* 2020). At the outlet, the velocity is set to zero-gradient while the pressure is constant with 0 kPa. At the walls, a slip boundary condition is initialised. An additional cell layer is initialised at the inlet to set the void fraction to 1. This additional cell layer ensures that the velocity at the boundary is equal to the superficial velocity.

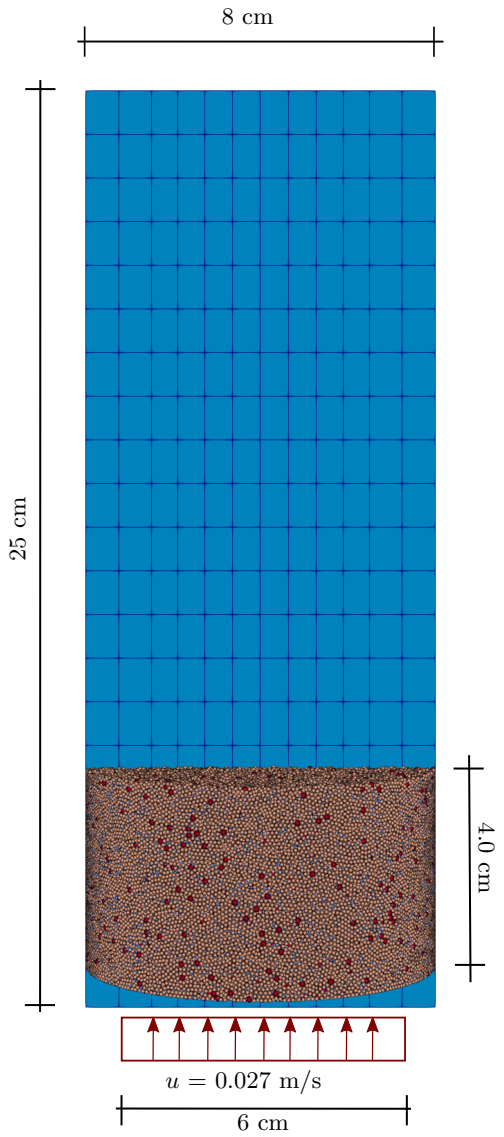


Figure 6.4: Setup of the numerical investigations of internal fluidisation of Hamburger Sand with unresolved coupled CFD-DEM

6.3.3 Coupled simulation with unresolved CFD-DEM

The simulated time is 6 s whereby the velocity at the inlet is set to zero after 5 s of simulated time. Likewise, the sedimentation of the particles can be analysed as well. The coupling interval between the DEM- and the CFD-solver is set to 100. The DEM time step is $t_{\mathrm{DEM}} = 1 \times 10^{-6}$ s and the CFD time step is $t_{\mathrm{CFD}} = 1 \times 10^{-4}$ s. The drag force model of Koch and Hill (2001) is employed for the interaction of particulate and fluid phase.

6.4 Experimental results

Fig. 6.5 depicts the fluidisation behaviour of medium dense Hamburg Sand subjected to seepage flow. A PIV analysis with PIVLab (Thielicke and Stamhuis, 2014) is carried out to visualise the motion of the sand grains. A vector representation is chosen, whereby the vector length is scaled by 40 to improve visibility. It can be observed that already after 1 s the material begins to fluidise. On the right side of the column, the fluid is breaking through the material resulting in a strong material outflow. The sand "bubble" reaches a height of 7 cm. At the same time, it can be observed that not the whole sand body is fluidised, but fluidised channels form, where material transport occurs. The sand bed can be subdivided into a static and a fluidised region. In the static region, no particle movement occurs while in the fluidised region, significant particle motion appears. After 2 s of seepage flow, the fluidised channels widen and turbulences at the top of the sand bed begin to form. The fluidised material follows the turbulent motion of the fluid and hits the top of the sand bed at a high velocity. The particle velocities do not increase significantly. After 3 s, the sand is fluidised to a greater extent, and two sand "bubbles" evolve. The width of the fluidised channels does not increase. However, the turbulences at the top of the sand bed increase inducing a stronger erosion.

The maximum height of the outbursting material is 7 cm above the bottom. This maximum height applies for the whole fluidisation time. After 4 s of fluidisation, the same behaviour of the sand bed is observed. The channel width stays constant, while the turbulences and the resulting erosion at the surface increase. The seepage flow stops after 5 s. Only one fluidised channel remains, and the fluid velocity decreases. The material starts to settle, and the turbulences at the sand bed surface decrease visibly. The motion of the material stops completely after 6 s. Only fine material is still settling. The sand bed is static and has a height of $h_{\text{medium dense,f}} = 4.4$ cm. A slight loosening of the material occurs after the fluidisation. The void ratio after ceasing the seepage flow is $n_{\text{exp,medium dense,f}} = 0.41$ ($D = 0.346$). Consequently, although the material has been fluidised to a great extent, the difference in the packing density ($\Delta n_{\text{medium dense}} = 0.03$) is small.

Fig. 6.6 shows the fluidisation behaviour of the very dense sand. In contrast to the medium dense sand, no instant fluidisation of the sand body occurs. Instead, the very dense sand forms a plug, which the seepage flow transports upwards. At the bottom of this plug, the material settles, and the fluid erodes the material. After 2 s, the plug starts to collapse. The fluid breaks through the plug at its right side. The seepage flow erodes material from the bottom and the sides, and the vortices erode the material from the top. As a result, the internal stability and the interparticle contact forces of the sand vanish. This results

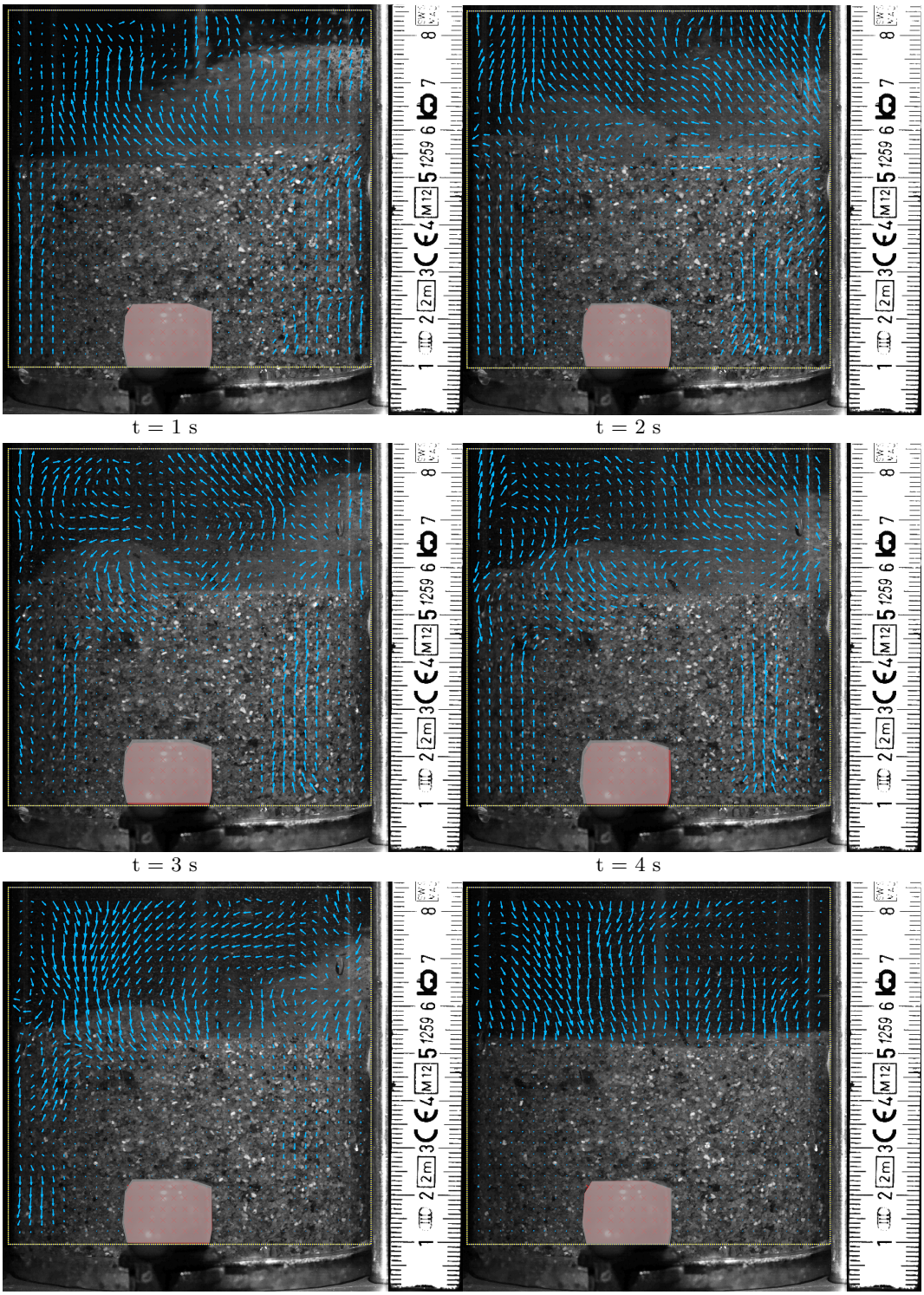


Figure 6.5: Fluidisation behaviour of the medium dense sand at different time steps; vector representation of the movement resulting from the PIV analysis; the grey area marks the region, which is left out of the analysis (location of the ball valve)

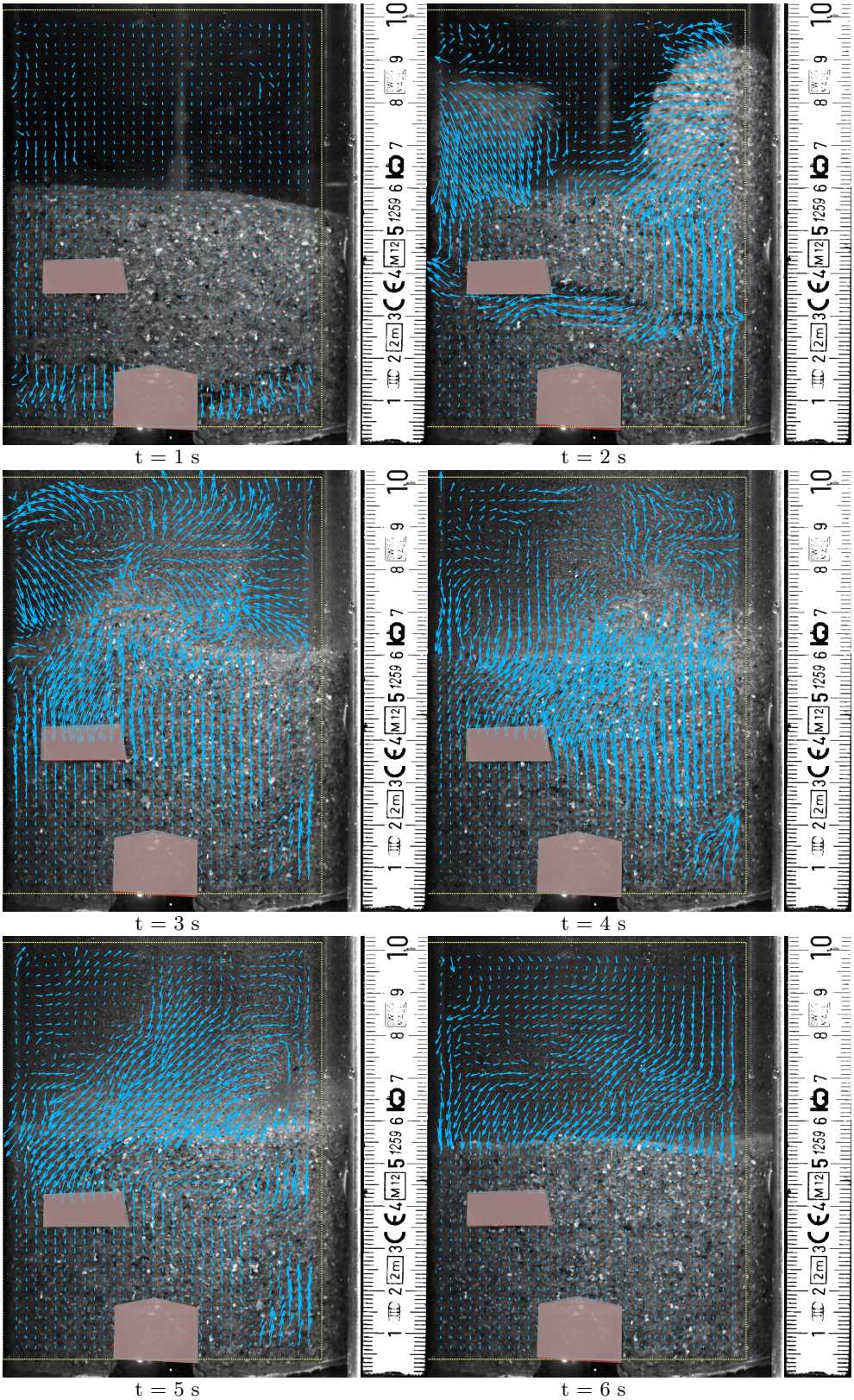


Figure 6.6: Fluidisation behaviour of the very dense sand at different time steps; vector representation of the movement resulting from the PIV analysis; the grey area marks the region, which is left out of the analysis (location of the ball valve)

in sudden fluidisation with a stronger motion compared to the medium dense sand (cf. Fig. 6.5). The material outflow is strong. The material reaches a maximum height of 8 cm. After 3 s, the whole sand bed is fluidised. In contrast to the medium dense sand, no static bed appears. The material reaches a height of approximately 7 cm. At the same time, the whole bed is heaved to a height of 5 cm due to seepage flow. At 4 s, the fluidisation of the sand results in a circular motion of the material. It flows downwards at the visible side of the cylinder. The velocity of the material is thereby higher on the right side, which indicates a non-linear motion. At the right bottom side, it is observed that the material is transported upwards towards the non-visible part of the cylinder. The maximum height of the material is unaltered.
At 5 s, the seepage flow stops, and the material starts to slow down. The motion is still circular and comparable to the motion at 4 s of seepage flow. The bed is not static. The sand reaches a static state after 6 s, when the bed has completely settled. Compared to the medium dense sand, the fines require more time to settle. Due to the stronger fluid motion, the particles are transported to a greater height. Additionally, the motion of the fines is circular rather than straight. Hence, the momentum of the seepage flow still affects their settling process. This circular motion results in a more irregular bed surface compared to the medium dense sand. The final height of the formerly very dense sand is $h_{\text{very dense,f}} \approx 4.8\,\text{cm}$. Hence, the fluidisation of the very dense sand results in a significant loosening of the soil body as the final void ratio is $n_{\text{exp,very dense,f}} = 0.43$. This results in a difference of the initial and final void ratio of $\Delta n_{\text{very dense}} = 0.08$. Loosening of the very dense sand due to fluidisation is more significant compared to the medium dense sand because of stronger fluidisation in the overall bed. After fluidisation of the very dense sand, the packing density is very loose ($D = 0.15$).

6.5 Numerical results

Fig. 6.7 depicts the numerical results of the fluidisation of the medium dense soil. After 1 s of simulated time, the sand column begins to fluidise. As observed in the experimental tests, channels at the boundary to the glass container are created, where the seepage flows upwards and transports the particles. In these channels, the fluid escapes from the packed bed in the form of slugs along the wall. The majority of the particle column remains static. Two regions of strong material outflow are identified after 1 s with a maximum height of the transported particles of around 7.5 cm. This is consistent with the experimental results. A cavity forms at the bottom right corner of the particle column. Cavities are important for fluidisation to occur. In order for the packed bed to overcome the effective stresses and move, sufficient space must be available to allow the grains to dilate. The creation of cavities in fluidised beds is called raceway phenomenon. It represents the internal circulating flow of particles (A. B. Yu and Xu, 2003).
After 2 s of seepage flow, the fluidised channels become more distinct. Compared to the results after 1 s, the fine particles are washed out, and the coarser fraction of the particle bed is transported higher. The particles reach a maximum height of 6 cm. In addition to the straight fluidised channel at the right side, a supplementary channel evolves, which has a circular motion. After 3 s, the motion of the particles continues to increase, accompanied

by a higher material transport to 7 cm. Instead of two "bubbles" of material, the fluidised channels have connected to a broad fluidised channel while a new one develops at the left side of the particle bed. This behaviour is consistent with the experimental results after 3 s. The fluidised channel increases in intensity with succeeding time so that after 4 s the maximum height of particle transport remains at 7 cm consistent with the experimental results. The motion of the particles after 5 s has the same tendency as after 4 s. The ceasing of the seepage flow, however, results in a collapse of the particle "bubbles". The intensity of the particle motion decreases. The particles have finally settled after 6 s. The resulting particle bed height after fluidisation is 4.8 cm, which is in good agreement to the experimental results. In general, in agreement to the experimental results, two zones can be identified during the fluidisation in the packed bed: a static zone, where the particles are immobile and a mobile zone, where the particles move.

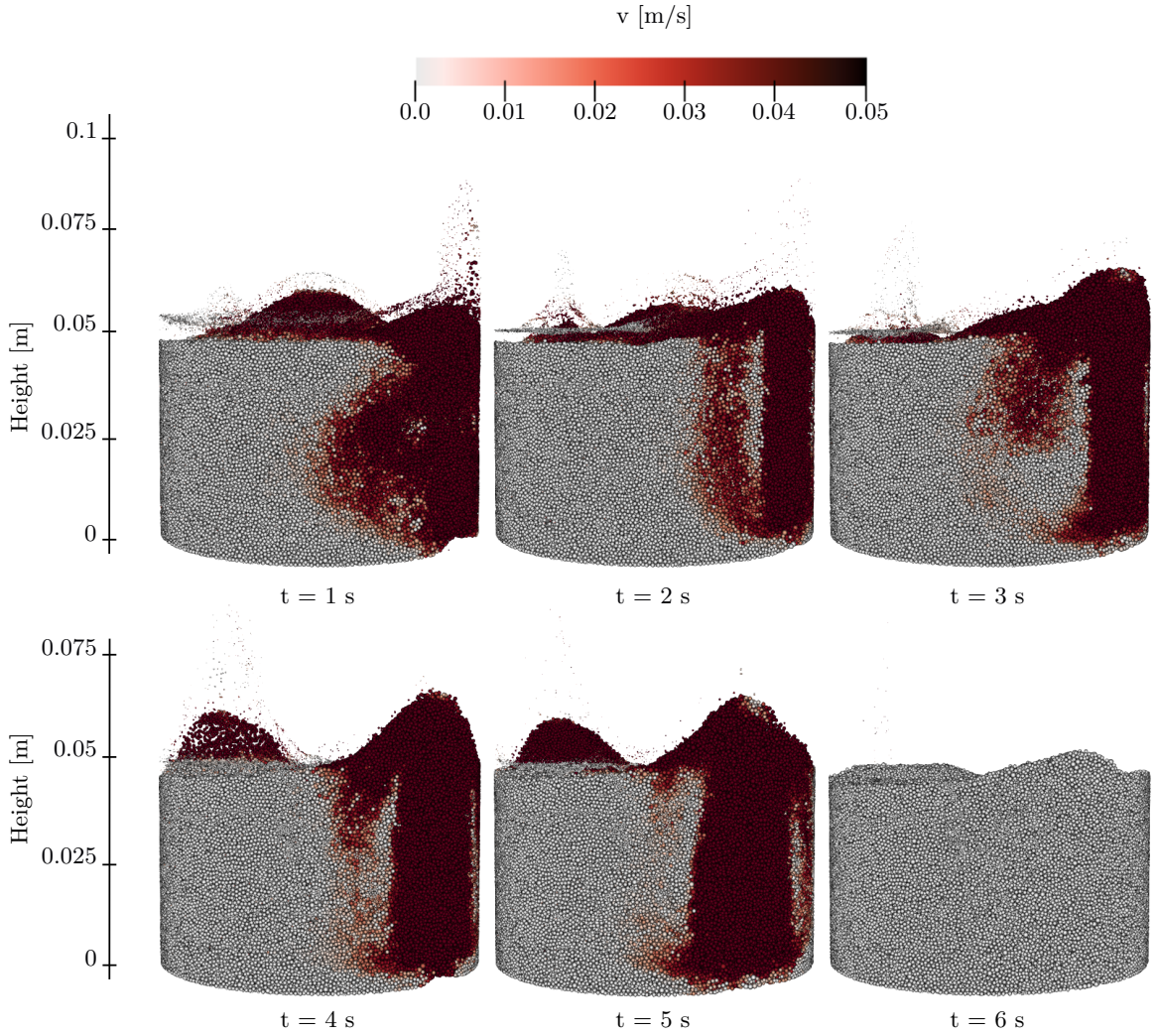


Figure 6.7: Numerical result of the fluidisation behaviour of medium dense Hamburger Sand

The results of the numerical simulation of the fluidisation behaviour of the very dense sand is presented in Fig. 6.8. After 1 s of simulated time, the seepage flow in the cylinder results

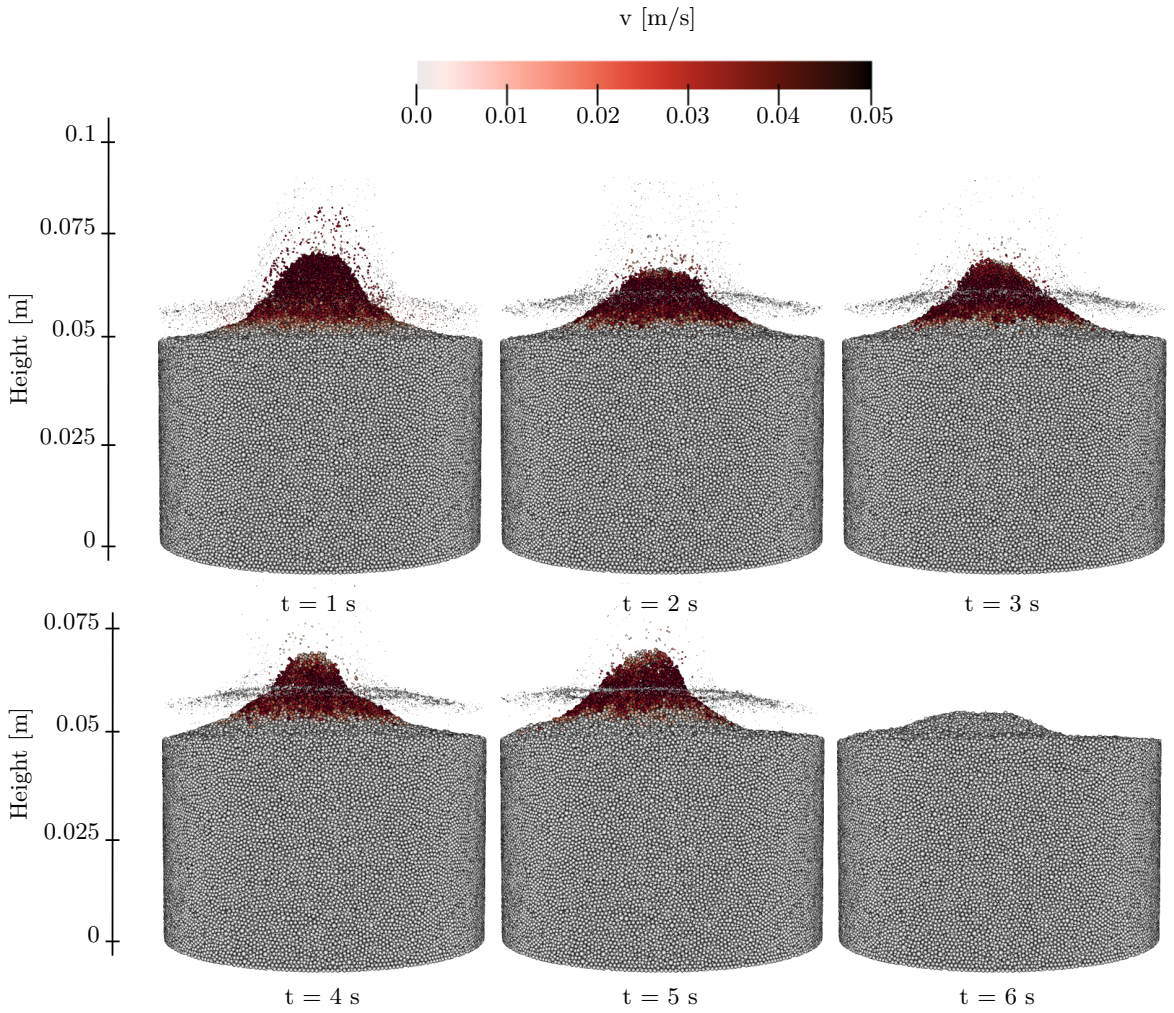


Figure 6.8: Numerical result of the fluidisation behaviour of very dense Hamburger Sand

in a volcano-like outflow of material in the middle of the packed bed. This is in strong contrast to the experimental results shown in Fig. 6.6, where a plug forms. After 2 s, the volcano is still present and the change between 1 s and 2 s is negligible. The static zone is stronger than the mobile zone in the very dense sand. While in the experimental results, a stronger fluidisation behaviour than in the medium dense sand could be observed, the numerical results show the opposite. Throughout the whole simulation, the fluidisation behaviour of the very dense sand is unchanged. The seepage flow stops after 6 s, and after sedimentation of the particles, the final height of the very densely packed bed is 4.9 cm. Consequently, the void fraction change in the medium dense sand is more pronounced than in the very dense sand, which is, again, in contrast to the experimental results.
From these results, it becomes clear that the plug creation in very dense sand is crucial for the accurate depiction of the fluidisation behaviour. Due to the plug formation, a big cavity occurs, where the fluid accumulates. Consequently, when it escapes from this cavity, the fluidisation is more pronounced as the amount of escaping fluid is higher compared to the medium dense sand. The calibration of the material properties is performed with dry samples. In the case of the friction coefficient, the calibration is carried out in a shear test (cf. Sec. 5), where the friction between the particles and the wall cannot be determined. Likewise, for the sake of simplicity, the friction coefficient for particle-particle interaction and particle-wall interaction is assumed to be identical and then calibrated. However, in the presented case, the difference of inter-particle friction and friction between particles and wall could have a significant effect. A sensitivity analysis of the friction coefficient for particle-wall contact is carried out to verify whether different friction coefficients lead to a better depiction of the predominant fluidisation mechanisms in very dense sand.

6.5.1 Sensitivity analysis of the particle-wall friction coefficient

For the sensitivity analysis, the following values for the particle-wall friction coefficient are investigated:

- $\mu_{p-w} = [0.6, 0.57, 0.55, 0.54, 0.53, 0.52, 0.51, 0.505, 0.5]$

To analyse its influence on the plug creation in very dense sand, 1 s of seepage flow is modelled. The results are depicted in Fig. 6.9.
Fig. 6.9 reveals that the reduction of the friction coefficient between particles and wall promotes the formation of a plug. The adhesion between the grains is greater than the friction between wall and particles. This difference allows the particles to migrate upwards together as a bulk. The transition between the volcano-like material outflow and the plug creation lies between $\mu_{p-w} = 0.54$ and $\mu_{p-w} = 0.5$. With $\mu_{p-w} = 0.54$, the flow breaks through at the edge while half of the sand body moves upwards. There is no disconnection of the sand body yet. This disconnection occurs with a further reduction of μ_{p-w} to 0.53. A clear creation of the plug is still not given, but this tendency increases with the further reduction of μ_{p-w}. Its decrease results in a reduction of material outflow at the boundary to the cylinder walls.
The plug fully disconnects at $\mu_{p-w} = 0.51$. The material outflow at the left side of the sand body causes a tilting of the plug accompanied by fluidisation of the material. The tilting is also observed in the experimental tests, but material fluidisation did not occur at this time

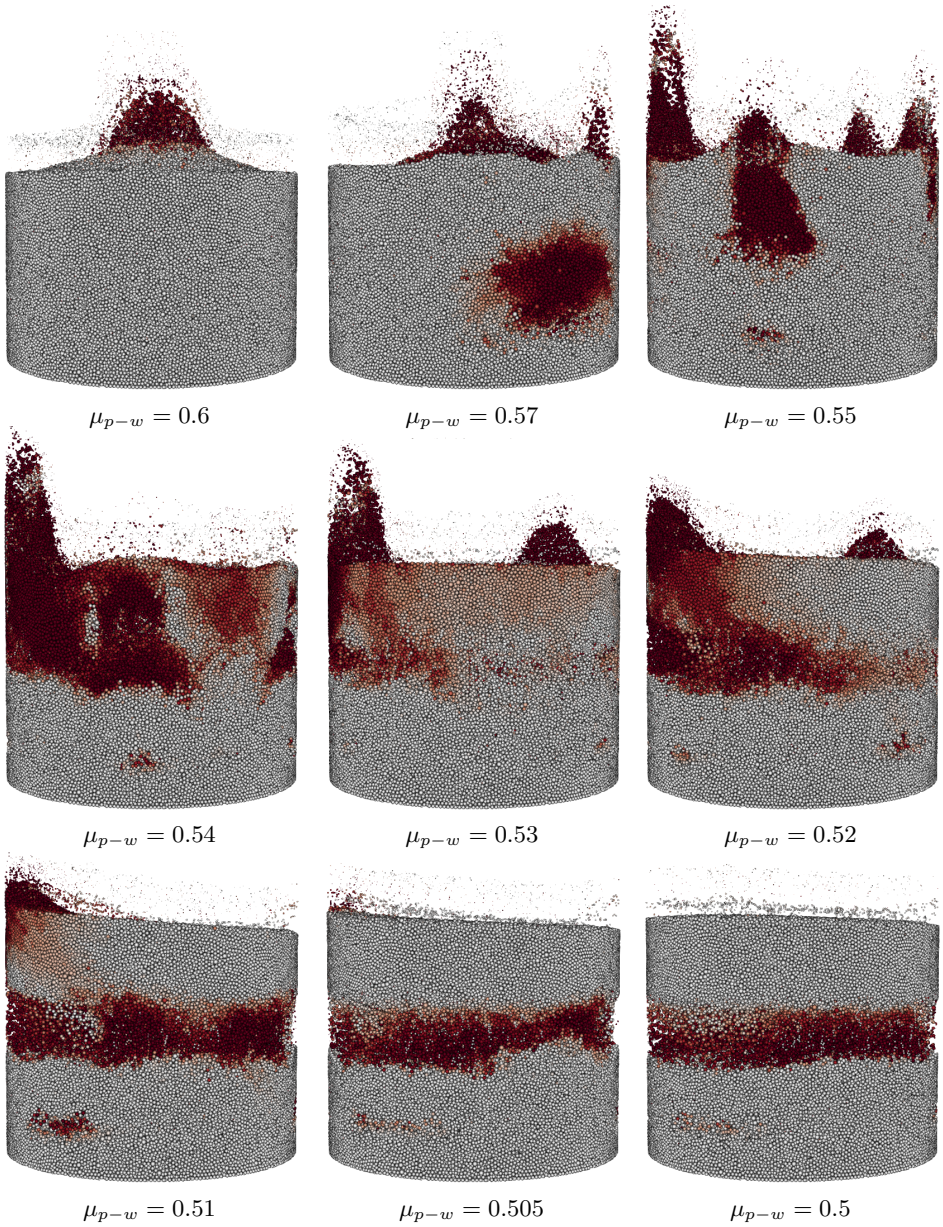


Figure 6.9: Influence of the particle-wall friction coefficient on the plug creation in a very dense sand bed by seepage flow after 1 s

step. Decreasing μ_{p-w} to 0.505 leads to a tilted plug while the seepage flow is not strong enough to cause fluidisation at the boundary to the cylinder walls. A further reduction in friction finally results in a flat formation of the plug surface. At this lower boundary of the plug, the particles settle in consistence with the experiments. The dimension of the lower, static part of the particle column is independent of the friction coefficient μ_{p-w}. The height of the static part is rather dependent on the inter-particle frictions, which determines the internal stability of the bed. Thus, the inter-particle friction force is greater than the imposed drag force. This observation also explains the volcanic-like material discharge in the very dense sand with the same friction coefficient values for particle-particle and particle-wall contact. At $\mu_{p-w} = 0.6$, the friction forces between the particles and between wall and particles are greater than the drag force. The body tenses and the fluid flows through the structure's weakest point, which is located in the middle of the cylindrical sand body. Based on the comparison of the plug formation of the sensitivity analysis and the experimental results, further investigations are carried out with a friction coefficient of $\mu_{p-w} = 0.505$. The tilting plug agrees well with the experimental results.

Fig. 6.10 and Fig. 6.11 depict the numerical results of the fluidisation process with $\mu_{p-w} = 0.505$ for the medium dense and very dense sand bed respectively. The reduced friction coefficient between wall and particles has a minor impact on the fluidisation behaviour of the medium dense sand compared to the very dense sand.

The comparison with the results of the medium dense sand with $\mu_{p-p} = \mu_{p-w}$ shows that reducing μ_{p-w} leads to an increased material transport height after 2 s. Instead of a stable material outflow after 3 s observed in Fig. 6.7, the sand pile at the right side of the packed bed is collapsing in itself. This collapse leads to a reduced height after 4 s. The fluidised channels are, however, still active. At the same time, the material fluidisation at the left side of the medium dense sand bed intensifies. In general, the reduction of μ_{p-w} results in more fluidised regions in the medium dense sand compared to the results presented in Fig. 6.7. After 5 s the fluidisation behaviour of the medium dense sand with reduced μ_{p-w} is comparable to the behaviour of the medium dense sand with $\mu_{p-w} = \mu_{p-p}$. Ceasing the seepage flow after 6 s leads to the sedimentation of the particles. The final height of the particle bed is 4.8 cm. Compared to the results of the fluidisation of the medium dense sand with $\mu_{p-w} = \mu_{p-p}$, the surface of the settled bed is more irregular. This is a result of the increased amount of fluidised channels. In general, the reduction of μ_{p-w} results in a more dynamic fluidisation behaviour in the medium dense sand. The fluidised channels with the respective material outflow are less stable and vary. This agrees well with the experimental results. Overall, unresolved coupled CFD-DEM captures the fluidisation behaviour of the medium dense sand well.

The difference of the numerical results with a reduced μ_{p-w} and the results with $\mu_{p-w} = \mu_{p-p}$ in the fluidisation behaviour of very dense sand is striking. After 1 s, the seepage flow through the very dense sand results in a plug creation, which gradually moves upwards. This agrees very well with the experimental results (cf. Fig. 6.6). The plug is heaved to a height of 5.7 cm, which agrees with the experimental results. However, in contrast to the experimental results, the immobile part of the very dense sand bed is greater. After 2 s, the plug collapses, and a fluidised channel forms at the left side of the very dense sand bed. The fluidised material reaches a height of 7.5 cm, which is a little less than the maximum height observed in the experiment. Additionally, in contrast to the numerical

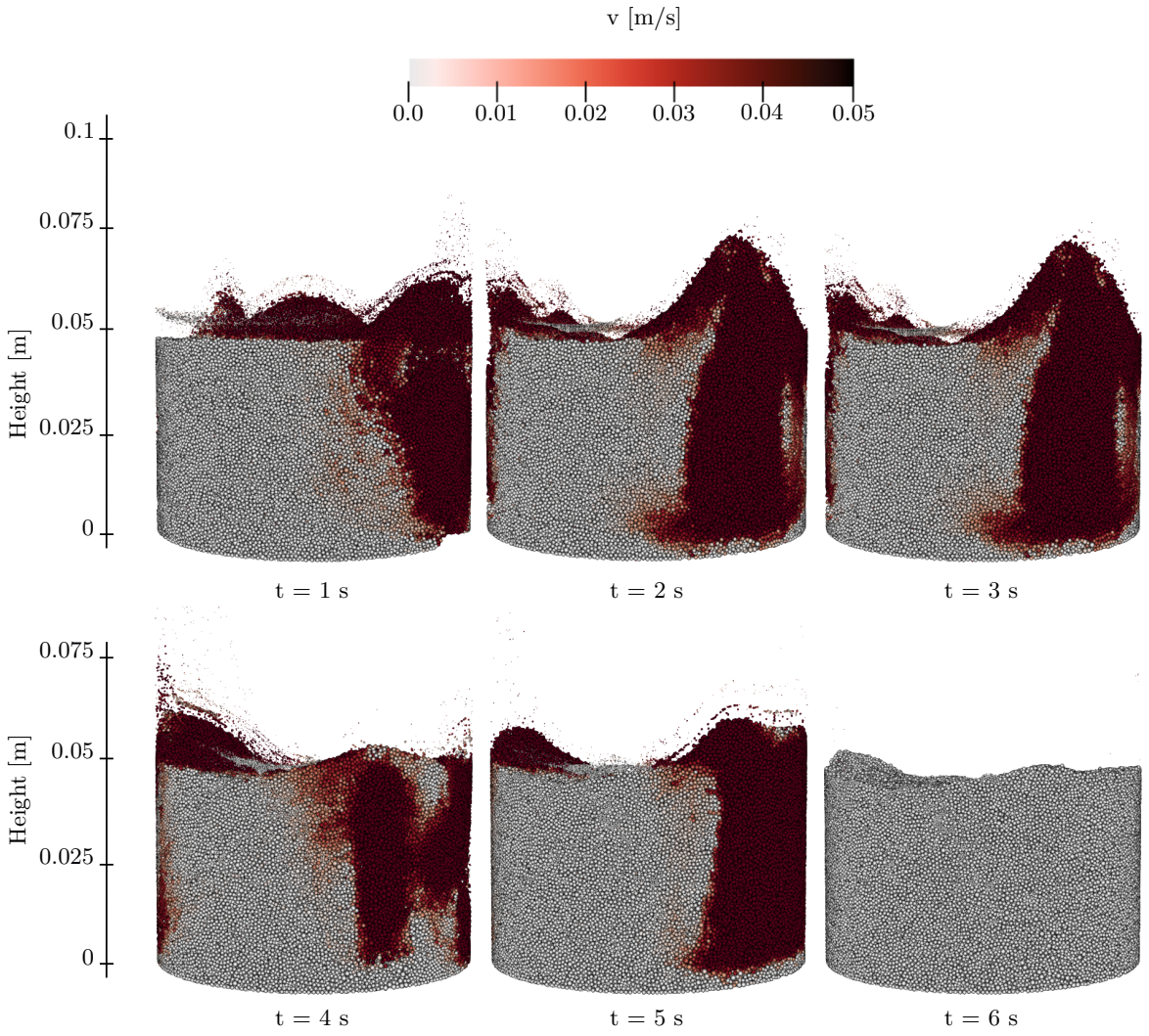


Figure 6.10: Numerical result of the fluidisation behaviour of medium dense Hamburger Sand with reduced particle-wall friction coefficient

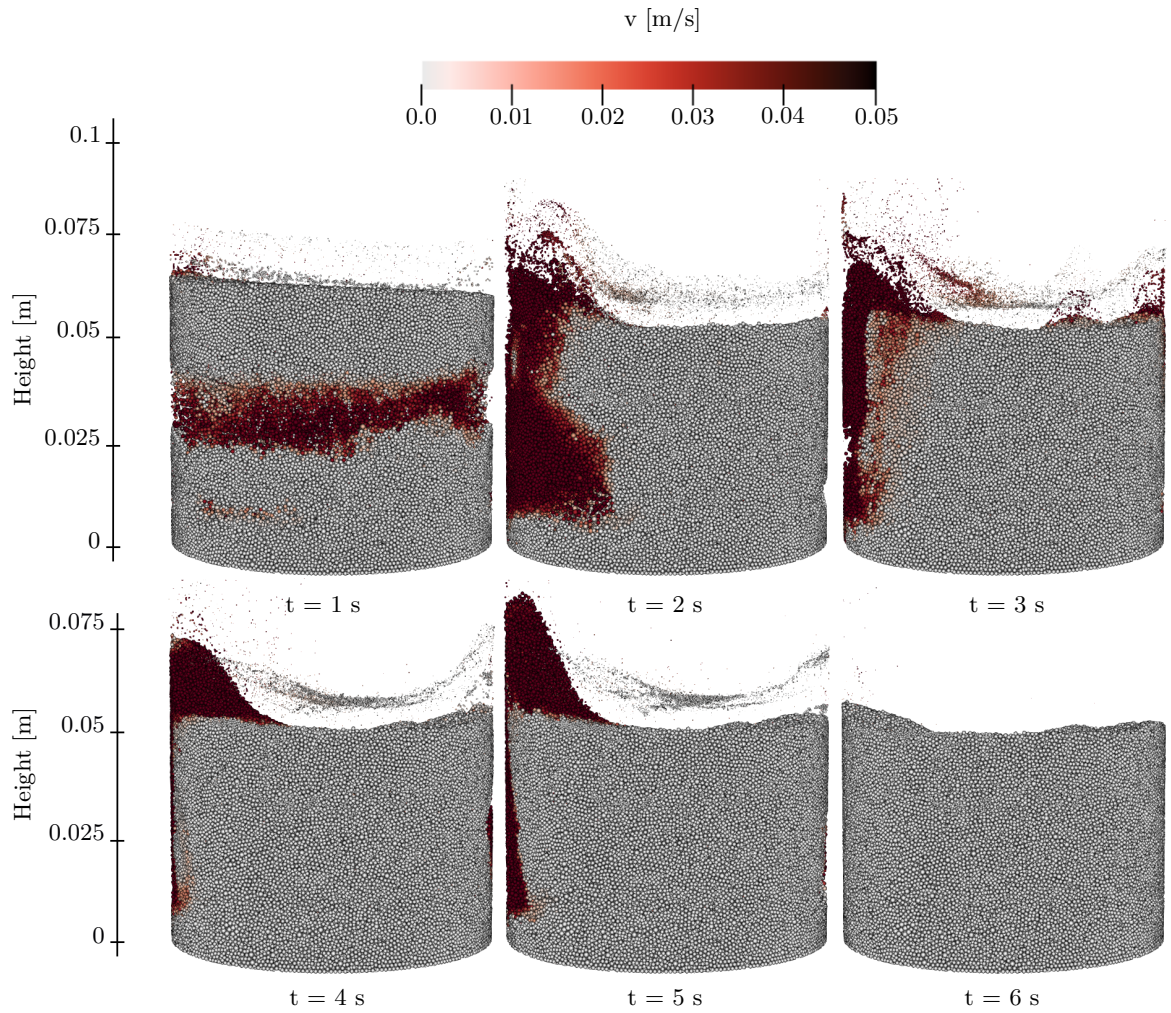


Figure 6.11: Numerical result of the fluidisation behaviour of very dense Hamburger Sand with reduced particle-wall friction coefficient

results, the plug can still be identified in the experimental results after 2 s. After 3 s of seepage flow through the very dense sand, more fluidised channels are formed, and a small cavity can be identified at the left side of the packed bed. As a result, the intensity of the fluidisation increases in this region after 4 s. The intensity continues to increase until 5 s and the material reaches a height of 8 cm. The major part of the very dense sand remains static, while it is loosened to a great extent. The loosening results in an increased particle bed height of 5.1 cm. When ceasing the seepage flow, the sand settles. The very dense sand reaches a static state after 6 s. The final height of the sand bed is 5.1 cm, which is consistent with the experimental results. In comparison to the results with $\mu_{p-w} = \mu_{p-p}$ (cf. Fig. 6.8), the loosening of the very dense sand bed is greater due to the fluidisation. In general, the reduction of μ_{p-w} leads to a good agreement with the experimental results in regards to the fluidisation behaviour of very dense sand.

6.5.2 Normal particle contact forces during the fluidisation of medium densely and very densely packed sand bed

Fig. 6.12 and Fig. 6.13 present the normal contact force distribution during fluidisation of medium dense and very dense sand respectively. The resulting forces are illustrated as tubes, and the force scales their radius. Hence, greater forces result in a greater radius of the tube, and when a loss of contact occurs, the tubes are no longer visible. This representation allows us to identify the fluidised locations in the packed bed. A comparison with the void fraction evaluated over time in these regions can finally give an insight into the change between fluidised suspension and possibly stable soil during seepage flow.

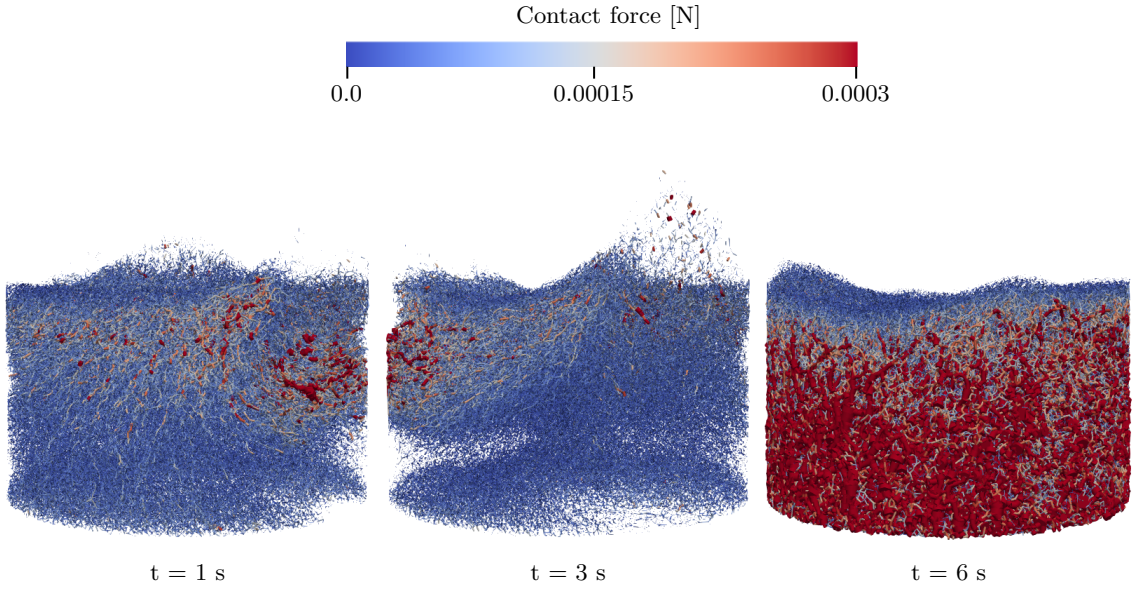


Figure 6.12: Distribution of the normal particle contact forces during the fluidisation of medium dense soil - contact forces are scaled by their value

Fig. 6.12 reveals that the static part of the medium dense sand is not stable as the contact forces tend to zero. Due to the seepage flow, the particles are lifted by the drag force and

separated from each other. This results in a decrease of contact forces. At 1 s, fluidised regions and cavities can well be identified at the right side of the particle bed. In these regions, no contact between the particles occurs any more. The sand particles are fully suspended. At some regions, the contact forces are higher. This is caused by particles which are impacting with other particles at high velocities. At 3 s, more fully fluidised regions can be identified. The suspension of the particles reaches further to the inside of the particle bed. It is interesting to notice that just above the fluidised parts of the bed locates a region with higher contact forces. This could signify that the fluidised material pushes the overlaying material upwards. This leads to compaction above the fluidised region. The fluidised material must then find another path to the top, which results in the observed circular motion of the fluidised sand. This behaviour occurs until the drag force of the seepage flow exceeds the contact forces. The fluid then transports the material, and the fluidised channels reach a straight shape. After the sedimentation of the sand after 6 s, the bed reaches a stable state visible by the increased contact forces, which are constant over the whole area. At the top of the bed, the contact forces are very low. The top is accordingly composed of unstable sand.

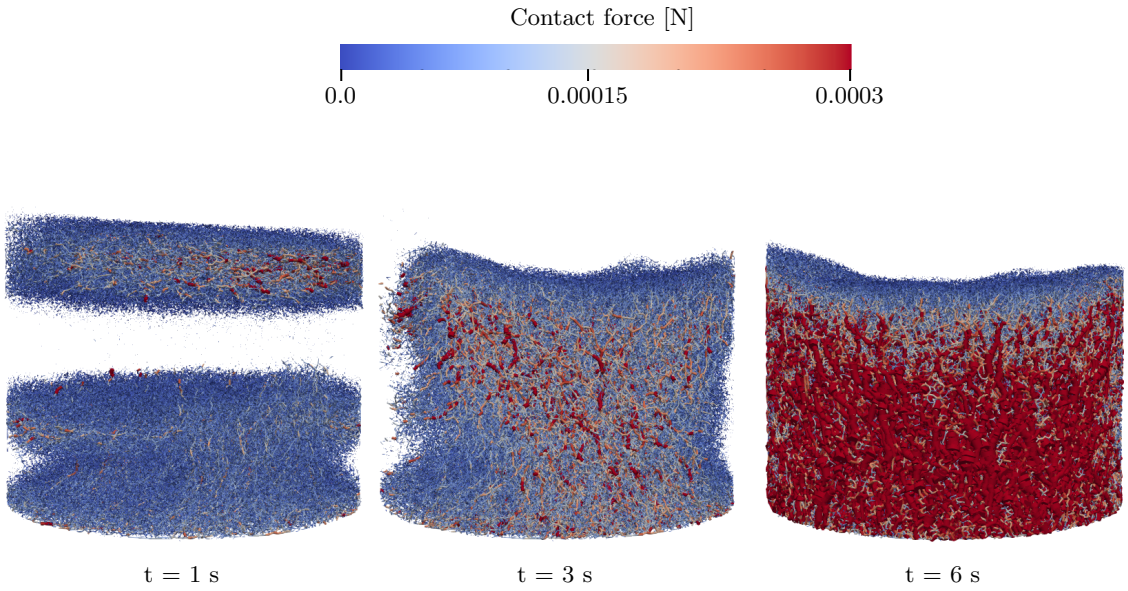


Figure 6.13: Distribution of the normal particle contact forces during the fluidisation of very dense soil - contact forces are scaled by their value

Fig. 6.13 presents the contact force distribution during fluidisation in very dense sand. The contact force visualisation reveals the clear disconnection of the plug with the bottom part of the sand body after 1 s. As with the medium dense sand, the static part of the sand bed is not stable but loosened by the seepage flow. As a result, the contact forces are very low. In the plug itself, the direction of the contact forces is horizontal. This signifies increased hoop stress. At the lower corners of the bottom part, two fluidised or almost disconnected parts can be identified. These fluidised parts, as well as the partly horizontal contact forces, indicate that a plug begins to form in the bottom part of the sand bed.

After 3 s, when the plug has collapsed, we can observe a comparable contact force distribution to the medium dense sand. The visualisation of the contact forces now reveals higher dynamics in the sand bed than assumed from the results in Fig. 6.11. There is an ongoing change between fluidisation and compaction due to sedimentation of particles leading to possibly stable soil. The direction of the contact forces is mostly vertical, which is indicated by the inclination of the force tubes. In contrast to the medium dense sand, the regions with higher contact forces are not primarily located above a fluidised region. Hence, we can assume that the regions of increased contact forces in the very dense sand after 3 s results from particles impacting the particle bed surface. Their impact leads on the one hand to a denser particle packing and on the other hand, to an increased velocity of the underlying particles.
In general, we need to distinguish between two phenomena that lead to increased particle contact forces:

1. Fast particles: The high velocities of the particles lead to increased contact forces when they impact with another particle. This results in isolated high particle contact forces, as can be observed especially in medium dense soil. They do not lead to a more stable structure in the soil.

2. Stable bed and compaction: With either stable or very dense bed, the confinement generates higher particle forces. This is the case when an increase in particle contact forces can be observed over a large area. This behaviour occurs partially in very dense sand.

Just as with medium dense sand, the sedimentation of the particles after 6 s leads to a stable bottom with a weakly bearing layer at the top.
The void fraction over time in the fluidised channels, which could be identified in Fig. 6.12 and Fig. 6.13, is presented in Fig. 6.14 for medium dense and very dense sand. The median void fraction in these channels, as well as the median void fraction in the whole sand bed, are plotted over time.
At the beginning of the simulation, the very dense sand has a median void fraction of $n = 0.35$ and the medium dense sand of $n = 0.38$. The void fraction for medium dense and very dense sand in the experiment is hence identical to the numerical void fraction for medium dense and very dense sand respectively. This proves that the sample preparation methods applied in the presented numerical simulations are appropriate. When the seepage flow starts, the void fraction is gradually increasing. In the medium dense sample, the creation of fluidised channels can be identified by sharp increases of the void fraction (e. g. at 0.7 s). The plug creation in the very dense sand leads to a more constant increase of the void fraction. However, the moment of the collapsing plug can be identified by the sudden increase of the void fraction at 1.5 s followed by a sharp decrease. In general, an increase of the void fraction, i. e. fluidised channel, seems to be followed by a sudden decrease. In the case for the very dense sand, where these large fluctuations occur between 1.5 s and 3.5 s, the same behaviour is observable. The median void fraction decreases from a value of $n = 0.87$ to a minimum of $n = 0.47$, which is slightly higher than $n_{\max}$ of the investigated Hamburger sand ($n_{\max} = 0.446$). These jumps indicate raceway conditions. When the cavity has formed and fluid escapes from the packed bed, new material is flowing into these cavities. Thus, the void fraction decreases.

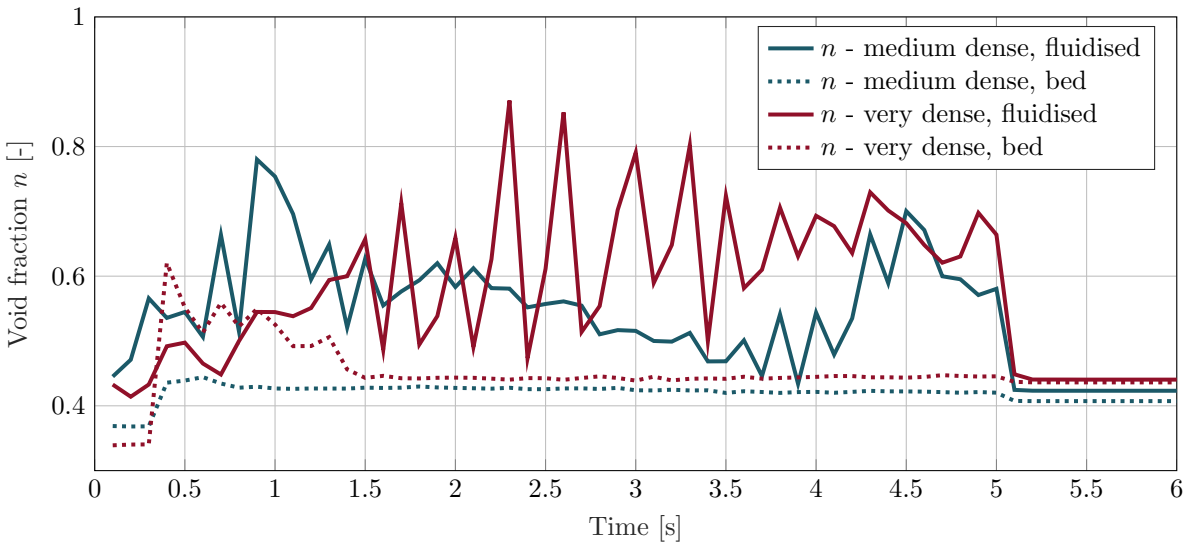


Figure 6.14: Development of median void fraction over time in the fluidised channels and in the whole bed for medium dense and very dense sand

The void fraction over time furthermore reveals that higher fluidisation dynamics occur in the very dense sand. In the medium dense sand, the void fraction gradually decreases to $n = 0.46$ at 3.5 s until seepage flow evolves in a fluidised channel. The void fraction consequently increases to $n = 0.7$, which greatly exceeds the maximum void fraction of Hamburger Sand revealing full fluidisation. At the same time, at 3.5 s, the changes in the void fraction in very dense sand decrease while the void fraction is still high ($n = 0.7$). Hence, this almost constant void fraction is a result of continuous seepage flow through the sand bed. At 5 s, the seepage flow is ceased, which is reflected by the sudden decrease of the void fraction. The sedimentation of medium dense and very dense sand is equally long, which contrasts to the experiments.

The overall void fraction of the medium dense bed stays nearly constant over the whole fluidisation process. The static part of the bed is greater than the fluidised part. Thus, its influence on the void fraction is more significant. However, the bed is visibly loosened by the seepage flow. The void fraction changes from $n = 0.38$ at the beginning to $n = 0.43$ during fluidisation. The overall void fraction of the very dense sand bed experiences more fluctuations over time, especially at the beginning. The plug heave results in an increase of the void fraction n. The analysed domain for the overall void fraction contains more fluid cells with a lower amount of particles due to the heave compared to the medium dense sand. After the plug's collapse, the median value of the void fraction in the very dense sand bed reaches a steady value of $n = 0.44$ during fluidisation. As with the medium dense sand, the major part of the bed is static, resulting in the constant void fraction over time.

As the maximum void fraction of the investigated Hamburger Sand is $n_{\max} = 0.446$ and taking into account the analysis of the contact forces (cf. Fig. 6.12 and Fig. 6.12), it is questionable whether load-bearing sand is present or whether the sand is completely suspended during fluidisation.

The final void fraction is $n_{\text{num,medium dense,f}} = 0.4$ for the medium dense sand and $n_{\text{num,very dense,f}} = 0.42$ for the very dense sand. This is consistent with the experimental results. The deviation between the experimental and the numerical final void fraction is negligible revealing a quantitative agreement.

6.5.3 Review of flow regimes to predict fluidisation behaviour

In reality, to predict whether a soil risks to be fluidised can rarely be carried out using numerical simulations with unresolved coupled CFD-DEM as it requires careful material calibration and high computational power. Therefore, flow regimes can be used to estimate at which pressure or fluid velocity, the investigated soil will likely fluidise. In Sec. 6.1, two criteria were introduced to assess the risk of possible fluidisation: The minimum fluidisation velocity u_{mf} proposed by Ergun (1952) and the criterion by Terzaghi (1943) that assesses the fluidisation of a soil with the critical hydraulic gradient i_c. It is calculated by the equilibrium between the buoyant weight of the sand bed and the fluid force, cf. Eqn. 6.5. The medium dense sand has a void fraction of $n = 0.38$, which leads to a critical hydraulic gradient of:

$$i_c = \frac{(1-n)(\gamma_s - \gamma_w)}{\gamma_w} = \frac{(1-0.38)(2650-1000)}{1000} = 1.023 \tag{6.10}$$

From this follows the pressure drop across the bed required for fluidisation of the medium dense sand:

$$\Delta P = i_c \Delta h \rho_w g = 1.023 \cdot 0.04 \cdot 1000 \cdot 9.81 = 401.43\,\text{Pa} \tag{6.11}$$

As the minimum fluidisation velocity u_{mf} indicates the moment before reaching this constant pressure drop representing the criterion of Terzaghi (1943), it is investigated what happens inside the soil at these two different fluidisation stages. Therefore, the fluid velocity through the medium dense soil bed is increased step-wisely from $u = 0.001\,\text{m/s}$ to $u = 0.05\,\text{m/s}$ to model the different stages of fluidisation of the medium dense sand bed. Fig. 6.15 depicts the pressure drop across the bed during the increase of the fluid velocity. Fig. 6.16 presents the particle velocity in the sand bed at selected fluid velocities, which are highlighted in Fig. 6.15.

Fig. 6.15 shows that the minimum fluidisation velocity u_{mf} is reached at $u = 0.0126\,\text{m/s}$ after a linear increase of the pressure drop across the sand bed. It is marked by (1). Fig. 6.16 depicts that at u_{mf} the sand bed is not yet fluidised, and only some fine particles start to lift. After reaching u_{mf}, the pressure drop decreases until a pressure of $\approx 400\,\text{Pa}$, which corresponds to the pressure drop calculated with the hydraulic gradient i_c. The fluid velocity at point (2) indicates the stage during the decrease to the constant pressure drop. At this fluid velocity, the whole sand bed begins to lift. Hence, the sand bed begins to lose its internal stability, cf. Fig. 6.16. At a fluid velocity of $u = 0.022\,\text{m/s}$ ((3)), the pressure drop across the bed is reaching a constant level. At this moment, a continued lifting of the sand bed can be identified accompanied by fluidised channels beginning to develop, cf. Fig. 6.16. Thus, fluidisation of the whole sand bed starts. The further increase of the fluid velocity leads to an almost constant pressure drop across the sand bed in agreement to the fluidisation theory described in Sec. 6.1. (4) and (5) in Fig. 6.15 and Fig. 6.16 reveal

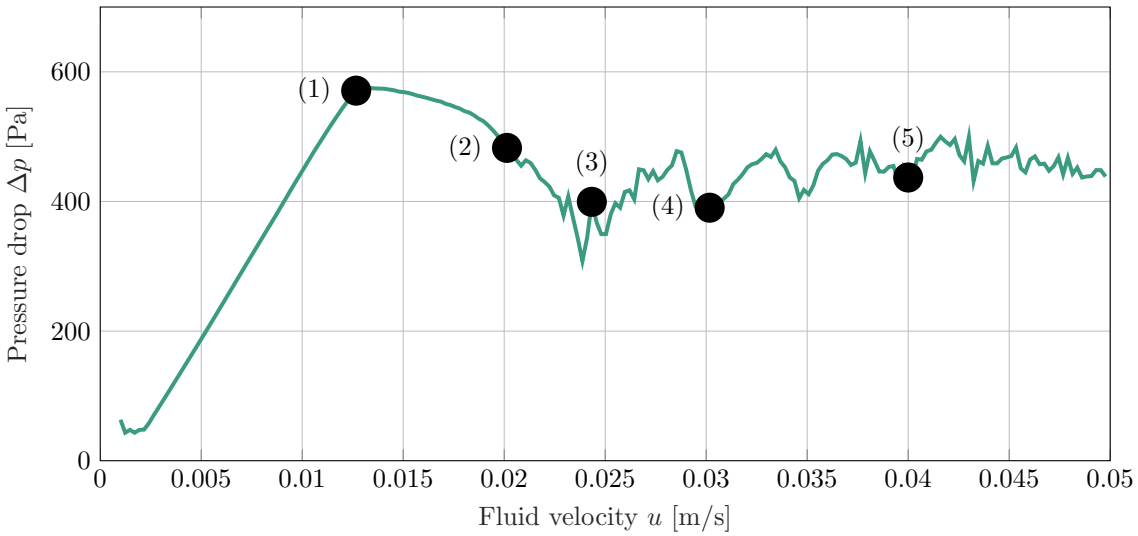


Figure 6.15: Pressure drop over the medium dense sand bed vs. fluid velocity u

what occurs in the sand bed with this further increase. At (4) with a fluid velocity of $u = 0.03\,\mathrm{m/s}$, the sand bed is fluidised. The fluidised channels are fully developed, and the material outflow is strong. The increase to $u = 0.04\,\mathrm{m/s}$ at (5) leads to an ongoing very strong fluidisation dynamic with a circular motion of particles across the bed and broad fluidised channels. It is noteworthy that the required pressure for fluidisation according to i_c for fluidisation to occur is already reached before fluidisation starts. This elevation of the pressure drop at u_{mf} compared to the pressure drop at i_c is caused by two factors: First, the medium dense packing of the investigated sand bed and second, the friction at the walls. Thus, an increased force is required to loosen the sand and overcome the friction at the walls. The drop in the net pressure occurring after reaching u_{mf} defines the moment of developing cavities accompanied by the beginning of fluidised zones. However, in general, both u_{mf} and i_c are well suited to define the moment of fluidisation. As this analysis reveals u_{mf} defines the beginning of the development of fluidised zones in the sand bed and i_c describes the moment of full fluidisation.

As the assessment of hydraulic failure is carried out by calculating the required pressure for the soil to fluidise, the required fluid velocity u cannot be determined as the pressure drop is constant. The minimum fluidisation velocity u_{mf} is therefore useful, when the assessment of a possible hydraulic failure is carried out by the estimation of the required fluid velocity.

6.6 Summary

The fluidisation of medium and very dense sand was investigated with unresolved coupled CFD-DEM in a small setup. The numerical models were validated against experimental tests to ensure that the models depict the right physical behaviour. The motion of the sand was recorded with a high-speed camera in the experimental tests, and PIV analyses were

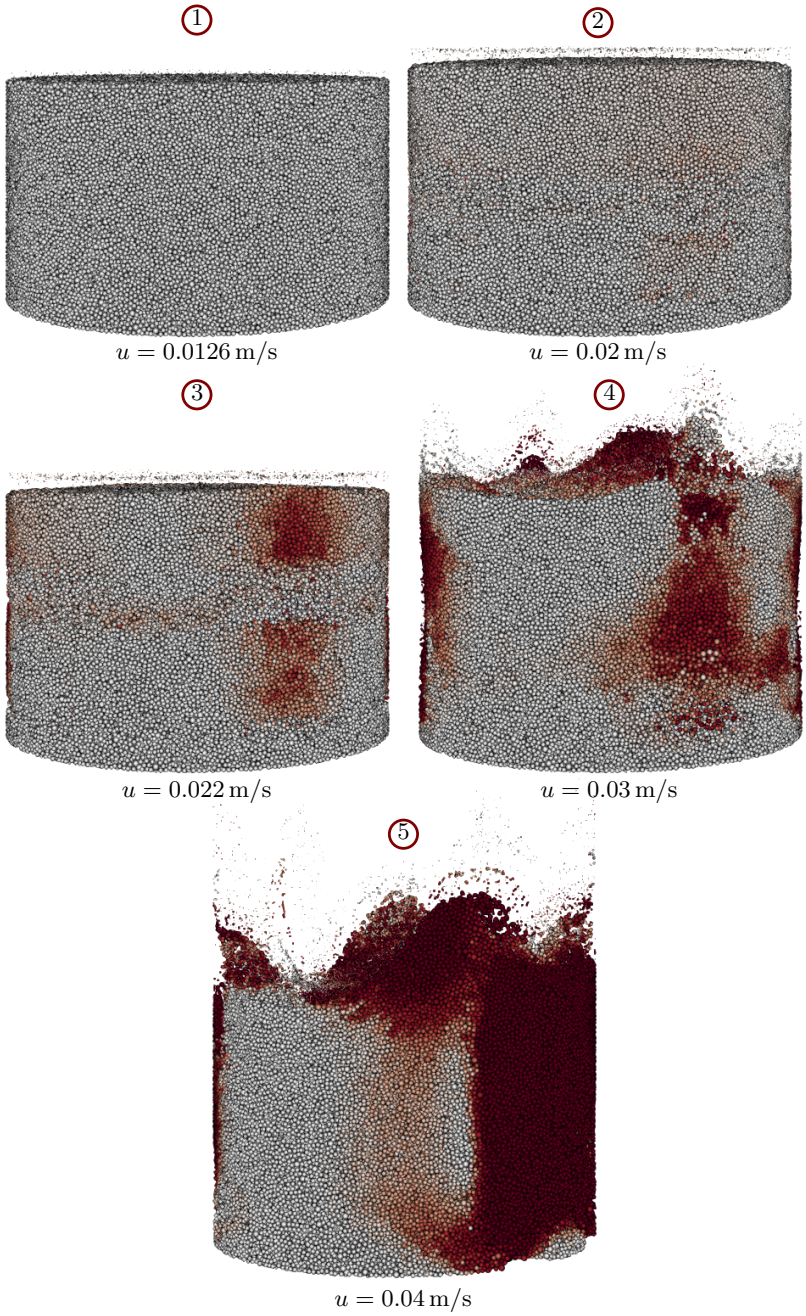


Figure 6.16: Particle velocities and fluidisation behaviour of the medium dense sand bed with increasing fluid velocity u

carried out. The following findings can be summarised from the investigation of fluidisation in medium dense and very dense sand:

1. Fluidisation occurs in both medium dense and very dense sand. A plug formation accompanies the fluidisation of the very dense sand. The plug is heaved by the seepage flow until it collapses, which leads to high fluidisation dynamics. Sedimentation occurs almost instantly after ceasing seepage flow in medium dense and very dense sand.

2. The comparison of the numerical results with the experimental results shows a good agreement in regards to the medium dense sand. In case of the very dense sand, the numerical model fails to depict the plug creation with the subsequent fluidisation.

3. A calibration of the friction parameter μ_{p-w} between particles and wall is necessary to model the fluidisation of very dense sand accurately. With $\mu_{p-w} = 0.505$ the plug creation and subsequent fluidisation is modelled accurately. Validation of the numerical model is hence successful.

4. Both experimental and numerical results reveal a significant loosening of the sand after sedimentation. The numerical model can, in both cases, reproduce the final void fraction. It was found that the loosening of very dense sand is greater than of medium dense sand ($\Delta n_{\text{medium dense}} = 0.02$ & $\Delta n_{\text{very dense}} = 0.07$).

5. The investigation of the normal particle contact forces shows the total loss of contact in suspended zones. Furthermore, it could be observed that the contact forces in the whole sand bed reduce significantly, which reveals a noticeable loss of stability not suspected from the experimental tests.

6. The investigation of the void fraction in the sand bed points to the same conclusion. It further shows that already during fluidisation, the very dense sand is loosened to a greater extent than the medium dense sand.

7. The pressure drop across the medium dense sand with increasing fluid velocity was modelled to investigate the fluidisation behaviour of the sand bed at minimum fluidisation velocity u_{mf} and at the critical hydraulic gradient i_c. It was found that at u_{mf}, the sand bed is not fluidised and only some particles begin to lift. Full fluidisation of the sand bed occurs at i_c. However, between u_{mf} and i_c, the sand bed starts already to lift significantly and begins to lose its stability. Fluidised zones begin to develop.

These results show that unresolved coupled CFD-DEM is well suitable for investigations on fluidisation and the respective loss of stability in sands. The method can, therefore, be used to determine the risk of possible fluidisation in cohesionless soil.

7 Suffusion

Suffusion is a process in a cohesionless gap-graded soil where a fraction of the fine particles does not receive the effective stresses and can move freely between the coarser fraction. The channels between the coarse particles have to be broad enough for suffusion to occur. Suffusion in soil structures, such as earth dams and dykes, is a serious problem for long-term stability. Thus, the assessment of possible suffusion in soil is important. Therefore, we need to capture the erosion process of fine grains accurately. While laboratory tests do not allow to look "insight" the structure, numerical tools can be of adequate help. This chapter presents the numerical investigation of suffusion in a bidisperse packing with a special focus on the employed drag force correlation. The results are compared to experimental data.

7.1 Introduction

When exposed to seepage, internal erosion can disturb the soil structure resulting in soil particle migration. The term internal erosion thereby refers to the following effects (Fell and Fry, 2014):

1. Erosion in a concentrated leak: The water flows through a crack or a hole and is eroding the walls.

2. Backward erosion: Water flow erodes the surface of the soil in an upstream direction, causing erosion from its exit.

3. Contact erosion: Water flows through soils with different permeabilities, causing erosion at their interface.

4. Suffusion: Water flow erodes the fine grains through the pores of the coarser grains.

Suffusion increases the permeability and porosity of the soil while the bulk density decreases, which leads to a minor overall resistance of the soil. Generally, two criteria define whether a soil tends to suffusion or not.
The first criterion is a geometric condition reviewing whether the pore space of coarser particles is large enough for the free passage of finer particles without clogging. An initial check to assess internal stability can be carried out using this geometric criterion. Terzaghi (1943) considers the distance ratio between the characteristic filter grain diameter d_{15} and the characteristic diameter of the base material d_{85} as an indication for suffusion. The following equation was derived from investigations by Bertram (1940) (Terzaghi, 1943; Terzaghi and R. B. Peck, 1961)

$$\frac{d_{15}}{d_{85}} < 4 \tag{7.1}$$

Besides, the Federal Waterways Engineering and Research Institute (BAW) recommends the methods by Ziems (1969), Kenney and Lau (1985), and Burenkova (1992) to assess suffusion. They are based on geometrical criteria calibrated through laboratory tests. In general, these methods have a wide range of applications, are easy to use and provide reliable results.

The second criterion is a hydraulic condition, which defines whether the hydrodynamic load can mobilise and transport the fines. There have been some attempts to provide a general hydraulic criterion (M. Li, 2008; Goltz et al., 2010). However, M. Li (2008) emphasises that the proposed critical gradient i_c for the mobilisation of the fine particles is a local and non-intrinsic value. It varies with the dimension of the test tube and with its boundary conditions. Hence, the determined i_c is dependent on the test conditions and can, therefore, not be applied to general cases.

Semar et al. (2010) evaluate the different filter criteria proposed in the literature. They conclude that these approaches are limited in their usability as they are mainly valid for soils, which are comparable to those analysed. Furthermore, local effects and structural changes, which can lead to settlements or influence the hydrodynamic conditions, are entirely neglected. Hence, the need for further research is very high. In general, suffusion has been widely studied at a macroscopic scale. These efforts improved our understanding of the macroscopic effects of suffusion, but the mechanisms at microscopic scale associated with the initiation and evolution of suffusion remain unclear.

Numerical studies can, therefore, give valuable insight into the leading mechanisms of suffusion and its consequences on the soil matrix. Wood et al. (2010) investigated the effect of suffusion on the mechanical response of a soil specimen by manually removing fine particles using DEM. They observed that this change of the soil matrix leads to a variation of the critical state and the soil strength. There exist a variety of investigations on suffusion with DEM (Scholtès et al., 2010; Shire and O'Sullivan, 2013; Zhang et al., 2019). However, the key mechanisms leading to suffusion as seepage flow and the solid-fluid interaction cannot be modelled with pure DEM simulations. Likewise, the onset of suffusion and possible initiation of piping is not captured. Yerro et al. (2017) performed numerical investigations on suffusion with a two-phase MPM model. A simple erosion law was included in the constitutive equations for the soil. The applied erosion law controls the detachment of the fines in the soil matrix. With this extension of the constitutive law, they were able to model internal erosion. However, the migration of the fines is dependent on the chosen erosion law. Using a coupled approach like the coupled CFD-DEM, an erosion law to model the detachment of fines in a soil skeleton becomes irrelevant. Kawano et al. (2018) used the coupled CFD-DEM to investigated the change of the stress state before and after suffusion in loose and dense sand specimens with different hydraulic gradients. Their results indicate that stress is a crucial determinant of whether or not particles are likely to erode. Once the particles have less than three contact partners, they can move freely in the soil matrix and are transported by the seepage flow. They concluded that in loose sands where the particles experience lower stress than in dense sands, the fines are more likely to erode.

Hu et al. (2019) investigated seepage flow in gap-graded and well-graded soil samples with unresolved coupled CFD-DEM. They performed a parametric study on the effect of initial fines content and the hydraulic gradients on the erosion kinetics. Their results showed that

the ultimate fines content is independent of the imposed hydraulic gradient once erosion is initiated. Regarding the well-graded sand, partial clogging and blowouts of the fine particles occurred, resulting in a stable state after these rearrangements. However, Hu et al. (2019) did not perform a validation of the model, and gravitation on the particles was neglected during seepage flow. Accordingly, their results must be treated with caution. Hu et al. (2020) investigated the differences in the mechanical response between suffusion numerically modelled by particle removal, unresolved coupled CFD-DEM and reconstituted samples. Reconstituted samples have a PSD of already eroded soil. They first applied a seepage flow on the soil samples and then carried out a triaxial test on the eroded soil. They found that the samples, where particles were removed, experienced a strain-hardening while the reconstituted samples experienced strain-softening. The different mechanical behaviour stems from the discrepancies of the initial void ratios of the samples before shearing. Additionally, they found that compared to the two other methods, the coupled CFD-DEM simulation resulted in more fines that are likely to erode. The seepage flow through the sample leads to uneven erosion processes in the soil specimen, which cannot be captured by removal of particles or reconstituted soil samples. This result emphasises the need for accurate simulations with coupled CFD-DEM as the seepage flow clearly influences the overall mechanical response of the investigated soil sample. Kanitz and Grabe (2019b) investigated the influence of different drag force models on the migration behaviour of fines in a bidisperse particle bed with an intense seepage flow of 1.25 m/s. They found that those models lead to different loss of fines, different migration paths in the soil and consequently, different void ratio evolutions in the investigated samples. They concluded that the choice of the drag force model is crucial for an accurate depiction of the suffusion process in soil.
Therefore, the investigations presented herein focus on the influence of the used drag force model on the onset of suffusion by seepage flow and the migration behaviour of the fines. The whole suffusion process - until all the fines are eroded - and the influence of confinement are not investigated.

7.2 Drag force in particle assemblies

As the investigations on suffusion focus on the influence of the drag force on the migration behaviour of fines in a soil sample, the mostly used drag force correlations are presented in this section. The basic information on the drag force correlations were briefly introduced in Sec. 4.3. This section provides a more detailed presentation of the existing drag force correlations for particle assemblies. Generally, the drag force for an isolated particle can be determined by:

$$F_{D0} = C_D \pi \rho_f d_p^2 |\boldsymbol{u} - \boldsymbol{v}| (\boldsymbol{u} - \boldsymbol{v}) /8 \tag{7.2}$$

where C_D is the drag coefficient, d_p the particle diameter, $\boldsymbol{u}$ the fluid velocity and $\boldsymbol{v}$ the particle velocity. C_D is thereby closely related to the Reynolds number and can be determined through (Schiller and Naumann, 1935):

$$C_D = \begin{cases} \frac{24}{Re_p}\left(1 + 0.15 Re_p^{0.687}\right) & Re_p < 1000 \\ 0.44 & Re_p \geq 1000 \end{cases} \tag{7.3}$$

Re_p is the particle Reynolds number and defined by $Re_p = \rho_f d_p n|u - v|/\mu_f$. Wen and Y. H. Yu (1966) extended this formulation for the pressure drop in dilute particle assemblies by including a momentum exchange coefficient β between the fluid and the solid phase. They derived a correlation for β by correlating their numerical results with experimental data for bed pressure drop experiments. Gidaspow, 1994 then combined the correlation of Wen and Y. H. Yu (1966), which is suitable for dilute systems, with the correlation of Ergun (1952), only suitable for dense systems. At the boundary between the two regimes at $n = 0.8$, Gidaspow (1994) adopted a step change, which was reported not to be elegant from a numerical point of view (Kafui et al., 2002). To overcome this problem, Di Felice (1994) proposed a continuous single-function correlation. Di Felice, 1994 investigated how the drag force acting on a particle assembly needs to be modified from the drag force on a single particle using the drag coefficient of Dallavalle (1948). On this basis, Di Felice (1994) elaborated a voidage function $f(n)$. Evaluating $f(n)$ for fluidised bed and fixed bed experiments, Di Felice (1994) derived a parameter χ, which depends solely on the Reynolds number. Koch and Hill (2001) and Koch and Sangani (1999) established a correlation depending on the Reynolds particle number Re_p and the void fraction n using LBM-DEM simulations of a fluidised bed reactor. An overview of these mostly used drag correlations based on empirical correlations can be found in Tab. 7.1.

Table 7.1: Some frequently used drag force correlations

Author	**Drag force** F_D	**Drag coefficient** C_D
Schiller and Naumann (1935)	$F_D = C_D \pi \rho_f d_p^2 \lvert \boldsymbol{u} - \boldsymbol{v} \rvert (\boldsymbol{u} - \boldsymbol{v}) /8$	$C_D = \begin{cases} \frac{24}{Re_p}\left(1 + 0.15 Re_p^{0.687}\right) & Re_p < 1000 \\ 0.44 & Re_p \geq 1000 \end{cases}$
Ergun (1952)	$F_D = \beta V_p (\boldsymbol{u} - \boldsymbol{v})$ with $\beta = 150 \frac{(1-n)^2 \mu_f}{n (d_p \phi_p)^2} + 1.75 (1-n) \frac{\rho_f}{\phi_p d_p} \lvert u - v \rvert$	
Gidaspow (1994)	$F_D = \beta V_p (\boldsymbol{u} - \boldsymbol{v})$ when $n \geq 0.8$: $\beta = \frac{3}{4} C_D \frac{n \lvert u - v \rvert \rho (1-n)}{d_p} n^{-2.65}$ when $n < 0.8$: $\beta = 150 \frac{(1-n)^2 \mu_f}{n (d_p \varphi_s)^2} + 1.75 (1-n) \frac{\rho_f}{\varphi_s d_p} \lvert u - v \rvert$	$C_D = \begin{cases} \frac{24}{Re_p}\left(1 + 0.15 Re_p^{0.687}\right) & Re_p < 1000 \\ 0.44 & Re_p \geq 1000 \end{cases}$
Di Felice (1994)	$F_D = C_D \pi \rho_f d_p^2 n^{-\chi+2} \lvert \boldsymbol{u} - \boldsymbol{v} \rvert (\boldsymbol{u} - \boldsymbol{v}) /8$ with $\chi = 3.7 - 0.65 \exp\left[-1/2 \left(1.5 - \log(Re_p)\right)^2\right]$	$C_D = \left(0.63 + \frac{4.8}{\sqrt{Re_p}}\right)^2$
Koch and Hill (2001)	$F_D = F_0(\phi) + 0.5 F_1(\phi) Re_p^2 \quad Re_p < 20$ $F_D = F_0(\phi) + 0.5 F_3(\phi) Re_p^2 \quad Re_p > 20$ $F_0(\phi) = \frac{1 + 3\sqrt{\phi/2} + (135/64)\phi \ln \phi + 16.14\phi}{1 + 0.681\phi - 8.48\phi^2 + 8.16\phi^3} \; (\phi < 0.4)$ $F_0(\phi) = 10\phi/(1-\phi)^3 \; (\phi \geq 0.4)$ $F_1(\phi) = 0.110 + 5.10 \cdot 10^{-4} \exp(11.6\phi)$ $F_3(\phi) = 0.0673 + 0.212\phi + 0.0232(1-\phi)^5$	

Note: It is important to clarify that $\boldsymbol{u} - \boldsymbol{v}$ is the relative and not the superficial velocity, ϕ denotes the solids fraction.

7.3 Influence of different drag force model on suffusion

This section presents a preliminary investigation of the influence of the use of different drag force models on the migration behaviour of fine particles in a bidisperse soil column according to the investigations by Kanitz and Grabe (2019b). In their contribution, the seepage flow has a velocity of $u = 1.25\,\mathrm{m/s}$. The investigations presented here are carried out with a significantly slower seepage flow to verify if the observed differences still occur. Therefore, a particle column with a diameter of 0.08 m and a height of 0.1 m is modelled. The constant seepage velocity is $u = 0.035\,\mathrm{m/s}$ with a respective zero-gradient boundary for the pressure field (*OpenFoam documentation, Boundary conditions* 2020). Two different types of particles are used: particles with 1 mm diameter and particles with 5 mm diameter. The content of the fine fraction is 12.5 %. The coarse particles are not allowed to move. In this way, only the fine particles can travel through the pore channels, and no heave of the particle bed will occur. In the CFDEM® coupling software-package, it can be chosen between the following drag force models: Schiller and Naumann (1935), Gidaspow (1994), Di Felice (1994) and Koch and Hill (2001). These four drag force models are investigated in the presented numerical simulation. The simulated time is 120 s. The DEM time step is $t_{\mathrm{DEM}} = 1 \times 10^{-5}\,\mathrm{s}$ and the CFD timestep is $t_{\mathrm{CFD}} = 1 \times 10^{-3}\,\mathrm{s}$ with a coupling interval of 100. The initial configuration of the bidisperse packing is depicted in Fig. 7.1, which is the same for all four numerical models.

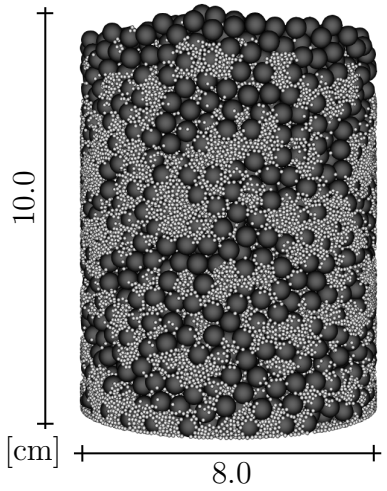


Figure 7.1: Initial configuration of the particles before seepage flow in a well-mixed assembly

The resulting migration of the fine particles through the soil column after 120 s of seepage is shown in Fig. 7.2. The use of these four drag models leads to visible differences in the migration of fine particles through the coarse particle matrix. As already observed in Kanitz and Grabe (2019b), no significant suffusion occurs using the model of Schiller & Naumann. The model of Di Felice shows a significant migration of the fine particles towards the top of the column. The fines content in this section has increased by a significant amount compared to the initial configuration, cf. Fig. 7.1. Compared to the numerical simulations with the other drag models, the model of Di Felice leads to a more pronounced accumulation of fines in the upper part of the column. Some particles are already washed

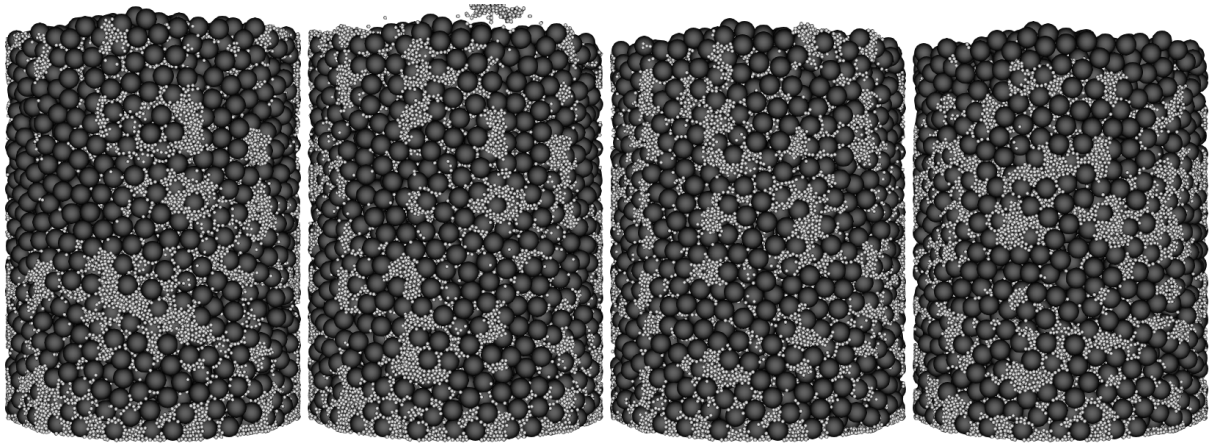


Figure 7.2: Numerical results of the particle migration after 120 s of seepage flow with the drag force models of Di Felice, Gidaspow, Koch & Hill and Schiller & Naumann

out of the column. The amount of fines in the lower part is significantly reduced. The same applies to the results with the drag model of Gidaspow. The erosion of the fines out of the column is even more substantial than using the model of Di Felice. The modelling of suffusion with the drag model of Koch & Hill leads to a more uniform distribution of the fines in the coarse particle matrix.
Fig. 7.3 shows the erosion of fines over the column after 120 s of seepage flow. The representation of the erosion rate over the particle column allows a more detailed investigation of the influence of the drag force on the erosion of the fine particles. Now it becomes clear that the model of Schiller & Naumann does not lead to significant suffusion. The erosion rate remains close to zero. For Di Felice, Gidaspow and Koch & Hill, the seepage flow causes a clear erosion of the particles. The different drag models yield significant changes in the erosion rate, especially at the bottom and the top of the column. The erosion of fines is most significant at the bottom of the column, where the drag force model of Gidaspow yields the highest erosion followed by the model of Di Felice and the model of Koch & Hill. The highest accumulation of fines occurs at the top part of the layer, where the model of Di Felice yields the highest accumulation, followed by the model of Gidaspow and then the model of Koch & Hill. However, the model of Gidaspow leads to a stronger erosion of fines out of the column compared to the model of Di Felice represented by the accumulation of fines in height above 0.1 m. Between 0.02 m and 0.08 m, an ongoing change between erosion and accumulation of fines is observable. In general, the different drag force models result in a similar pattern regarding the accumulation and erosion of fines. However, the differences in the amount of fines are significant. As already observed in Fig. 7.2, the fine particles are deposited on the column as a result of suffusion. These fines are eroded out of the column. The loss of fines from the column is:

- Drag force model of Di Felice: $\Delta n_{\text{fines}} = 236$
- Drag force model of Gidaspow: $\Delta n_{\text{fines}} = 970$
- Drag force model of Koch & Hill: $\Delta n_{\text{fines}} = 2$

Thus, the differences between the drag model of Di Felice, Gidaspow and Koch & Hill are crucial.

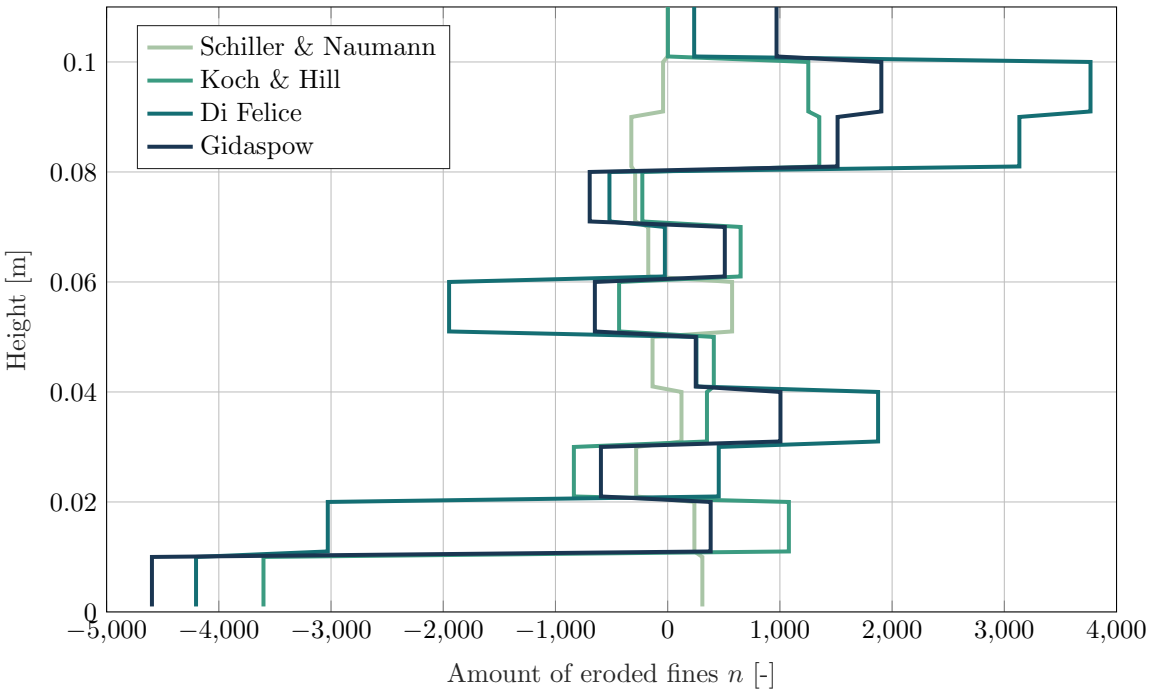


Figure 7.3: Erosion of fines over the column height after 120 s of seepage flow

Fig. 7.4 shows the composition of the fluid-particle interaction forces which are acting on the fines. The numerical model includes the pressure gradient force, viscous forces, Mei lift force (Mei, 1992) and the respective drag force. This analysis shows that the fluid-particle interaction forces consist mainly of the drag force. For all numerical simulations, the viscous forces and the Mei lift force are negligible compared to the drag force and the pressure gradient force. The pressure gradient force is around half of the drag force for all simulations. In regards to the magnitude of the drag force, the model of Di Felice yields the highest drag force, then, in descending order, the model of Koch & Hill, Gidaspow and Schiller & Naumann. The Schiller & Naumann drag thereby results in a significantly lower drag force, which explains the reduced suffusion. It is interesting to note that although the Koch & Hill model has the second-largest drag force, it has the second-lowest erosion rate (cf. Fig. 7.3). Additionally, the drag model of Di Felice resulting in the highest drag force does not yield the highest erosion. Thus, the erosion rate does not necessarily depend linearly on the drag force. In the framework of this analysis, it is not possible to judge whether the increased drag force causes more fine particles to be transported at once and thus clog the pore channels. However, this analysis demonstrates that in the modelling of suffusion, the drag force has the most considerable influence on the particles. It is therefore particularly important to simulate the drag force accurately.
In summary, the differences in the migration behaviour of the fine particles and consequently, the influence of the used drag force model on suffusion analyses are striking. Thus, the numerical modelling of suffusion requires an appropriate choice. We cannot yet say which model is best suited to model suffusion, and we do not know what causes the different results

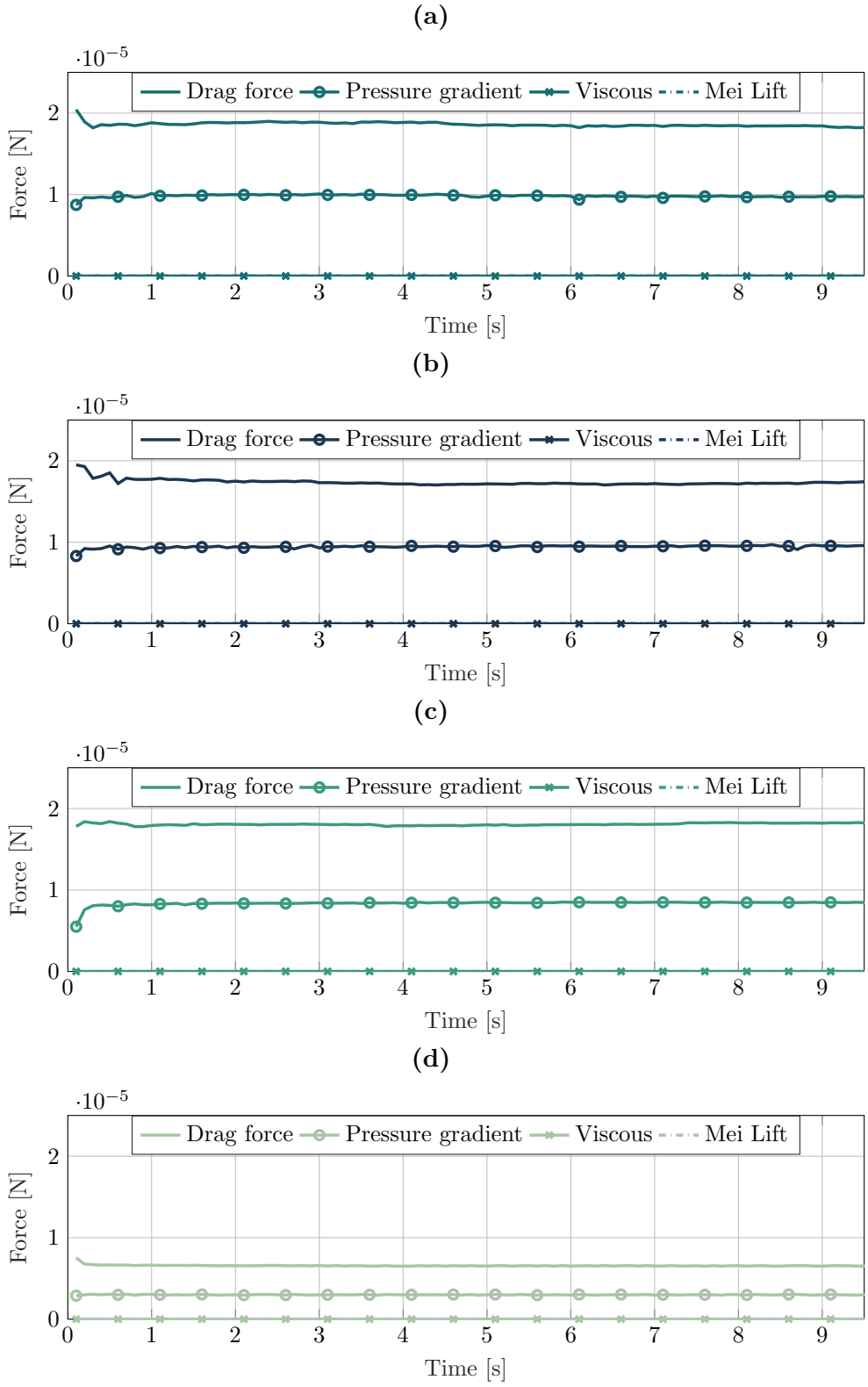


Figure 7.4: Composition of the fluid-particle interaction forces acting on the fines with (a) Di Felice drag, (b) Gidaspow drag, (c) Koch & Hill drag and (d) Schiller & Naumann drag

regarding the migration of the fines. The investigated drag force models are validated against sedimentation of a single particle, fluidised bed reactors and the pressure drop in a fixed bed. The Ergun equation (cf. Eqn. 6.6) describes the pressure drop in a fixed bed. The problem of suffusion is similar to a fixed bed, but with a small fraction of moving particles, i. e. the fines. As mentioned in Sec. 6.1, the Ergun equation is only valid until the minimum fluidisation velocity u_{mf}. Thus, when the gravitational forces are greater than the hydrodynamic forces. Fig. 7.5(a) depicts the pressure drop in the investigated particle column with increasing fluid velocity to investigate the influence of the fine fraction on the validity of the Ergun equation and therefore the calibration of the investigated drag force models. Fig. 7.5(b) presents the results with the same velocity increase but with fixed fine particles realised by a "freeze"-command (*Liggghts documentation, fix freeze command* 2020). This commands zeroes out the forces and torques acting on the particles.
The red line shows the Ergun equation predicting the pressure drop in a fixed bed. It can be identified that the motion of the small particles noticeably influences the pressure drop (cf. Fig. 7.5(a)). In contrast to the Ergun equation, the pressure drop is almost linear for the investigated drag force models. A change of inclination is visible at $u \approx 0.035\,\mathrm{m/s}$. At this point, the motion of the fines increases, which results in a reduction of the pressure drop. The Ergun equation does not predict the pressure drop in this case. In contrast, the pressure drop in the numerical model with fixed particles reproduces the Ergun equation as expected (cf. Fig. 7.5(b)). This emphasises the significant influence of the motion of the fines on the pressure drop. It should be noted that the minimum fluidisation velocity is $u_{mf} = 0.22\,\mathrm{m/s}$ caused by the coarse particles. However, as the finer particles have a smaller u_{mf} and start to move, the Ergun equation is no longer valid. Hence, this analysis shows that a calibration of the drag force models against the pressure drop in a fixed bed is not applicable to a suffusion problem.
For this reason, detailed investigations are carried out in the following concerning the numerical modelling of suffusion with different drag force models. The numerical results are compared with model tests to evaluate their plausibility.

7.4 Experimental setup

The experimental investigation of suffusion is carried out in the same test cylinder, which was used for the fluidisation tests (cf. Sec. 6.2). Glass beads with a diameter of 5 mm and 1 mm are used to investigate the process of suffusion. The spherical nature of the glass beads ensures that the shape effects of the material can be neglected. The glass beads with 5 mm diameter are coloured in black while the 1 mm glass beads are transparent. This colour difference ensures the visibility of the small glass beads during the recording with the high-speed camera. Light from the LEDs is reflected from their surface while the black particles are almost invisible for the camera. Likewise, the migration of the fine particles throughout the column can be captured accurately. In an experimental setup, a particle packing with a fines content of 25 % is produced. The moist tamping method by Ladd (1978) is used to avoid segregation of the material. Likewise, the particles are mixed at a water content of 4 % and stored in an air-tight container during the night. The arising capillary forces stick the particles together and prevent the segregation. In the next step,

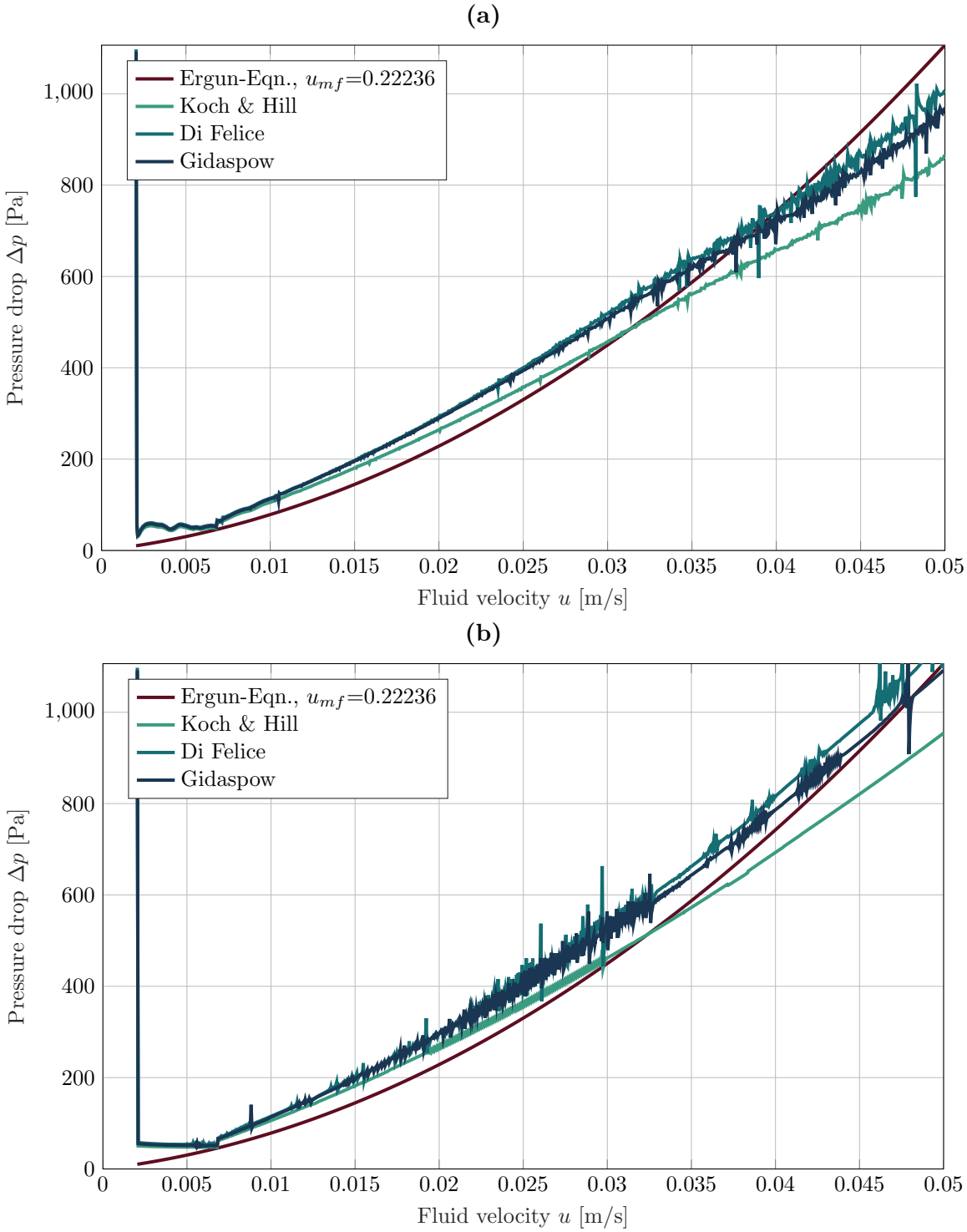


Figure 7.5: Pressure drop in the particle bed with (a) rearranging fines and (b) fixed fines

the particle mix is poured carefully in the empty test cylinder. It is essential to mention that when partially saturated material is watered, an essential amount of air bubbles is trapped in the pore volume (Bear, 2012; A. J. Peck, 1969, 567pp.). The saturation of the test cylinder for approximately 12 h can already reduce the air content, but not completely. Likewise, after the saturation of the soil column, the test cylinder is connected to a vacuum pump to de-air the system completely. This de-aeration has to be carried out carefully to prevent the soil skeleton from rearranging too much because of the rising air bubbles.
Partial segregation at the top of the test cylinder could not be prevented using this method. This segregation resulted in a top layer containing the 5 mm glass beads only. The height of this layer is dependent on the duration of the de-aeration with the vacuum pump. Fig. 7.6 depicts a packing after 3 h and a packing after 23 h of de-aeration. Fig. 7.6 shows that a shorter interval of de-aeration leads to an increased amount of entrapped air compared to a longer interval. However, the longer interval also leads to stronger segregation of the particle packing. This partial segregation leads to uncertainties in regards to the homogeneity of the particle mix. The previous fine fraction of 25 % is now much higher in the unsegregated region. In order to evaluate the existing drag force models in regards to their application on suffusion, this setup is not preferable. The final distribution of the particles is not known and can hence not be reproduced in an accurate way for the numerical simulations. Hence, even the initial state of the suffusion tests cannot accurately be captured. Additionally, the entrapped air causes a stronger particle migration during the test as the air travels faster than the water leading to an overestimation of the suffusive process. As the numerical simulation does not take into account the presence of air, the experimental and numerical results will not be comparable. In conclusion, a different experimental setup is required to improve the reproducibility of the tests and to carry out a thoroughly numerical simulation, which captures the same initial state as in the experimental tests.
Therefore, a layered setup is created. The setup consists of alternate layers of black 5 mm and transparent 1 mm glass beads. In total, three layers of fine particles and four layers of coarse particles are installed. In this way, the perforated plate lies directly on the topmost layer to prevent any uplifting of the particle column while the fluid pressure drop due to passing the coarse layer is minimised. The glass beads can now be installed in a saturated state. Entrapment of air can thus be omitted. In total, the cylinder consists of four layers with black 5 mm and three layers with 1 mm glass beads beginning with the 5 mm glass beads. The black glass beads layers have a height of 4.5 cm and the layers with the 1 mm glass beads have a height of 0.5 cm. The material is poured carefully in the water-filled cylinder with a tablespoon. The bed surface is levelled after every layer. The coarse particle layer has a void fraction of $n_{\text{coarse}} = 0.4$. The fine particle layer has a void fraction of $n_{\text{fine}} = 0.36$.
Fig. 7.7 depicts the final arrangement of the material in the test cylinder. A perforated plate is mounted on top of the particle column to prevent motion of the coarse particles. The openings have a diameter of 3 mm. Likewise, the motion of the coarse particles is restricted while the fine particles can move freely. The plate is mounted carefully to prevent confined conditions. Fig. 7.8 shows the sketch of the experimental setup. The high-speed camera tracks the particle motion at 125 fps. The inflow is constant with a velocity of 0.027 m/s over the orifice opening of 6.0 cm. The orifice consists of a perforated plate, with

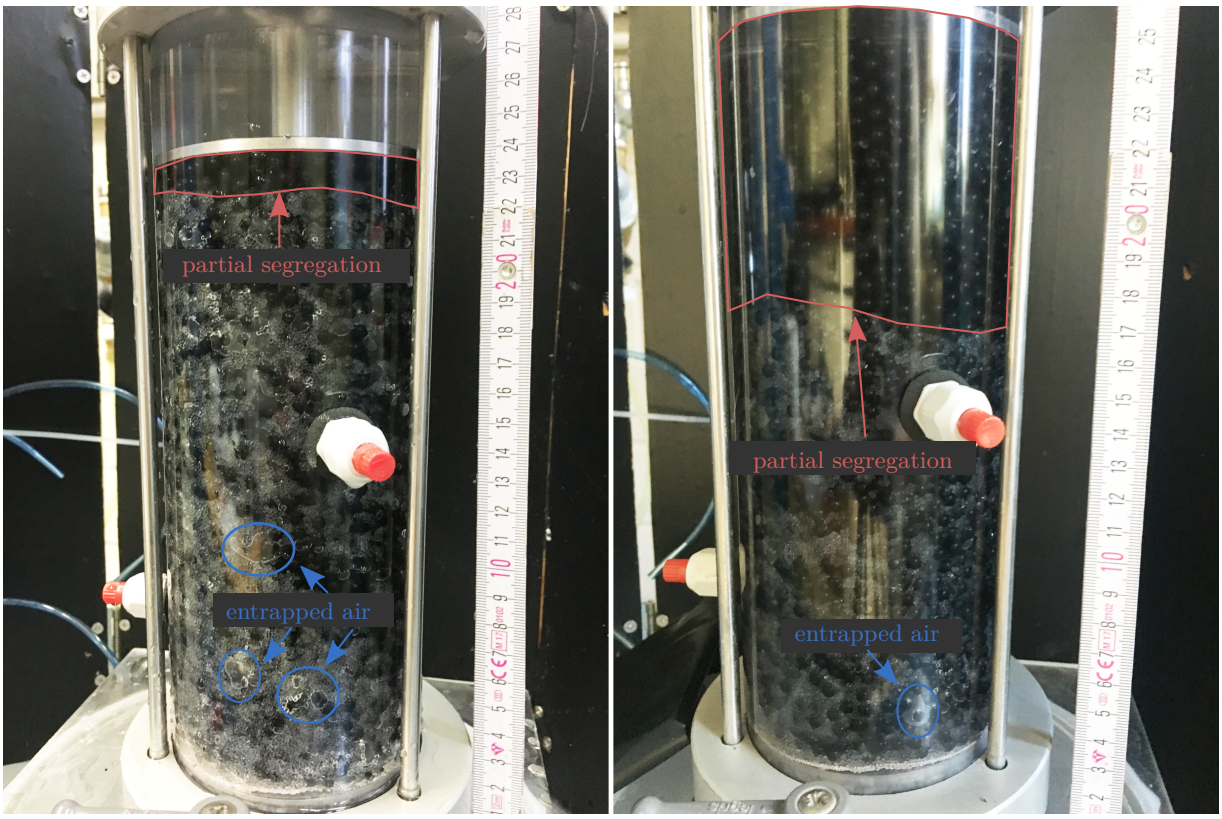


Figure 7.6: Suffusion setup with completely mixed packing using the moist tamping method by Ladd (1978) after 3 h (left) and 23 h (right) of de-aeration

an edge distance of 1 cm (cf. Fig. 7.8). A fine-mesh filter membrane is located on this orifice. Thus the flow is constant over a width of 6 cm and depositing of particles in the orifice inlet is prevented. The fluid velocity was measured both in the filled and in the empty test cylinder by measuring the outflow with a scale. Every test was carried out three times. Seepage flow through the soil column is active for 40 s. The outflow is connected to a container with a scale to verify the seepage flow velocity.

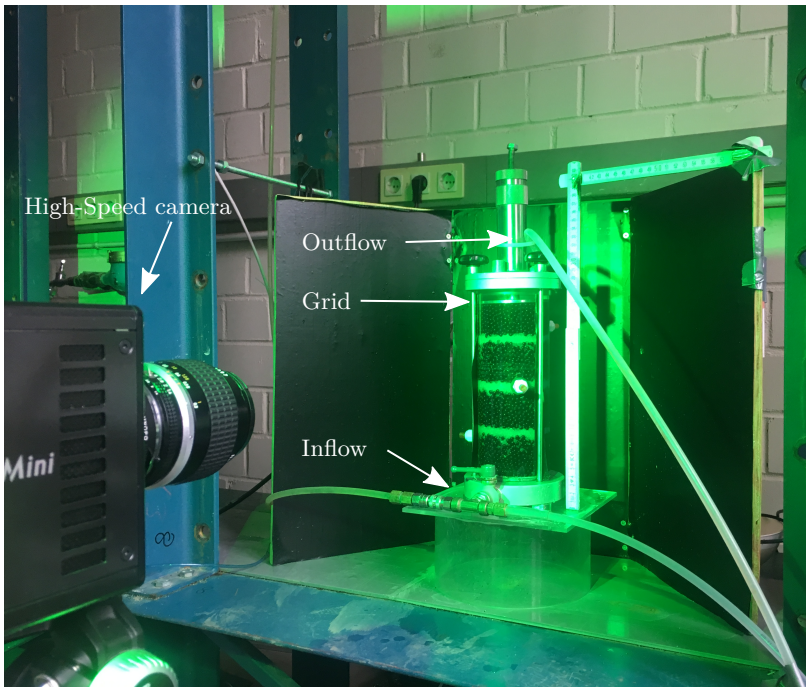


Figure 7.7: Experimental setup of investigation of suffusion in a particle bed with 5 mm and 1 mm particles with a layered setup

7.5 Numerical setup

Fig. 7.10 depicts the numerical setup to investigate the suffusion with unresolved coupled CFD-DEM.

7.5.1 Geometry and initial conditions

The dimensions of the numerical setup are identical to the dimensions of the model test. In order to save computational time, only one layer of fine particles is investigated. According to the experimental setup, 5 mm and 1 mm glass beads are chosen. A mesh with the same grid size as in the experimental setup is placed on top of the coarse layer to prevent motion of the 5 mm glass beads. The particles are initialised in a pure DEM computation. Each layer is initialised separately, whereby gravitation is not activated. After initialisation of the layer, the particles are allowed to settle under gravitation. Once the particles are at rest, the next layer is initialised. Tab. 5.3 depicts the material parameter for glass beads.

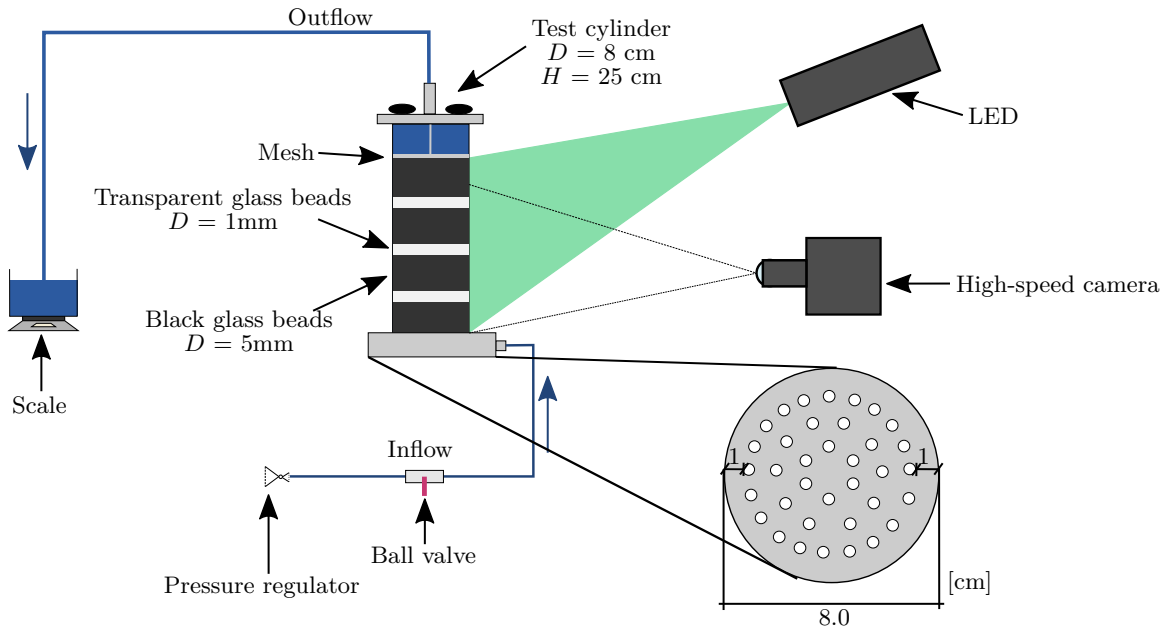


Figure 7.8: Sketch of the test setup for the investigation of suffusion

Since a smaller time step is required in the DEM calculation with stiffening particles, the numerical simulations are performed with $E = 1 \times 10^7\,\mathrm{N/m^2}$. The simulated fluid has the properties of water at a temperature of 20 °C. Its density is $\rho_f = 1000\,\mathrm{kg/m^3}$ and the kinematic viscosity is $\nu_f = 1 \times 10^{-6}\,\mathrm{m^2/s}$.

In unresolved coupled CFD-DEM simulation, the volume of the particles in the individual CFD cells must be sufficiently large that the average value does not depend on the size of the cell. Pirker et al. (2011) and Marshall and Sala (2013) suggested $3 \cdot d_p$ as the lower boundary for the mesh grid size to ensure that the value for K_{pf} has minimal variations (cf. Sec. 4.2). In the presented numerical setup, the particle size difference is large (1:5), which raises the question about the correct mesh size. Therefore, a mesh sensitivity analysis was carried out to verify which discretisation leads to accurate results without computational errors. Kanitz and Grabe (2020) showed that different degrees of discretisation lead to different erosion rates in suffusive particle assemblies, which results from the variations in K_{pf} with a poor mesh size. To verify whether the analysed discretisations lead to erroneous results, the pressure drop across the bed is investigated and plotted against the Ergun equation. Therefore, the simulation is carried out with fixed particles via a "freeze"-command (*Liggghts documentation, fix freeze command* 2020) to prevent the particles from moving. Mobile particles lead to deviations from the Ergun pressure drop. Fig. 7.9 (left) presents the pressure drop Δp across the bed with increasing fluid velocity u. It shows that both the medium and the fine mesh result in significant fluctuations. Additionally, the medium discretisation leads to a strong deviation from the Ergun equation. The coarse discretisation results in a smooth pressure drop curve representing the Ergun equation. Therefore, the presented simulations of suffusion are carried out with the coarse discretisation. The mesh size is hence 1.6 cm × 2.0 cm × 1.0 cm (cf. Fig. 7.10 (right)).

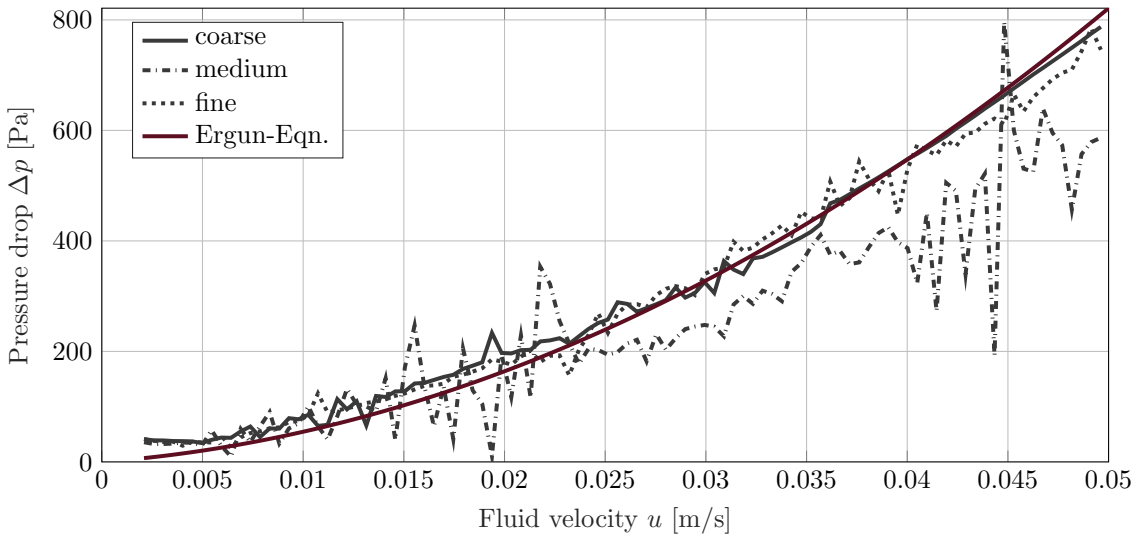


Figure 7.9: Pressure drop across the bed using a coarse (1.6 cm × 2.0 cm × 1.0 cm), a medium (0.8 cm × 1.0 cm × 1.0 cm) and a fine discretisation (0.8 cm × 1.0 cm × 0.5 cm) (Kanitz and Grabe, 2020)

7.5.2 Boundary conditions

The inlet boundary has a constant flow velocity of $u = 0.027\,\mathrm{m/s}$ over a width of 6 cm. Therefore, the groovyBC-utility available in OpenFOAM is used. The pressure boundary condition at the bottom is a zero-gradient boundary. At the top of the column, the velocity boundary condition is zero-gradient, and the pressure boundary condition constant with $p = 0$. A slip boundary condition is assigned at the walls. At the bottom of the column, an additional layer of CFD cells without particles is added. There, the void fraction is equal to 1. In this way, it is ensured that the applied velocity boundary is the superficial velocity.

7.5.3 Coupled simulation with CFD-DEM

The coupling interval between DEM and CFD is 100, e. g. after 100 DEM time-steps the particle information are passed to the CFD solver, and the NSE are solved. The simulated time is 40 s consistent with the experimental tests. The time steps for the CFD and DEM solver are $t_{\mathrm{CFD}} = 1 \times 10^{-3}\,\mathrm{s}$ and $t_{\mathrm{DEM}} = 1 \times 10^{-5}\,\mathrm{s}$.

7.5.4 Investigation of drag force correlations

The preliminary results in Sec. 7.3 showed differences in the migration behaviour of the fine particles and their consequent erosion. The comparison of the numerical with the experimental results will hence first show the results of the numerical simulation using the conventional drag force correlations by Di Felice, Gidaspow, Koch & Hill and Schiller & Naumann. In the subsequent section, an extension of the drag force model of Schiller & Naumann is presented, which allows analysing the erosion of fines with increasing drag force.

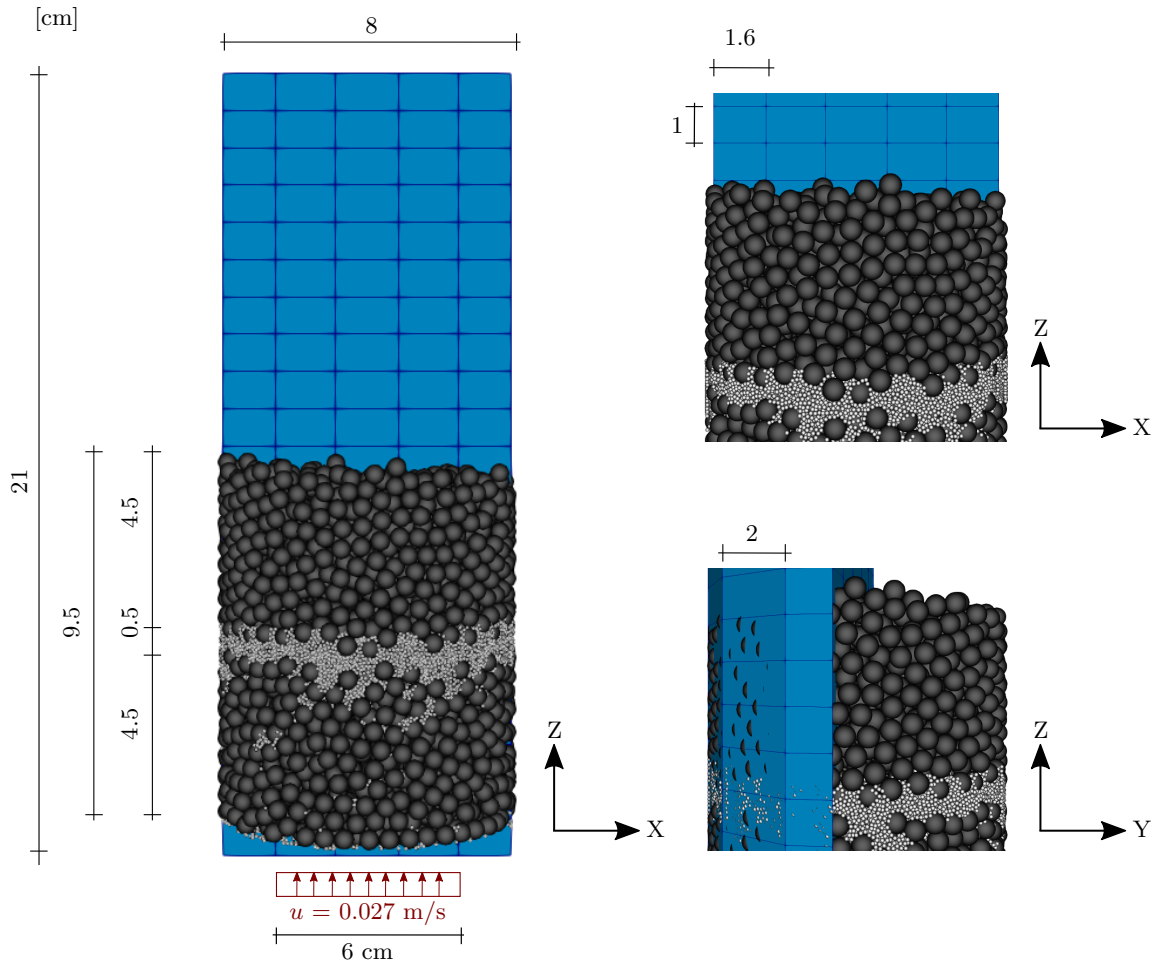
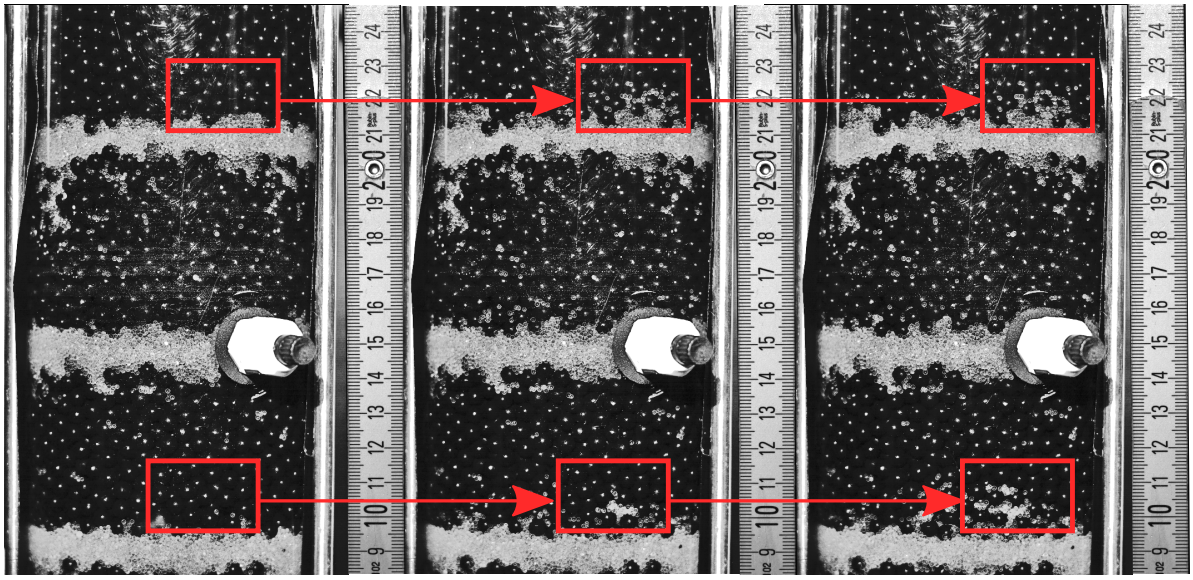


Figure 7.10: Numerical setup of the suffusion investigation (left) and the mesh-to-particle ratio (right)

7.6 Experimental results

Firstly, the suffusion process in the whole column is investigated. Fig. 7.11 shows the test cylinder at its initial stage (left), after 1 s of seepage flow (middle) and after 10 s of seepage flow (right). When the seepage flow is initialised, the particles begin to flow quickly into



t = 0 s t = 1 s t = 10 s

Figure 7.11: Particle positions at the beginning (left) after 1 s (middle) and after 10 s (right) in the experiment

the upper coarse layers. This initial movement finishes after ≈ 1 s. Thereby, the majority travels in groups of particles, and only some few single particles have migrated into the upper layer. At the boundary between fine and overlying coarse particle layer, contact suffusion occurs. In the fine particle layer, the process continues as internal suffusion, and the single particles travel further upwards. After this first and fast migration process, the upward motion of the particles slows down significantly, and the travel distance stays almost constant. Instead, the particles are moving freely in the pore space and start to rotate with the flow. Other particles are restricted in their further movement, which can be observed by the minimal change in the particle positions between 1 s and 10 s. The migration of a particle is thereby dependent on the available pore space. If the pore space is too large, the particle rotates in the flow until finding a contact, which allows it to climb further upward. If the channel is too narrow, e. g. by several fine particles in this channel, the particle motion is restricted. The suffusion process is most pronounced at the start of the seepage flow because the pore space of the coarse particle layers is large enough for a high amount of particles to flow inside side-by-side. Likewise, they have enough contact partners. After the channels are packed tightly with the fine particles, the motion stops for a while. When the seepage flow washes out particles of these channels, the near-equilibrium state vanishes and new particles start to migrate into the coarse particle layer.
By observing the general movement of the particles in all three layers, it can be observed that the motion in the bottom layer is the most pronounced. In this layer, the amount

of particles travelling into the coarser layer is higher compared to the middle and top layer. The difference of the particle position after 1 s and 10 s of seepage flow is strongest. Likewise, for a more detailed investigation Fig. 7.12 shows the particle positions in the bottom layer. After 1 s, the highest distance that the particles have travelled into the coarse layer is around 0.8 cm. Only some single particles can be observed, which have moved further into the column. For improved visibility, a red circle highlights the location of the single particles. In the interval between 1 s and 10 s, the motion of the fine particles has continued, and more particles are washed into the coarse layer over the whole width of the layer. The migration of the fine particles is thus not restricted to single spots. The majority of the particles travel in groups. The amount of single particles in the coarse layer has not increased significantly. By focussing onto the particle group in the right of the layer, it can be seen that these groups have travelled into the coarse layer via one pore channel. Due to the continuing particle motion, the particles are further pushed into the layer. They evade into the adjacent pore spaces resulting in the T-shaped form of the particle group after 10 s.
The location of the red circle indicating the position of the single particles has not changed during seepage flow. Likewise, the motion of the particles is more pronounced when they travel in groups. They then have contact partners with which they can climb up. The single particles tend to have a rotational motion in the free pore space without being washed further upwards. Clogging of the particles occurs after 10 s. The particle motion decreases significantly after 10 s. Some minor blowouts are observed within this time range, but no intense erosion occurs. The highest travel distance which can be measured after 40 s of seepage flow is 1.8 cm for the single particles and an average of 0.8 cm concerning the particle groups. The particles reach this height after already 10 s. There is thus no linear relation between the travel distance of the particles and the seepage flow time.

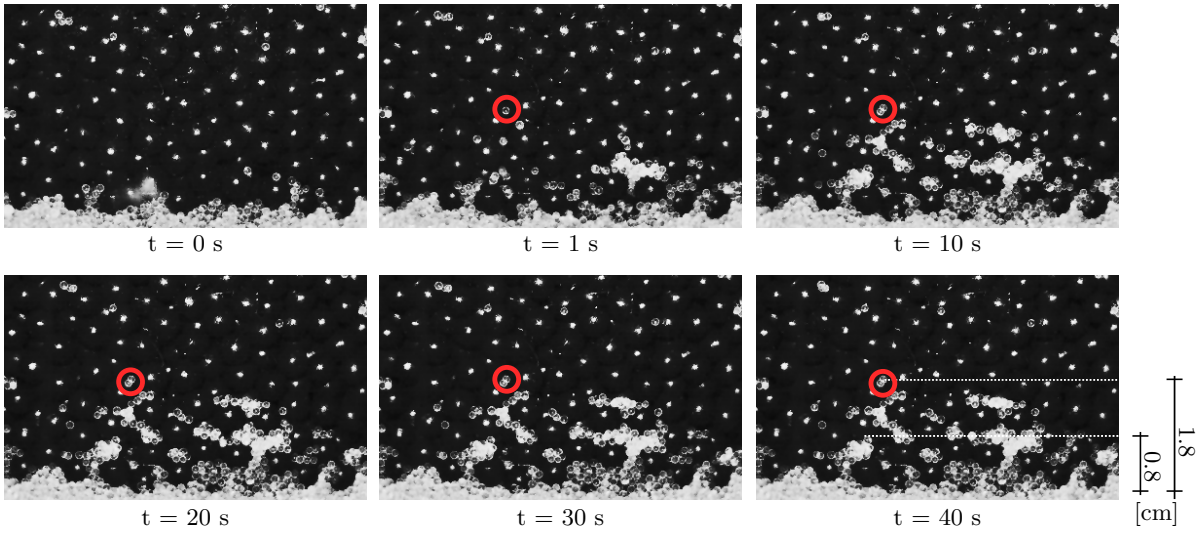


Figure 7.12: Detailed view on the particle positions during seepage flow

The particle displacement cannot sufficiently be tracked with PIV as the particle movement is too small. However, the injection of tracer particles in the inlet of the test cylinder allows the investigation of the seepage flow. The tracer particles have a mean size of 57 µm

and a density of 1.016 g/cm^3. Likewise, the particles are small enough to move through the pore network freely, and their density allows them to flow with the fluid flow. The results of the PIV analysis are depicted in Fig. 7.13. Three ROI were defined to analyse the water flow in the different layers. The regions coloured in red are excluded from the PIV analysis as they are immobile particles. For the extraction of the fluid velocity over the height, a path through the bed is defined. This path lies only inside the pore channels. Furthermore, care must be taken to ensure that the results in the selected pore channels are unambiguous. This means that a single PIV analysis is performed for each layer. The preprocessing regarding image quality and subset size can be adjusted for each layer. The path with the smallest fluctuations in the velocity is best suited for the evaluation of the flow velocity.

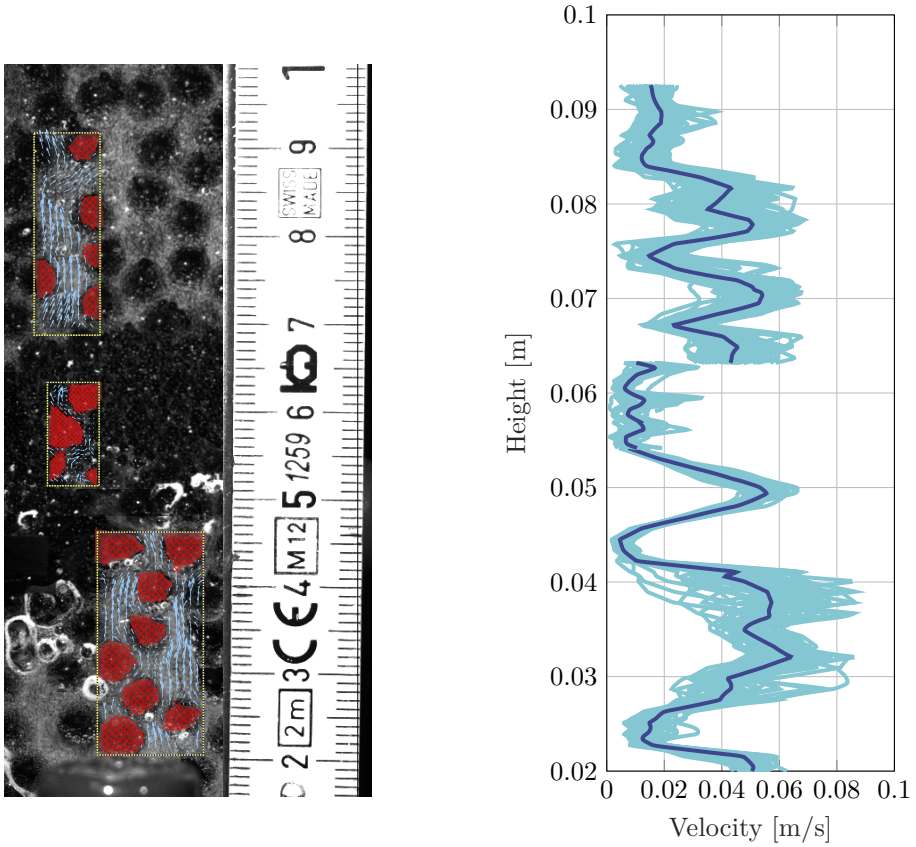


Figure 7.13: Experimental analysis of the velocity field using PIVLab (Thielicke and Stamhuis, 2014); fields of investigation with respective ROI, where the immobile coarse particles are left out of the analysis and marked in red (left) and extraction of the velocity over the height (right), the dark blue line represents the moving mean of the data

It can be seen that the fluid velocity in the bottom coarse and the top coarse layer are comparable. The mean value of the fluid velocity in these layers varies between 0.05 m/s and 0.06 m/s. Considering the inlet velocity $u_0 = 0.027\,\mathrm{m/s}$ and the void fraction of the coarse layer $n_{\mathrm{coarse}} = 0.4$, the interstitial velocity concludes to $u = u_0/n = 0.0675\,\mathrm{m/s}$.

The differences between the theoretical interstitial velocity and the computed interstitial velocity with PIV result from the fact that the void fraction n is a mean value for the whole layer. Thus, the pore space is averaged over the whole area whereby with the PIV analysis, the real pore space is considered. The sharp jumps to zero can be explained by the fact that in these points the pore channel is very narrow. In this case, there are not enough data points available for the PIV analysis, and the resolution becomes too coarse to detect single tracer particles transported through these narrow pore channels. The same applies to the PIV analysis in the fine particle layer. In this layer, the fluid velocity decreases significantly to around 0.01 m/s. This substantial decrease seems unreasonable. Therefore, the fluid velocity data of this layer cannot be used for a comparison with the numerical data.

7.7 Numerical results

Fig. 7.14 presents the particle configuration before seepage flow. This initial state is valid for all investigated drag force correlations.

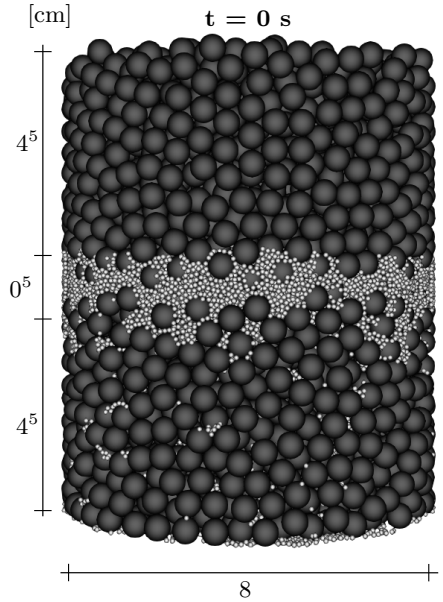


Figure 7.14: Initial particle configuration of the layered setup for the numerical investigations of suffusion

7.7.1 Suffusion process using the conventional drag force models

The influence of the usage of the drag force models of Di Felice, Gidaspow, Koch & Hill and Schiller & Naumann on the initiation of suffusion is depicted in Fig. 7.15. It shows the numerical results after 1 s, 10 s and 40 s of seepage. Only the bottom part of the column is modelled as the experiments revealed the most significant erosion processes in this layer. Likewise, for the sake of computational efficiency, only the bottom part is modelled and analysed subsequently. As expected, the drag force model of Schiller & Naumann does

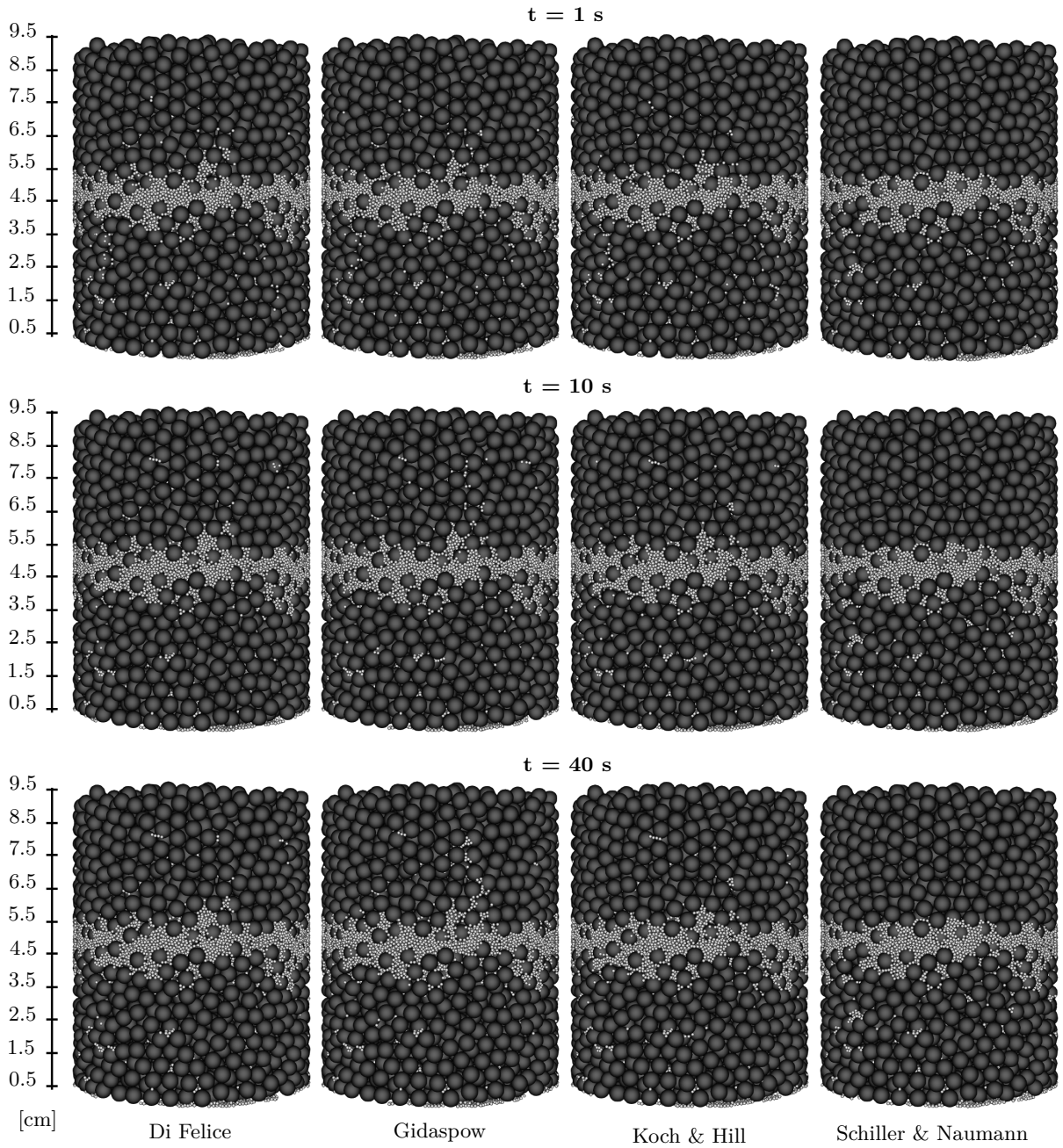


Figure 7.15: Particle positions after 1 s, 10 s and 40 s of simulated time using Di Felice drag, Gidaspow drag, Koch & Hill drag and Schiller & Naumann drag

not lead to a suffusive behaviour of the fine particles. The reason could be that the drag model formulation does not include a void fraction term and the resulting drag force is therefore low. Throughout the whole simulation, the particles stay immobile. Regarding the other investigated drag force correlations, the results are very similar. Individual particles migrate into the upper, coarser layer and at the boundary to the coarse layer, the fine particles travel in groups, which agrees with the observations from the experimental tests. Contact suffusion occurs at the boundary to the upper coarse particle matrix, which is continued as internal suffusion regarding the migration of the single particles. The general erosion of the fines into the coarse particle matrix is very similar using the drag force models of Di Felice, Gidaspow and Koch & Hill. The motion of the particle already slowed down significantly after 1 s. The differences between 1 s and 10 s and consequently after 10 s and 40 s are minor. Only the distance of the single particles increases between 1 s and 10 s. Clogging of fine particles occurs at the upper boundary between fine and coarse particle layer after 1 s. Thus, the overall motion at this boundary almost vanishes after 1 s. This behaviour is observable for the drag models of Di Felice, Gidaspow and Koch & Hill. DEM allows an accurate determination of the particle positions. Accordingly, the travel distances of the fine particles can be monitored. The maximum distance of the migrating single particles is 2.7 cm for the model of Di Felice, 2.8 cm for the model of Gidaspow and 2.7 cm for the model of Koch & Hill. The average distance of the particle groups washed into the coarse particle matrix is 0.5 cm for all drag force models except the one of Schiller & Naumann. It is, thus, not possible to evaluate which drag force model is best suited to model suffusion as the numerical results are very similar (except for the Schiller & Naumann drag force model) and a comparison to the experimental results is quite difficult. Only the particle displacement at the outer boundary of the particle column can be analysed in the experiments. However, the drag models of Di Felice, Gidaspow and Koch & Hill qualitatively depict the general behaviour of the particles in the experiment.

Fig. 7.16 depicts the total erosion of fines over time into the upper coarse particle matrix. Throughout the whole simulation, the model of Schiller & Naumann does not lead to an erosion of fine particles into the upper coarse particle matrix. Fig. 7.16 reveals differences in the erosion rate using the drag force models of Di Felice, Koch & Hill and Gidaspow. While the drag force of Di Felice leads to clogging of the particles after 10 s, the erosion continues using the drag force model of Koch & Hill and Gidaspow. This results in a higher amount of eroded fines after 40 s of seepage flow. As a consequence, at the end of the seepage flow, $\approx$ 150 particles more are eroded into the upper coarse layer using the drag force model of Koch & Hill and Gidaspow. Then again, the drag force model of Di Felice results in a stronger migration of fines in the first second of seepage flow compared to the drag force models of Koch & Hill and Gidaspow.

For a more detailed analysis of the erosion rate over the column height and the differences between the drag force models, Fig. 7.17 shows the amount of fine particles over the column height compared to the initial state. In general, the loss of fines over the height of the column shows a different tendency observed in the mixed setup (cf. Fig. 7.3). The model of Koch & Hill results in the strongest erosion, then the model of Gidaspow followed by Di Felice. In the mixed setup, the model of Di Felice resulted in the most substantial erosion and the model of Koch & Hill in the lowest. However, the difference between the models of Koch & Hill and Gidaspow is less than the one between the model of Di Felice. As

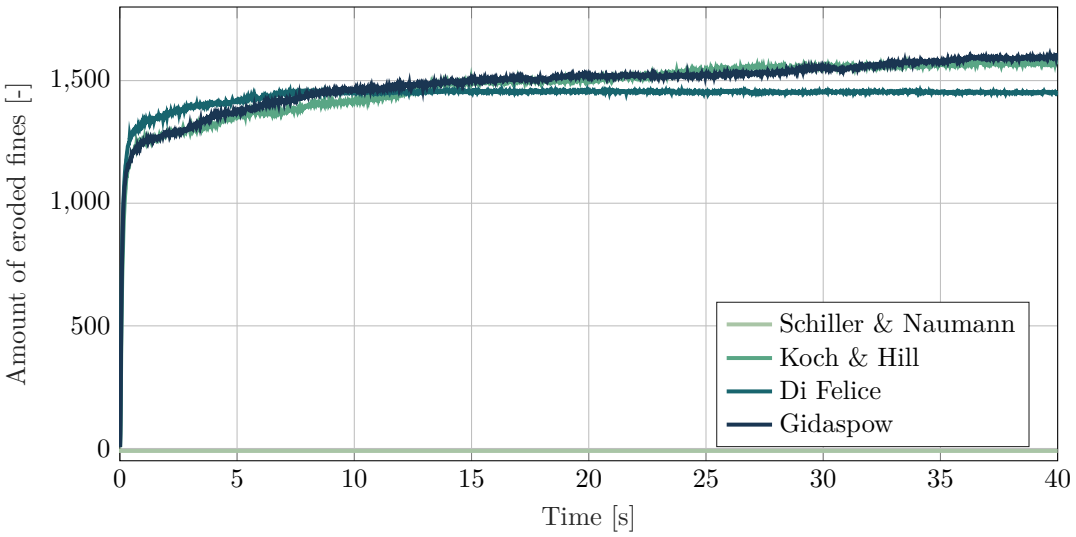


Figure 7.16: Erosion of fines into the upper coarse particle matrix over time using the drag force model of Schiller & Naumann, Koch & Hill, Di Felice and Gidaspow

expected, the highest erosion rate appears in the fines layer, highlighted in Fig. 7.17 by the light green rectangle. The fine particles are partially carried into the overlying layer, which results in a lower erosion rate there. This layer is called "migration" layer and highlighted by the light blue rectangle. In this layer, the model of Gidaspow and Di Felice lead to a similar erosion, while the model of Koch & Hill yields less erosion. It is interesting to notice that the model of Koch & Hill leads to a displacement of the fine particles from the fines layer towards the underlying layer. In comparison to the other drag force models, a higher increase is observable underneath the fines layer. This explains the lower erosion into the "migration" layer despite the higher erosion in the fines layer concerning the model of Koch & Hill. However, the model of Koch & Hill results in a stronger erosion in the layer above the "migration" layer starting from 6 cm compared to the model of Di Felice. The model of Gidaspow yields a similar amount of eroded fines in comparison to the model of Koch & Hill. Due to the strongly reduced amount of eroded fines in this layer, it can be concluded that only single particles and no groups of particles assemble in this layer. Thus, the observations at the outer surface of the particle column from Fig. 7.15 comply with the analysis of the amount of eroded fines throughout the column. The investigation of the particle positions from Fig. 7.15 revealed almost identical maximum distances of the transported single particles around 2.8 cm above the fines layer. This behaviour is also reflected by the amount of eroded fines in the layer from 7 cm to 8 cm. The erosion rate is almost the same for all models and significantly reduced. Above this layer, no erosion of fine particles occurs for all investigated drag force models which correspond to the precedent observations of Fig. 7.15. However, as already observed in Fig. 7.15, the differences in the erosion rate are not significant. Fig. 7.17 further reveals that also the amount of fines is comparable for all investigated models. In general, the investigation of the erosion rate shows fewer differences than was found with the mixed particle column.

Fig. 7.18 depicts the velocity profile over the column at 40 s of simulated time using the drag force model of Schiller & Naumann, Gidaspow, Di Felice and Koch & Hill. The impact

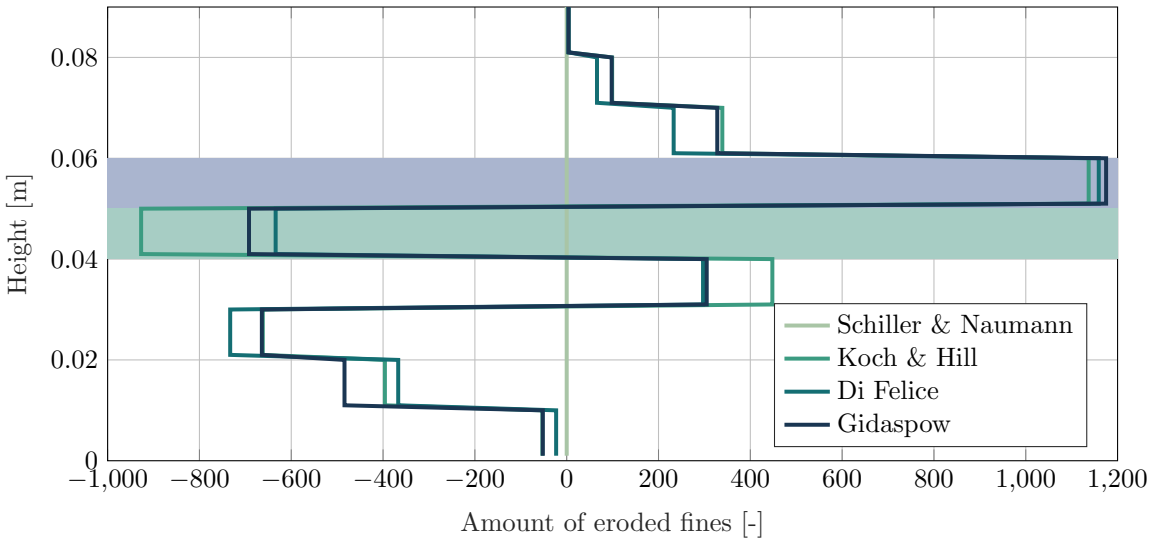


Figure 7.17: Erosion of fines over the column height after 40 s of seepage flow using the conventional drag force models; the light green rectangle highlights the fines layer, the light blue rectangle highlights the "migration" layer into where the fines are mainly washed

of the drag force models on the fluid velocity u is minor. The small differences are caused by differences in the void fraction resulting from the erosion of the fines. The comparison with the experimental result of the fluid velocity analysed with PIV (cf. Fig. 7.13) shows qualitative agreement of the fluid velocities. The numerical model results in slightly elevated fluid velocities compared to the experimental results, but the general evolution of the fluid velocity agrees. The numerical results allow a more detailed analysis of the fluid velocity in the particle column and the influence of the particle erosion on the fluid velocity. It is interesting to notice that the fluid velocity decreases significantly in the layers with the most substantial erosion processes. This velocity decrease is caused by the strong fluid-particle interaction leading to energy dissipation.

Due to the different formulation of the investigated drag force models in Fig. 7.15, it is difficult to identify the parameter that significantly controls the suffusive behaviour of the particles. These drag force models have mainly been calibrated against experimental and numerical data from fluidised bed tests and the pressure drop in densely packed bed. The physics in this test differ significantly from the micromechanical actions that take place during suffusion. In suffusion problems, the influence of the drag force onto the finer particles and especially onto individual particles is essential. In fluidised bed reactors, a large amount of particles travels together, which is not the case in suffusion. In Sec. 7.3, the analysis of the pressure drop in the suffusive particle column revealed a deviation from the Ergun equation, which is used for the calibration of drag force models.

The investigations show that the drag model of Schiller & Naumann does not lead to a suffusive behaviour of the soil. Accordingly, this model can serve as a starting point to investigate which parameter leads to suffusive behaviour and to what extent. The following section will introduce an extended drag force model of Schiller & Naumann and investigate the influence of the drag force on the suffusive behaviour of the fine particles.

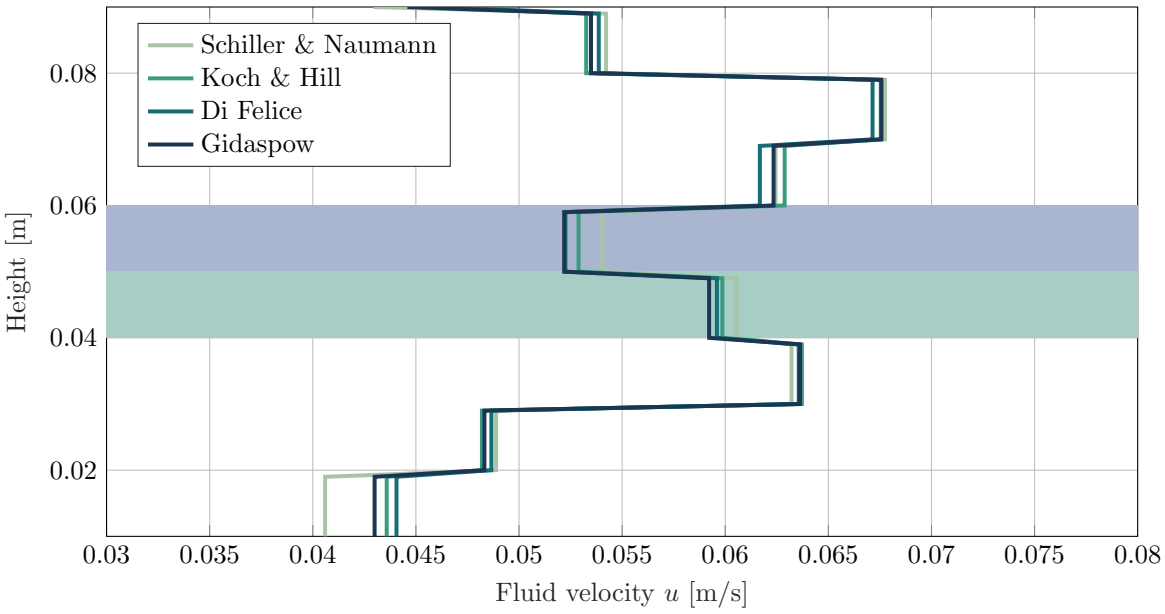


Figure 7.18: Fluid velocity over the column height at 40 s of seepage flow using the conventional drag force models; the light green rectangle highlights the fines layer, the light blue rectangle highlights the "migration" layer into where the fines are mainly washed

7.7.2 Suffusion process with an extended drag force model

In general, the problem of suffusion is classified as a near-equilibrium problem as the particle motion remains limited compared to e. g. fluidised bed reactors. Nevertheless, the flow in the narrow channels between the grains plays a crucial role regarding the particle migration. Hence, the direct application of the existing drag correlations without analysing the influence of the small void fraction changes could be uncertain. Comparing the drag correlations listed in Tab. 7.1, it is peculiar that there are two correlations for the drag coefficient C_D, whereby the most used is the one from Schiller & Naumann. The only differences are then the various extensions with either a voidage function $f(n)$ or a different correlation for the momentum exchange coefficient β. Du et al. (2006) found that β mainly influences the pressure drop in the bed while for the particle motion, the void fraction term $f(n)$ has a subtle but complex influence on the drag force. This thesis is therefore limited to investigations on the influence of the void fraction term in a drag force model.

To understand how the different drag force correlations can affect the erosion process of fines in suffusion and lead to the observed differences in Sec. 7.3, we have to look up the different drag force formulations in detail. The drag force model of Koch & Hill and Gidaspow are not considered. The model of Koch & Hill consists of a wide variety of empirically gained parameters making it difficult to carry out a comparison to the other drag force models. The model of Gidaspow represents the Ergun equation in the considered regime. There, also a variety of empirical fits can be found. Di Felice (1994) derived a formulation of χ, which solely depends on the particle Reynolds number Re_p. To investigate, how this dependence affects the suffusive behaviour of the fine particles in a soil column, Re_p and

C_D are plotted against the velocity difference $(u - v)$ in Fig. 7.19 and Fig. 7.20. Re_p is calculated with a void fraction of $n = 0.4$ and a particle diameter of 1 mm.

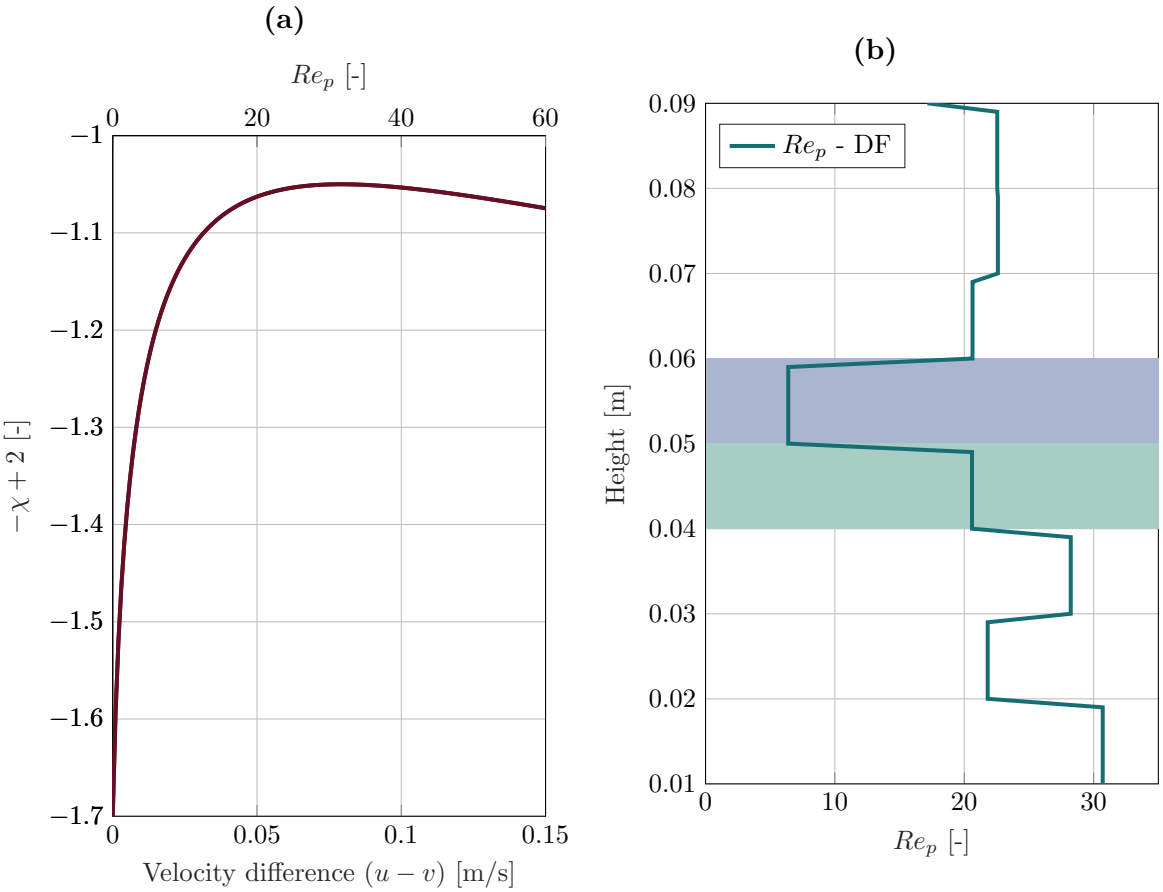


Figure 7.19: (a) Fluid velocity over height of the particle column for Koch & Hill, Di Felice, Gidaspow drag and the extended drag model of Schiller & Naumann with different values for χ - (b) Re_p over height of the particle column for drag models of Di Felice

Fig. 7.19(a) shows the logarithmic evolution of $-\chi + 2$ against Re_p and $(u - v)$. While at $(u - v) \to 0$, $-\chi + 2$ is -1.7, it reaches a saddle point at $(u - v) = 1.05$. But already at $(u - v) = 0.01$ $-\chi + 2$ tends to a value of -1.27. Hence, for low seepage flow velocities and particles transported by the fluid and travelling at a similar speed, $-\chi + 2$ is higher than with an increasing difference in the velocities. In the case of suffusion, the fines are restricted in their movement and accordingly their velocity by the confinement of the coarse particle matrix. They are unlikely to reach similar velocities as the fluid. The high values for $-\chi + 2 \to 0$ will hence not apply. Fig. 7.19(b) shows the evolution of Re_p over the height of the particle column. The fluctuations are minor and range from $Re_p = 8$ to $Re_p = 30$. Using these results, we can conclude that the exponent of the voidage function varies between -1.15 and -1.05.
The evolution of C_D over the velocity difference $(u - v)$ of fluid and particle for the formulations of Schiller & Naumann and Di Felice reveals no difference in the investigated flow regime (cf. Fig. 7.20).

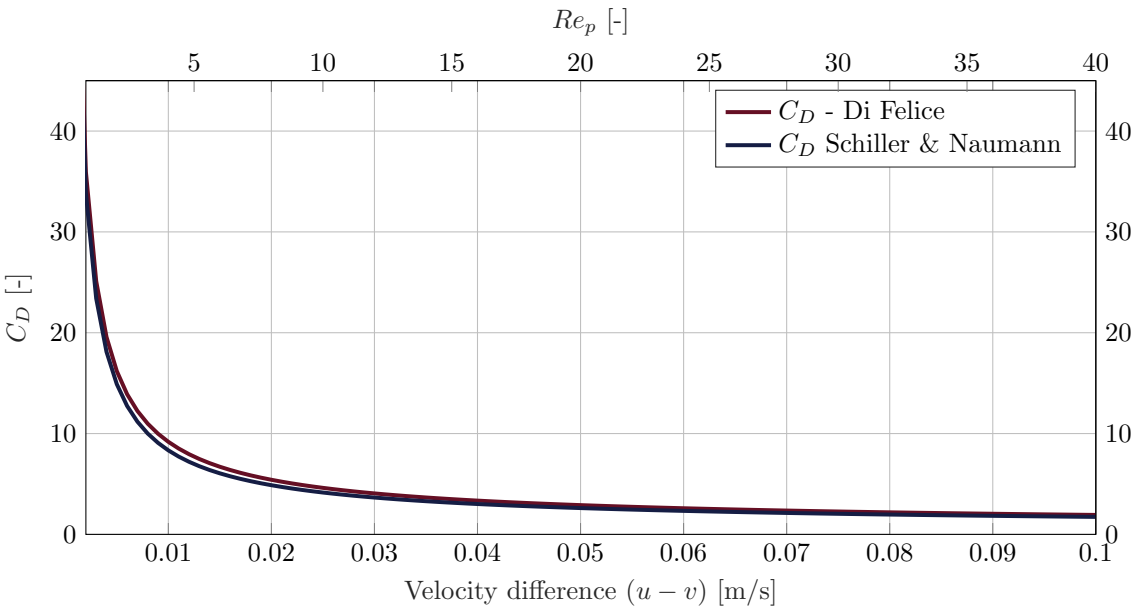


Figure 7.20: Development of C_D over $(u - v)$ for the formulation of Schiller & Naumann and Di Felice.

These findings show that in case of suffusion, which occurs with smaller fluctuations of Re_p, the influence of Re_p on the exponent of the voidage function is small. Thus, for a further investigation of how the drag force influences the erosion process of fine particles in suffusive particle assemblies, the exponent χ can be assumed constant.
The investigations of the conventional drag force models show that the drag model Schiller & Naumann does not lead to a significant suffusive behaviour of the particles. Accordingly, this model can serve as a starting point for further investigations. In order to identify the mechanisms in a suffusion problem that play a role for the drag force correlation, the formulation of Schiller & Naumann for the drag coefficient C_D is extended with a voidage function $f(n)$ in the form of:

$$f(n) = n^{-\chi} \quad \text{with} \quad \chi \in \mathbb{Q}^+ \tag{7.4}$$

The influence of the void fraction n on the drag force is consequently varied with the factor χ. n is computed every CFD-time step according the used void-fraction scheme (cf. Sec. 4.4). The extended drag force correlation for suffusion concludes to the following expression:

$$F_D = C_D \pi \rho_f d_p^2 n^{-\chi} |u - v| (u - v) / 8 \tag{7.5}$$

$$C_D = \begin{cases} \frac{24}{Re_p}\left(1 + 0.15 Re_p^{0.687}\right) & Re_p < 1000 \\ 0.44 & Re_p \geq 1000 \end{cases} \tag{7.6}$$

With increasing χ, the void fraction has an increasing influence on the drag force and the drag force increases correspondingly. It is important to mention that if $\chi < 0$ the presence of the particles reduces the particle-fluid interaction forces, which would lead to a wrong physical behaviour. Hence, χ needs to be positive.

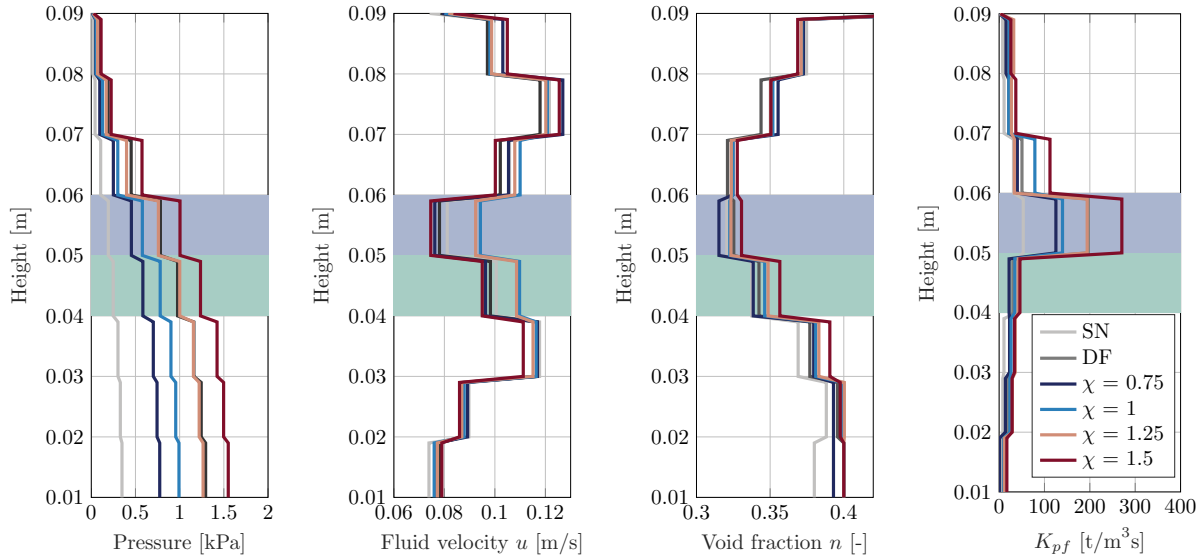


Figure 7.21: Fluid pressure, fluid velocity, void fraction and interaction force coefficient K_{pf} evolution over the soil column after 1 s for the model of Schiller & Naumann, the drag model of Di Felice and extended drag models with varying χ; the light green rectangle highlights the layer of fine particles; the light blue area highlights the "migration layer" (Kanitz and Grabe, 2020)

Kanitz and Grabe (2020) investigated the effects of the void fraction term and subsequently the parameter χ on suffusion using the same numerical setup but with a higher seepage velocity of $u = 0.035\,\mathrm{m/s}$. They found that the impact of the void fraction on the drag force and consequently on the particle migration has a significant influence on the travel distance into the coarse layer and the tendency of blowouts of fine particles after clogging. Likewise, increasing the parameter χ leads to an increased travel distance of the particles while clogging occurs earlier with increasing χ. Additionally, the effect of the drag force model variation on the fluid field was investigated, cf. Fig. 7.21. The light green rectangle highlights the layer of fine particles; the light blue area highlights the "migration layer", into where the particles are washed. While the variation of the parameter χ does not significantly affect the fluid velocity, it has a considerable impact on the fluid pressure and the fluid-particle interaction force coefficient K_{pf}. Fig. 7.21 shows that with increasing χ, both the fluid pressure in the bed as well as K_{pf} increase with increasing value for χ.

Hence, for the subsequent investigation, χ is increased in the interval of [0.5,1.8]. The numerical results of the particle displacements after 1 s of seepage flow in the upper coarse particle matrix using the extended drag model of Schiller & Naumann with the parameter χ is shown in Fig. 7.22.

In general, the fine particle migration increases with the increase of χ. While $\chi = 0.5$ and $\chi = 0.6$ result in only some single particles eroding into the upper coarse particle matrix, starting from $\chi = 0.7$, the erosion of single particles is observable. Generally, these migrate further upwards with increasing χ. The increase is significant until $\chi = 1.3$. Further increasing χ yields less noticeable differences concerning the maximum erosion distance. At the same time, the erosion of groups of particles at the boundary between the fine layer

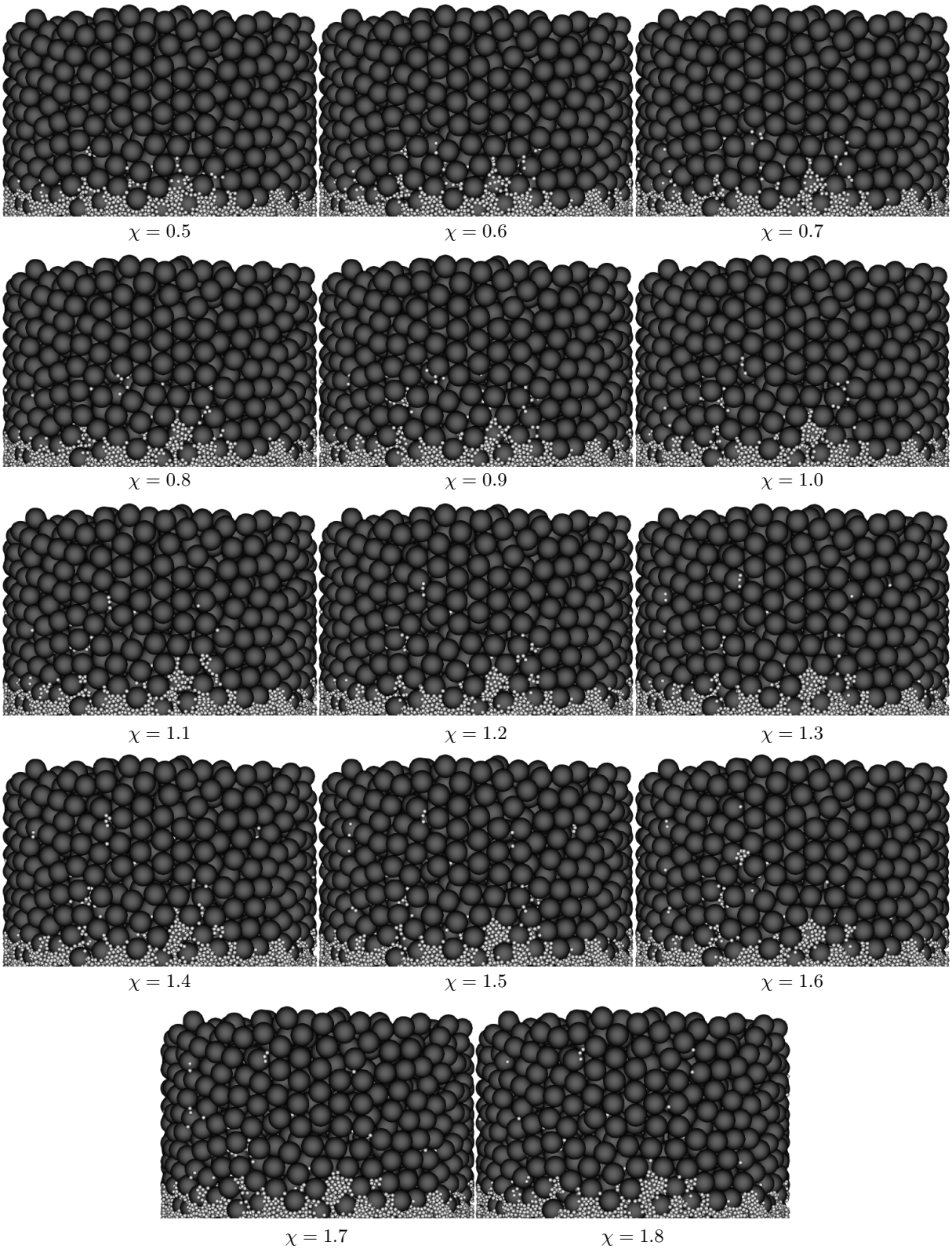


Figure 7.22: Particle positions after 1 s of simulated time using extended Schiller & Naumann drag with increasing value of χ

and the upper coarse layer increases significantly until $\chi = 1.0$. A further increase results in similar particle arrangements at this boundary and clogging occurs. These observations reveal the influence of increasing the drag force on the erosion of fines. While clogging leads to a similar particle arrangement in the vicinity of the fines layer and the differences are less significant with an increase of χ starting from $\chi = 1.0$, increasing the drag force yields a higher erosion distance of single particles.

As Fig. 7.22 reflects a momentary situation of the particles and their arrangement at the outer boundary of the particle column, an investigation on the erosion rate is presented in the following. Fig. 7.23 depicts the total erosion of fines into the upper coarse particle matrix over time. It directly occurs that the increase of χ and subsequently the drag force acting on the particles yields a faster clogging and a greater erosion. However, the highest drag force (occurring with $\chi = 1.8$) does not result in the highest erosion rate. This occurs for $\chi = 0.7$ to $\chi = 1.2$. Nevertheless, the increase at the beginning of the seepage flow steepens with increasing χ. The erosion occurs faster. A continuous increase after 0.5 s is observable for $\chi = 0.6$ to $\chi = 1.2$. Thus, $\chi > 1.2$ leads to a fast blowout of particles accompanied by early clogging. Lower values of χ and consequently of the drag force show the tendency of an ongoing erosion, which is similar to the results with the drag force of Gidaspow and Koch & Hill. Clogging of the fine particles in the upper coarse particle matrix occurs later in comparison to higher values of χ. These findings signify that higher drag forces cause a fast and intense erosion of fine particles into the coarse particle matrix. Clogging occurs early as the amount of fines in the coarse particle layer is increased within a small amount of time. The particles are restricted in their movement. Decreasing the drag force by reducing χ causes reduced erosion at the beginning of the seepage flow. As a consequence, the pore space is less limited, and the particles can move freely. Clogging occurs once the pore space is restricted due to the ongoing erosion of fines. The decrease of χ leads to clogging at a later time.

This analysis reveals that increasing the drag force only yields a higher amount of eroded fines up to a certain limit caused by early clogging. Fig. 7.24 underpins this observation. Fig. 7.24 depicts the total amount of eroded fines vs. the value of χ after 20 s of erosion. A fitting curve shows the trend of the amount of eroded fines with increasing values of χ. It reveals a peak in the interval of $\chi = [0.7, 0.9]$ followed by a decline until $\chi = 1.2$. With increasing χ, the amount of eroded fines reaches a steady value. While until $\chi = 0.7$, the increase of eroded fines is significant, the erosion reaches a limit at $\chi = 1.3$ with ≈ 1400 particles similar to the results with the drag force model of Di Felice. This observed limit corresponds to the preceding observations, where a similar trend could be observed by analysing the particle migration into the upper coarse column (cf. Fig. 7.22) and the total amount of eroded fines (cf. Fig. 7.23). This analysis reveals that increasing χ and consequently, the drag force has an increased impact on the total amount of eroded fines until a value of $\chi = 0.9$. A further increase favours clogging of the particles and the total amount of eroded fines decreases.

So far, we have only analysed the influence of increasing the drag force on the total erosion. Fig. 7.25 presents the erosion of fines after 1 s and 20 s of seepage flow in the different layers in the upper coarse particle matrix. This allows the investigation on the arrangement of the eroded fines in the upper coarse particle layer and how the increase of the drag force influences the distribution of eroded fines over the height. Furthermore, it can be analysed

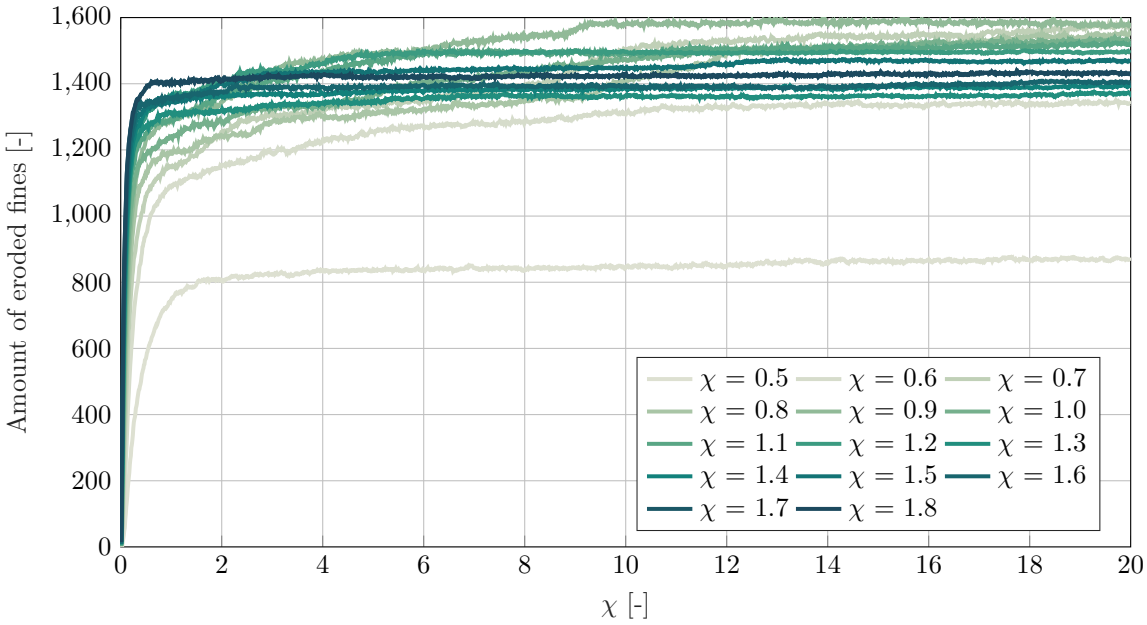


Figure 7.23: Amount of eroded fines into the upper coarse particle matrix over time with increasing value for χ

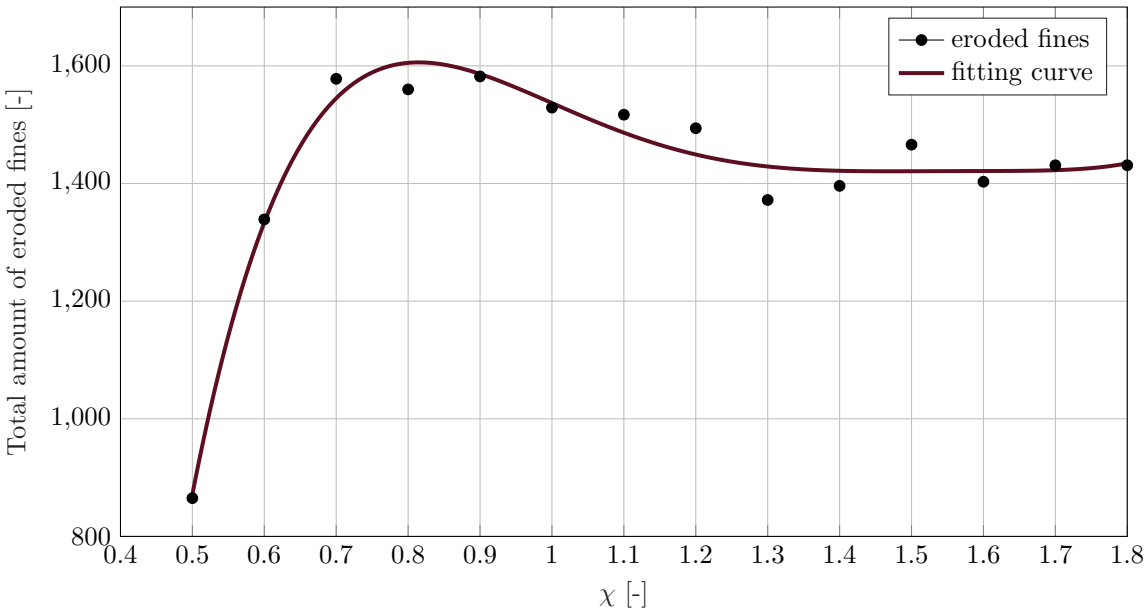


Figure 7.24: Amount of eroded fines vs. χ after 20 s of seepage flow

how the clogging mechanism affects the particle erosion and in which layer clogging occurs. For improved visualisation, the erosion into the upper coarse particle matrix is only depicted for seven values of χ.

After 1 s of seepage flow, the amount of eroded fines directly above the fines layer (from 0.055 m to 0.06 m) increases with increasing χ. This behaviour changes with increasing distance to the fines layer. In the height of 0.06 m to 0.065 m, $\chi = 0.7$ results in the highest amount of eroded fines, while the amount of fines is already reduced significantly using $\chi = 0.5$. With increasing χ, the amount of eroded fines reaches a similar value around 300 particles. In the overlying layer, $\chi = 0.7$ causes a significant reduction of fines, and only some single particles are eroded to this height. In this layer, $\chi = 0.9$ reaches the highest number of eroded fines, while only some particles accumulate in the next layer (from 0.07 m to 0.075 m) with $\chi = 0.9$. This trend continues for all investigated values of χ after 1 s of seepage flow: For every $\chi \leq 1.5$, a maximum distance can be identified in which the corresponding χ leads to the highest amount of eroded fines compared to higher values of χ. After the particles have reached this maximum distance, only some single particles gather in the next layer, and a significant decrease of eroded fines occurs. This distance increases with increasing value of χ. Only for the values of $\chi = 1.5$ and $\chi = 1.8$, the increased drag force causes a more continuous distribution of fines over the coarse particle matrix above a height of 0.06 m. After 1 s of seepage flow, the highest erosion distance of the fine particles resumes to 0.08 m to 0.085 m using $\chi = 1.5$ and $\chi = 1.8$.

After 20 s of seepage flow, this trend somehow continues, but some mechanisms of clogging can be identified. While $\chi = 0.5$, $\chi = 0.7$ and $\chi = 0.9$ result in the same behaviour of particle accumulation observed after 1 s of seepage flow only with an increased amount, the number of eroded fines with $\chi = 1.5$ and $\chi = 1.8$ is similar to the results after 1 s of seepage flow. Thus, for $\chi = 1.5$, the amount of fines until a height of 0.07 m remains almost constant. Clogging of the particles occurs, and the particles are not washed further upwards. However, in the overlying layer, in the height of 0.07 m to 0.075 m, the particles are mobile and migrate further upwards to a maximum distance of 0.08 m to 0.085 m. It is interesting to notice that in the underlying layer (0.075 m to 0.08 m) fewer fines accumulate, which could indicate a blowout of fines from this layer into the overlying layer. Concerning the drag force model with $\chi = 1.8$, the amount of fines leads to less significant changes in comparison to the results after 1 s of seepage flow. Only some particles from the layer of 0.075 m to 0.08 m have migrated further upwards resulting in a constant amount of fines over the height from 0.075 m to 0.085 m. The maximum distance of eroded fines using $\chi = 1.8$ is 0.09 m, which is the highest distance among all values for χ. In general, the early clogging of the fine particles causes a significant decrease in erosion in the case of $\chi = 1.5$ and $\chi = 1.8$. Thus, we can observe that in agreement with the results of Kanitz and Grabe (2020) the increase of the drag force leads to a higher erosion distance accompanied by a continuously decreasing amount of fines over the column height. Additionally, increasing χ reduces the erosion out of the fines layer with progressing time. The difference in the amount of eroded fines between 1 s and 20 s of seepage flow directly above the fines layer reduces significantly with increasing χ. This observation explains why the total amount of eroded fines does not noticeably increase as time progresses: Increasing χ causes early clogging of the fine particles in the pore space as already in the first second of seepage flow, the maximum capacity of particles in the free pore space is reached. Thus, the significant

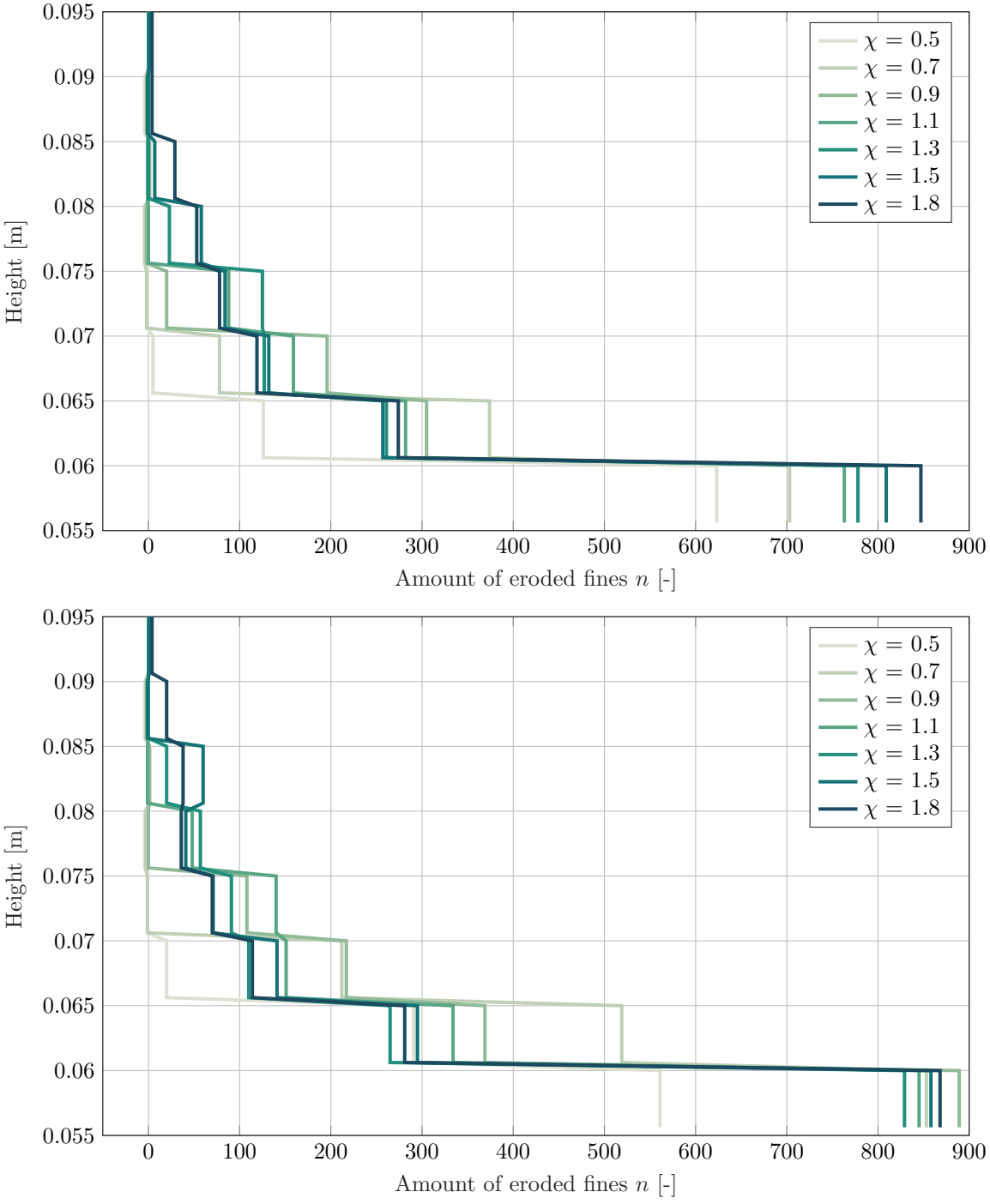


Figure 7.25: Erosion of fines into the upper coarse particle matrix after 1 s (left) and 20 s of seepage flow with increasing value for χ

decrease of the amount of eroded fines signifies single particles, which are washed out of this clogged particle groups by actions of blowouts. In summary, we can state that high values of χ result in early clogging with an increased tendency towards blowouts, which transport the fine particles further upwards into the column. Lower values of χ cause a more continuous erosion of the fines into the column.

7.8 Influence of the seepage velocity on the drag force models

The investigations of suffusion in Sec. 7.3 showed different erosion rates using the drag force model of Di Felice, Gidaspow and Koch & Hill. However, little differences are observed in the layered setup presented in Sec. 7.7. Only by investigating the erosion of fines into the upper coarse particle matrix, some differences were observable. The setups differ in the seepage velocity. The seepage velocity in the mixed setup is $u = 0.035\,\mathrm{m/s}$ and $u = 0.027\,\mathrm{m/s}$ in the layered setup. To analyse how the seepage velocity influences the drag force, Fig. 7.26 shows the evolution of the drag force over the relative velocity $(u - v)$ for the drag force model of Di Felice, Gidaspow and Koch & Hill. Different values for the void fraction n are depicted to analyse its influence on the differences in the drag force. The limiting values for the void fraction are $n = 0.32$ and $n = 0.45$. These represent the lower and upper boundaries for the investigated case of suffusion, cf. Fig. 7.21.
In general, the differences between the respective models in all examined void fraction n increase with increasing seepage velocity. It is noticeable that at $n = 0.32$ the models of Di Felice and Koch & Hill still yield almost identical results and then move further and further apart as the fluid velocity increases. For all void fractions examined, the model of Koch & Hill yields the highest drag force except in a dense particle assembly with increasing fluid velocity, where the model of Di Felice causes the highest drag force. It is noteworthy that the differences between the respective drag forces become more pronounced with decreasing void fraction. The model of Di Felice changes the most by modifying the void fraction. Meanwhile, the Gidaspow model hardly reacts to a change in packing density. Nevertheless, the reaction of the drag force model to the change in packing density can be crucial when modelling suffusion. Concerning the model of Gidaspow and considering the investigations on the increase of the drag force in Sec. 7.7.2, this lower drag force explain the ongoing erosion in the layered particle column. As the drag force is lower in comparison to the model of Di Felice, the erosion of particles is more continuous, and the tendency towards clogging is low. However, in regards to the model of Koch & Hill, a different mechanism causes the ongoing erosion as the magnitude of the drag force is similar to the model of Di Felice, which results in early clogging of the particles.
In summary, it can be said that at higher seepage flow velocities, the drag models lead to significantly different results. This is especially the case in dense packings. The void fraction has a minimal effect on the Gidaspow model. However, the change in void fraction can be substantial in the analysis of suffusion. In general, at moderate flow velocities, i. e. $(u - v) < 0.015\,\mathrm{m/s}$, no significant effect of the drag models of Di Felice, Gidaspow and Koch & Hill on the results is expected. However, with increasing flow velocities, especially in dense packings, the choice of the drag model should be carefully considered.

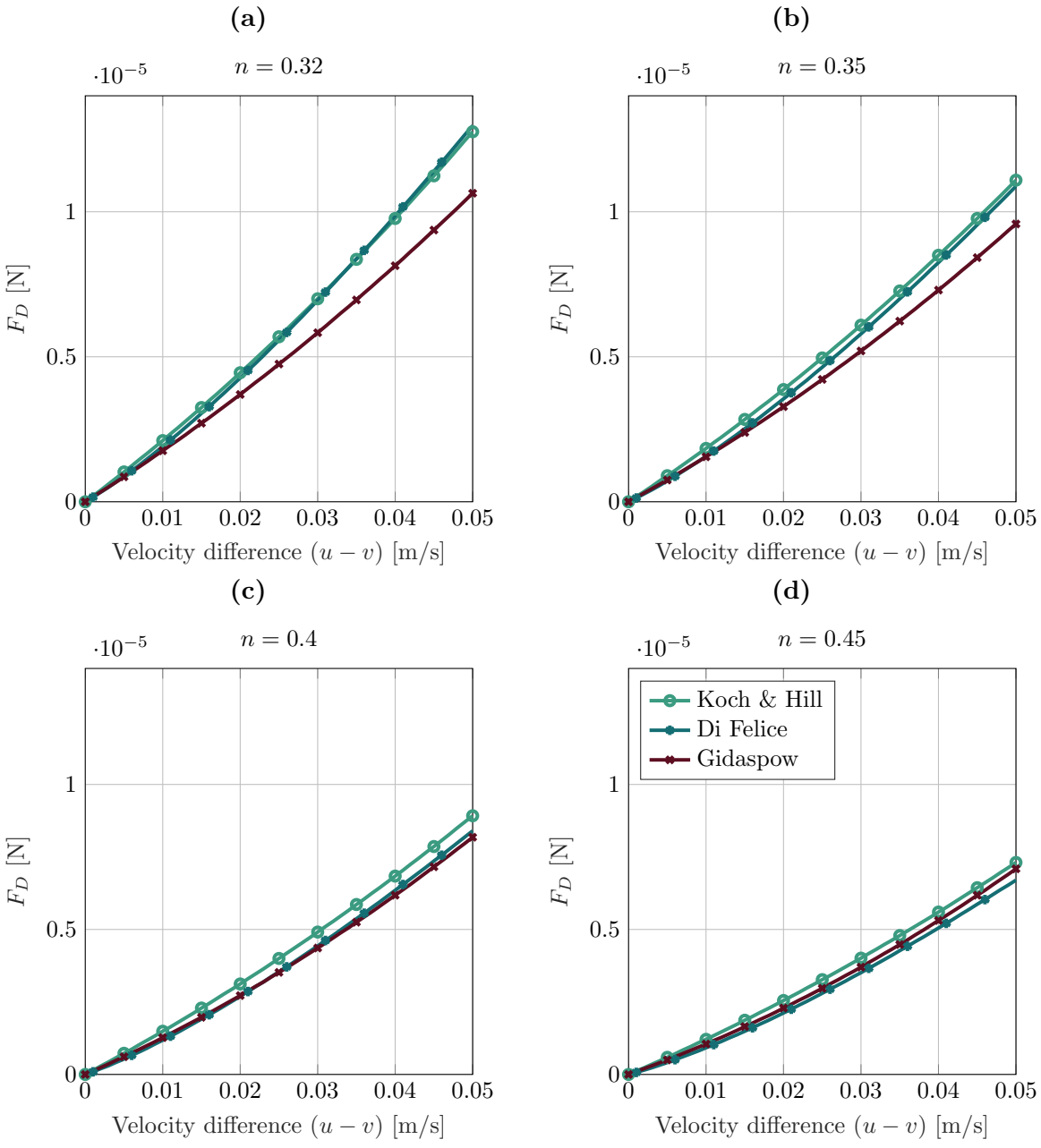


Figure 7.26: Drag force over $(u - v)$ for the drag force model of Koch & Hill, Di Felice, and Gidaspow for (a) $n = 0.3$ (b) $n = 0.35$, (c) $n = 0.4$ and (d) $n = 0.45$

7.9 Critical assessment of the investigations

The output from the experiments is limited, as only the migration of the particles at the boundary of the cylinder can be observed. The erosion happening in the inside of the specimen is invisible. The comparison of the experimental results in Fig. 7.12 with the drag force models in Fig. 7.15 reveals that all drag force models except for the model of Schiller & Naumann qualitatively agree. However, from the preliminary investigations of the well-mixed particle column in Sec. 7.3, it becomes clear that the use of different drag models leads to a different response of the particles and subsequently a different amount of washed-out fines, especially with increasing fluid velocity. Therefore, a different experimental setup is beneficial to obtain quantitative data.
The investigation of a well-mixed particle column can help to assess these problems by directly measuring the eroded fines. However, it has been found that the moist tamping method by Ladd (1978) to avoid segregation of the particles cannot be applied. Hence, using the presented particle configuration, a layered setup is still recommended. However, to visualise the erosion processes inside the column, suffusion tests in a CT scanner are favourable. This allows an insight into the particle column to compare the distribution of particles before, during and after erosion. Furthermore, the use of a particle sensor directly measuring the pressure field and the acting force is recommended as it leads to more data, which can be assessed for validation of the drag force models.

7.10 Summary

The influence of different drag force formulations on the erosion of fine particles ($D = 1\,\mathrm{mm}$) into a coarse particle matrix ($D = 5\,\mathrm{mm}$) induced by seepage flow was investigated with unresolved coupled CFD-DEM. The results with different drag force models were compared against experimental tests to assess the suitability of the investigated drag force models for the modelling of suffusion. A layered setup was chosen as it increases the reproducibility and comparability of the test due to a similar particle distribution in the column. Segregation of the particles is avoided, and air entrapment minimised as the particles can be installed in a saturated state. The displacement of the particles was recorded with a high-speed camera in the experimental tests. Tracer particles were used to visualise the seepage flow. The fluid velocity was determined using PIV analyses. The results were compared to numerical simulations with the conventional drag force models by Di Felice, Gidaspow, Koch & Hill and Schiller & Naumann. The model of Schiller & Naumann was further extended with a voidage function to investigate the effect of the void fraction changes and consequently the drag force onto the erosion of fine particles. The following findings can be summarised from the investigation of suffusion in a bidisperse particle column:

1. The usage of different drag force correlations for the numerical simulation of suffusion in a well-mixed particle assembly leads to different results. Validation of the numerical model is hence crucial. It cannot be carried out using standard validation tests alone, such as the sedimentation of a particle, as the responsible physical actions vary. These standard validation tests are often performed without further comparison to

the actual problem (cf. Hu et al. (2019)). The results of this contribution indicate that this might be problematic.

2. In the case of suffusion, the Reynolds number Re_p does not vary significantly. This leads to a constant exponent in the voidage function $f(n)$ in the drag model of Di Felice (cf. Fig. 7.19). This is especially true for mixed particle packings, as the constant distribution of the particles results in a uniform void fraction. As a result, the flow velocity changes less and thus also Re_p. Consequently, to investigate the effect of the increase of the drag force on suffusion, the model of Schiller & Naumann could be extended with a voidage function in the form of $n^{-\chi}$ with a constant value for χ.

3. The voidage function in the form of $f(n) = n^{-\chi}$ is responsible for modelling suffusion. The results of the numerical model with the drag model of Schiller & Naumann indicated no erosion of fine particles into the coarse particle matrix. Only by the extension of the drag force model of Schiller & Naumann with a voidage function $n^{-\chi}$ with constant χ led to suffusive behaviour of the fine particles.

4. A higher drag force does not directly yield a higher erosion rate. The investigation with the extended model with increasing value for χ revealed an increase of the erosion until $\chi = 0.9$. Further increasing χ leads to a reduction of the erosion until a limit is reached at $\chi = 1.2$. By analysing the erosion of fines over the upper coarse particle matrix, it could be concluded that lower values for χ result in an ongoing erosion of fines, while higher values of χ lead to early clogging of the particles with an increased tendency towards blow-outs of fines. At the same time, the maximum distance of eroded fines increases with increasing χ.

5. Increasing the seepage velocity results in increased differences regarding the drag force magnitude using different drag force models. This signifies that at low seepage velocities, the choice of the drag force model can be neglected, but it is more important when investigating higher seepage velocities.

The presented investigations on χ reveal its significant influence on the suffusion processes in a particle column. In future work, it is recommended to verify the drag force model of Di Felice carefully against suffusion problems. It is necessary to verify if calibrations of the exponent χ are required. This contribution reveals that χ can be adapted to reflect experimental results. By comparing the particle migration or measuring the flow field, the parameter χ can be calibrated so that the particle behaviour in the numerical model depicts the reality.

8 Suction dredging

For the foundation of heavy offshore structures, e. g. offshore gravity foundations, the marine seabed has to be excavated as its bearing capacity is too low. Hence, a pit is created, resulting in subaqueous slopes. There are different techniques to remove the marine soil, mainly hydraulic and mechanic dredging. The so-called suction dredging belongs to the hydraulic dredging techniques. Thereby, a pipe is lowered in the soil, applying suction to remove it. The implied suction loosens the soil, which then flows through the pipe as a soil-water-suspension (Been et al., 2012). The influence of suction dredging onto the failure mechanism of sandy submarine slopes is investigated in the following section. The dredging industry experienced that different failure types can occur depending on the soil properties. In order to be able to create steep and stable slopes, one must know what exactly happens with the seabed during dredging works. The following section first gives a brief overview of the known failure mechanisms of sandy submarine slopes. It then introduces the small-scale model tests of suction dredging, which serve for validation of the derived numerical model. Parts of the presented work are published in Kanitz and Grabe (2019a).

8.1 Failure mechanisms of subaqueous slopes

The failure mechanism of a subaqueous slope mainly depends on its material properties and its packing density. A slope fails when the average shear stress along a potential sliding line in the slope body exceeds its shear resistance (Terzaghi, 1956). The shear resistance is described by:

$$s = (\gamma' z - u_w) \tan \varphi \tag{8.1}$$

In this formulation, γ' is the submerged unit weight of the sediment, z is the depth below the surface, u_w is the pore water pressure, and φ represents the internal friction angle. According to this equation, a submarine slope under gravity forces is only always stable when its inclination is equal or smaller than φ. Though, when other loads, like hydrodynamic loads, are acting on the slope body, the submarine slope can fail even when its inclination angle is smaller than the internal friction angle. In general, there exist two different failure mechanisms in a subaqueous slope - liquefaction slope failure and breach failure. A mass of sand that suddenly starts to behave like a viscous fluid characterises the liquefaction slope failure. It occurs mainly in a saturated coarse-grained and loosely packed sand. The collapse happens suddenly due to an external triggering event. The main effect that is underlying the liquefaction slope failure is the strong tendency of loose sand to a contractant behaviour. In Fig. 8.1 on the left side, the liquefaction slope failure mechanism is outlined. Due to a shear load, resulting from an external triggering event, like e. g. the removal of the slope toe due to dredging or hydrodynamic loads, the loose soil skeleton suddenly densifies. The pore water prohibits the decrease of pore space resulting in excess

pore water pressure. This excess pore water pressure can exceed the grain-to-grain stresses of the soil skeleton, and hence the soil is behaving like a fluid as the shear resistance vanishes. The saturated slope starts to move downwards while the overpressured water tends to flow away from the liquefied mass in an upward direction leading to a rotational movement of the collapsing sand masses (van den Berg et al., 2002). This process stops when the excess pore water pressure dissipates due to the outflow of the pore water of the pores. Consequently, the effective stresses increase and the slope reaches an equilibrium state. The second failure mechanism of a sandy subaqueous slope is the so-called breach failure, cf. Fig. 8.1 on the right side. It is characterised by a regressive failure of the slope with very steep slope inclinations (Torrey, 1995), which can be stable for some time, depending on the geometry of the slope. This failure mechanism occurs in densely packed slopes and is a result of the shear-dilatancy effect (Breusers, 1974; Meijer and van Os, 1976). Dilatancy is the opposite of contractancy. Whereby in loose sand, the pore volume suddenly compacts when it experiences a shear load, the dense sand suddenly loosens. This loosening results in an increase in the pore volume. Negative excess pore water pressure with respect to the hydrostatic pressure builds up, increasing the grain-to-grain stresses. Hence, the resistance of the soil significantly increases as well.
Further information on the failure behaviour of subaqueous slopes can be found in Meijer and van Os (1976), van Rhee (1998), Mastbergen and van den Berg (2003) and van den Berg et al. (2002).

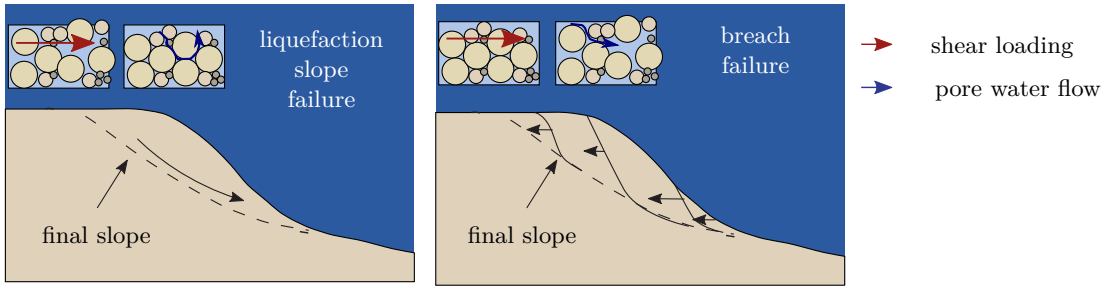


Figure 8.1: Subaqueous slope failure mechanisms - liquefaction slope failure (left) and breach failure (right) (Kanitz and Grabe, 2019a)

8.2 Experimental setup

Small-scale model tests are performed to investigate the behaviour of suction dredged subaqueous slopes. For this purpose, an acrylic glass model tank with the dimensions of 90 cm × 40 cm × 30 cm (L × H × W) is built. In Fig. 8.3 the experimental setup is illustrated. As can be identified, a vertical wall serves as a support for the submerged slope, which is located at 20 cm from the outer boundary. It separates the water inflow area from the area containing the submerged slope. In this area, hoses are fixed to an inner acrylic glass barrier to reduce the turbulent area due to the constant inflow by the hoses, cf. Fig. 8.2. An overflow is installed at the right side of the model container to ensure a constant water height. A dull black layer is glued to the back wall to minimise any reflection that would disturb the recording with a camera. The model container is

placed on a hydraulic hoist so that the tank can be lifted at various heights. In this way, a hydraulic gradient is used to apply suction as the tank is at a greater height than the outflow of the model suction dredger. The higher the hydraulic gradient, the stronger the applied suction. The model suction dredger (cf. Fig. 8.3 b) is composed of two flexible tubes connected via a ball cock and a triangular-shaped suction dredger nozzle. The nozzle has a width of 30 cm to cover the whole model tank width and to prevent three-dimensional effects from arising. Suction is activated and deactivated by opening and closing the ball cock. The outflow of the model suction dredger is placed at the bottom ground in a trough with a sieve. This enables the measurement of the removed material during the test. The

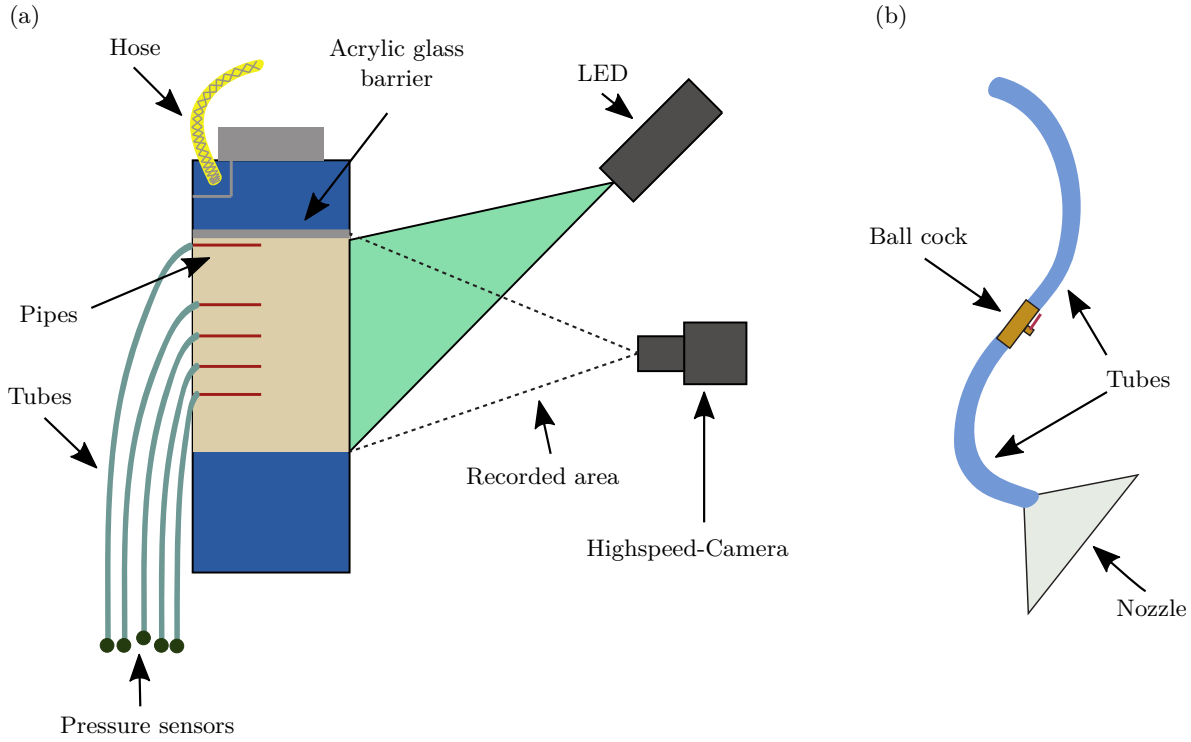


Figure 8.2: Sketch of the experimental setup for the investigation of suction dredging - (a) acrylic test container (b) suction dredger (Kanitz and Grabe, 2019a)

experiment starts by lifting the model tank at 1.80 m. Preliminary tests showed a sufficient suction applied to the submerged slope at this height. The body end of the suction dredger is placed in the trough on the ground. The trough has an overflow at the height of 0.1 m above the ground. The removed water from the acrylic glass container is gathered in the trough. Due to the outflow, the water level stays constant, which ensures a constant pressure applied by the suction dredger as both the water level in the model test container and in the trough remain constant. The model suction dredger is placed in the model tank with the ball cock closed. The model suction dredger is manually filled with water and then quickly placed in the water to ensure a steady suction. The dredger tube system is de-aired by opening the ball cock. After the de-aeration of the dredging system, the nozzle is placed on top of the slope. The ball cock is reopened, and the suction dredging process starts. The removed material is gathered in the sieve. After 18 s, the ball cock is closed, and the experiment finishes.

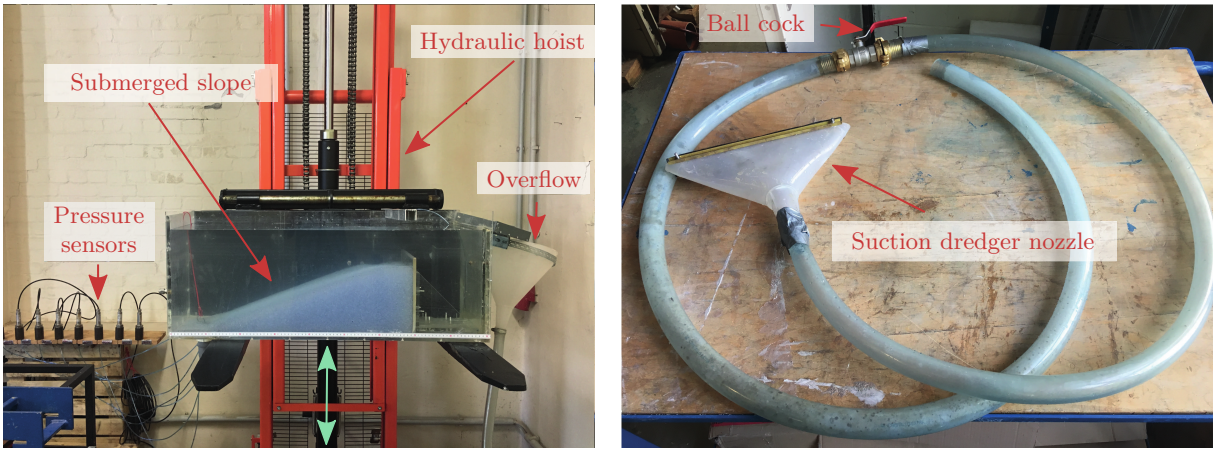


Figure 8.3: Experimental setup (left) and model suction dredger (right)

During the suction dredging process, the pore water pressure changes are measured within the slope body. For that purpose, eight piezoresistive transducers are used. Elastic tubes connect the transducers with small pipes, which reach into the middle of the soil bed. These pipes have a diameter of 1 mm and a length of 140 mm. The dimensions guarantee that the pore water pressure is measured in the middle of the bed, where no boundary influences occur and without further disturbances by the pipes themselves. The transducers are fixed on a mount outside the model tank, cf. Fig. 8.3 left. Fig. 8.4 shows the location of the pore water pressure transducers. A high-speed camera tracks the sand particle movement with a framerate of 250 fps. One high power LED illumination source (ILA 5150 LPS System) with continuous green light up to 25 W ensures a sufficiently bright illumination.

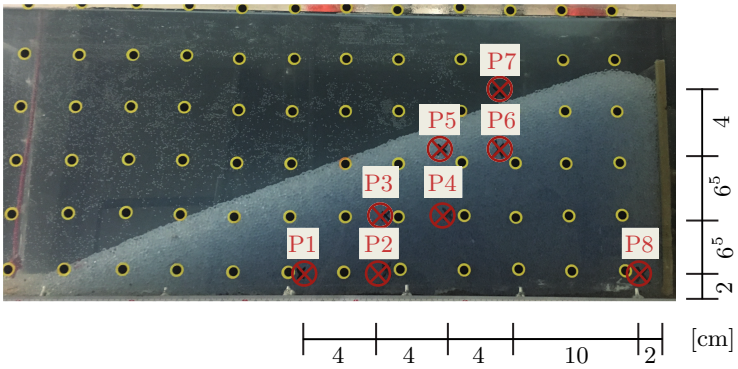


Figure 8.4: Location of the pore water pressure transducer in the slope body during suction dredging

The tests are conducted with different materials, namely glass beads of 3 mm and 1 mm diameter and Hamburger Sand. The material parameters, such as permeability and critical slope angle, were investigated prior to the suction dredging tests. The parameters can be found in Tab. 8.1. The test record of the permeability tests can be found in the appendix B.4. As the glass beads are monodisperse and perfectly spherical, a variation in the packing density can be neglected. The Hamburger Sand is investigated with two different packing densities, a looser and a denser packing density. For a looser packing, the

sand is poured in layers of 2.5 kg into the water-filled model tank. The material is released from a constant drop height to ensure a constant packing density. For this purpose, a shelf is placed on top of the model tank. The material is then poured at a constant velocity and from a constant height into the tank. Thereby, the reached slope angle is equivalent to the angle of repose φ_0 of the different materials, which are listed in Tab. 8.1. For a denser packing, the sand is poured into the model tank as with looser sand, but each layer is compacted by vibration. The looser sand has a void fraction of $n = 0.39$ and can be classified as medium dense ($D = 0.54$). The denser sand has a void fraction of $n = 0.35$, which corresponds to very dense packing ($D = 0.923$).

Table 8.1: Material parameters for 1g model tests of suction dredging

Material	K_f [m/s]	φ_c [°]	φ_0 [°]
Glass beads ($D = 3\,\mathrm{mm}$)	4.95×10^{-2}	27.0 °	21.0 °
Glass beads ($D = 1\,\mathrm{mm}$)	3.54×10^{-3}	33.0 °	24.0 °
Medium densely packed sand	9.24×10^{-4}	33.9 °	31.0 °
Very densely packed sand	6.4×10^{-4}	36.4 °	30.0 °

The investigation of the influence of suction dredging onto a slope built of glass beads is of high importance for the validation of the numerical model. Due to the coarse and spherical nature of the particles, neither liquefaction nor breach failure is expected to occur. However, to be able to judge if the complex hydrodynamic actions, which are happening during suction dredging works, can be captured by the method, it has to be ensured that the overall mechanism can be computed. In that way, it is more effective to clarify which behaviour unresolved coupled CFD-DEM method can capture and which not.

8.3 Numerical setup

The numerical setup to model suction dredging of a subaqueous slope is presented in Fig. 8.5.

8.3.1 Geometry and initial conditions

The dimensions of the numerical model and the subaqueous slope are identical to the dimensions in the model tests. In Fig. 8.5, the geometry of the slope represents the geometry of the sandy slopes. The material parameters are adopted according to the calibrated parameters presented in Tab. 5.3. The numerical simulations are performed with $E = 5 \times 10^6\,\mathrm{N/m^2}$ for glass beads and Hamburger Sand to reduce computational costs. The simulated fluid has the properties of water at a temperature of 20 °C. Its density is $\rho_f = 1000\,\mathrm{kg/m^3}$ and the kinematic viscosity is $\nu_f = 1.004 \times 10^{-6}\,\mathrm{m^2/s}$. To reduce computational costs, a coarse-graining factor of 2 (Bierwisch et al., 2009) is applied to the particles in the numerical simulation with Hamburger Sand. The void fraction in the numerical setup is consistent with the void fraction in the experimental tests. The very dense packing density of the model tests could not be initialised in the numerical model

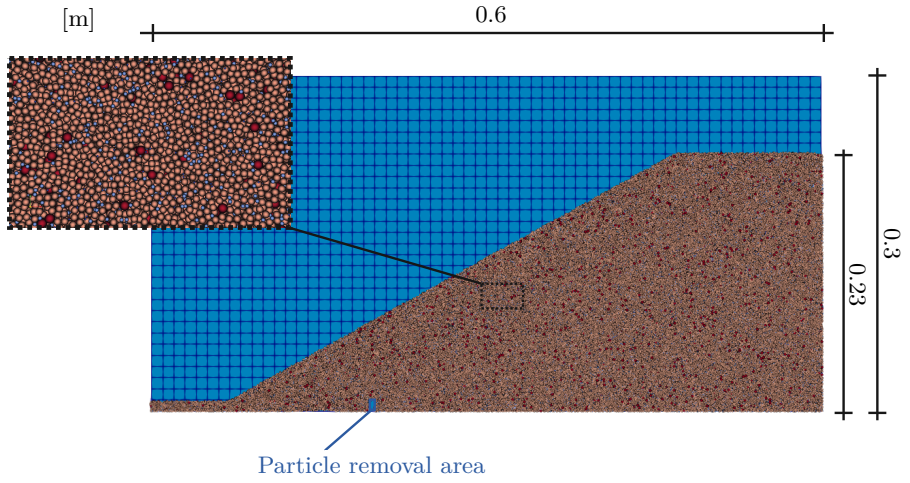


Figure 8.5: Numerical setup of a suction dredged submerged slope (Kanitz and Grabe, 2019a)

due to the spherical nature of the particles. However, in the CFD solver, a weighting factor of 1.1 was included. The void fraction of the particle assembly is divided by this factor for the computation of the Navier-Stokes equations.

8.3.2 Boundary conditions

The numerical simulation is a pseudo two-dimensional simulation. Therefore, a periodical boundary is applied in y-direction in the DEM solver. For an accurate computation of the interaction forces of the particles, by experience one requires a thickness of approximately ten particles in y-direction ($y_{\text{cell}} \approx 10 d_p$). For a polydisperse particle distribution like Hamburger Sand, the mean diameter can be taken for dimensioning the constant width of the y-dimension. The mean diameter is $d_{50} = 0.75\,\text{mm}$ without taking into account the coarse-graining. The y-dimension is then discretised with one CFD cell with a boundary condition of type empty (*OpenFoam documentation, Boundary conditions* 2020). Due to the coarse-graining of the Hamburger Sand, a thickness of approximately eight particles is reached in y-direction.
A standard $k-\varepsilon$ turbulence model is used. As the grid size needs to be coarse in unresolved coupled CFD-DEM (cf. Sec. 4.2) a wall function is set at the bottom boundary for k and ε to exploit the universal logarithmic wall law (*OpenFOAM v6 User Guide: 7.2 Turbulence models* 2019).

8.3.3 Coupled simulation with CFD-DEM

A coupling interval of 100 is chosen. The DEM time step is $t_{\text{DEM}} = 1 \times 10^{-6}\,\text{s}$ and consequently the CFD time step is $t_{\text{CFD}} = 1 \times 10^{-4}\,\text{s}$. The drag force model of Koch and Hill (2001) is used. Two actions model the suction dredging process:

1. In the DEM solver particles are constantly removed from the area where the suction dredger is located.

2. In the CFD solver a suction pressure boundary is implied at the same location where the particles are removed.

This procedure ensures that both particle removal, as well as applied suction on the soil body, is modelled. Thus, a possible effect of the suction pressure on the soil body can be investigated.
The removal area is highlighted in Fig. 8.5. According to the hydraulic height in the small-scale model tests, a suction pressure of $-17\,\mathrm{kPa}$ is initialised as boundary condition in the region of removal. Otherwise, the pressure boundary is $0\,\mathrm{kPa}$ for the bottom plate. For reasons of numerical stability, the pressure is increased during a simulated time of $0.2\,\mathrm{s}$. In this time frame, the particles are excluded from time integration to prevent that they start to move. This non-uniform boundary condition is realised by the groovyBC-utility available in OpenFOAM.
The removal of the particles is adapted to the removal rate determined in the experiment for every material. In the experiments, the removed material is gathered in a sieve during the $18\,\mathrm{s}$ of suction dredging. The removed mass for the different materials is specified in Tab. 8.2.

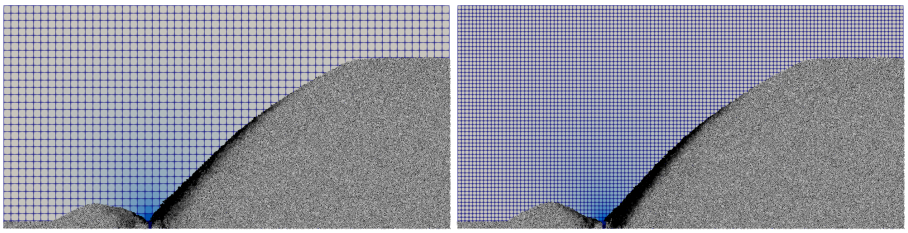
Table 8.2: Removed material weight during suction dredging

Material	Removed mass [kg]	Percentage of total mass [%]
Glass beads ($D = 3\,\mathrm{mm}$)	6	18
Glass beads ($D = 1\,\mathrm{mm}$)	10	32
Hamburger Sand, medium dense	8	20
Hamburger Sand, very dense	7	17.5

A mesh sensitivity analysis has been carried out to verify if the chosen mesh size leads to accurate results. Therefore, the very dense sandy slope is modelled with a grid of 0.01 m × 0.012 m × 0.01 m (coarse) and a grid of 0.005 m × 0.012 m × 0.005 m (fine). The results of the simulation after $1.8\,\mathrm{s}$ are presented in Fig. 8.6. The figure shows that the coarse and fine discretisation result in a very comparable failure behaviour of slope. Thus, the numerical simulations are performed with the coarse discretisation to reduce computational costs. The mesh size in the presented numerical simulations is, therefore, 0.01 m × 0.01 m in x- and z-dimension. The y-dimension varies due to the different size of the particles. The width of the cells in y-dimension is $y_{\mathrm{cell,G3}} = 0.03\,\mathrm{m}$ for the $3\,\mathrm{mm}$ glass beads, $y_{\mathrm{cell,G1}} = 0.01\,\mathrm{m}$ for the $1\,\mathrm{mm}$ glass beads and $y_{\mathrm{cell,HS}} = 0.012\,\mathrm{m}$ for the Hamburger Sand.

8.4 Results

This section will present the experimental and numerical results of suction dredged submarine slopes. The failure mechanism of the different materials is identified by analysing the displacement of the particles during dredging. Subsequently, the pore water pressure evolution during failure is evaluated and connected to the observed failure stage. It is



(a) coarse mesh (b) fine mesh

Figure 8.6: Mesh sensitivity analysis with a coarse mesh (a) of 0.01 m × 0.012 m × 0.01 m and a fine mesh (b) of 0.005 m × 0.012 m × 0.005 m; failure of a very dense slope after 1.8 s of suction dredging

verified if the elaborated numerical setup depicts the observed phenomena and the correct micro-mechanical processes.

8.4.1 Displacement of the slope

The displacement and hence the failure of the slope is monitored with the high-speed camera. The failure stages of the slopes with the different materials are displayed in Fig. 8.7 - 8.10. The blue dotted line represents the initial slope geometry.

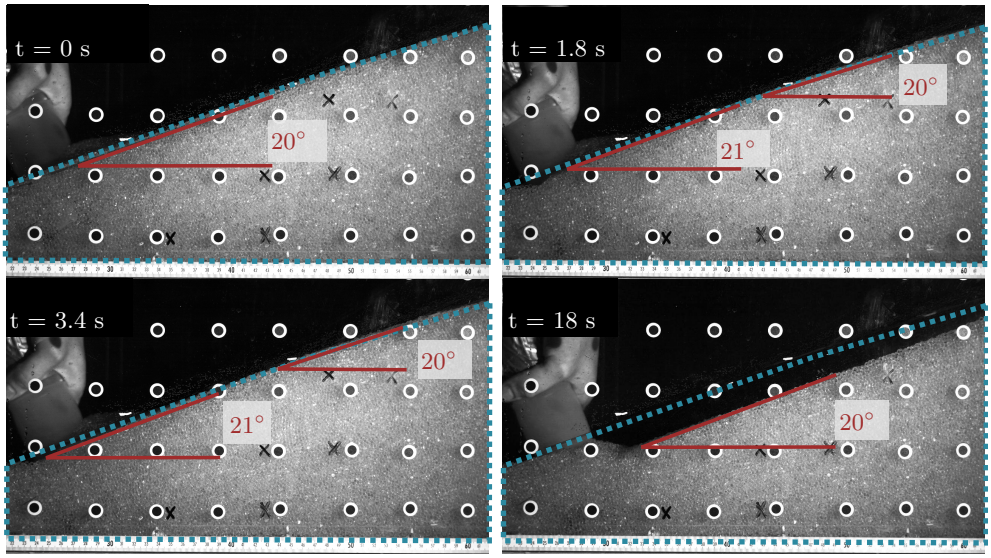


Figure 8.7: Failure of the submerged slope with 3 mm glass beads

During suction dredging, the inclination and shape of the slope with 3 mm and 1 mm glass beads are almost not changing (cf. Fig. 8.7 and Fig. 8.8). The removal of the particles is uniform, and no slumps can be observed. The slope inclination φ_{G3mm} remains at the angle of repose φ_0 of the 3 mm glass beads. Concerning the glass beads with a diameter of 1 mm, a slight curvature develops during the suction process. The inclination of the slope during dredging is not identical with the initial inclination. At 1.8 s, in the vicinity of the suction dredger, the inclination is $\varphi_{\mathrm{G1mm}} = 26°$. In the upper part of the slope, the inclination of the slope remains at $\varphi_{\mathrm{G1mm}} = 22°$. The inclination at the slope toe increases

to 28° at 3.4 s. The final slope inclination with 3 mm and 1 mm glass beads are identical to the initial one. The slope is in its equilibrium state, and no steeper slope angle occurs due to suction dredging.

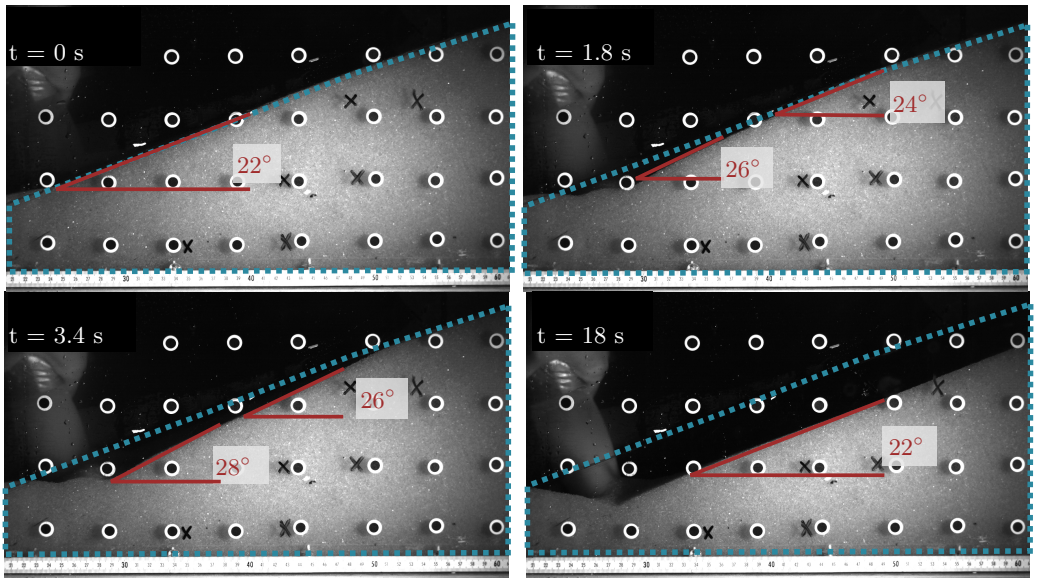


Figure 8.8: Failure of the submerged slope with 1 mm glass beads

These observations signify that due to the suction no increased stability of the slopes or tendency towards a breach failure mechanism can be identified. The steady movement of the glass beads is also not typical for a liquefaction failure. Hence, neither liquefaction nor breach failure occurs. The slightly steeper slope inclination of the 1 mm glass beads after 1.8 s can be explained by the lower permeability compared to the bigger glass beads. The applied suction is maintained for a while leading to an increased inclination. The upper part of the slope is not affected by the disturbance as it does not exceed the shear resistance in the downward part despite the steeper slope inclination. However, the movement of the glass beads is uniform and does not match the characteristics of liquefaction or breach failure.

Fig. 8.9 presents the failure of the medium dense Hamburger Sand. After 1.8 s a strong curvature of the slope of the medium densely packed Hamburger Sand develops in the vicinity of the suction mouth. The slope angle increases to 48° exceeding the critical slope angle. With increasing distance to the disturbance, the slope is less affected by the dredging process, and the shape of the slope remains unchanged. After 3.4 s, the disturbance of the suction dredger and the removal of the sand mass leads to an inclination of $\varphi_{\text{medium dense}} = 40°$ to $\varphi_{\text{medium dense}} = 45°$. The slope starts to collapse, and liquefied masses of sand are running down the slope. Hence, three different slope angles are developing. The zone between the lower slope angle of $\varphi_{\text{medium dense,1}} = 40°$ and the upper slope angle of $\varphi_{\text{medium dense,3}} = 30°$ can be characterised as a transition region with an inclination of $\varphi_{\text{medium dense,2}} = 45°$. In this transition zone, the sand starts to collapse and to run down in a liquefied manner leading to the inclination of $\varphi_{\text{medium dense,1}} = 40°$. At the end of the experiment after 18 s, the initial and final slope angle are equal. The final slope angle is $\varphi_{\text{medium dense}} = 32°$.

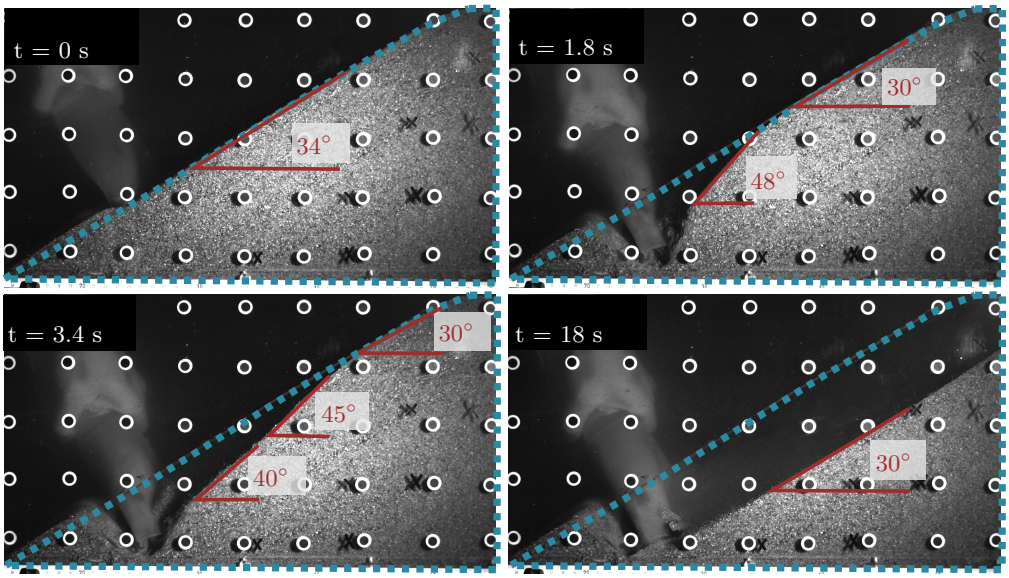


Figure 8.9: Failure of the submerged slope with medium densely packed Hamburger Sand (Kanitz and Grabe, 2019a)

Increased stability of the slope can be observed during suction dredging as the slope inclination is higher than its critical angle. As the permeability of the medium dense Hamburger Sand is lower compared to the glass beads of 1 mm diameter, the suction causes the excess of the critical angle by increasing the effective stresses. At $\varphi_{\text{medium dense,2}} = 45°$, the slope inclination exceeds the shear resistance of the slope despite the suction and sand starts to move down the slope in a liquefied manner. After a runout distance of several centimetres, the slope angle flattens, and the movement is steady. Thus, dredging of medium dense Hamburger Sand shows a slight tendency towards breach failure mechanism as the slope fails retrogradely. Nevertheless, the leading failure mechanism is liquefaction characterised by the quickly collapsing sand masses.

The suction dredging of the very dense Hamburger Sand results in a very steep inclination after 1.8 s ($\varphi_{\text{very dense}} = 70°$), which exceeds the critical angle significantly (cf. Fig. 8.10). The rest of the slope is not affected by the disturbance of the suction dredger. The slope remains stable after 3.4 s and the slope inclination does not alter. After 18 s, at the end of the experiment, the slope has collapsed by retreating slices running down the slope, and a straight surface develops. The final slope angle directly at the end of the experiment is $\varphi_{\text{very dense}} = 38° = \varphi_c$. The described failure behaviour is characteristic for a breach failure, where the slope body is stable for a certain amount of time. Compared to the final slope angle of the medium dense slope $\varphi_{\text{medium dense}}$, the influence of the very dense packing on the stability of the slope is significant - suction dredging of very dense sand results in a slope angle equal to its critical angle.

The numerical results of the suction dredged submarine slopes are illustrated in Fig. 8.11 - Fig. 8.14. The snapshots are taken at the same time steps as in Fig. 8.7 - 8.10. As can be observed, the failure behaviour of the numerical simulation with the glass beads of 3 mm diameter matches the experimental results very well (cf. Fig.8.11). The slope inclination is 22° in the lower part and 21° in the upper part of the slope after 1.8 s. After 3.4 s, the slope

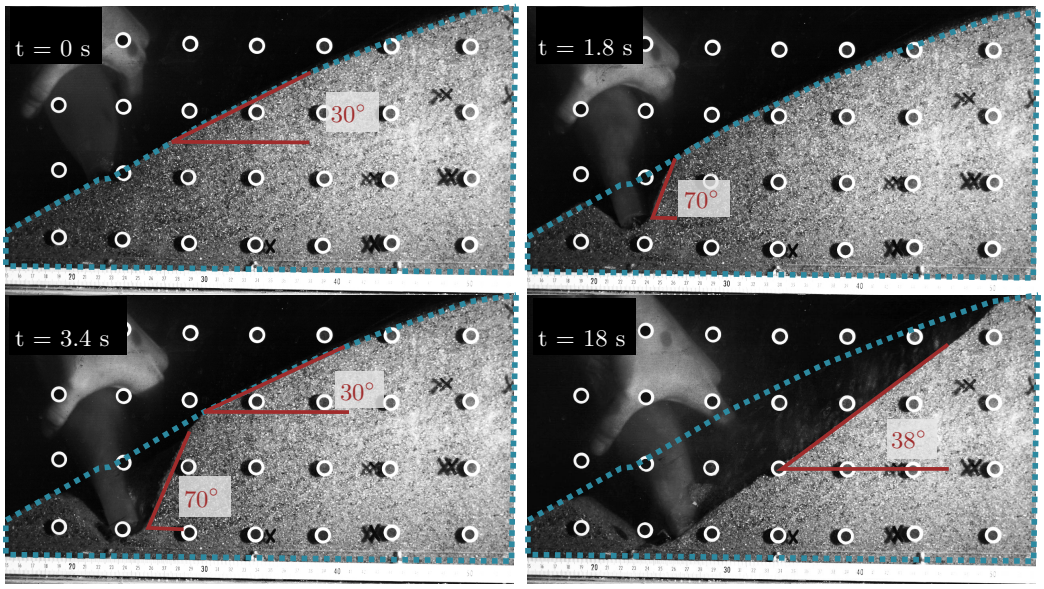


Figure 8.10: Failure of the submerged slope with very densely packed Hamburger Sand (Kanitz and Grabe, 2019a)

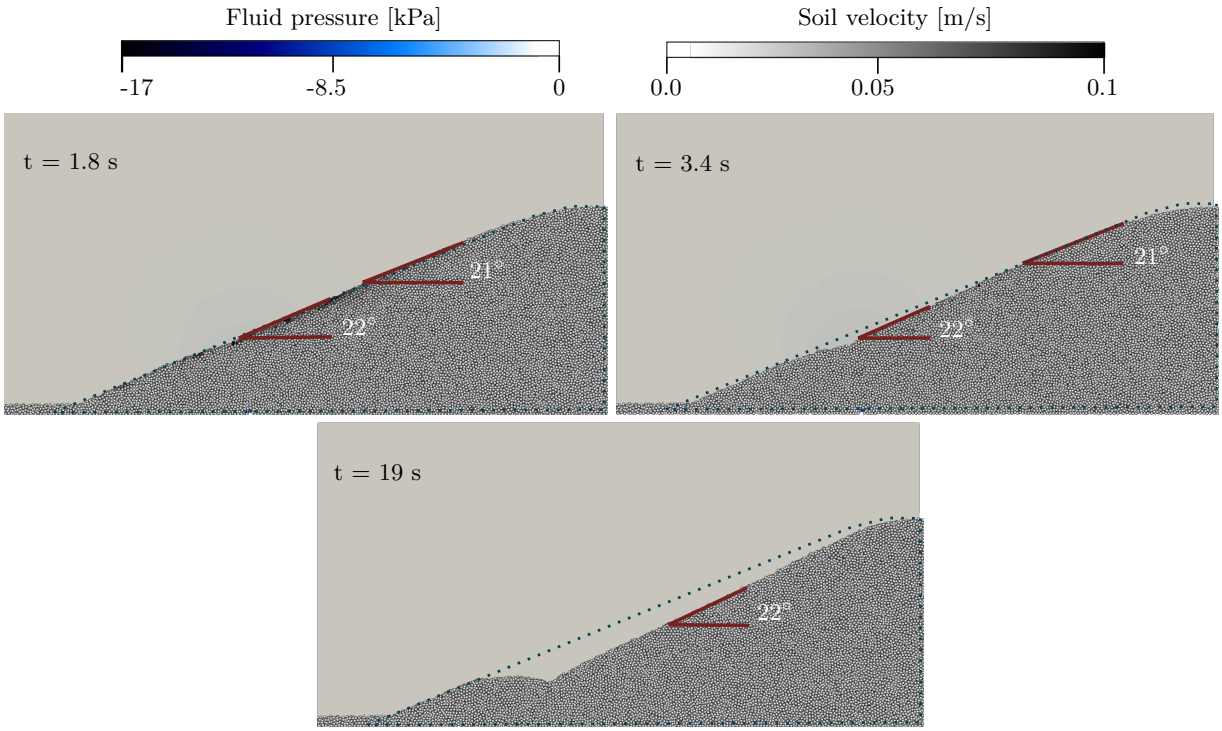


Figure 8.11: Numerical results of the failure of a suction dredged submerged slope with 3 mm glass beads

angle remains the same, signifying a difference of 1° between experimental and numerical results. The final state of the numerically modelled slope is reached after 19 s, which agrees well with the model tests. The final inclination of the slope is 22°. The deviation between the numerical and the experimental results is 2°, showing a good agreement.

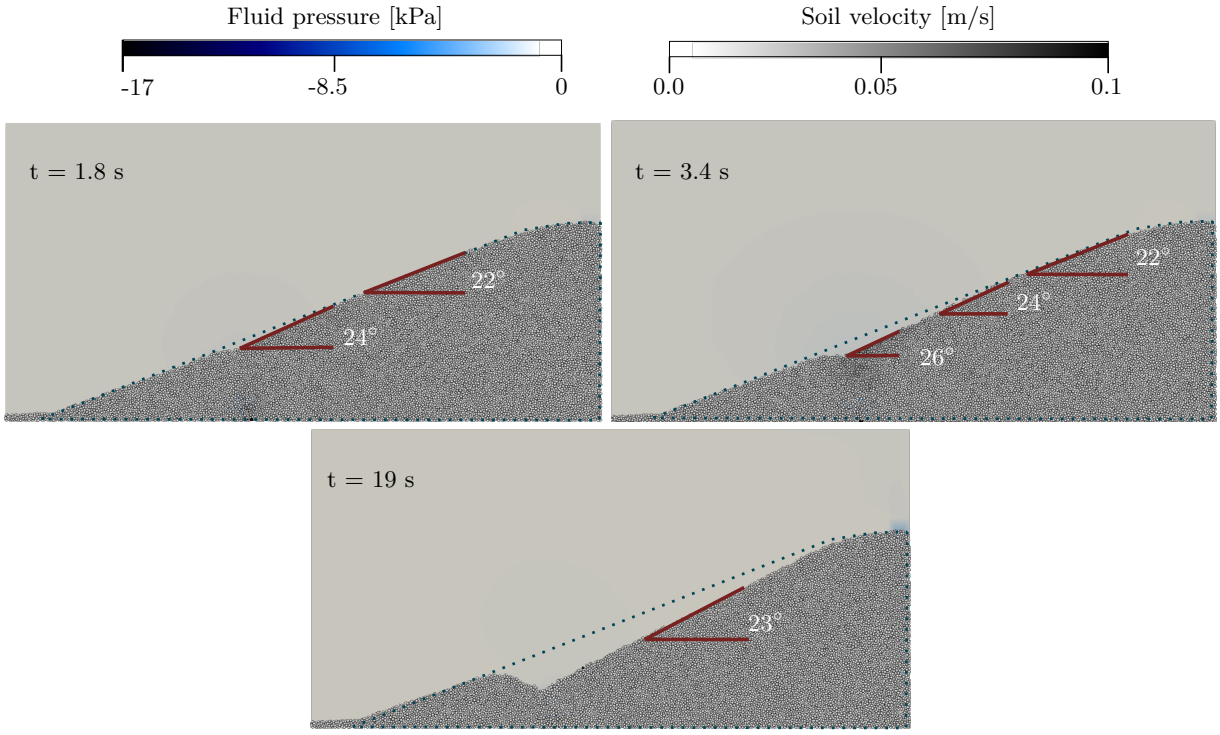


Figure 8.12: Numerical results of the failure of a suction dredged submerged slope with 1 mm glass beads

The failure process of the submerged slope with 1 mm glass beads in the numerical model is depicted in Fig. 8.12. In the experimental results (cf. Fig. 8.8) different slope angles could be observed. The same applies to the numerically modelled slope. After 1.8 s, the slope inclination towards the suction mouth is 24° and 22° in the upper part of the slope. Hence, there is a 2° deviation to the inclination at the slope toe compared to the experimental results. This trend continues after 3.4 s where slope inclinations of 26° and 24° occur. After ceasing the pressure, the slope remains at equilibrium with 23° slope inclination. The comparison to the experimental results shows a good qualitative agreement with minor deviations with regards to the slope inclination. The numerical model depicts the increased slope angle in the vicinity of the suction pressure.
Fig. 8.13 shows the failure of the medium dense slope. Similar to the experiments, a strong curvature of the slope shape towards the suction occurs. The angle measures 47° and the upper part of the slope is not affected by the dredging. These inclinations are consistent with the model tests, where the same behaviour is observed. The difference in slope angle is negligible. After 3.4 s of simulated time, the dredging process generates different failure stages of the submarine slope. The downwards part of the medium dense slope (cf. Fig. 8.13 middle) has an inclination of 48°. The transition to the undisturbed part of the slope with 30° inclination has a slope angle of 40°. This behaviour is contrary

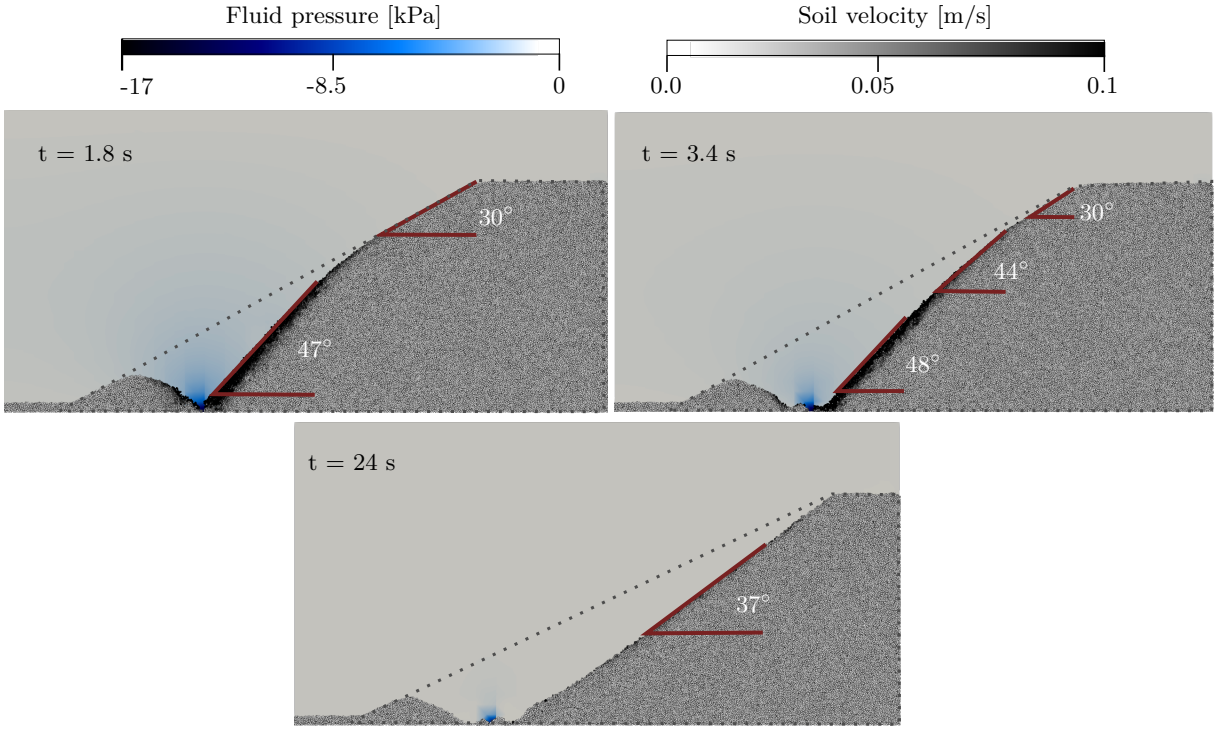


Figure 8.13: Numerical results of the failure of a suction dredged submerged slope with medium dense Hamburger Sand (Kanitz and Grabe, 2019a)

to the model tests, where the downward part of the slope is flatter than the middle part. As mentioned before, the steeper inclination in the transition zone causes liquefied masses, which run down the slope, resulting in a flatter inclination at the slope toe. This behaviour cannot be identified in the numerical simulations. The particle velocities indicate that the particles are rolling down uniformly. The steep slope angle in the slope toe can be a result of the suction pressure in the removal area. However, the upward part of the slope, which is not affected by the dredging, corresponds very well to the results of the model tests.

Fig. 8.14 shows the dredging process of a very dense submarine slope. After 1.8 s of dredging, the model of the very dense slope results in a nearly identical behaviour as the medium dense slope. The very steep inclination of $\varphi = 70°$, which occurs in the model tests and results from the breach failure mechanism, cannot be identified in the numerical model. The comparison of the failure behaviour of the medium dense and the very dense slope (cf. Fig. 8.14 middle) shows no difference. The inclination of the slopes is identical. This is a significant difference to the model tests, where the slope fails in breaches, and the slope inclination remains constant at 70°. The increased grain-to-grain stresses resulting from the suction are thus not modelled.

When the dredging process finishes, the slope reaches an equilibrium state. In the experiments, this occurs almost directly after ceasing the suction pressure after 18 s. In the numerical model, however, it requires more time to reach the equilibrium state. A simulated time of 24 s is necessary (cf. Fig. 8.13 and 8.14 bottom). The final slope inclination for the medium dense and the very dense slope is 37°. This is in agreement with the final state of the very densely packed slope, but it does not agree with the results of the medium

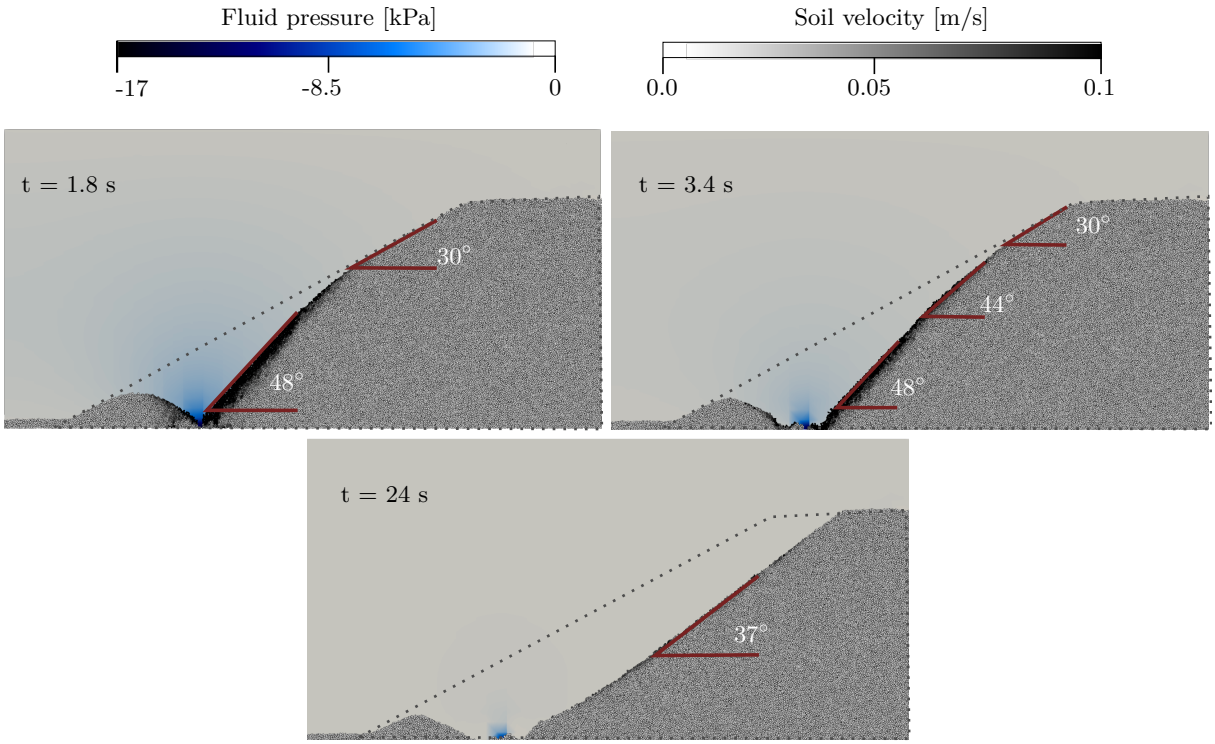


Figure 8.14: Numerical results of the failure of a suction dredged submerged slope with very dense Hamburger Sand (Kanitz and Grabe, 2019a)

densely packed slope. The numerically modelled sandy slopes need more time to reach an equilibrium state as the particle motion is more uniform and hence, slower than in the model tests. In summary, the observations lead to the conclusion that the failure process of the submerged slope is very well depicted by the numerical model when it consists of glass beads. With regards to the sand slopes, the numerical model depicts the failure process only to a certain extent. The agreement between the medium dense sand in the experimental and the numerical model is qualitatively good. However, liquefaction cannot be observed. With regards to the very dense slope and the breach failure, the numerical model cannot depict the failure process. In the next section, the pore water pressure changes are investigated to analyse why the numerical model fails at depicting liquefaction and breach failure.

8.4.2 Pore water pressure changes

This section presents the pore water pressure changes in the experimental and numerical setup for all materials.
Fig. 8.15 presents the pore water pressure measurements during the model tests. It can be identified that for all materials, the applied suction results in a sudden pressure drop at transducer P1. The magnitude is thereby dependent on the material. The highest magnitude occurs for the glass beads of 1 mm diameter and the medium dense Hamburger Sand ($p = -0.2\,\mathrm{kPa}$). The lowest magnitude is visible for the glass beads of 3 mm diameter ($p = -0.1\,\mathrm{kPa}$).

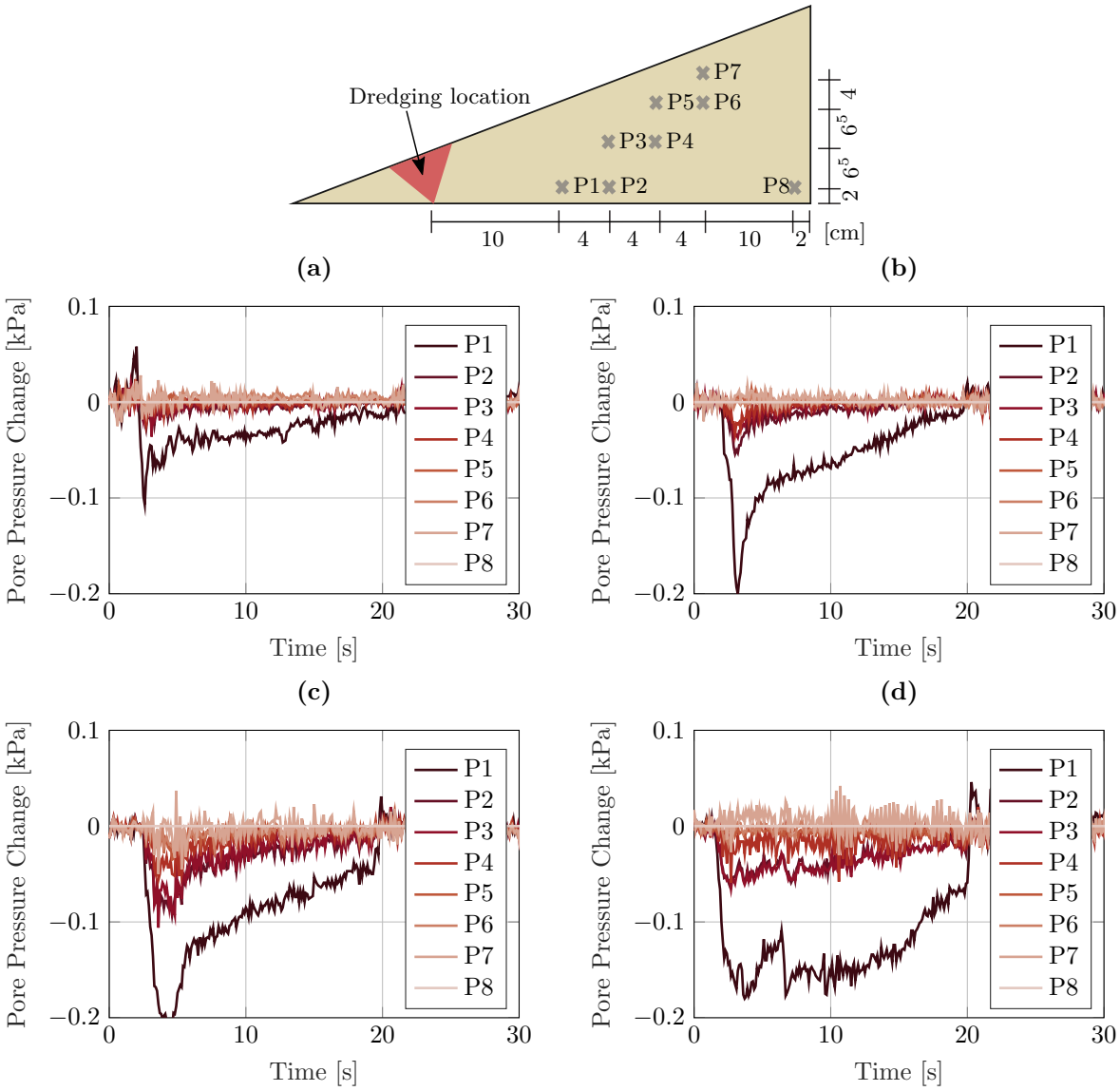


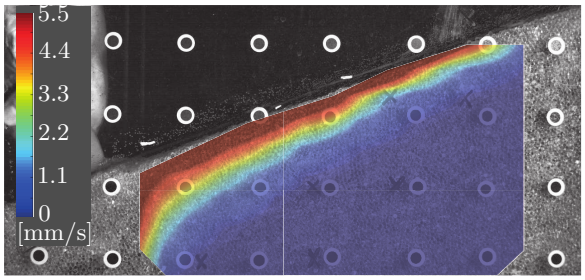
Figure 8.15: Pore water pressure changes in the experiments with (a) glass beads of 3 mm diameter, (b) glass beads of 1 mm diameter, (c) medium densely packed Hamburger Sand and (d) very densely packed Hamburger Sand

After peaking, the measurements in the glass beads show a fast but linear increase of the pressure. In the medium dense sand, the other pressure locations (P2 - P6) experience a sudden pressure drop as well. The pressure level is constant for approximately 1 s followed by a linear increase until the end of the experiment after 18 s for the transducers P2 - P6. At sensor P1, a cascaded increase is observed, meaning that an increase is followed by a small plateau, which is then followed by a new linear increase. The pressure measurements in the very dense sand differ quite significantly from the other materials. The negative pressure is measured in the transducer P1 - P4 only, but no distinct peak exists. Instead, the pressure is maintained in the soil body except for a sudden increase at transducer P1 in the time interval of 4 s to 7 s. A linear increase, which occurs in the other materials, is observed at P1 after 16 s.

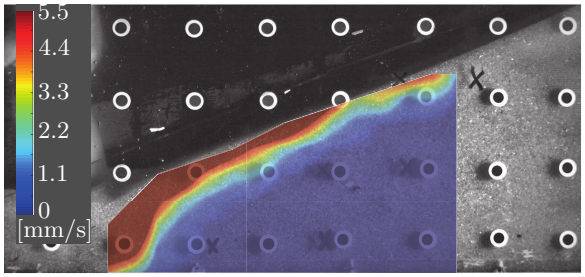
The downward motion of the particles causes the linear increase that can be observed in the pore water pressure measurements. Hence, when the slope fails, and the particles start to move, fluid flow is initiated. This flow compensates the negative excess pore water pressures by pushing water inside the pores. Likewise, the increase in the pressure indicates the slope failure. The cascaded increase observed in the medium dense sand signifies a periodical change between liquefaction and enhancement of the material. When the suction dredging starts, significant suction pressure is measured in the soil body. Due to the lower permeability of the medium dense sand compared to the glass beads, this negative excess pore water pressure is maintained for a certain amount of time leading to a plateau in the measurements. However, due to the constant material removal, the shear loading, which the material experiences by removing the slope toe, increases. This disturbance leads to a rearrangement of the particles in the upper layers of the slope. The contractant nature of the medium dense sand leads to densification. This densification increases the pore water pressure, and finally, the effective stresses vanish. The sand slices collapse and run down the slope in a liquefied manner. This moment can be captured in the pore water pressure measurements by the sudden increase of the pressure as the movement of the particles initiates a seepage flow pushing pore water in the pores of the slope body. This linear increase of the pressure is thereby shorter in time than the observed plateau as the material moves very quickly. The suction meanwhile continues leading to a new plateau and equivalently an enhancement until a new slice starts to fail due to the excess of the shear resistance. Overall, the medium dense sand has a partially drained behaviour. This observation can also explain the evolution of the pore water pressure in the very dense slope. The suction pressure is applied, leading the negative excess pore water pressures in the slope toe. In contrast to medium dense sand, the dilatant nature of the very dense slope results in a loosening due to the disturbance. This leads to additional negative excess pore water pressures. Hence, the particles stop moving and accordingly, no water seeps into the pores of the slope. As a result, the negative excess pressure is maintained, enhancing the overall shear resistance. The very dense sand experiences undrained behaviour.

Additionally, the lower permeability restricts the water to seep inside the pores. The lower the permeability, the lesser water can flow inside the pores and, more importantly, it is harder for the water to flow inside. Thus, the water flow induced by the suction dredging cannot mainly flow through the slope body as the low permeability does not permit this. It needs to find another way. Water always follows the path with the lowest effort. Hence, the flow is more likely to chose a way around the slope. Accordingly, the water will need more

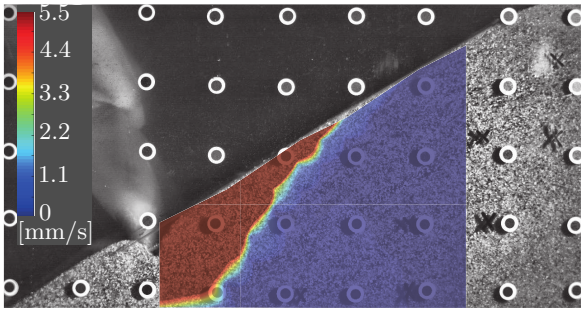
time to seep inside the pores to compensate for the negative excess pore water pressures. When the disturbance at the slope toe gets too high, the sand starts to collapse and runs down quickly.
By comparing all the pore water pressure measurements, the question about the determining factor for the maximum pore water pressure magnitude arises. The highest magnitudes occur in the glass beads with 1 mm diameter and the medium dense sand and the lowest in the glass beads with 3 mm diameter. The maximum pore water pressure of the very dense slope lies in-between. As we know from the failure analysis, neither the small glass beads nor the medium dense sand shows a significant enhancement of the slope body. Hence, the maximum magnitude does not define the resistance of the slope body.
In order to understand this behaviour, the particle velocities in the model tests are investigated with PIV (cf. Fig. 8.16). Likewise, we can compare the pore water pressure magnitude with the maximum velocity of the particles.



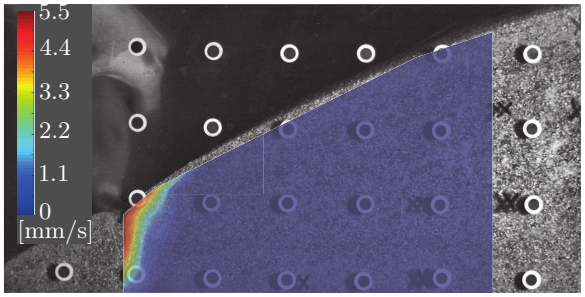
(a) Glass beads $D = 3$ mm



(b) Glass beads $D = 1$ mm



(c) Medium dense Hamburger Sand



(d) Very dense Hamburger Sand

Figure 8.16: PIV measurements of material velocity of submarine slopes with 3 mm glass beads (a), 1 mm glass beads (b), medium densely packed sand (c) and very densely packed sand (d) carried out with GeoPIV-RG

The PIV measurements outline the highest velocity for the medium dense sand and the slope of 1 mm glass beads, and the lowest for the slope of 3 mm glass beads. By now taking into account these measurements, it can be stated that the highest pore water pressure magnitude develops with the highest particle velocities. After Bernoulli's principle, the increase in the velocity of a fluid co-occurs with a more significant decrease in the fluid pressure. Considering this, one can now explain why the highest negative excess pore water pressure is measured in the experiments with the 1 mm glass beads and the medium dense sand. This observation signifies that the magnitude of the pore water pressure is not mainly dependent on the permeability of the slope body, but rather on the sliding velocity of the soil masses running down the slope. Likewise, a great magnitude of the

pore water pressure does not indicate a shear resistance enhancement of the slope. As the measurements in the very dense sand show, the key factor for enhanced stability is how long the negative excess pore water pressure is maintained in the slope body. Two factors cause the enhancement in very dense sand:

1. The dilatant behaviour: As the particles depart from each other due to removing the slope toe, suction pressure develops between the grains. The resulting increase in the grain-to-grain stresses impedes particle motion. The pressure is maintained, and the slope is stable.

2. The lower permeability: The permeability of the very dense sand restricts the water to seep inside the pores easily. The dilatant behaviour increases the effect as the pore channels do not widen as a result of the stable particle package.

The investigation of the numerically computed pressure in the fluid field can reveal if the particle motion affects the fluid pressure in the numerical model and if the applied suction pressure influences the pressure field in the slope body. It shows why neither breach nor liquefaction failure is depicted correctly. The computed pressure in the fluid phase is extracted at the same positions as in the experimental setup. The pressure evolution of the glass beads, as well as the medium dense and very dense sand, is depicted in Fig. 8.17. The pore water pressure differs majorly from the experimental results. A sudden decrease at the very beginning of the applied suction in the pressure level occurs for all materials, whereby the magnitude of the minimum pore water pressure significantly depends on the material. The 3 mm glass beads reveal the lowest pressure drop with -0.02 kPa. In the numerical model with the 1 mm glass beads, the pressure drop is slightly higher with -0.21 kPa. Only the Hamburger Sand, both medium dense and very dense, shows a significant decrease in the pore water pressure. In contrast to the glass beads, some small deviations of the pore water pressure can be identified in regards to the different locations of the extracted data. The minimum magnitude of the pressure level develops in the medium dense sand with -3.7 kPa and in the very dense sand with -6 kPa. In all materials, the sudden pressure drop vanishes quickly within approximately 0.01 s. After this time interval, the pressure level stays constant except for some numerical noise.
By comparing the numerical results with the experimental measurements, it is evident that the pressure evolution is not depicted accurately by the numerical model. Tab. 8.3 summarises the pressure magnitudes of the experimental and the numerical results and depicts the difference. The magnitude of the pressure drop in the glassy slopes is comparable to the experimental data, but the pressure drop in the sandy slope is greatly overestimated. From the experiments, it was concluded that the pressure drop magnitude is dependent on the material velocity. This relationship cannot be established in the numerical model. Undoubtedly, the glass beads have a lower velocity than the sand (cf. Fig. 8.11 and Fig. 8.12), which can explain the low pressure drop magnitude. Nevertheless, there is no significant difference in the velocity of the medium dense and very dense sand (cf. Fig. 8.13 and Fig. 8.14), which is why this cannot be the reason for the remarkable difference in the pressure drop magnitude in the numerical model. The different pressure drop magnitudes can be explained by the different amount of particles lying within the individual computational cells. The sudden pressure drop appears directly after activating

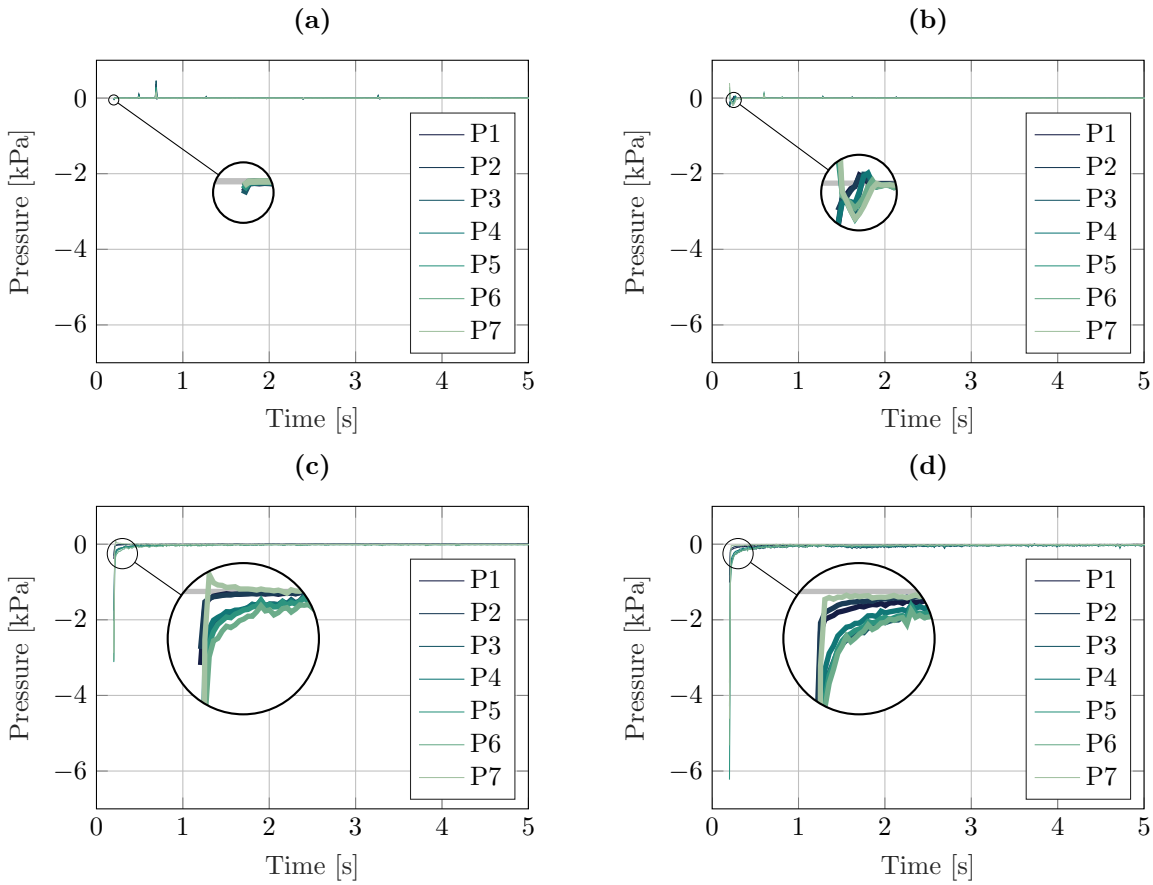


Figure 8.17: Numerically modelled pore water pressure changes with (a) glass beads of 3 mm diameter, (b) glass beads of 1 mm diameter, (c) medium densely packed Hamburger Sand and (d) very densely packed Hamburger Sand

the pressure boundary and the removal of particles from the cells. The amount of particles in the glass bead slopes is comparably low with regards to the Hamburger Sand due to their monodisperse nature. Hence, the number of particles removed in one time step is lower than compared to the Hamburger Sand. The sudden removal of the particles results in a volume that is suddenly „empty“. This sudden removal causes the pressure to drop. Accordingly, when more material lies in the cell, e. g. the cell has a lower void fraction, the difference between „full“ and „empty“ is more pronounced. This can also be the reason for the vast difference in the pressure levels between medium dense and very dense sand as a very dense packing contains more material than a medium dense packing. The quick vanishing of the pore water pressure in the numerical model further shows that the suction pressure has no significant impact on the slope. This explains the substantial differences in the failure mechanisms between the numerical and the experimental results. In the numerical model, the failure results solely from the particle removal. Neither partially drained nor undrained behaviour of the material occurs. The applied suction pressure does not cause seepage flow in the slope body. As a cause, no fluid motion is visible in the slope body (cf. Fig. 8.18). Likewise, in contrast to the experiments, the applied suction is

restricted to its close vicinity. Additionally, it can be concluded that the pressure changes due to the particle motion (hence contractancy and dilatancy) is not captured.

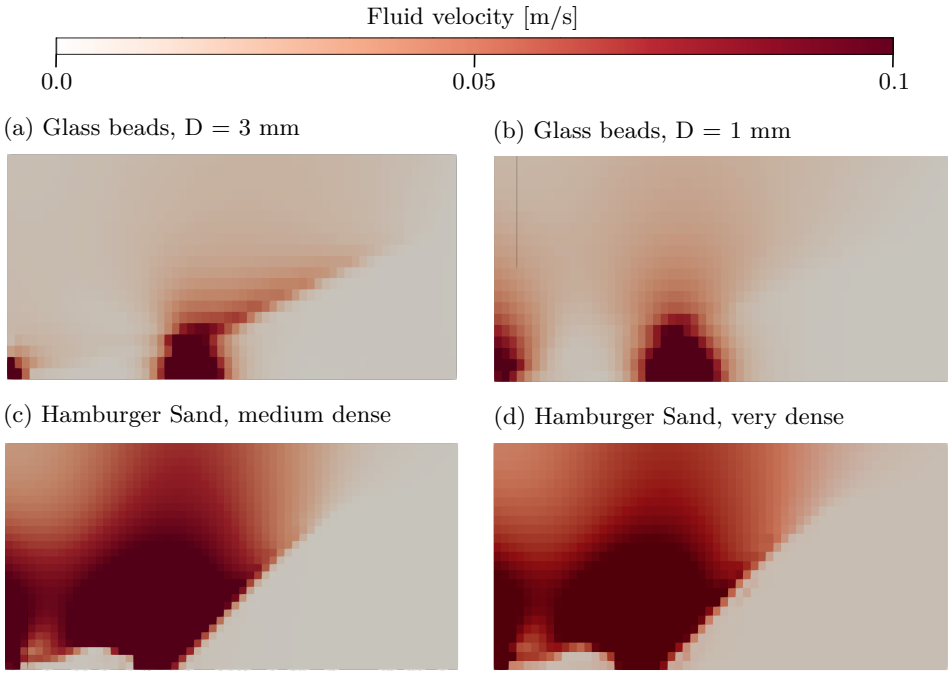


Figure 8.18: Computed fluid velocity at $t = 1.8\,\mathrm{s}$ of simulated time for (a) glass beads of 3 mm diameter, (b) glass beads of 1 mm diameter, (c) medium densely packed Hamburger Sand and (d) very densely packed Hamburger Sand

Table 8.3: Experimental and numerical maximum peak value of the pressure measurements in the slope body

Material	p_{exp} [kPa]	p_{num}[kPa]	$p_{\mathrm{num}} - p_{\mathrm{exp}}$ [kPa]
Glass beads ($D = 3\,\mathrm{mm}$)	-0.1	-0.02	-0.08
Glass beads ($D = 1\,\mathrm{mm}$)	-0.2	-0.21	0.01
Hamburger Sand, medium dense	-0.2	-3.7	3.5
Hamburger Sand, very dense	-0.18	-6	5.82

The following three major conclusions can be obtained from this comparison:

1. The overestimation of the pressure peak magnitude in the numerical model results from the sudden particle removal from the computational cells. It is solely a result of slight numerical instability.

2. The motion of the particles in the numerical model does not affect the fluid phase in the soil body. Partially drained and undrained behaviour are not captured. The pressure vanishes quickly inside the slope body, which is a result of unresolved coupled CFD-DEM. The fluid pressure is computed in the cell centre and then interpolated to the faces of the same cell. Hence, when the numerical damping due to this

interpolation gets too strong, fluid properties like pressure and velocity vanish quite quickly. Due to unresolved couped CFD-DEM, a lower limit of the CFD cells exists, which prohibits a finer discretisation.

3. The numerical model cannot depict breach failure as well as liquefaction failure. The plateaus observed in the model tests for the medium dense and very dense sand result in enhanced stability as the pore water does not flow freely to equalise the negative pore water pressure. Thus, unresolved coupled CFD-DEM is not suitable to model breach or liquefaction failure as the fluid flow changes due to dilatant, and contractant behaviour need to be captured. The effects of small changes of the void fraction onto the fluid pressure cannot be computed.

8.4.3 Summary

The experimental and numerical investigation of suction dredging in submarine slopes revealed the following findings:

1. The coarser the material, the more uniform the failure and the movement of the material as the pore water flows freely through the pores. Effects of pore water-soil interaction are minor.

2. The failure of the medium dense sand is a combination of breach and liquefaction failure. A periodical change between liquefaction and enhancement occurs. The pore water pressure reflects this behaviour by a cascaded evolution. Partially drained behaviour occurs.

3. Breach failure occurs in the very dense sand, which results in a very steep slope inclination. The negative pore water pressure is maintained in the soil body, and undrained behaviour can be observed.

4. Material movement leads to water flow pushing water inside the pores, which results in the vanishing of the negative excess pore water pressure.

5. The faster the material flows, the higher is the maximum magnitude of the pore water pressure. The magnitude of the pore water pressure has thereby no influence onto the stability of the slope. The shear resistance enhancement is a result of the ability of the material to maintain the negative pore water pressure.

6. Unresolved coupled CFD-DEM is not able to capture the interaction between pore water and soil skeleton. Consequently, breach and liquefaction failure are not modelled, although the inclination and overall result for medium dense sand are in qualitative agreement.

7. The numerical simulation of glass beads agrees very well with the experimental results, but in this case, the interaction between pore water and soil skeleton has no considerable effect on the failure mechanism.

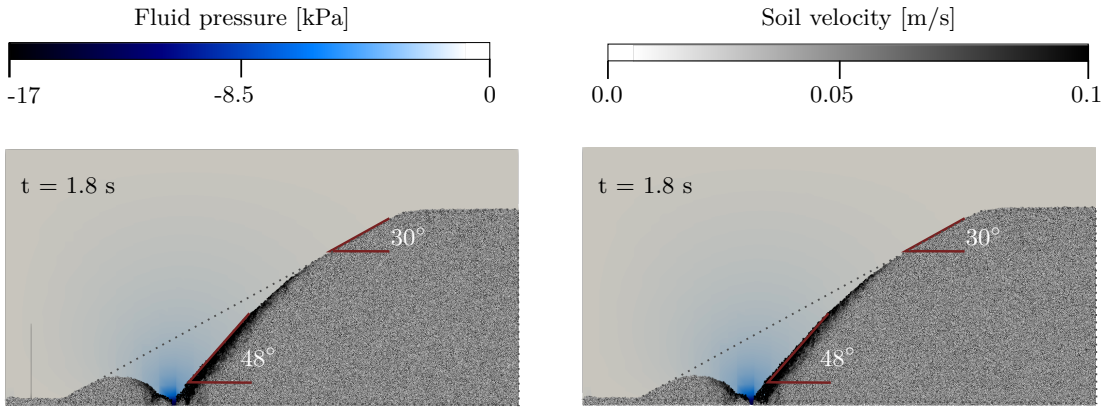
8. In the numerical model, the failure only depends on the material properties. This is the reason why the medium dense and the very dense slope result in the same failure behaviour.

8.5 Approaches to model shear-dilatancy response in fluid

It is now striking that unresolved coupled CFD-DEM cannot be used to model submarine slope failure. The main question is, why the unresolved CFD-DEM method fails in depicting the interaction of pore water and soil skeleton in regards to the computation of pore water pressure changes due to contractant and dilatant behaviour of the material. In the governing equations of the unresolved coupled CFD-DEM method, cf. Eqn. 4.18, the first term $(\frac{\partial}{\partial t}n)$ computes the influence of the change of void fraction in the computational cells on the fluid flow. It is therefore the responsible term to depict the change of the fluid flow due to contractancy and dilatancy. However, the computation of this term is numerically unstable due to the sudden and little changes in the void fraction. For this reason, in usual simulations with the software package CFDEM®coupling, this term is neglected by default. The user can choose to switch it on despite its numerical instability (called ddt-Model A) or to compute it by the divergence of the particle fluxes at the boundaries via

$$\frac{\partial n}{\partial t} = \nabla \cdot (\boldsymbol{v}\,(1-n)) \tag{8.2}$$

which is called ddt-Model B.
Numerical simulations of the very densely packed slope are carried out once again to investigate the impact of ddt-Model A and B on the failure mechanism of the submarine slopes. Fig. 8.19 presents the results of the very densely packed slope after 1.8 s of simulated time using ddt-model A and B.



(a) Very densely packed slope, ddt-Model A

(b) Very densely packed slope, ddt-Model B

Figure 8.19: Numerical simulation of the very densely packed slope after 1.8 s of simulated time including the time derivative of the void fraction - (a) Numerical model with ddt-Model A, (b) Numerical model with ddt-Model B

It can be observed that neither ddt-Model A nor ddt-Model B have a major influence on the failure behaviour and fail to depict the breach mechanism. CFD computes the pressure

and fluid flow in the cell centre and interpolates it then onto the cell faces. Accordingly, if two particles are getting closer or further away from each other while located in the same cell, the change of the fluid flow cannot be computed. The lower size limit of a CFD cell is $3 \cdot d_p$ leading to a comparably high loss of information concerning the fluid flow state between the particles. Even if the void fraction term can be computed correctly, it is questionable if this would lead to the correct physical behaviour in regards to the shear-dilatancy effect on the fluid flux.

Hence, without additional effort, the pressure change due to a sudden displacement of the particles cannot be modelled. In the literature, the majority of the investigations concerning the pore-pressure response due to dilatant or contractant soil behaviour is based on macroscale approaches. Iverson (2005) investigated the influence of landslide motion with dilatant and contractant behaviour by introducing a model that couples Coulomb friction with the evolution of shear zones dependent on the dilation angle ψ. He featured the model with a formulation for the excess pore pressure that incorporates the feedback between the landslide displacement and the shear zone dilation, which modulates the excess pore water pressure. The formulation of the excess pore water pressure generation is based on Darcy flow with the permeability K_f. Later, Iverson and George (2014) incorporated these approaches in a depth-averaged, two-phase model.

Bouchut et al. (2016) developed a two-layer model with a thin fluid layer on top of a two-phase mixture layer to incorporate the effects of dilatancy and contractancy on the motion of saturated avalanches. The mass and momentum conservation is satisfied by the Jackson model (Anderson and Jackson, 1967) for the solid-fluid mixture with a closure relation involving the solids dilation. This closure relation is based on the dilation law by Roux and Radjai (2010) extended with the formulation of Pailha et al. (2008). It includes the dilation angle ψ, the volume fraction and a calibration constant K. The latter is called dilation constant. It describes the effect of enforcing the soil friction at dilation and diminishing it at contraction caused by pore pressure changes. Bouchut et al. (2016) performed numerical tests for uniform flows. The comparisons of their results with the results of Iverson and George (2014) and Pailha et al. (2008) showed equivalent results.

In a recent study C.-H. Lee and Huang (2018) investigated a submerged granular column collapse with the two-fluid method. To model the effect of the void fraction onto the failure mechanism, the particle response time t_p is extended with a function after Hsu et al. (2004), which includes the influence of the void fraction on the particle-fluid interaction force. The particle response time is used to parametrise the drag force between the fluid and the solid phase. It also affects the dissipation of high and low pore pressure built up in the granular medium (Das and Sobhan, 2014). C.-H. Lee et al. (2016) combined the models of Richardson and Zaki (1997) and Engelund (1953) with the extension of Camenen (2008) for high concentration regions. Using this method, the drag force acting on the particles is increased, but the actual negative pore water pressure resulting from the dilatancy effect is not modelled. However, with this formulation, C.-H. Lee and Huang (2018) were able to simulate the collapse of a submerged granular column with a general agreement for both loose and dense sand.

These studies are all based on macro-scale approaches taking into account either calibration or macroscopic parameter such as the permeability. Using DEM, we have, however, the possibility to model the effects of dilatancy and contractancy on the fluid directly through a

suitable coupling between the particle movement and the generated pressure. Likewise, the next section presents a new model in the framework of a cohesion model in DEM to compute the effects of dilatancy and contractancy on the behaviour of saturated non-cohesive soil. It is important to clarify here that the term "cohesion model" only stems from its framework in the DEM environment. It is not meant as a material property of sand. A submerged granular column collapse is investigated and compared against experimental results to verify this newly developed cohesion model. This setup is a typical benchmark for numerical methods as it is easy to compute, and the computational costs are relatively low due to the small dimensions of the test.

8.5.1 Cohesion model in DEM

The presented cohesion model aims to compute the force of the excess pore pressure resulting from contractancy and dilatancy in saturated states directly onto the particles. Using a cohesion model in DEM enables the computation of a force between two particles as their exact velocities and distances from each other are known without being restricted by the CFD cell sizes. The next advantage of using DEM is that we do not need to model dilatancy via the dilation angle ψ, a material constant that can be dependent on the shear rate, the stress state, and the void fraction. There is still no fundamental theory linking all these quantities (Jaeger et al., 1996; Puckett et al., 2011). DEM directly computes the rearrangement of the particles caused by dilatant or contractant behaviour. Yang et al. (2012) showed that pure DEM captures the effect of dilatancy on the shear resistance by carrying out biaxial tests with drained and undrained (constant volume) conditions. Hence, dilatancy and contractancy is captured by DEM, in particular by the interparticle contact friction and the rolling friction causing interlocking of the particles, but the question remains how the fluid is affected by the rearrangement. Therefore, the following investigations and assumptions are only related to the force exerted by the fluid onto the particle due to their rearrangement.

Fig. 8.20 depicts the rearrangement of a dense and a loose particle configuration when applying a shear force. In the dense particle configuration, the dilatant nature of the particles causes a pore volume increase by the particle rearrangement. This rearrangement results in particles, which are departing from each other. This is highlighted by the solid line. The length of the solid line increases when changing from a dense to a loose particle configuration. At the same time, as the particles are not getting into suspension, contact is still established and there are particles, where the distance from each other is not affected. This is highlighted by the dotted line. Applying a shear load to a loose particle configuration, the rearrangement causes a pore volume reduction. In this case, the solid lines reduce in length, meaning the particles are getting closer to each other. So in summary, it is important to highlight that, during shearing, in a dense particle configuration, particles are departing from each other and in a loose configuration, particles are getting closer. In a water saturated state, this signifies that in dilatant-behaving sand, fluid has to flow into the opening pores and no empty voids are allowed. In a contractant-behaving sand, the fluid is expelled from the closing pores.

Let us now introduce the basic idea of the presented model to depict the force exerted by the fluid due to the particle rearrangement: when two particles in a water saturated

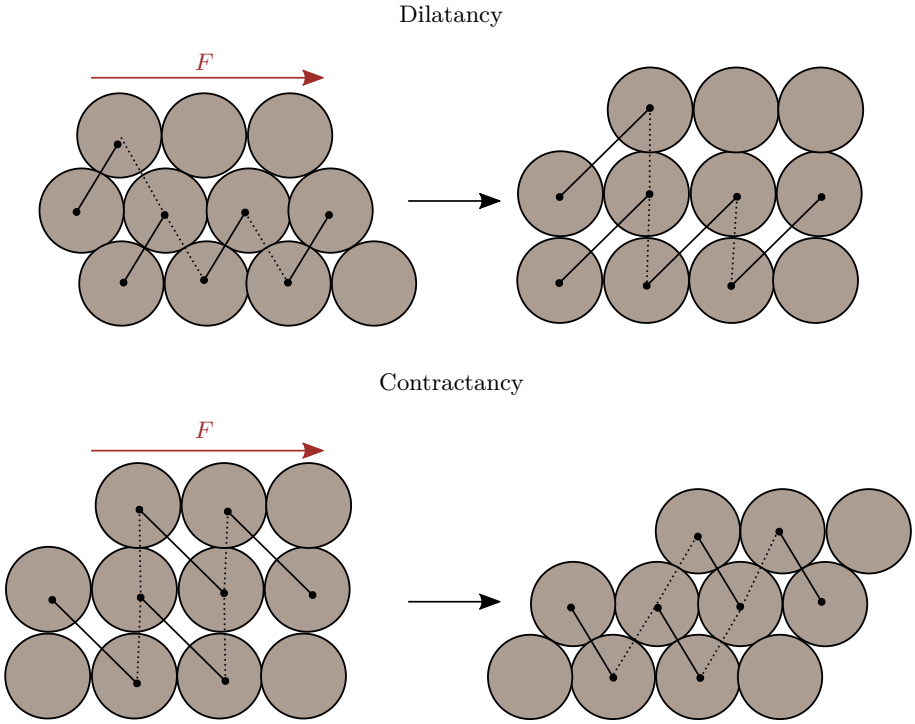


Figure 8.20: Rearrangement of particles in dense (top) and loose (bottom) state by applying a shear force F; solid line illustrates a change in distance; dotted line illustrates constant distance

environment suddenly move away from each other, a force is aiming to stick them together, and when they are approaching, this force represents a resistance from collision. Thus, the force is always acting against the movement of the particles. Hence, both liquefaction and breach failure can be computed with the same model. In the DEM framework, it can be understood as a new cohesion model. It adds a supplementary force which is active when the particle surfaces are close.
It is essential to understand how the fluid behaves at the particle-scale level during dilation and contraction of the saturated soil skeleton to derive the required relationship between the force resulting from excess pore water pressure and the movement of the particles. Therefore, the next sections give a brief introduction of the hydrodynamic forces acting on moving spheres.

Hydrodynamic forces on moving spheres

When particles depart from each other, negative excess pore water pressure occurs, and when they approach, positive excess pore water pressure builds up. The question is: What exactly causes this negative or respectively positive excess pore water pressure at particle-scale? When the particles start to move, fluid must flow and the fluid pressure distribution cannot be hydrostatic. Drag forces arise by the interaction between the fluid and the moving particle. The variation of the fluid velocity results in a variation of the fluid pressure. The void fraction changes determine fluid influx (dilatant behaviour of soil) or fluid efflux (contractant behaviour). In the macroscopic approach by Iverson (2005), the

drag force and thus the change of the fluid pressure is described by Darcy's law. It describes the excess pore pressure gradient that develops in reaction to the fluid inflow or outflow (Iverson, 2005). Darcy's law cannot be applied directly in DEM as it incorporates the macroscopic property K_f. Hence, the next section gives an introduction into the derivation of the drag force to visualise and clarify the evolution of the fluid pressure accompanied by particle rearrangements.

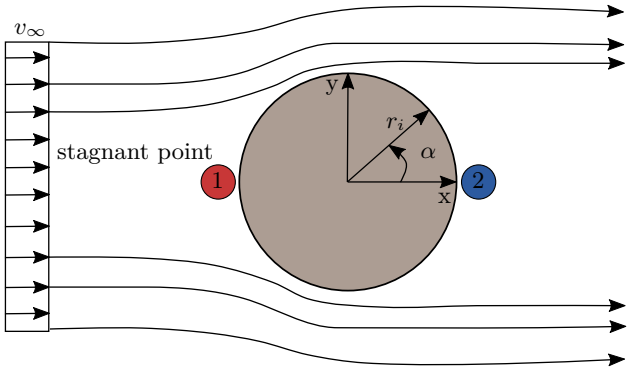


Figure 8.21: Flow field around sphere according to potential flow

Consider a single sphere i in a fluid. When the fluid now flows around this body, there are large velocity gradients perpendicular to its contour and direction of flow. A pressure difference at the frontside (1) and the backside (2) evolves, cf. Fig. 8.21. Using potential flow theory, the pressure at these two stagnation points can be determined (Surek and Stempin, 2007). Assuming that the flow velocity before and after the stagnation points corresponds to the inflow velocity v_∞, the resulting velocity on the circular contour can be determined:

$$v = 2v_\infty \sin\alpha. \tag{8.3}$$

The Bernoulli equation gives the pressure distribution on the surface of the sphere i under the assumption that the water level h is constant:

$$p_\infty + \frac{\rho_f}{2} v_\infty^2 = p + v^2 \tag{8.4}$$

The velocity v in the stagnant zone is zero so that the pressure difference results in $\Delta p = \rho_f / 2 v_\infty^2$. Multiplying the pressure with the area $A = \pi r_i^2$ of the sphere gives the resulting force arising from the pressure difference. Since in potential flow it is not important whether fluid flows around a stationary particle i or the particle i moves through stationary fluid, it follows that $v_\infty = v_i$. The resulting force on the sphere concludes to:

$$F_{\mathrm{D0}} = \Delta p \cdot A = \frac{\rho_f}{2} v_i^2 \pi r_i^2 \tag{8.5}$$

To account for the different flow regimes, F_{D0} is multiplied with the drag coefficient C_D, which leads to the well-established drag force laws for the flow around a single sphere. Fig. 8.22 illustrates the drag coefficient vs. the Particle Reynolds number.
The effects of dilatancy and contractancy on the fluid pressure are likely to occur in slow flow regimes. Thus, the Stokes regime applies. This leads to the following formulation of

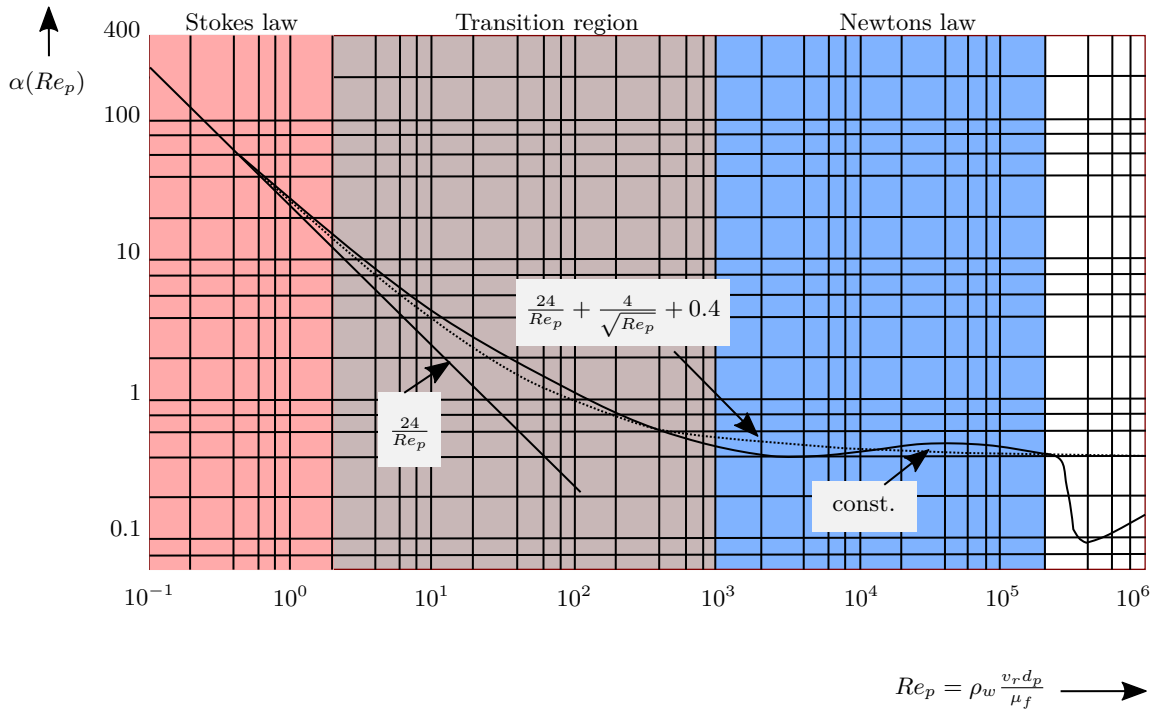


Figure 8.22: Drag coefficient vs. Particle Reynolds number of a sphere (Crowe et al., 2012)

the drag force on a sphere:

$$F_{\mathrm{D}} = 6\pi\mu_f r_i v_i \tag{8.6}$$

The effect of dilatancy on the shear resistance of a saturated soil structure is comparable to the behaviour of a shear-thickening fluid (STF). An STF is a fluid where the viscosity grows with increasing shear rate. This behaviour is caused by a thick suspension of particles in this fluid. If a shear rate is applied to these particles, they reorder as a response to the shear rate. If the applied shear rate is low, the particles have enough time to reorder. The repelling forces of the particles are higher than the hydrodynamic forces. If the shear rate is high, the repulsive forces between the particles are overwhelmed, and they stick together to form hydroclusters (Rapp, 2017). These are resulting from hydrodynamic lubrication forces between the particles. In the lubrication theory, a modification of the drag force F_{D} describes the forces acting on immersed particles close to contact.

Lubrication theory

Dry particle collisions generally describe the contact of particles in DEM. However, in an immersed system, kinetic energy dissipates at particle collision, which affects the post-collision particle trajectory in a non-linear way. If we consider two approaching immersed particles, at the moment they come close to each other, the thin layer between their surfaces will have a lubrication damping effect. As a result, the thin fluid layer between them is “squeezed”, and kinetic energy dissipates. This dissipation can lead to particle agglomerations if the resulting decrease of particle velocity is high enough. Tomac and Gutierrez (2014) accounted for this effect in a coupled CFD-DEM approach by introducing a new contact model based on the theoretical two-particle collision model by Davis and

Serayssol (1986). The model is based on a criterion that predicts whether two particles will stick together or rebound from each other. The normal lubrication force $F_{\mathrm{L},n}$ is derived by Davis and Serayssol (1986) with the assumption of Stokes flow:

$$F_{\mathrm{L},n} = \frac{6\pi\mu_f r_{ij}^2 v_r}{a} \tag{8.7}$$

where v_r is the relative velocity of the approaching particles, and a is the distance between the particle surfaces. The lubrication force is active at small distances. Therefore, the lubrication contact model is activated when:

$$x_{\min} < a < x_{\max} \tag{8.8}$$

where $x_{\min}$ is a lower and $x_{\max}$ the upper bound respectively.

Derivation of a new cohesion model

The lubrication force determines the resulting forces when two particles are close to contact. This is a mechanism that occurs in the framework of excess pore water pressures due to the rearrangement of the soil grains. Hence, the lubrication force model by Tomac and Gutierrez (2014) is used as a starting point to derive a new cohesion model. In the classic lubrication theory, only the presence of two particles is considered. Hence, any kind of confinement is neglected. Due to the close arrangement of particles in a soil, the pore space is narrow, which limits the fluid flow. The particles are located in a confined environment. Cardinaels and Stone (2015) investigated the influence of confinement on the lubrication force acting on two spheres. They found that confinement increased the normal lubrication force by a factor of ≈ 800. Thus, to account for the presence of other particles in close vicinity, the lubrication force is extended with $\frac{n_{\min}^{-\chi}}{1-n_{\min}}$ comparable to the drag force models presented in Sec. 7.2. $n_{\min}$ is the minimum void fraction of the investigated material. These extensions lead to:

$$F_{\mathrm{Lub,ext}} = 6\pi\mu_f r_{ij} v_r \frac{r_{ij}}{a} \frac{n_{\min}^{-\chi}}{1-n_{\min}} \tag{8.9}$$

Herein, only the normal part of the lubrication force is investigated. Kempe and Fröhlich (2012) showed that the effect of the tangential component of the lubrication force is negligible. Eqn. 8.5.1 presents the first cohesion model to be investigated (Type A).
A second type of cohesion model is investigated, which includes the same modifications as carried out for the lubrication force model, but applied to the Stokes drag force F_{D} (Type B). The second model concludes to:

$$F_{\mathrm{D,ext}} = 6\pi\mu_f r_{ij} v_r \frac{n_{\min}^{-\chi}}{1-n_{\min}} \tag{8.10}$$

Likewise, the influence of the distance between the particles is neglected.
Once the particles reach a certain distance from each other, it is assumed that the pore channels will be broad enough that the velocity gradients diminish and the increased force vanishes. Likewise, an upper limit of $4 \cdot r_{ij}$ is included in the model to ensure that the force will not take into account particles that are too far away from each other. Additionally, a maximum relative velocity of $v_r = 0.25\,\mathrm{m/s}$ is included to ensure numerical stability. The source code of the implemented model can be found in the appendix C.

8.6 Verification of the new cohesion models

For the verification of the cohesion models type A and B in DEM, a submerged very dense granular column collapse is investigated. In general, the failure process of a submerged very dense granular column can be subdivided into three stages (Kumar et al., 2017):

1. Initiation phase: Undrained conditions in the column body generate negative excess pore water pressures. As a result, the column is stable. Only a distinct failure surface is formed.

2. Runout phase: The initial vertical collapse motion is converted to a horizontal acceleration. The flow of granular material is fully mobilised. This behaviour is coupled with avalanching. Avalanching is a result of the interaction of the surrounding water with the surface of the granular mass. Vortices are created, which lead to small regions with different slope inclinations.

3. Settlement phase: A slope has evolved, and the movement stops. The slope is in an equilibrium state.

The experimental and numerical results will be compared. This allows an evaluation of the chosen approach to model the consequences of dilatancy and contractancy on the failure behaviour of submerged granular assemblies.

8.6.1 Experimental investigation

The model tests are performed by Plenker (2020). In this test, a submerged soil column of very dense Hamburger Sand fails rapidly due to the loss of support at one side. This is represented by a wall that is lifted at a velocity of $v = 0.5\,\mathrm{m/s}$. The different stages of failure are presented in Fig. 8.23.

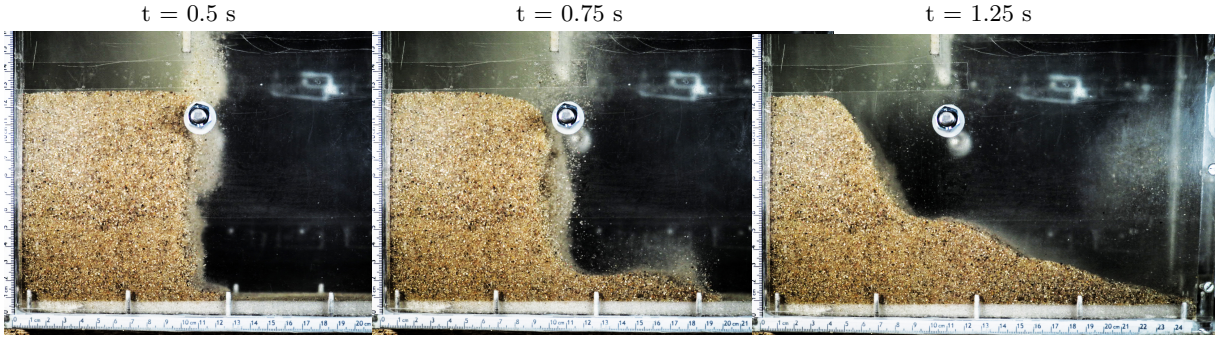


Figure 8.23: Failure of submerged sand column provided by Plenker (2020)

Fig. 8.23 shows the failure of the submerged granular column at different time steps. After 0.5 s, the first phase of a submerged granular column collapse is observable. The wall is completely lifted, and the column remains vertical. Some particles are lifted upwards due to the flow, which is induced by lifting the wall. At the bottom, the sand starts to flow out. After 0.75 s, more material flows out of the column at the bottom while the column

remains almost vertical. The runout distance of the mobilised material increases. This stage can be defined as the transition between the initiation and the runout phase. After 1.25 s, the runout phase is reached, and the column starts to fail and to form a slope. Thereby, the typical behaviour of a breach failure can be observed. The slope fails in slices, which results in three different slope angles. Thereby, the inclination of the slope becomes steeper with increasing distance to the failure front. The settlement phase is not reached within this time frame.

8.6.2 Numerical setup

The numerical simulation of the submerged granular column collapse is carried out first without an extension to model dilatancy-effects and then with the newly developed cohesion models. The results are compared with the experimental results.

Geometry and initial conditions

The geometry of the numerical setup is considered the same dimensions as in the experimental setup. The particle parameters and distribution are chosen consistent with the calibrated material for Hamburger Sand, cf. Tab. 5.3. The investigated void fraction is $n = 0.35$. The material height is 13 cm, and it has a length of 9 cm. The particles are initialised in a pure DEM computation. This reduces computational costs significantly. The packing density is chosen following the experimental setup. The very dense state of the particles is reached by reducing the rolling friction coefficient μ_r and the friction coefficient μ during the initialisation of the particles. No gravitation acts during the initialisation to prevent the particles from clogging. When the initialisation is finished, and all particles have the desired radius, the gravitation is activated. The material starts to settle. The final particle arrangement is reached when the kinetic energy is below a level of 5×10^{-7} J. Since a smaller time step is required in the DEM calculation with stiffening particles, the numerical simulations are performed with $E = 1 \times 10^7\,\mathrm{N/m^2}$. The lifted wall is represented by a group of particles, which are lifted according to the experimental test with $v = 0.5\,\mathrm{m/s}$. This technique ensures to model the induced fluid flow by lifting the wall. These wall-particles are assigned to properties of acrylic glass. The mesh size in the presented numerical simulations is 0.001 m × 0.01 m × 0.005 m in x-,y- and z-dimension. The occurring vortices near the lifted wall require a fine discretisation. Preliminary tests showed that this discretisation leads to stable results. A standard $k - \varepsilon$ turbulence model is used. The simulated fluid has the properties of water at a temperature of 20 °C. Its density is $\rho = 1000\,\mathrm{kg/m^3}$ and the kinematic viscosity is $\nu_f = 1.004 \times 10^{-6}\,\mathrm{m^2/s}$.

Boundary conditions

At the inlet and outlet, a no-slip condition is in place, while for the top patch a total pressure boundary condition is used in combination with zero-gradient for the velocity. The numerical simulation is a pseudo two-dimensional simulation. The y-dimension is thus discretised with one CFD cell with a boundary condition of type empty (*OpenFoam documentation, Boundary conditions* 2020). A periodical boundary is applied in the y-direction in the DEM solver. For an accurate computation of the interaction forces of

the particles, by experience, one requires a thickness of approximately ten particles in the y-direction. For a polydisperse particle distribution like Hamburger Sand, the mean diameter can be taken for dimensioning the constant width of the y-dimension. The mean diameter is d_{50} =0.75 mm. The particle wall represents the lifted acrylic wall. The friction μ and rolling friction μ_r between the particles and the acrylic glass wall is reduced to $\mu_{\text{p-w}} = 0.05$ and $\mu_{r,\text{p-w}} = 0.001$.

Coupled simulation with unresolved CFD-DEM

The simulated time is 5 s. The coupling interval between the DEM- and the CFD-solver is set to 100. The DEM time step is t_{DEM} =1 × 10^{-5} s and the CFD time step is t_{CFD} =1 × 10^{-3} s. Consistent with the investigations on the numerical modelling of suction dredging, the drag force model of Koch and Hill (2001) is used.

8.6.3 Numerical results without the new cohesion model

In Fig. 8.24, the results of the numerical simulation without an extension to model the dilatancy-induced enhanced stability of the material is depicted. Different time steps are shown. The results show that the column collapses faster compared to the experimental results. In contrast to the failure stage in the model test after 0.5 s the column has already collapsed, and the flow of the particle mass is fully mobilised. The first phase of the failure process of a submerged granular column collapse is not observed. After 0.5 s, the failure process is already in the second phase, the runout phase. The runout distance of the mobilised particle mass is significantly higher compared to the model test. At the same time, the inclination of the mobilised zone is flatter in comparison to the model test. The same applies to the results after 0.75 s. Most of the material is mobilised, and a slope is developing. Avalanching processes are taking place at the slope toe. The inclination of the failing column continues to flatten. At 1.25 s, the granular column has reached the settlement phase. The slope is fully evolved and stable. This is in strong contrast to the results from the model tests, where the column is still in the runout phase.

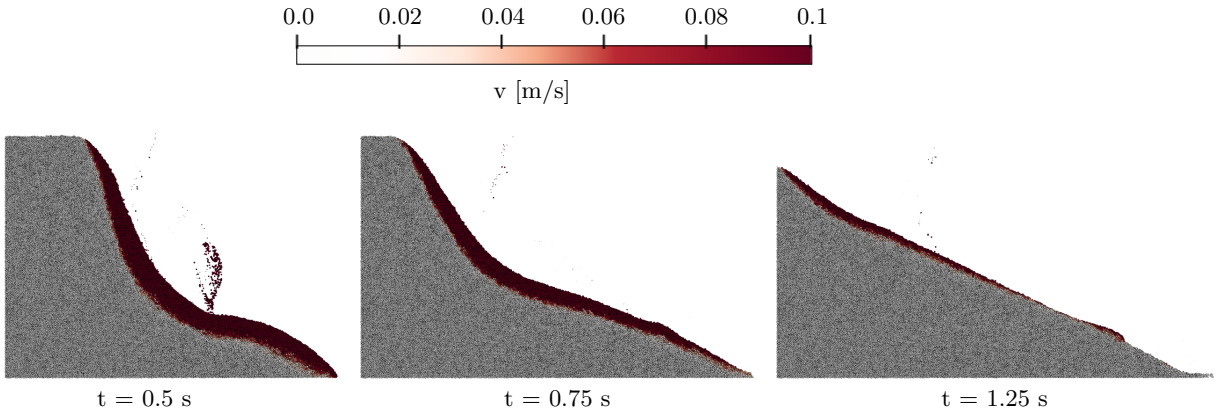


Figure 8.24: Numerical results of submerged granular column collapse of very dense Hamburger Sand without an extension to model the dilatancy-induced enhanced stability

The wall consists of particles, which can lead to an overestimation of the interaction with the particles using a cohesion model. This affects the failure mechanism of the column. Likewise, to exclude this effect, a simplified model is used. The setup remains identical except that the wall is instantly removed to introduce the failure of the column. Fig. 8.25 shows the results of the column collapse with the simplification of a removed wall. The change in the failure mechanism is negligible. The results are very similar to the results with a wall. After 0.5 s, the column is already in the runout phase. A part of the column is still stable, but the slope angle is slightly flatter than in the numerical model with the wall. Also, the runout distance is a little larger. After 0.75 s, the results with and without wall have the same tendency: A large part of the column has failed, and a slope evolves. Avalanching processes are observable at the slope toe. After 1.25 s, the slope is in its final state.
In general, the agreement with the numerical model with and without a wall is very high. Therefore, further investigations with the simplified model are performed without the simulation of the lifted wall.

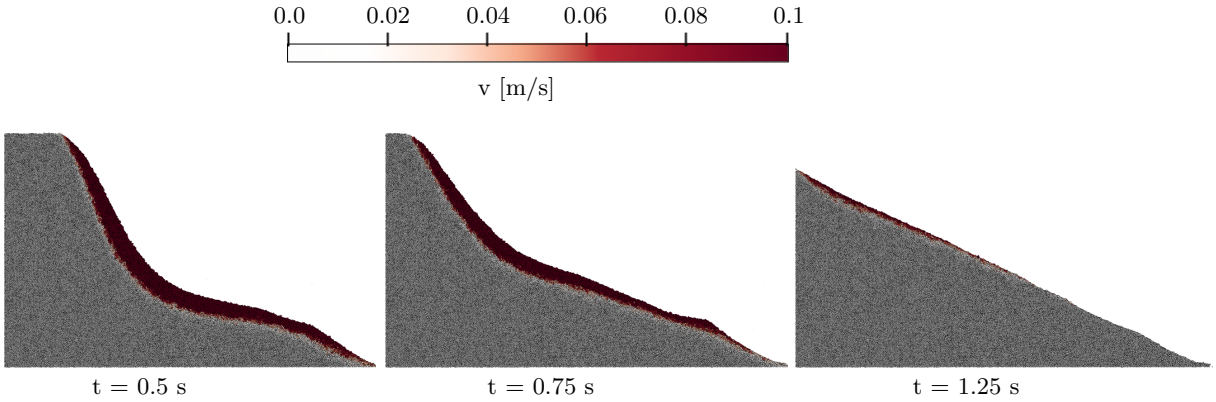


Figure 8.25: Numerical results of submerged granular column collapse of very dense Hamburger Sand with simplification of instantly removed wall

8.6.4 Numerical results with the new cohesion model

The following sections present the numerical investigations with the new cohesion model. Cohesion model type A and type B are first investigated and varied to analyse the influence of the different extensions. Only the first 0.4 s of failure are modelled to reduce computational costs. Then, the most suited model is chosen to model the total collapse of a submerged granular collapse.

Numerical study on the influence of cohesion model type A and B

The modifications of the lubrication force model (cohesion model type A) and the modification of the Stokes drag force (cohesion model type B) are analysed using the test setup of a column collapse. Additionnaly, the impact of the lubrication force model by Tomac and Gutierrez (2014) and of the Stokes drag force on the failure mechanism is investigated. The numerical model configuration is identical to the original model. The minimum void

fraction of the investigated material is $n_{\min} = 0.35$. Fig. 8.26 presents the results of the column collapse after 0.4 s with the different extensions of the lubrication force model.

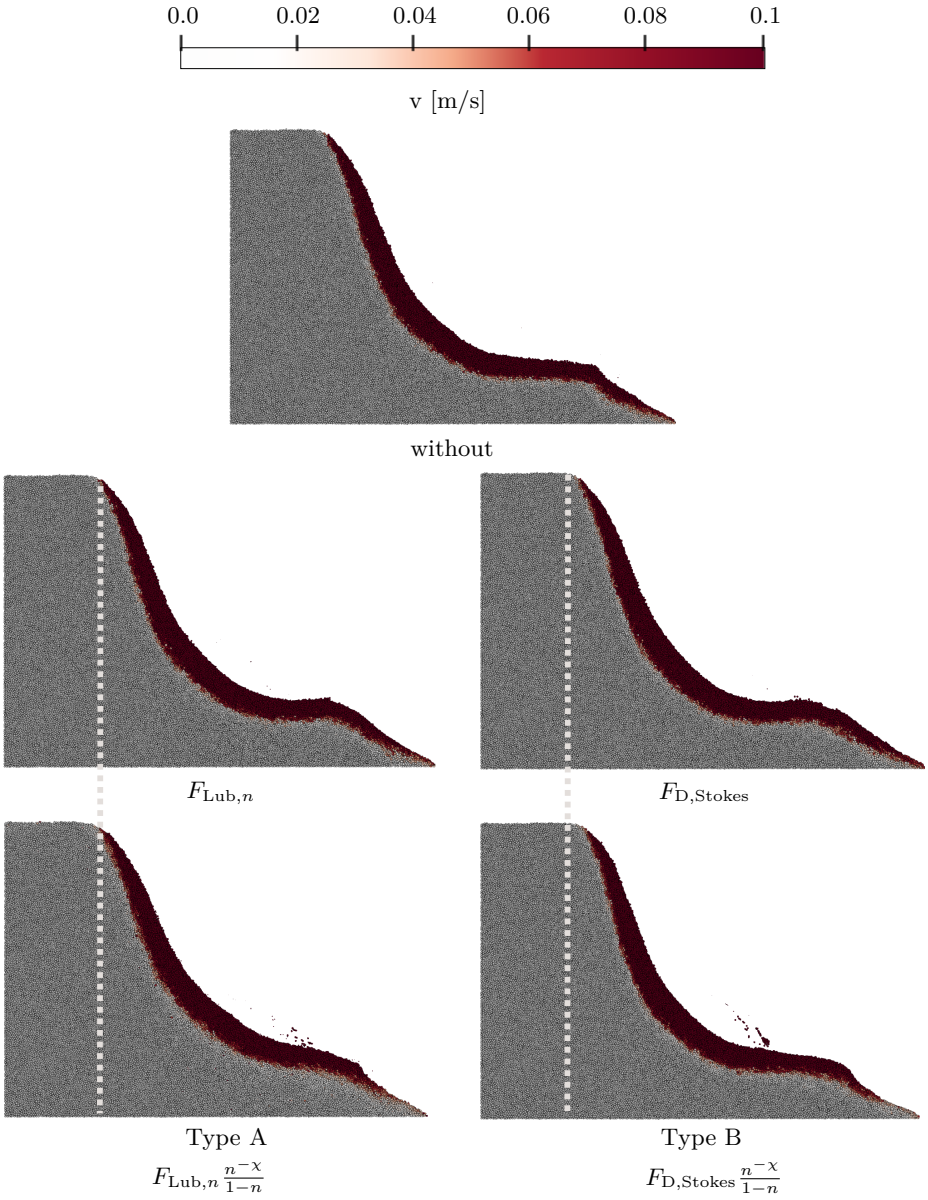


Figure 8.26: Numerical model of the submerged granular column collapse with the lubrication model (Tomac and Gutierrez, 2014), the Stokes drag model, cohesion model type A and cohesion model type B - failure stage after 0.4 s

Fig. 8.26 reveals that the lubrication model by Tomac and Gutierrez (2014) does not change the failure mechanism of the submerged granular column significantly. Only the runout distance decreases slightly. A further decrease of the runout distance is observed while the avalanching of the material behaviour is increased using the type A cohesion model. Compared to the results with the lubrication model, less material is mobilised. However, overall, no significant impact of the type A cohesion model on the failure mechanism is

observable. Comparing the impact of the Stokes drag force with the results without a cohesion model, the change of the failure mechanism is minor. Nevertheless, the extension of the Stokes model (cohesion model type B), leads to a significant decrease in the runout distance while at the same time, less material is mobilised. The top surface of the column is wider compared to the Stokes model. This is a good indicator for further development of the model as enhanced stability can be concluded from these results. The enlargement of the top surface of the granular column is not observed using the type A cohesion model. Thus, the following investigations focus on the effect of χ in the type B cohesion model on the failure mechanism.

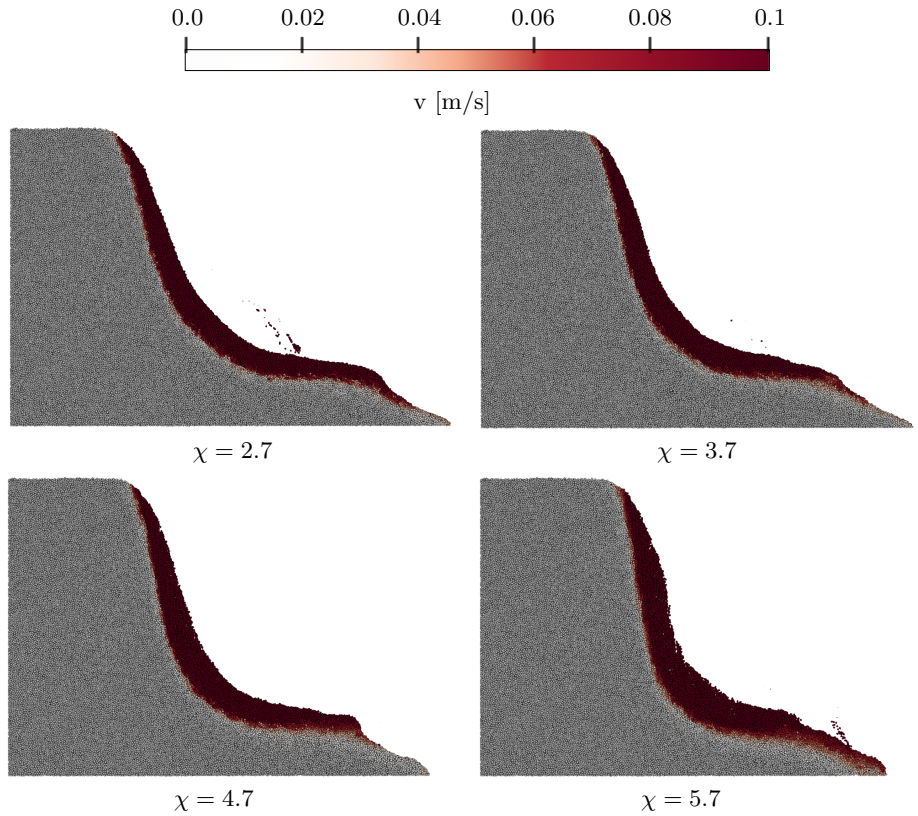


Figure 8.27: Variation of the exponent χ in the cohesion model type B - failure stage after 0.4 s

Fig. 8.27 depicts the results of the submerged granular column collapse using the type B cohesion model with increasing values for χ. The increase of χ leads to a visible enhancement of the column. The undisturbed part of the top of the column increases with increasing χ. At the same time, the inclination of the mobilised material steepens by increasing χ. Furthermore, avalanching at the slope toe gets more significant. At $\chi = 5.7$ also a tendency towards liquefaction failure at the surface of the mobilised zone is observable. The inclination of the failure line is $\approx 90°$, which is consistent with the results of the model test. In general, $\chi = 5.7$ represents the best fit in comparison to the experimental results and is further used for verification purposes.

Numerical results of submerged granular column collapse with new cohesion model

Fig. 8.28 depicts different failure stages of the submerged granular column collapse modelled with the cohesion model type B and $\chi = 5.7$. After 0.5 s, the failure line of the mobilised mass is steep and inclines of $\approx 90°$ consistent with the experimental results. However, the runout distance is significantly higher compared to the runout distance in the model test. After 0.75 s, the runout phase has progressed. Similar to the results without a cohesion model, only the upper part of the column is still stable. Avalanching is observable at the slope toe. This behaviour is in strong contrast to the experimental results, where the column is still in in the initiation phase. In comparison to the numerical results without a cohesion model, the downward part of the slope is already motionless while the runout distance is significantly lower. After 1.25 s, the failure process has finished the settlement phase. The slope inclination is steeper compared to the numerical results without a cohesion model. However, in comparison to the results from the model tests, there is no agreement.

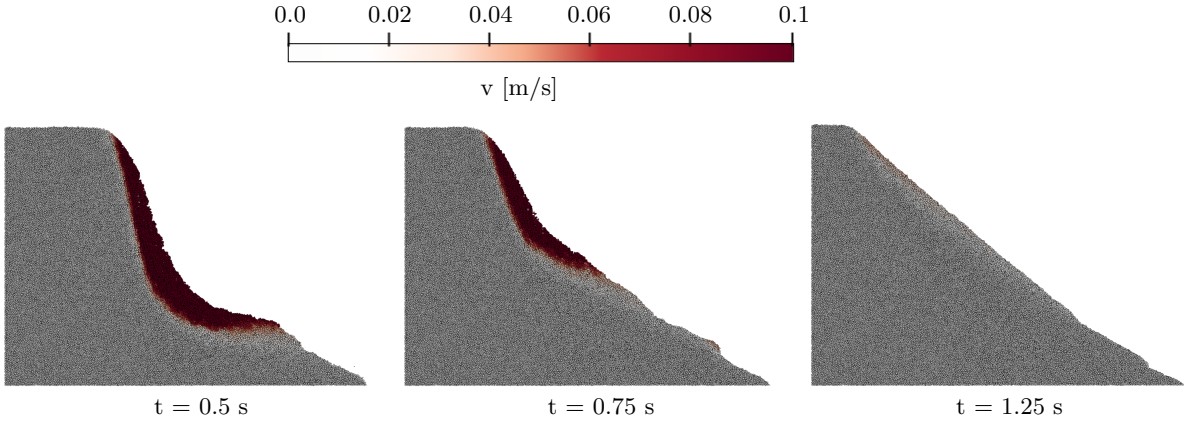


Figure 8.28: Numerical results of submerged granular column collapse with cohesion model type B and $\chi = 5.7$

In summary, the early state of the column with the increased strength due to dilatancy-effects is well represented by the developed cohesion model. Concerning the further course of failure of the submerged column, strong deviations are observable. The increased strength of the soil matrix cannot be maintained over the same period as in the model test. However, since the early state is well in agreement, the developed cohesion model type B is used in the following for the numerical simulation of the very dense submarine slope. Although the numerical modelling of the complete failure of the collapse of the submerged column with the developed cohesion model does not succeed, the aim is to check whether this model can be considered as a starting point for the numerical modelling of breach failure.

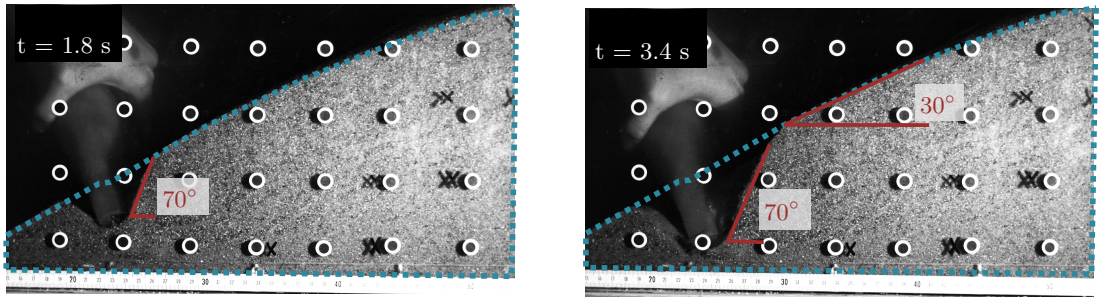
Submarine slope failure with cohesion model

Fig. 8.29 depicts the failure behaviour of the very dense submarine slope in the experiments (a), with the developed cohesion model (b) and without the cohesion model (c). It can be identified that the cohesion model alters the failure mechanism at the beginning of the suction dredging. After 1.8 s, the influence of enhanced resistance is significant. The slope inclination in the vicinity of the disturbance increases by 7° compared to the results

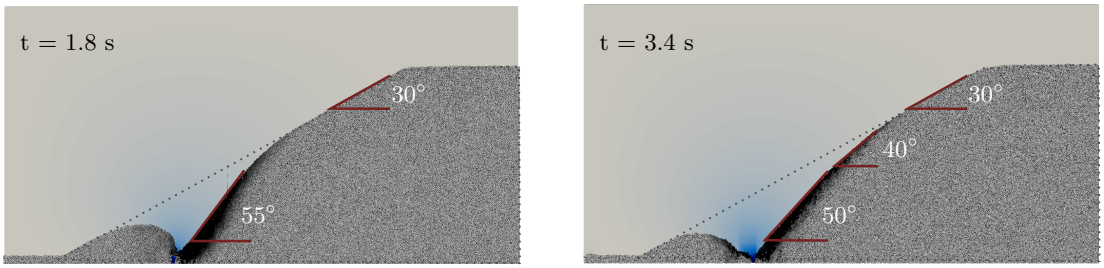
without the cohesion model. Additionally, only a third of the slope is affected by the disturbance of the suction dredging, which agrees with the results of the small-scale model tests. The curvature of the slope surface is more pronounced, resulting in a comparable behaviour observed in the small-scale model tests. After 3.4 s, the surface of the failing slope masses is less straight in comparison to the results without the cohesion model. Nevertheless, comparable to the results of the submerged column collapse, the influence of the cohesion model on the failure mechanism vanishes. The differences in the slope inclinations between the results with and without the cohesion model decrease significantly, and the failure behaviour is comparable. In summary, the failure of the submerged column and the submarine slope show the same tendency: At the beginning of the failure, the influence of the developed cohesion model is significant, but it vanishes with progressing time.

8.6.5 Concluding remarks on the developed cohesion model

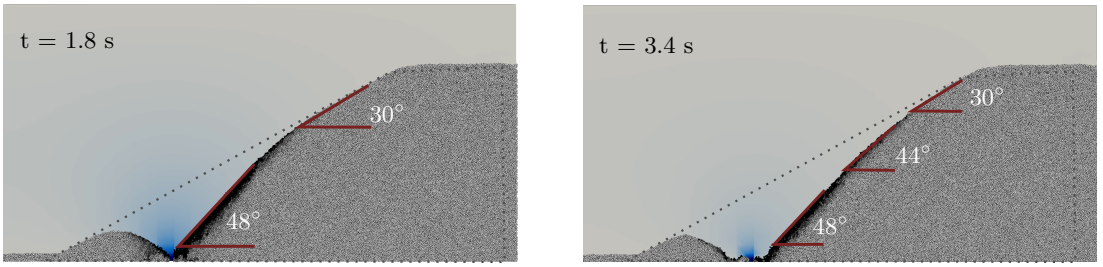
This section presented an approach to model the resulting force due to the change of the fluid pressure field in a dilatant and contractant saturated soil skeleton based on a cohesion model in the framework of DEM. As a starting point, the lubrication force model by Tomac and Gutierrez (2014) was chosen as the literature review indicated that the lubrication force is the predominant force occurring between submerged rearranging particles. This model was extended by a void fraction term to include the effects of confinement of the particles. The confinement results in an enhanced force and more complex fluid flow. Therefore, different variations of this term were investigated and verified with a submerged granular column collapse test. An extension of the lubrication force (type A), as well as an extension of the Stokes drag force (type B), was analysed. A minimum void fraction $n_{\min}$ was implemented and its effect varied by a parameter χ in the form of $n_{\min}^{-\chi}$. The comparison with a respective model test performed by Plenker (2020) revealed that a variation of the lubrication force does not lead to a suitable result. Thus, further investigations were performed with the type B model. The parameter χ was increased until the numerical results matched qualitatively with the model tests. The results showed a good agreement at the beginning of the failure for $\chi = 5.7$, but with progressing time, the response deviated from the results of the model test. The same applies for the numerical modelling of a very dense submarine slope failure. It needs to be emphasised that the developed cohesion model could only be calibrated empirically and by qualitative comparison. A better approximation of the acting force on suspended and rearranging particles in this confined regime is thus required. To the author's knowledge, there is no quantitative measurement of this force available. These quantitative measurements are necessary to model the shear-dilatancy effect on the fluid pressure accurately. This could be achieved by utilising a particle sensor that directly measures the pressure acting on the particle surface. In this way, both short-range and long-range forces acting on the particle can be analysed. Furthermore, implementing the coordination number, i. e. the number of particle contacts, could serve to reflect the degree of confinement. However, the presented investigations showed that modelling the shear-dilatancy effect on the fluid by means of a cohesion model in DEM is a promising approach. These analyses can serve as a starting point for further investigations by taking into account the proposed measures.



(a) Failure of very dense slope



(b) Dense sand with cohesion model



(c) Dense sand without cohesion model

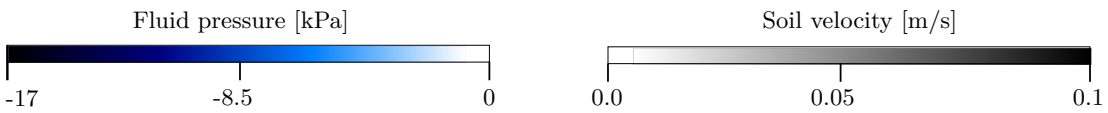


Figure 8.29: Experimental result of the failure of a very dense slope after 1.8 s and 3.4 s (a) and respective numerical simulation with cohesion model type B and $\chi = 5.7$ (b) and without cohesion model (c)

9 Extraction resistance of embedded objects

Floating offshore structures experience a growing interest as their application possibility is flexible regarding water depth and geographical location (Statoil ASA, 2018). Different types of anchors can be used to moor the structure within the marine seabed. Detailed knowledge about the resistance of these anchors is crucial. On the one hand, hydrodynamic loads, like waves, tidal currents i. a., lead to a complex loading state of the offshore system during its lifetime and on the other hand, the anchors have to be removed from the seabed at the end of their lifetime. Investigations of the extraction resistance of the anchors embedded in the saturated marine soil are necessary in order to evaluate its dependency on different factors, like the embedding depth, the soil properties and the extraction velocity. The following sections present the analysis of the extraction resistance of an embedded plate in saturated soil. These investigations are partly published in Kanitz et al. (2019).

9.1 Introduction

The extraction resistance of structures embedded in saturated soil depends on different factors, like the embedding depth, the soil properties and the extraction velocity. Several investigations on the mechanisms acting during the extraction of embedded objects in saturated soil have already been performed. First studies were carried out by Muga (1967) in laboratory tests and field experiments at the US Naval Civil Engineering Laboratory. Muga (1967) investigated objects with different shapes embedded in San Francisco Bay mud and proposed empirical equations enabling calculations of the extraction resistance causing an immediate breakout. Vesic (1969) elaborated analytical relations for the extraction resistance depending on the pore water pressure, the shear surfaces and the embedding depth. A schematic representation of the assumptions proposed by Vesic (1969) is shown in Fig. 9.1. Once the plate lifts, suction pressure develops underneath the plate as a reaction to the plate motion. Additionally, Vesic (1969) assumed that the extraction of a plate from a relatively low embedding depth in dense sand causes a convex toric shear surface, cf. Fig. 9.1 case (a). In loose sand, the shear surface would be vertical, cf. Fig. 9.1 case (b). The shear surfaces determine the zone in the soil, which is acting on the extracted plate. Thus, in the case of dense sand, the extraction resistance increases as the sand volume acting on the plate is greater. Murray and Geddes (1987) investigated the relation of the embedding depth on the load-displacement response in a cohesionless soil for the vertical extraction of an anchor plate. Assuming a vertical shear surface, Murray and Geddes (1987) developed an analytical solution to determine the extraction resistance of rectangular plates. This approach takes the overburden pressure, the vertical component of the shear

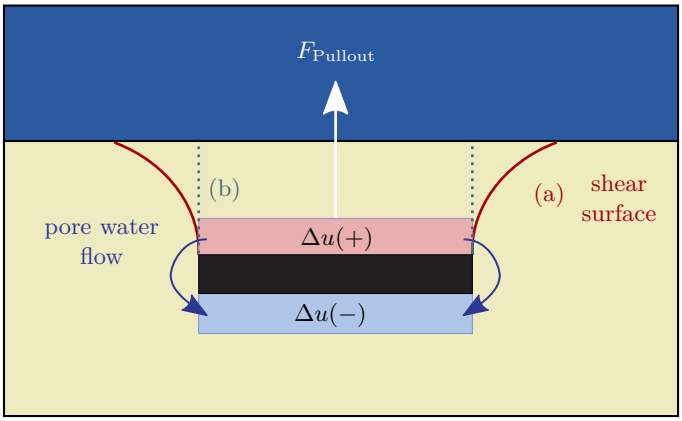


Figure 9.1: Failure mechanism of an object embedded in saturated sand with (a) shear surface formation in dense sand and (b) shear surface formation in loose packed sand (Kanitz et al., 2019)

resistance and the weight of the soil in the shear wedge into account. Nevertheless, the analytical solutions only slightly match the laboratory tests. H. J. Lee (1973) pointed out that a rapidly increased force causes undrained conditions in soil, which result in suction pressure providing significant extraction resistance. Hence, the presence of undrained conditions is dependent on the extraction velocity v. Finnie and Randolph (1994) showed that undrained conditions can be described with a non-dimensional loading rate $\dot{v}$:

$$\dot{v} = \frac{vd}{c_v} \begin{cases} < 0.1 & \text{drained condition} \\ > 30 & \text{undrained condition} \end{cases} . \tag{9.1}$$

d describes the dimension of the embedded object and $c_v = K_f E_s / \gamma_w$ the consolidation coefficient. It is determined with the permeability coefficient K_f, the stiffness modulus E_s and the specific weight of water γ_w. Lehane et al. (2008) performed centrifuge tests with shallow square footings founded in clay and sand. The tests showed that the suction effect due to negative excess pore water pressure increases with the extraction velocity. This indicates a notable rate-dependency for the extraction of footings founded on clay. A rate-dependency could not be observed for footings on sand. However, Lehane et al. (2008) only investigated loose sand.

9.2 Experimental setup

For the validation of the numerical model with unresolved coupled CFD-DEM, experimental tests of an embedded anchor plate in dense sand are carried out. The plate is lifted vertically with an actuator. The extraction resistance, the evolution of pore water pressure at the bottom of the plate and in the soil body, and the shear band formation in the soil are monitored. A sketch of the experimental setup is shown in Fig. 9.2.
The extraction resistance is measured by a load cell installed at the actuator, which lifts the plate. In order to measure the suction pressure created by the upward movement, four total pressure transducer are installed. The pressure transducer are located outside

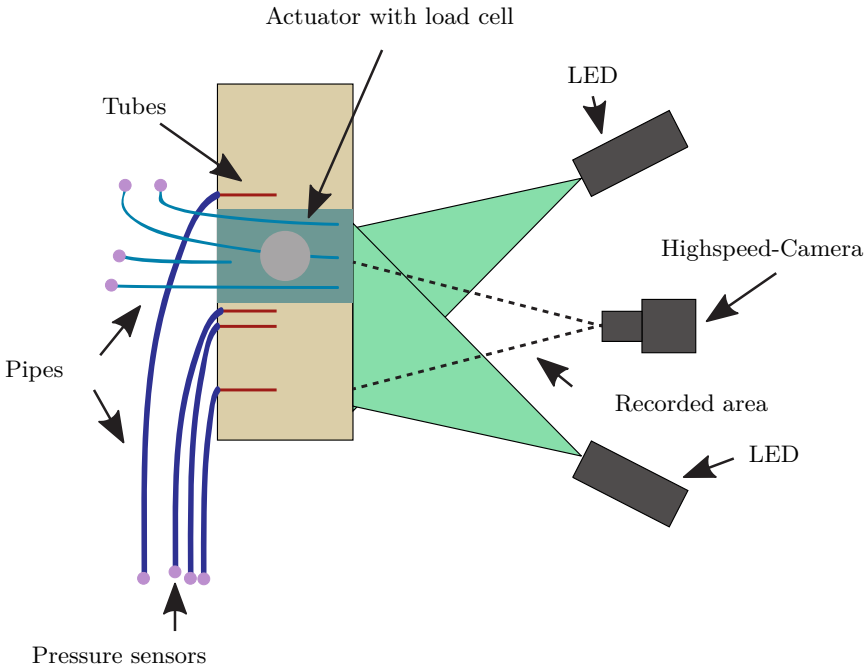


Figure 9.2: Sketch of the experimental setup for the investigation of the extraction of a plate (Kanitz et al., 2019)

of the acrylic glass container (cf. Fig. 9.2). The transducers are connected to thin tubes, which end at the bottom of the plate to measure the pressure underneath it. The tubes are attached to the plate to prevent exceeding movement or distortion of the tubes during the experiment. For this reason, the extracted plate consists of two plates, which are connected by steel rods, cf. Fig. 9.3 (a). The anchor plate is attached to the actuator via a screw connection. Fig. 9.3 (b) depicts the location of the measurement locations.
The pore water pressure changes in the soil body are measured at eight different locations shown in Fig. 9.4 with total pressure transducer by Keller. This enables the investigation of the drainage regime in the sand bed. As for the pressure measurements at the bottom of the plate, the pressure transducers are not located in the acrylic glass container to minimise disturbances in the sand bed. As in the investigations on suction dredging, the Keller pressure transducers are connected to thin pipes with flexible tubes. These tubes reach into the centre of the soil body. The pore pressure changes are measured in the middle of the soil body, as indicated in Fig. 9.2. In this way, the pore pressure can be measured without boundary effects of the walls while minimising their influence on the soil body.
The displacement of the soil body is captured with a high-speed camera. The recorded area reaches from the middle of the extracted plate towards the right until the point of no movement in the sand bed, cf. Fig. 9.2. The whole setup is not recorded with the camera for the sake of a proper pixel resolution while recording at a frame rate of 250 fps. The area of interest consists of the sand bed directly next to the extracted plate to identify the evolution of the shear band.
Two green light LEDs are placed in front of the acrylic glass container with an angle of approximately 45° to reduce reflections on the front. The back front is made of a dull black PVC to avoid reflections and disturbance due to incoming light from the back.

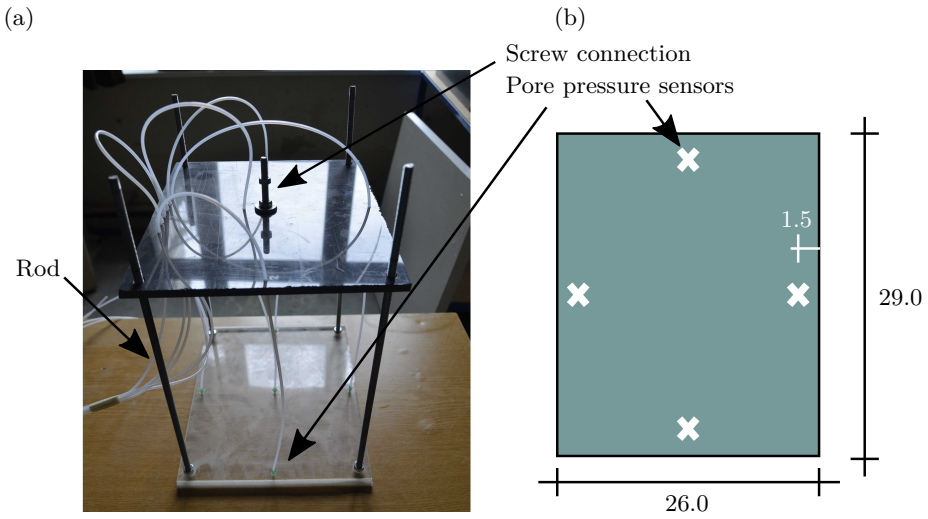


Figure 9.3: Extracted plate - 1 g model of extracted plate (a) and location of pore water pressure transducer (b) (Kanitz et al., 2019)

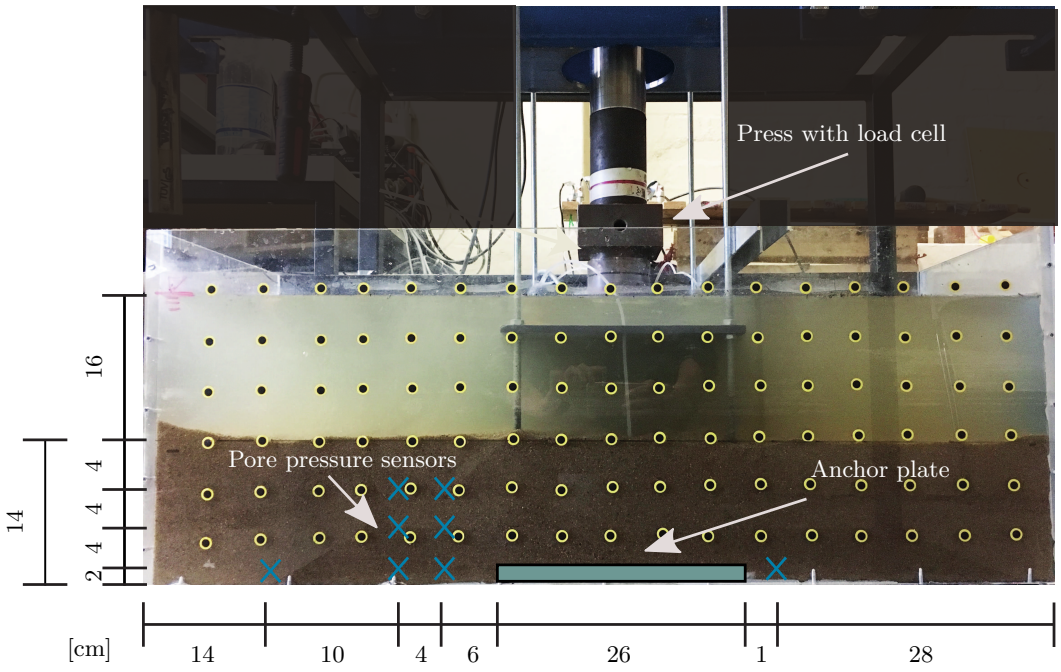


Figure 9.4: 1 g model of the extraction of a plate embedded in saturated soil (Kanitz et al., 2019)

The model tests are carried out with dense Hamburger Sand. In order to obtain a constant packing density, the sand is poured in layers of 5 kg each into the water-filled glass container. Each layer is compacted with vibrations to obtain a dense packing. In this way, the sand bed reaches a void fraction of $n = 0.35$. This is equivalent to a relative density of $I_D = 0.965$ (very dense).

Two different extraction velocities are investigated, $v_\mathrm{f} = 300\,\mathrm{mm/min}$ (*f: fast*) and $v_\mathrm{s} = 100\,\mathrm{mm/min}$ (*s: slow*). v_f is the maximum pull velocity of the actuator. The extracted plate is installed directly on the bottom of the glass container in order to investigate the highest extraction resistance that could occur in the seabed. This setup represents the most sensible case with regards to the numerical method as the changes in the pore pressure are abrupt and high, which could be a possible source of instabilities. If the numerical model can compute the sharp pore pressure changes, different embedding situations, e. g. installed on a layer of sand, can be modelled as well. In terms of repeatability of the model tests, this situation is also preferable as variations in packing density of the underlying sand are avoided.

9.3 Numerical setup

9.3.1 Geometry and initial conditions

The numerical model has the same dimensions as the experimental setup. A coarse-graining factor of 2 is used to reduce computational costs (Bierwisch et al., 2009). The numerical setup is depicted in Fig. 9.5. A mesh refinement towards the lower boundary is required to increase the accuracy and stability of the computation of the fluid field. To further expedite the computation, the creation of the particle bed is considered as a pure DEM calculation. The coupled simulation is started when the particle bed has relaxed, and no effects of the particle creation are transferred to the following simulation of the lifted anchor plate.

9.3.2 Boundary conditions

A pseudo two-dimensional simulation is carried out. Consequently, the CFD mesh has a depth of one cell and the particle domain has a depth of approximately ten particle diameters. The walls are considered periodic. At the bottom and the side walls (called inlet and outlet), a no-slip boundary condition is in place. For the top patch, a total pressure boundary condition is used in combination with a zero-gradient condition for the velocity. Due to the pseudo two-dimensional manner of the case setup, the front and back walls are of type empty. These are standard OpenFOAM® boundary conditions. Additional information can be found in *OpenFoam documentation, Boundary conditions* (2020). On the DEM side, the bottom, as well as the sidewalls, consist of rigid walls while the front and back walls are of type periodic. The anchor plate is inserted before the generation of the particle bed in order to avoid artificial, critical overlaps with the generated particles.

9.3.3 Coupled simulation with CFD-DEM

The solver used in the coupled simulation is the *cfdemSolverPiso*. When using *cfdemSolverPiso*, the plate is only included in DEM but not in the CFD computation. As discussed in Sec. 9.4, the missing representation of the plate on the CFD side leads to a significant under-estimation of the pressure drop. Hence, a new solver *cfdemSolverPisoIBm* was developed, which allows for the immersed boundary (IB) representation of the plate (cf. Sec. 4.5). The case setup remains the same. The only difference is that the plate is represented as a body with a finite thickness. A coupling interval of 100 is chosen. The DEM time step is $t_{\mathrm{DEM}} = 1 \times 10^{-6}\,\mathrm{s}$ and consequently the CFD time step is $t_{\mathrm{CFD}} = 1 \times 10^{-4}\,\mathrm{s}$. The drag force between the particles and the fluid is computed with the model of Koch and Hill (2001).

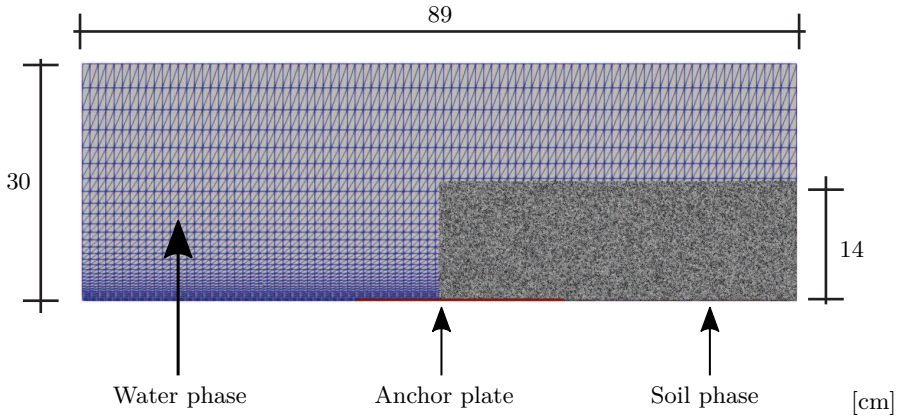


Figure 9.5: Numerical model of the extraction of an anchor plate embedded in saturated sand (Kanitz et al., 2019); the soil body is cut in half to visualize the mesh refinement

The plate is lifted at the same velocities as in the experiments ($v_{\mathrm{f}} = 300\,\mathrm{mm/min}$ and $v_{\mathrm{s}} = 100\,\mathrm{mm/min}$).

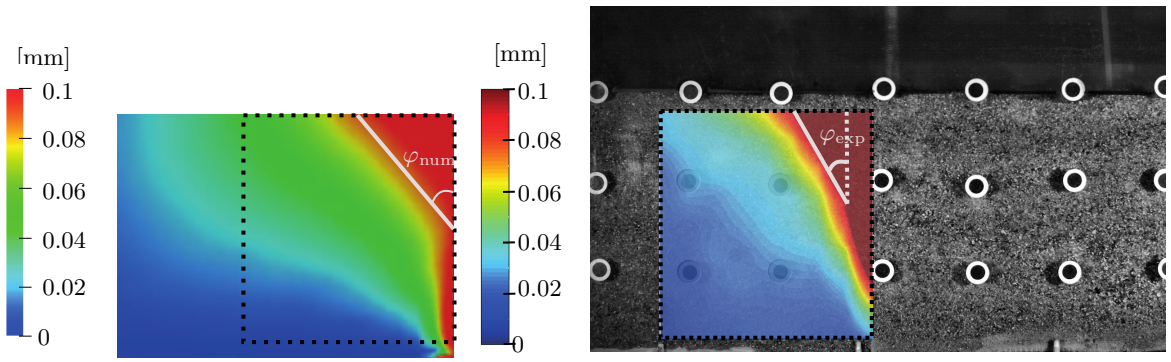
9.4 Results

This section presents the results obtained from the experimental and numerical analyses. The results are compared to quantify to what extent unresolved coupled CFD-DEM is capable of depicting the governing physical processes that occur during the extraction of a plate.

9.4.1 Shear band evolution

Fig. 9.6 shows the displacement of the soil particles after 0.25 s obtained from the numerical model (a) and the experimental results evaluated with GeoPIV-RG (b). The dashed line in the numerical results shows the location of the PIV picture. The analysis shows that the uplift of the plate results in an inclined shear surface both in the experiments and

numerical simulations. This agrees with the theoretical assumptions of Vesic (1969) for dense sand. The shape of the shear band is independent of the extraction velocity, as discussed in Kanitz and Grabe (2018a). The inclination of the numerically modelled shear surface is $\varphi_{\text{num}} = 38°$. The inclination of the shear surface in the experiment is $\varphi_{\text{exp}} = 37°$. Hence, the experimental and numerical results agree. Additionally, the shape of the soil's displacement fields in the experiment and the simulation shows a comparable response to the extraction. Fig. 9.6 shows that directly above the plate, the soil bed motion is steeper. The displacement then starts to spread from approximately the middle of the soil bed. This behaviour is more pronounced in the numerical simulation. The shear surface defines the failure line in the sand bed where the shear resistance is exceeded. Inside this zone, the sand is stable. The particle contact forces are greater than the gravitational forces. Fig. 9.6 (b) shows that this zone does not have a distinct boundary, but vanishes with increasing distance to the extracted plate. The soil does not start to flow downwards at this stage and is static.



(a) Displacement in numerical result

(b) Displacement in experimental result

Figure 9.6: Shear band evolution in the (a) numerical and (b) experimental setup after 0.25 s (Kanitz et al., 2019)

9.4.2 Pore water pressure evolution

The experimental results for the measured pore water pressure evolution in the surrounding soil body for an extraction velocity of 300 mm/min and 100 mm/min are presented in Fig. 9.7.
The measurements show an undrained response of the sand caused by the extraction. The process can be divided into three different phases. Fig. 9.8 shows the evaluation of the sand movement with PIVLab during extraction in these three phases. By considering these results, it is explained what happens during these phases:

- Phase I: The upward motion of the plate starts, a shear band is formed. The pore water seeps out from the soil towards the void that is created underneath the plate. As a result, negative excess pore water pressure occurs and undrained behaviour is observed.

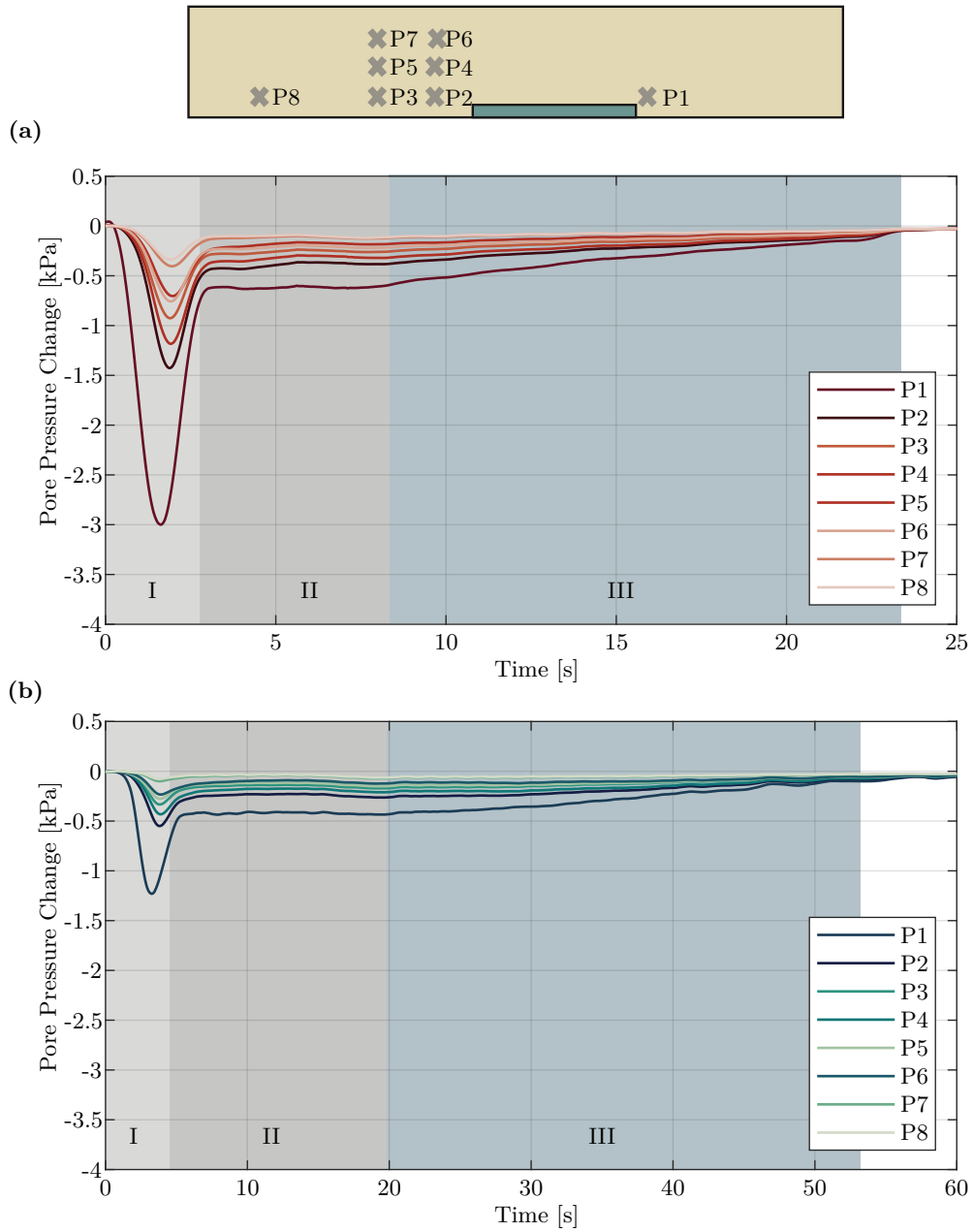


Figure 9.7: Measured pore water pressure evolution at an extraction velocity of (a) 300 mm/min and (b) 100 mm/min (Kanitz et al., 2019)

- Phase II: The pressures reach a plateau. The suction pressure at the bottom of the plate and in the sand bed is in equilibrium. Fig. 9.8 shows that the soil flow is restricted to the edge of the plate. It only expands, reaching the end of phase II. Thus, to fill the increasing space underneath the plate, pore water must seep out of the neighbouring sand bed. The permeability of the sand specifies how much pore water can seep into the pores in a defined time. The suction in the pores cannot be equalised directly and additionally, pore water from the sand bed flows under the plate. As a result, both at the bottom of the plate and in the sand bed, the suction pressure is constant. This phase is characterised by partially drained behaviour of the sand.
- Phase III: The suction pressure decreases linearly. At the same time, the sand flow channel increases significantly and reaches the top of the sand bed (cf. Fig. 9.8). Water from the top of the sand bed can flow directly under the plate. The flow channel is wide enough to equalise the suction pressure at the bottom of the plate. As a result, the suction pressure in the sand vanishes in the same manner due to seepage flow.

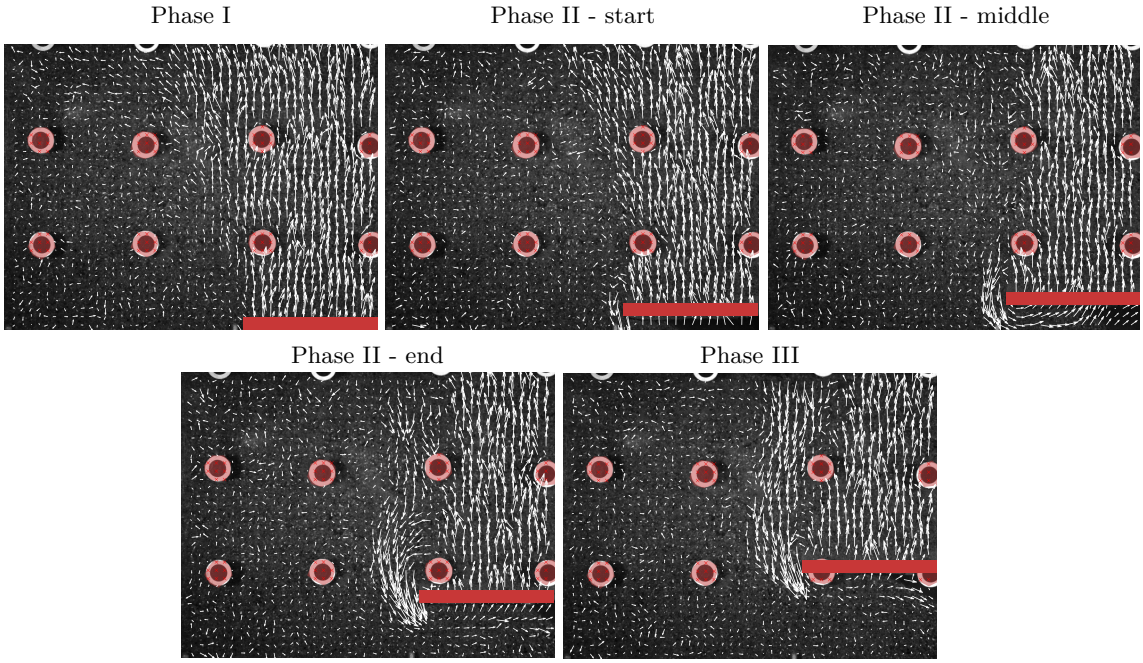


Figure 9.8: PIV results for the Phase I, II and III - carried out with PIVLab

Comparing the measurements for the different extraction velocities shows that all phases are longer at a slower extraction velocity of 100 mm/min. The slower extraction requires more time to create the flow channels, which are wide enough to provide the seepage flow necessary for filling the void under the plate. The fast extraction results in an approximately doubled peak magnitude of the negative excess pore water pressure. This also complies with the suction pressure in phase II.
In the first simulations the classical unresolved CFD-DEM solver, *cfdemSolverPiso*, is used. The pore pressure peak in phase I cannot be observed (cf. , Fig. 9.9 (a) – “simulation

old"). The missing peak can be explained by the fact that in classical unresolved coupled CFD-DEM the plate exists only on the DEM side, whereas the area is permeable on the CFD side. This leads to an under-predicted pressure drop. To overcome this deficiency, an unresolved CFD-DEM solver, which accounts for the plate as an immersed body, is applied. As shown in Fig. 9.9 (a), the magnitude of the pressure drop underneath the plate matches, if this method (*cfdemSolverPisoIBm*) is employed.
In the experiments, the highest negative excess pore water pressure peaks occur after approximately 2 s and 3 s and decay slowly. In contrast, in the simulations, the highest negative pressure level appears almost instantaneously and is reduced much faster. This discrepancy stems from the difference in the two setups: while in the simulations, the plate starts to rise immediately and at a constant velocity, the actuator needs to accelerate until it reaches the target velocity due to mechanical inertia.
This can be considered in the scaling of the time. Fig. 9.9 (b) shows a comparison of the experiments and the simulations, where the time scale of the latter is multiplied by a factor of 6.5. This factor needs to be calibrated with the experimental data, i. e. the duration of phase I. The results show that the magnitude of the pressure difference can be back-calculated sufficiently with the chosen numerical approach. Regardless, phase II cannot be captured. The pore water pressure plateau is not visible in the numerical results.
The computed pore pressure evolution in the soil body next to the plate is investigated (cf. Fig. 9.10) using the same time extrapolation as in Fig. 9.9 (b). This enables to analyse why phase II, which is caused by partially drained behaviour of the soil, is not captured in the numerical simulations. It becomes obvious that the pore pressure evolution in the sand bed is not consistent with the measured one. The extraction of the anchor plate results in a drained response of the soil bed at the beginning. The different phases in the experimental results (cf. Fig. 9.7) are not observed. First, there is an excess pore pressure in the numerical results. It declines fastly until the pressure is zero. Afterwards, a negative excess pore pressure develops, which occurs when the suction pressure at the bottom of the plate vanishes (cf. Fig. 9.9 (b)), indicating the start of phase II. This negative excess pore water pressure reveals that a tendency towards partially drained behaviour is modelled. There is hence a seepage flow from the surrounding soil under the plate. However, the numerical model overestimates the seepage flow. The pore pressure level is significantly lower in comparison with the experiments. Afterwards, the pore pressure does not change noticeably. The small changes result from numerical noise. Overall, the pore pressure evolution in the soil body reveals a fully drained response.
As the extraction of the plate does not yield a pressure peak in the surrounding sand, it can be concluded that the water can seep freely through the sand bed. The sand has a fully drained behaviour. In unresolved coupled CFD-DEM, the pressure is computed in the centre of the computational cells and then interpolated to the faces. Due to this interpolation, the pressure is damped quite fast with increasing distance to the extracted plate, which could be the reason why neither the peak of phase I nor the correct magnitude of the plateau in phase II is computed at the locations of the pressure measurements in the numerical model. The chosen drag force model can have an influence on these results. The drag force mainly drives the pressure drop in the particle bed due to fluid-particle interaction forces. The numerical simulations are carried out again using different drag force models available in CFDEM®coupling to investigate if a different drag force model is

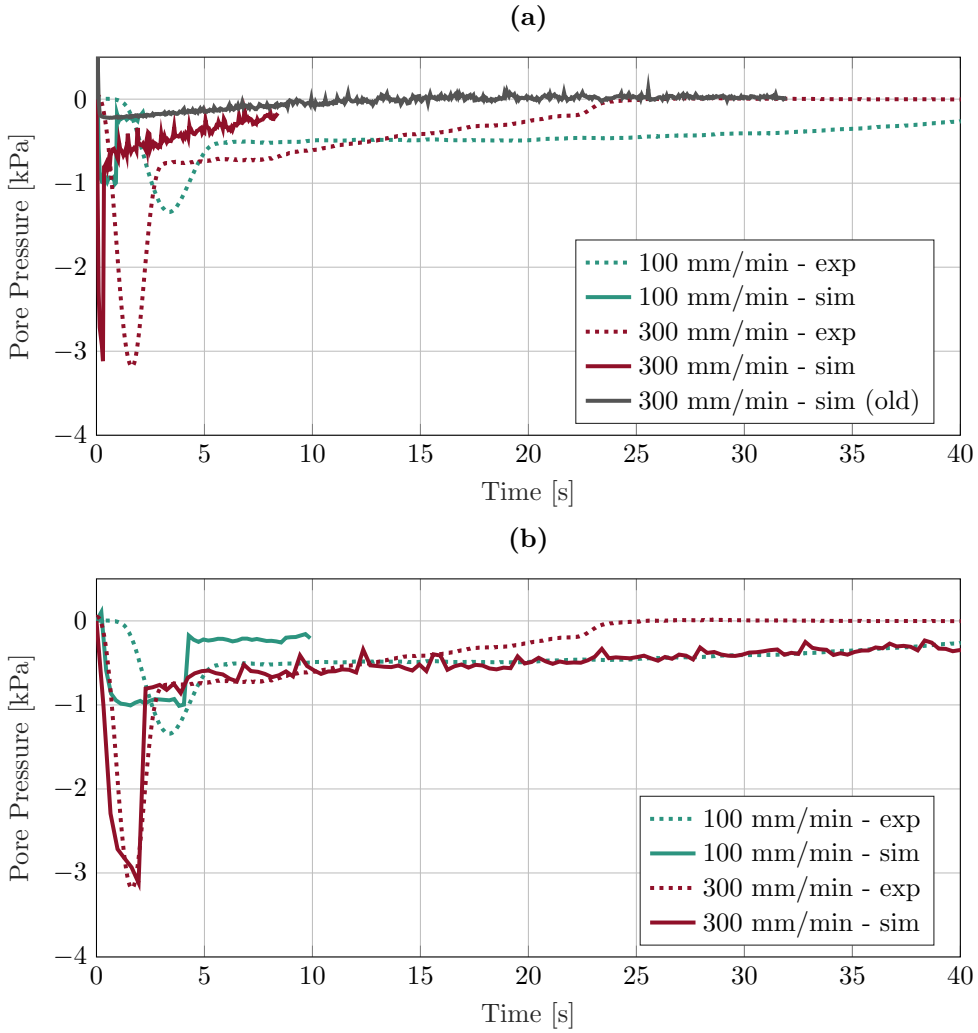


Figure 9.9: Comparison of measured and simulated pressure underneath the anchor plate - without time extrapolation of the numerical results and comparison to "old" simulation of plate (a) - with time extrapolated numerical results and simulation with the immersed boundary method (b) (Kanitz et al., 2019)

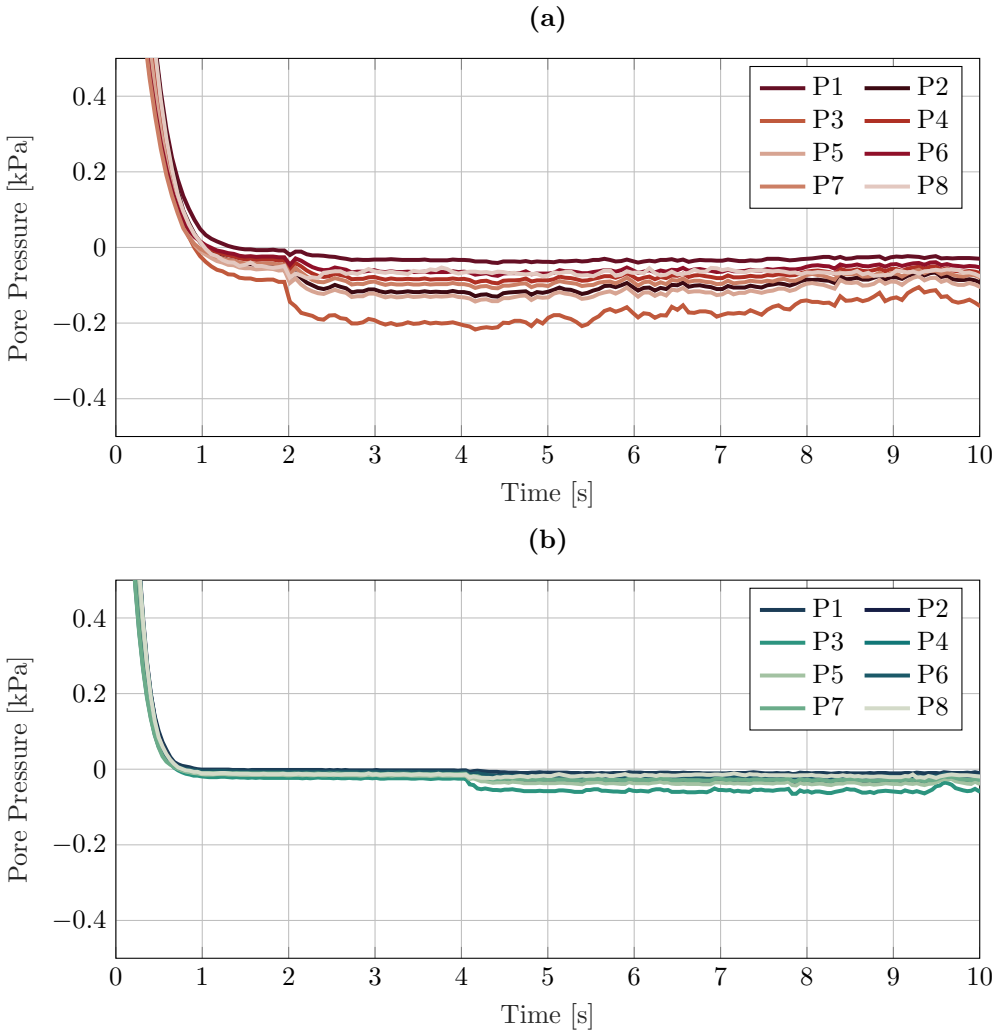


Figure 9.10: Modelled pore water pressure evolution at an extraction velocity of 300 mm/min and 100 mm/min(a) without and (b) with time extrapolation (Kanitz et al., 2019)

more suitable. The results of the pressure evolution using the different drag force models are plotted in Fig. 9.11. It is shown that the utilisation of the different drag force models does

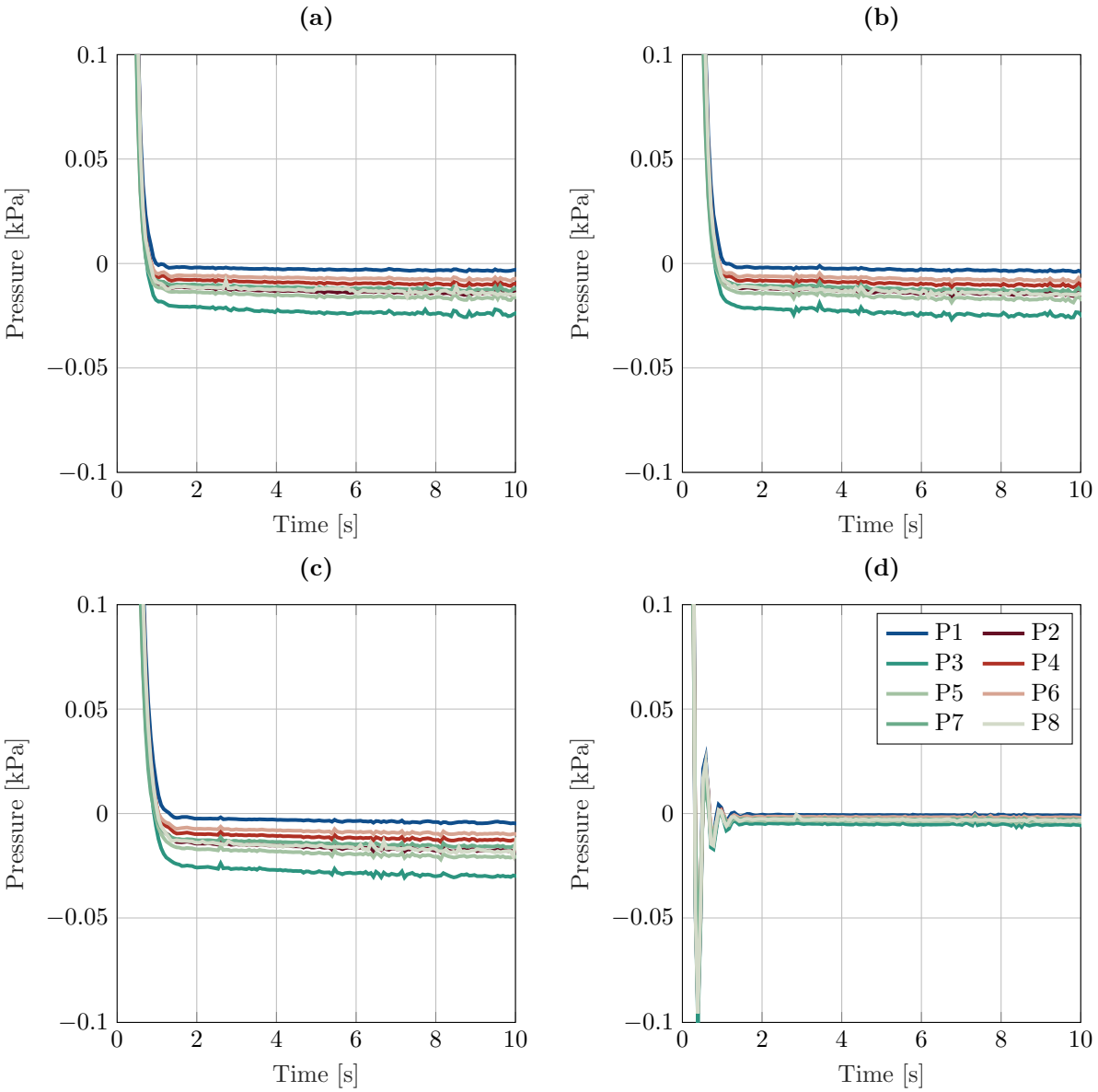


Figure 9.11: Resulting pressure evolution in the soil body with an extraction velocity of 100 mm/s using the drag model of (a) Di Felice (1994), (b) Gidaspow (1994), (c) Koch and Hill (2001) and (d) Schiller and Naumann (1935)

not lead to a noticeable change in pressure evolution. The drag force models of Di Felice (1994), Gidaspow (1994) and Koch and Hill (2001) yield the same the pressure response. Only the drag force model of Schiller and Naumann (1935) shows different behaviour. In contrast to the other drag force models, where the pressure reaches a plateau and decreases slightly over time, the pressure in the fluid phase using the model of Schiller and Naumann (1935) results in oscillations. This is most likely a sign of numerical instability, which declines after 1 s of simulated time. Consequently, the available drag force models cannot

depict the excess pore water pressure development in the soil bed during the extraction of the anchor plate.

9.4.3 Extraction Force

Finally, the resulting extraction force onto the extracted plate is investigated. The force is measured in the experiments via a load cell that is installed in the actuator. In the numerical model, the force is calculated as the sum of all forces that the DEM-plate-mesh is experiencing. The results are displayed in Fig. 9.12. As with the pore pressure development at the bottom of the plate (cf. Fig. 9.9), the computed force is shown with the solver *cfdemSolverPiso* and with the new solver *cfdemSolverPisoIBm*, as well as the influence of time extrapolation. It can be observed that the resulting force correlates strongly with the pressure evolution underneath the plate. When the upward movement starts, a significant pressure peak develops, resulting in a force peak. It is significant that without IBM, this peak cannot be computed accurately (cf. Fig. 9.12 (a)). With IBM, the magnitude of the peak in the numerical simulations matches the measured force peak. For a better comparison of the force peak, the numerical results are plotted again with the same time extrapolation as for the pressure measurements at the bottom of the plate, which is shown in Fig. 9.12 (b). The force difference caused by the decrease in the extraction velocity is about 100 N. Thus, the chosen numerical method captures the difference of force magnitude due to different extraction velocities. It is worth noting that the time extrapolation can only serve for an investigation of the first force peak. Afterwards, the time extrapolation leads to a wrong interpretation of the pressure decline. When the actuator reaches the final extraction velocity, the original time scale has to be used. Accordingly, the force decrease due to the pressure decrease and the loosening of the soil has to be taken from Fig. 9.12 (a) without time extrapolation. Regarding the decrease of the resulting force due to loosening of the soil, the experimental and numerical data have the same inclination. As the pressure level in the soil bed next to the anchor plate cannot be modelled correctly, the plateau in the force evolution is not displayed by the numerical data. However, comparing the interval between 1 s and 8 s and the interval between 8 s and 30 s, only a small difference in the decline is observed. Overall, the numerical and experimental results for the extraction force show a qualitative agreement.

9.4.4 Summary

The extraction of an embedded anchor plate in a saturated dense sand bed was investigated experimentally and numerically. The experimental and numerical results were compared. The shear band evolution in the soil was investigated with PIV-analyses. Pressure transducer measured the pore water pressures in the soil body and at the bottom of the plate. The resulting extraction resistance of the anchor plate was monitored with a load cell. The comparison of these results with the numerical data supports the following findings:

1. The comparison of the displacement of the soil particles observed in the experiment and the numerical results obtained from unresolved coupled CFD-DEM agree - especially in regards of the inclination of the shear band. Hence, the chosen numerical

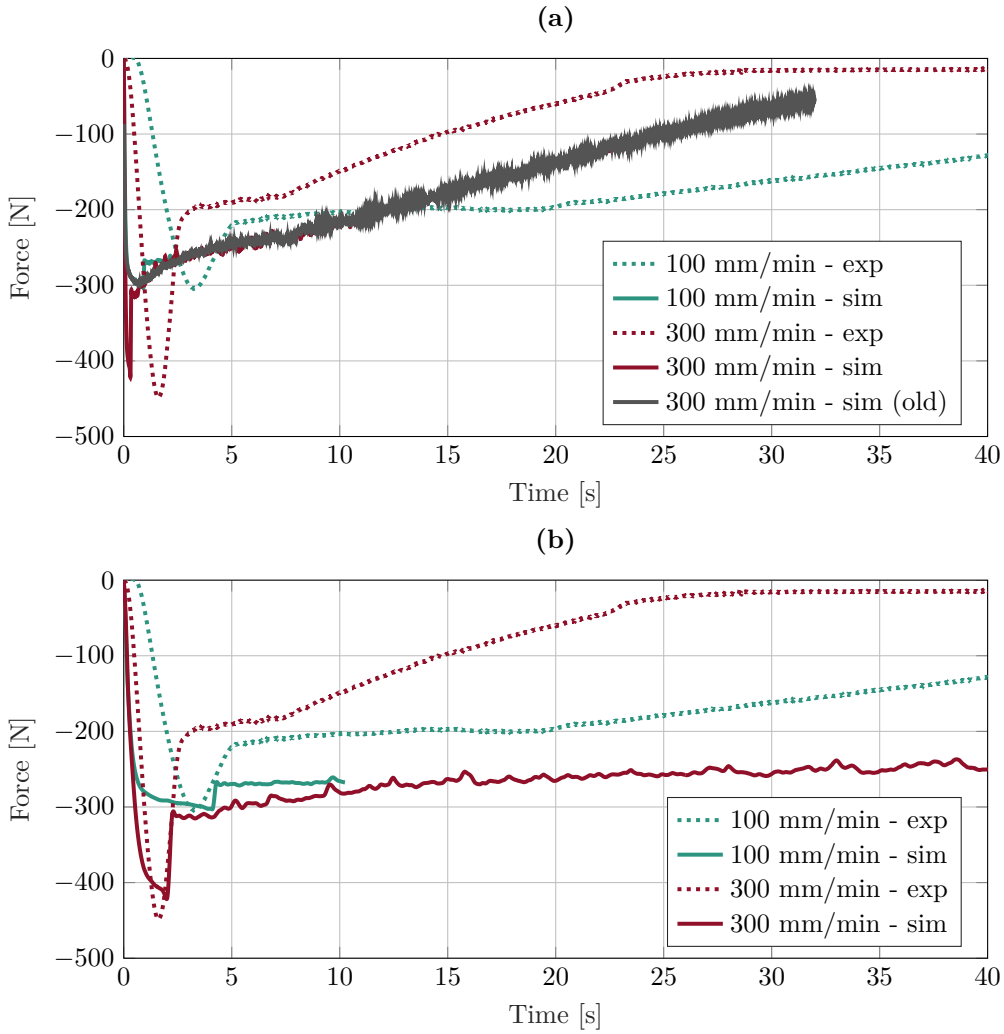


Figure 9.12: Force onto the plate - comparison of the experiments and simulations with and without IB representation for (a) without time extrapolation and (b) with time extrapolation (Kanitz et al., 2019)

method can depict the essential processes regarding the development of a shear surface due to the extraction of an anchor plate.

2. The pore water pressure development due to the extraction can be divided into three phases, where a different soil behaviour provokes an altered response of the pore water pressures. First, a peak develops as a result of the beginning upward motion of the plate and the creation of a gap underneath it (Phase I). Afterwards, the pressure reaches a plateau caused by an equilibrium between the suction pressure under the plate and the surrounding soil. Partially drained behaviour of the sand is observed. Pressure equalisation is limited by the permeability of the soil and narrow flow channels (Phase II). The last phase is characterised by linear regression of the pore water pressures due to the soil flow underneath the extracted plate and correspondingly increased flow channels (Phase III).

3. The comparison of the measured and the simulated pore water pressures at the bottom of the plate agree qualitatively. The usage of a new solver *cfdemSolverPisoIBm* with IBM allows the calculation of the suction pressure peak. A time deviation was identified, which can be explained by the mechanical inertia of the actuator. The target velocity is reached later than in the numerical model, where the velocity is reached instantaneously. At the bottom of the plate, the plateau in the pressure measurements of phase II is not modelled with unresolved coupled CFD-DEM. The comparison of the computed pore water pressures in the soil reached no agreement with the measured pore water pressures. Different drag force models were investigated, but no influence on the pore pressure evolution exists.

4. The comparison of the maximum measured and modelled extraction force magnitude shows sufficient agreement. The force peak is simulated accurately for both extraction velocities. The rate of the subsequent linear decrease must be modelled without the time extrapolation and is consistent with the experimental results.

5. The experimental and numerical results show an undrained behaviour of the investigated sand, although Eqn. 9.1 predicts drained conditions. This could be due to the installation of the extracted plate directly at the bottom of the acrylic glass tank. Likewise, the seepage flow is restricted to the sides of the plate and cannot flow from underneath it.

The comparison of the experimental and numerical data shows promising results. Although the second phase and hence the pore pressure evolution in the soil is not modelled correctly, the pressure peak and the resulting extraction force are computed accurately. As the maximum extraction force is crucial for the resistance of an anchor plate, the approach with unresolved coupled CFD-DEM is appropriate. However, the drainage behaviour of the sand bed is not consistent with the experimental results. The experimental results show an undrained behaviour while the numerical results yield a fully drained behaviour. The applied time extrapolation for the investigation of the extraction resistance is justified for the presented situation of an impermeable bottom as the first peaks only stem from the beginning upward motion of the anchor plate and the initialised fluid fluxes. However, the

extraction of an anchor plate founded on a layer of sand can result in a partially drained behaviour, which is rate-dependent. In these cases, time extrapolation cannot be applied.

10 Conclusion

The macroscopic behaviour of granular materials, such as soil, is controlled by interactions between individual particles as well as interactions with surrounding fluids. Understanding these mechanisms at particle-scale is therefore key for prediction and comprehension of macro-scale behaviour of soils. This thesis presents experimental investigations and numerical modelling of problems related to geotechnical engineering with unresolved coupled CFD-DEM. The key question of this thesis is how the interaction of soil grains and the surrounding fluid influences the behaviour of soil and how suitable is the unresolved CFD-DEM approach to be used in this context. This thesis furthermore deals with possible developments of this numerical method and its limits.
Therefore, four different problems were chosen: Fluidisation of sand, suffusion, suction dredging of sandy submarine slopes and the extraction of a submerged anchor plate. For the sake of validation of the numerical method, small-scale model tests were developed and carried out for each problem. This furthermore enables a combination of experimental and numerical investigations of the respective problem.

Fluidisation of sand The fluidisation of soil due to seepage flow was investigated in medium and very dense sand. Medium dense sand fluidised immediately after applying seepage flow. The very dense sand fluidised after the collapse of a plug, which formed in the sand bed. The numerical models depicted the fluidisation behaviour in both medium and very dense sand after calibration of the particle-wall friction coefficient μ_{p-w}. This calibration was crucial for the modelling of the plug formed in the very dense sand. The computed void fraction before fluidisation and after sedimentation corresponds to the void fraction in the experimental tests revealing a quantitative agreement. Loosening of the sand body due to fluidisation was observed after sedimentation. The loosening in the very dense sand was thereby more significant than in medium dense sand. Overall, unresolved coupled CFD-DEM is suitable for the numerical modelling of fluidisation in sandy soils and can assess the risk for soil to fluidise.

Suffusion Suffusion in a bidisperse particle packing was investigated. First numerical models revealed differences in the erosion rate by using conventional drag force models for particle assemblies. Thus, the following investigations focussed on their influence on suffusion. The conventional drag force models of Di Felice, Koch & Hill, Schiller & Naumann and Gidaspow were investigated. The results were compared with experimental tests. A layered setup was chosen to improve reproducibility and agreement regarding the initial particle arrangement. The investigations revealed that the model of Schiller & Naumann does not lead to suffusion, whereby the models of Di Felice, Koch & Hill and Gidaspow showed a similar response concerning the erosion of fines with some slight differences. A qualitative agreement with the experimental tests was found. To further

investigate the influence of the void fraction and the drag force on the erosion of fines, the drag force model of Schiller & Naumann was extended with a voidage term in the form of $n^{-\chi}$. The parameter χ was varied from [0.5,1.8], and thus, step-wisely increased. It was observed that higher drag forces result in early clogging of the fine particles with a higher tendency towards blow-outs of clogged fines. Decreasing χ leads to ongoing erosion of fines and less clogging mechanisms were identified. Furthermore, the increase of the drag force yields a higher erosion distance of single particles. The examination of the total amount of eroded fines revealed a maximum value for medium-range χ. Its further increase results in a reduction of eroded fines, whereby a constant value is reached. In order to examine why the results of the different drag models are so similar in the layered setup compared to the first analyses with a higher seepage flow velocity, the influence of the seepage flow velocity on the drag models was analytically evaluated. The analysis showed that in dense regimes, the differences in the models of Di Felice, Koch & Hill and Gidaspow increase for higher flow velocities. In summary, the numerical method allows a good possibility to model suffusion. For low flow velocities, the choice of the drag model is not critical. At higher flow velocities, however, detailed investigations should be carried out to determine which model is most suitable and whether parameters need to be adjusted if necessary. The investigations with the extended model of Schiller & Naumann revealed how the parameter χ influences the erosion rate. It can hence be used to calibrate the numerical model.

Suction dredging of sandy submarine slopes The influence of suction dredging on the failure mechanism of sandy submarine slopes was investigated in medium dense and very dense sand. Slopes of glass beads with diameters of 3 mm and 1 mm were investigated additionally. The glass beads slopes failed in a uniform motion. This failure mechanism is not influencing the pore water pressures. In the sandy slopes, liquefaction and breach failure were observed in medium dense and very dense sand respectively. The suction pressure is thereby maintained in very dense sand leading to enhanced shear resistance. The increased grain-to-grain stresses consequently lead to breach failure. Thus, a strong correlation between the failure mechanism and the pore water pressure was identified. Unresolved coupled CFD-DEM captures the failure in slopes with glass beads as the interaction with the pore fluid is negligible. However, it fails to model liquefaction or breach failure. The computation of the pore water pressure is not consistent with the experimental results. It could be found that the computation of the term $\frac{\partial}{\partial t}n$ in the governing equations of unresolved coupled CFD-DEM is numerically unstable. The linking between the displacement of the particles and the computation of the fluid flow is hence not possible. Therefore, a new cohesion model in DEM was developed to assess for the influence of pressure changes between the grains at contractant and dilatant behaviour. Therefore, the Stokes drag force for a single particle was extended with a voidage function in the form of $\frac{n_{\min}^{-\chi}}{1-n_{\min}}$ with the minimum void fraction of the investigated material. The model was verified against experimental tests of a submerged granular column collapse. Setting $\chi = 5.7$ yielded good agreement at the beginning of the failure. However, with proceeding time, the results deviated, and the influence of the cohesion model vanished. The cohesion model was further applied to the failure of a very dense submarine slope. The cohesion model altered the failure mechanism so that breach failure occurred. However, the

presented cohesion model does not depict the whole failure process, and further research is strongly recommended.

Extraction of a submerged anchor plate The extraction of an anchor plate embedded in dense saturated sand was investigated. The extraction causes suction pressure at the bottom of the plate and in the surrounding sand. As a cause, the extraction resistance increases significantly. Three phases in the evolution of the pore water pressure evolution and the corresponding extraction resistance formed. In the first phase, the pressure yields a peak as a result of the beginning upward motion of the plate. In the next phase, a plateau develops. It is caused by an equilibrium between the suction pressure under the plate and in the surrounding soil. Partially drained behaviour of the sand occurs. The last phase is characterised by linear regression of the pore water pressures due to the soil flow underneath the extracted plate. A new solver was implemented to model the fluid-particle-structure interaction. This solver enables computing the peak of the extraction and the suction pressure at the bottom of the plate. It includes the plate with the IBM in the CFD computation to consider the interaction with the fluid. Likewise, the peak of the extraction and the pore water pressure at the bottom of the plate is modelled consistent with the experimental data. However, the computation of the pore water pressure in the soil is erroneous. The pressure in the soil does not yield a peak. The subsequent partially drained behaviour is computed but only qualitatively. The use of different drag force models generates identical responses on the pore water pressure evolution in the soil. Hence, further research is required to model the full pore water pressure response in the soil.

Outlook

The investigations in this thesis showed that unresolved coupled CFD-DEM offers valuable insights into the behaviour of soil grains, especially in regards to the interaction with seepage flow without the need for sophisticated extensions. The investigations of contact force distributions and both individual particle and particle assembly motion help to understand the overall soil behaviour and to assess possible risks of instabilities in the soil structure. However, this thesis revealed that concerning the pore water-soil interaction improved methods have to be developed. This considers the modelling of the effect of rearranging particles on the fluid pressure field. The presented new cohesion model is a suitable approach to solve this issue. The investigations revealed good first results, but further research is required.

A critical issue to address is the ratio of CFD cell size to particle radius. Because the CFD cell must be at least $3 \cdot d_p$ in size, an accurate depiction of the fluid pressure field is not guaranteed, which was revealed by the investigations on suction dredging of submarine slopes and the extraction of objects embedded in saturated sand. Undrained behaviour of the soil could not be captured. This limit will be especially crucial when considering gap-graded soil with higher size differences than five, which were employed here, and soils with a wider particle size distribution.

Furthermore, improved measurement techniques are required to allow quantitative evaluation of the obtained results. In this thesis, only the measurement of the void fraction and

the extraction resistance of the anchor plate could be used for this purpose. As unresolved coupled CFD-DEM yields inaccuracies in the fluid pressure field, a comparison with the measured fluid pressure by the pressure transducers was not possible. Hence, most of the investigations and evaluations on the suitability of the numerical method are based on qualitative comparisons. Good agreement was found for the majority of the analyses. However, especially for further developments of unresolved coupled CFD-DEM, e. g. the presented cohesion model to depict the force arising from shear-dilatancy effects on the fluid pressure field and the investigation of the employed drag force model in suffusion, quantitative comparisons are crucial. Improved imaging techniques such as CT investigations or the utilisation of a particle sensor, which directly measures the pressure acting on its surface, are recommended to address this issue.
In summary, while the experiments only allow observing the soil behaviour at the outer boundary, unresolved coupled CFD-DEM offers the chance to look insight the soil body. However, the investigations show that this numerical method still lacks important features to capture some physical mechanisms accurately. Hence, the combination of both experimental and numerical methods allows combining the findings of each to gain a deeper understanding of the governing physical mechanisms. Where the experimental investigations on the pore water pressure evolution could be linked to the particle displacement observed with PIV to explain the behaviour of the soil, the numerical investigations could deepen our knowledge of the individual particle behaviour by analysing particle contact forces and erosion rates. This thesis clarifies how crucial the comparison of numerical with experimental results is. Only by the findings of the experimental tests, the limits of unresolved coupled CFD-DEM could be deduced and identified where developments are necessary. This thesis showed the capacity of unresolved coupled CFD-DEM to close knowledge gaps concerning the particle-scale behaviour of saturated soil, but we still need experimental tests to verify if the governing physical mechanisms are accurately captured. If in future investigations, the mentioned limits can be resolved by means of quantitative measurements, enabling accurate comparison and calibration, unresolved coupled CFD-DEM will be a valuable tool to investigate complex geotechnical problems.

References

Alsaydalani, M. O. A. and C. R. I. Clayton (2014). "Internal Fluidization in Granular Soils". In: *Journal of Geotechnical and Geoenvironmental Engineering* 140.3, p. 04013024. DOI: 10.1061/(ASCE)GT.1943-5606.0001039.

Anderson, T. B. and R. Jackson (1967). "A fluid mechanical description of fluidized beds". In: *Industrial and Engineering Chemistry Fundamentals* 6.4, pp. 527–538.

Antonyuk, S., S. Heinrich, J. Tomas, N. G. Deen, M. S. van Buijtenen, and J. A. M. Kuipers (2010). "Energy absorption during compression and impact of dry elastic-plastic spherical granules". In: *Granular Matter* 12.1, pp. 15–47. DOI: 10.1007/s10035-009-0161-3.

Auriault, J.-L. (1987). "Nonsaturated deformable porous media: Quasistatics". In: *Transport in Porous Media* 2.1. DOI: 10.1007/BF00208536.

Barkla, H. M. and L. J. Auchterlonie (1971). "The Magnus or Robins effect on rotating spheres". In: *Journal of Fluid Mechanics* 47.3, pp. 437–447. DOI: 10.1017/S0022112071001150.

Basset, A. (1888). *A treatise on hydrodynamics, with numerous examples*.

Bear, J. (2012). *Hydraulics of Groundwater*. Dover Publications.

Been, K., R. Bisschop, E. Broos, E. Bijlsma, H. Cloo, J. Cools, and A. van Gelder (2012). *Hydraulic fill manual: For dredging and reclamation works*. Boca Raton, Fla.: CRC Press/Balkema.

Bertram, G. E. (1940). *An Experimental Investigation of Protective Filters*. Harvard Soil Mechanics Series. Harvard University.

Bierwisch, C., T. Kraft, H. Riedel, and M. Moseler (2009). "Three-dimensional discrete element models for the granular statics and dynamics of powders in cavity filling". In: *Journal of the Mechanics and Physics of Solids* 57.1, pp. 10–31. DOI: 10.1016/j.jmps.2008.10.006.

Bolognin, M., M. Martinelli, K. J. Bakker, and S. N. Jonkman (2017). "Validation of Material Point Method for Soil Fluidisation Analysis". In: *Procedia Engineering* 175, pp. 233–241. DOI: 10.1016/j.proeng.2017.01.018.

Bouchut, F., E. D. Fernández-Nieto, A. Mangeney, and G. Narbona-Reina (2016). "A two-phase two-layer model for fluidized granular flows with dilatancy effects". In: *Journal of Fluid Mechanics* 801, pp. 166–221. DOI: 10.1017/jfm.2016.417.

Breusers, H. N. C. (1974). "Suction of sand". In: *Bulletin of the International Association of Engineering Geology* 10.1, pp. 65–66. DOI: 10.1007/BF02634636.

Burenkova, V. V. (1992). "Assessment of suffosion in non-cohesive and graded soils". In: *Filters in geotechnical and hydraulic engineering*. Ed. by J. Brauns. Rotterdam: Balkema, pp. 357–360.

Camenen, B. (2008). "Chapter 15 Settling velocity of sediments at high concentrations". In: *Sediment and ecohydraulics*. Ed. by T. Kusuda. Vol. 9. Proceedings in Marine Science. Amsterdam and London: Elsevier, pp. 211–226. DOI: 10.1016/S1568-2692(08)80017-4.

Cardinaels, R. and H. A. Stone (2015). "Lubrication analysis of interacting rigid cylindrical particles in confined shear flow". In: *Physics of Fluids* 27.7, p. 072001. DOI: 10.1063/1.4927219.

CFDEMcoupling documentation, divided void fraction (2020). https://www.cfdem.com/media/CFDEM/docu/voidFractionModel_dividedVoidFraction.html. accessed: 01-03-2020.

Crowe, C. T., J. D. Schwarzkopf, M. Sommerfeld, and Y. Tsuji (2012). *Multiphase flows with droplets and particles*. 2. ed. Boca Raton: CRC Press.

Cundall, P. A. and R. D. Hart (1992). "Numerical Modelling of Discontinua". In: *Engineering Computations* 9.2, pp. 101–113. DOI: 10.1108/eb023851.

Cundall, P. A. and O. D. L. Strack (1979). "A discrete numerical model for granular assemblies". In: *Géotechnique* 29, pp. 47–65.

Dallavalle, J. M. (1948). *Micromeritics : the technology of fine particles*. 2. ed. New York: Pitman.

Das, B. M. and K. Sobhan (2014). *Principles of geotechnical engineering*. Eighth edition/SI edition. Stamford, CT: Cengage Learning.

Davidson, J. F. (1971). *Fluidization*. London: Academic Pr.

Davies, J. M. (1949). "The Aerodynamics of Golf Balls". In: *Journal of Applied Physics* 20.9, pp. 821–828. DOI: 10.1063/1.1698540.

Davis, R. H. and J.-M. Serayssol (1986). "The elastohydrodynamic collision of two spheres". In: *Journal of Fluid Mechanics* 163, pp. 479–497.

Di Felice, R. (1994). "The voidage function for fluid-particle interaction systems". In: *International Journal of Multiphase Flow* 20.1, pp. 153–159. DOI: 10.1016/0301-9322(94)90011-6.

Du, W., X. Bao, J. Xu, and W. Wei (2006). "Computational fluid dynamics (CFD) modeling of spouted bed: Assessment of drag coefficient correlations". In: *Chemical Engineering Science* 61.5, pp. 1401–1420. DOI: 10.1016/j.ces.2005.08.013.

El Shamy, U. and M. Zeghal (2005). "Coupled Continuum-Discrete Model for Saturated Granular Soils". In: *Journal of Engineering Mechanics* 131.4, pp. 413–426. DOI: 10.1061/(ASCE)0733-9399(2005)131:4(413).

Engelund, F. (1953). *On the laminar and turbulent flows of ground water through homogeneous sand*. Danish Academy of Technical Sciences / Transactions. Akademiet for de tekniske videnskaber. URL: https://books.google.de/books?id=at9MtwAACAAJ.

Ergun, S. (1952). "Fluid flow through packed columns". In: *Fluid Flow Through Packed Columns* 48, pp. 89–94.

Fede, P., O. Simonin, and A. Ingram (2016). "3D numerical simulation of a lab-scale pressurized dense fluidized bed focussing on the effect of the particle-particle restitution coefficient and particle–wall boundary conditions". In: *Chemical Engineering Science* 142, pp. 215–235. DOI: 10.1016/j.ces.2015.11.016.

Fell, R. and J.-J. Fry (2014). *Internal Erosion of Dams and Their Foundations: Selected and Reviewed Papers from the Workshop on Internal Erosion and Piping of Dams and Their Foundations, Aussois, France, 25-27 April 2005*. Boca Raton: Chapman and Hall/CRC. URL: https://ebookcentral.proquest.com/lib/gbv/detail.action?docID=5379124.

Finnie, I. M. S. and M. F. Randolph (1994). "Punch-Through and Liquefaction Induced Failure of Shallow Foundations on Calcareous Sediments". In: *Chryssostomidis (Hg.) 1994 – Behaviour of offshore structures*, pp. 217–230.

Garcia, D. (2010). "Robust smoothing of gridded data in one and higher dimensions with missing values". In: *Computational statistics & data analysis* 54.4, pp. 1167–1178. DOI: 10.1016/j.csda.2009.09.020.

Gidaspow, D. (1994). *Multiphase Flow and Fluidization: Continuum and Kinetic Theory Descriptions*. San Diego: Elsevier Science. URL: http://site.ebrary.com/lib/alltitles/docDetail.action?docID=10597055.

Goltz, M., M. Aufleger, S. Perzlmaier, and P. Muckenthaler (2010). "Assessing the critical seepage velocity causing transport of fine particles – the approach of Muckenthaler". In: *Proc. of 8th ICOLD European Club Symposium*.

Guo, Z., C. Zheng, and B. Shi (2002). "An extrapolation method for boundary conditions in lattice Boltzmann method". In: *Physics of Fluids* 14.6, p. 2007. DOI: 10.1063/1.1471914. URL: https://aip.scitation.org/doi/pdf/10.1063/1.1471914.

Hager, A. (2014). "CFD-DEM on Multiple Scales - An Extensive Investigation of Particle-Fluid Interactions". Dissertation. Linz: Johannes Kepler Universität Linz.

Han, Y. and P. A. Cundall (2013). "LBM-DEM modeling of fluid-solid interaction in porous media". In: *International Journal for Numerical and Analytical Methods in Geomechanics* 37.10, pp. 1391–1407. DOI: 10.1002/nag.2096.

Hertz, H. (1881). "Über die Berührung fester elastischer Körper". In: *Journal für die reine und angewandte Mathematik* 92, pp. 156–171.

Hsu, T.-J., J. T. Jenkins, and P. L.-F. Liu (2004). "On two-phase sediment transport: sheet flow of massive particles". In: *Proceedings of the Royal Society of London. Series A: Mathematical, Physical and Engineering Sciences* 460.2048, pp. 2223–2250. DOI: 10.1098/rspa.2003.1273.

Hu, Z., Y. D. Zhang, and Z. X. Yang (2020). "Suffusion-induced evolution of mechanical and microstructural properties of gap-graded soils using CFD-DEM". In: *Journal of Geotechnical and Geoenvironmental Engineering* 146.5. DOI: 10.1061/(ASCE)GT.1943-5606.0002245.

Hu, Z., Y. Zhang, and Z. Yang (2019). "Suffusion-induced deformation and microstructural change of granular soils: a coupled CFD–DEM study". In: *Acta Geotechnica* 14.3, pp. 795–814. DOI: 10.1007/s11440-019-00789-8.

Iverson, R. M. and D. L. George (2014). "A depth-averaged debris-flow model that includes the effects of evolving dilatancy. I. Physical basis". In: *Proceedings of the Royal Society A: Mathematical, Physical and Engineering Sciences* 470.2170, p. 20130819. DOI: 10.1098/rspa.2013.0819.

Iverson, R. M. (2005). "Regulation of landslide motion by dilatancy and pore pressure feedback". In: *Journal of Geophysical Research* 110.F2, p. 65. DOI: 10.1029/2004JF000268.

Iwashita, K. (1998). "Rolling resistance at contacts in simulation of shear band development by DEM". In: *Journal of Engineering Mechanics* 124, pp. 285–292.

Jaeger, H. M., S. R. Nagel, and R. P. Behringer (1996). "Granular solids, liquids, and gases". In: *Reviews of Modern Physics* 68.4, pp. 1259–1273. DOI: 10.1103/RevModPhys.68.1259.

Kafui, K. D., C. Thornton, and M. J. Adams (2002). "Discrete particle-continuum fluid modelling of gas–solid fluidised beds". In: *Chemical Engineering Science* 57.13, pp. 2395–2410. DOI: 10.1016/S0009-2509(02)00140-9.

Kanitz, M. and J. Grabe (2018a). "Experimental Study of the Influence of the Pore Water Pressure Evolution and the Shear Band Formation on the Extraction Resistance of Submerged Anchor Plates". In: *Volume 9: Offshore Geotechnics; Honoring Symposium for Professor Bernard Molin on Marine and Offshore Hydrodynamics*. ASME, V009T10A004. DOI: 10.1115/OMAE2018-78306.

Kanitz, M. and J. Grabe (2018b). "Numerical investigations on the liquid-solid transition of a soil bed with coupled CFD-DEM". In: *Numerical Methods in Geotechnical Engineering IX*. Ed. by M. de Matos Fernandes. Milton: Chapman and Hall/CRC.

Kanitz, M. and J. Grabe (2019a). "Influence of Suction Dredging on the Failure Mechanism of Sandy Submarine Slopes: Revisited With a Coupled Numerical Approach". In: *Volume 1: Offshore Technology; Offshore Geotechnics*. American Society of Mechanical Engineers. DOI: 10.1115/OMAE2019-95151.

Kanitz, M. and J. Grabe (2019b). "Multiscale investigation of suffusion with coupled CFD-DEM". In: *Proceedings of 2nd International Conference on the Material Point Method for Soil-Water-Structure Interaction 2019*. Cambridge, UK, pp. 122–128. URL: http://mpm2019.eu/papers.

Kanitz, M. and J. Grabe (2020). "The influence of the void fraction on the particle migration: a coupled CFD-DEM study about drag force correlations". In: *International Journal for Numerical and Analytical Methods in Geomechanics*, accepted for publication. DOI: 10.1002/nag.3131.

Kanitz, M., J. Grabe, A. Hager, C. Goniva, and C. Kloss (2017). "Numerical Investigations of the Extraction of Submerged Foundations by Coupled CFD-DEM". In: *Proceedings of 36th International Conference on Ocean, Offshore & Arctic Engineering (OMAE)*, V009T10A017. DOI: 10.1115/OMAE2017-61299.

Kanitz, M., A. Hager, J. Grabe, and C. Goniva (2019). "Numerical and experimental analysis of the extraction mechanism of an anchor plate embedded in saturated sand". In: *Computers and Geotechnics* 111, pp. 191–201. DOI: 10.1016/j.compgeo.2019.03.014.

Kawano, K., T. Shire, and C. O'Sullivan (2018). "Coupled particle-fluid simulations of the initiation of suffusion". In: *Soils and Foundations* 58.4, pp. 972–985. DOI: 10.1016/j.sandf.2018.05.008. URL: http://www.sciencedirect.com/science/article/pii/S0038080618300945.

Kempe, T. and J. Fröhlich (2012). "Collision modelling for the interface-resolved simulation of spherical particles in viscous fluids". In: *Journal of Fluid Mechanics* 709, pp. 445–489. DOI: 10.1017/jfm.2012.343.

Kenney, T. C. and D. Lau (1985). "Internal stability of granular filters". In: *Canadian Geotechnical Journal* 22.2, pp. 215–225. DOI: 10.1139/t85-029.

Kloss, C., C. Goniva, A. Hager, S. Amberger, and S. Pirker (2012). "Models, algorithms and validation for opensource DEM and CFD-DEM". In: *Progress in Computational Fluid Dynamics, An International Journal* 12.2/3, p. 140. DOI: 10.1504/PCFD.2012.047457.

Koch, D. L. and R. J. Hill (2001). "Inertial effects in suspension and porous-media flows". In: *Annual Review of Fluid Mechanics* 33.1, pp. 619–647. DOI: 10.1146/annurev.fluid.33.1.619.

Koch, D. L. and A. S. Sangani (1999). "Particle pressure and marginal stability limits for a homogeneous monodisperse gas-fluidized bed: Kinetic theory and numerical simulations". In: *Journal of Fluid Mechanics* 400, pp. 229–263. DOI: 10.1017/S0022112099006485.

Kumar, K., K. Soga, and J.-Y. Delenne (2012). "Granular Flows in Fluid". In: *Discrete Element Modelling of Particulate Media*. The Royal Society of Chemistry, pp. 59–66. DOI: 10.1039/9781849735032-00059. URL: http://dx.doi.org/10.1039/9781849735032-00059.

Kumar, K., K. Soga, J.-Y. Delenne, F. Radjai, S. Nezamabadi, and S. Luding (2017). "Collapse of tall granular columns in fluid". In: *EPJ Web of Conferences* 140, p. 09041. DOI: 10.1051/epjconf/201714009041.

Ladd, R. S. (1978). "Preparing Test Specimens Using Undercompaction". In: *Geotechnical Testing Journal* 1.1, p. 16. DOI: 10.1520/GTJ10364J.

Landahl, M. T., E. Mollo-Christensen, and E. M. Christensen (1998). *Turbulence and random processes in fluid mechanics*. 2. ed., reprinted, [Nachdr.] Cambridge: Univ. Press.

Langston, P. A., U. Tüzün, and D. M. Heyes (1994). "Continuous potential discrete particle simulations of stress and velocity fields in hoppers: Transition from fluid to granular flow". In: *Chemical Engineering Science* 49.8, pp. 1259–1275. DOI: 10.1016/0009-2509(94)85095-X.

Lee, C.-H. and Z. Huang (2018). "A two-phase flow model for submarine granular flows: With an application to collapse of deeply-submerged granular columns". In: *Advances in Water Resources* 115, pp. 286–300. DOI: 10.1016/j.advwatres.2017.12.012.

Lee, C.-H., Y. M. Low, and Y.-M. Chiew (2016). "Multi-dimensional rheology-based two-phase model for sediment transport and applications to sheet flow and pipeline scour". In: *Physics of Fluids* 28.5, p. 053305. DOI: 10.1063/1.4948987.

Lee, H. J. (1973). "Breakout of Partially Embedded Objects from Cohesive Seafloor Soils". In: *Offshore Technology Conference*. DOI: 10.4043/1904-MS.

Lehane, B. M., C. Gaudin, D. J. Richards, and M. J. Rattley (2008). "Rate effects on the vertical uplift capacity of footings founded in clay". In: *Géotechnique* 58.1, pp. 13–21. DOI: 10.1680/geot.2008.58.1.13.

Li, J. and J. A. M. Kuipers (2003). "Gas-particle interactions in dense gas-fluidized beds". In: *Chemical Engineering Science* 58.3-6, pp. 711–718. DOI: 10.1016/S0009-2509(02)00599-7.

Li, M. (2008). *Seepage induced instability in widely graded soils*. DOI: 10.14288/1.0063080.

Liggghts documentation, fix freeze command (2020). https://www.cfdem.com/media/DEM/docu/fix_freeze.html. accessed: 07-04-2020.

Loha, C., H. Chattopadhyay, and P. K. Chatterjee (2012). "Assessment of drag models in simulating bubbling fluidized bed hydrodynamics". In: *Chemical Engineering Science* 75, pp. 400–407. DOI: 10.1016/j.ces.2012.03.044.

Maccoll, J. W. (1928). "Aerodynamics of a Spinning Sphere". In: *The Journal of the Royal Aeronautical Society* 32.213, pp. 777–798. DOI: 10.1017/S0368393100136260.

Mansouri, M., M. S. El Youssoufi, and F. Nicot (2017). "Numerical simulation of the quicksand phenomenon by a 3D coupled Discrete Element - Lattice Boltzmann hydromechanical model". In: *International Journal for Numerical and Analytical Methods in Geomechanics* 41.3, pp. 338–358. DOI: 10.1002/nag.2556.

Marshall, J. S. and K. Sala (2013). "Comparison of methods for computing the concentration field of a particulate flow". In: *International Journal of Multiphase Flow* 56, pp. 4–14. DOI: 10.1016/j.ijmultiphaseflow.2013.05.009.

Mastbergen, D. R. and J. H. van den Berg (2003). "Breaching in fine sands and the generation of sustained turbidity currents in submarine canyons". In: *Sedimentology* 50.4, pp. 625–637. DOI: 10.1046/j.1365-3091.2003.00554.x.

McLaughlin, J. B. (1991). "Inertial migration of a small sphere in linear shear flows". In: *Journal of Fluid Mechanics* 224, pp. 261–274. DOI: 10.1017/S0022112091001751.

Mei, R. (1992). "An approximate expression for the shear lift force on a spherical particle at finite reynolds numbers". In: *Inernational Journal of Mulitphase Flow* 18, pp. 145–147.

Meijer, K. L. and A. G. van Os (1976). "Pore Pressures Near Moving Underwater Slope". In: *Journal of the Geotechnical Engineering Division* 102.4, pp. 361–372.

Mindlin, R. W. and H. Deresiewicz (1953). "Elastic spheres in contact under varying oblique forces". In: *Journal of Applied Mechanics* 20, pp. 327–344.

Mittal, R. and G. Iaccarino (2005). "Immersed Boundary Methods". In: *Annual Review of Fluid Mechanics* 37.1, pp. 239–261. DOI: 10.1146/annurev.fluid.37.061903.175743.

Muga, B. J. (1967). "Bottom breakout forces". In: *Proceedings of Conference on Civil Engineering in the Oceans*, pp. 569–600.

Murray, E. J. and J. D. Geddes (1987). "Uplift of Anchor Plates in Sand". In: *Journal of Geotechnical Engineering* 113.3, pp. 202–2015.

Ngoma, J., P. Philippe, S. Bonelli, J. Delenne, and F. Radjai (2014). "Interaction between two localized fluidization cavities in granular media : Experiments and numerical simulation". In: *Geomechanics from Micro to Macro*. Ed. by K. Soga, K. Kumar, G. Biscontin, and M. Kuo. Vol. 2. CRC Press, pp. 1571–1576. DOI: 10.1201/b17395-286.

Niven, R. K. and N. Khalili (1998). "In situ fluidisation by a single internal vertical jet". In: *Journal of Hydraulic Research* 36.2, pp. 199–228. DOI: 10.1080/00221689809498633.

Norouzi, H. R., R. Zarghami, R. Sotudeh-Gharebagh, and N. Mostoufi (2016). *Coupled CFD-DEM Modeling*. Chichester, UK: John Wiley & Sons, Ltd. DOI: 10.1002/9781119005315.

OpenFoam documentation, Boundary conditions (2020). https://www.openfoam.com/documentation/user-guide/standard-boundaryconditions.php. accessed: 07-04-2020.

OpenFOAM v6 User Guide: 7.2 Turbulence models (2019). https://cfd.direct/openfoam/user-guide/v6-turbulence. accessed: 2019-12-20.

Pailha, M., M. Nicolas, and O. Pouliquen (2008). "Initiation of underwater granular avalanches: Influence of the initial volume fraction". In: *Physics of Fluids* 20.11, p. 111701. DOI: 10.1063/1.3013896.

Pan, B., W. Dafang, and X. Yong (2012). "Incremental calculation for large deformation measurement using reliability-guided digital image correlation". In: *Optics and Lasers in Engineering* 50.4, pp. 586–592. DOI: 10.1016/j.optlaseng.2011.05.005.

Peck, A. J. (1969). "Entrapment, stability, and persistence of air bubbles in soil water". In: *Soil Research* 7.2, p. 79. DOI: 10.1071/SR9690079.

Peng, Y. and L. T. Fan (1997). "Hydrodynamic characteristics of fluidization in liquid-solid tapered beds". In: *Chemical Engineering Science* 52.14, pp. 2277–2290. DOI: 10.1016/S0009-2509(97)00061-4.

Peskin, C. S. (1973). "Flow patterns around heart valves: a digital computer method for solving the equations of motion". In: *IEEE Transactions on Biomedical Engineering* BME-20.4, pp. 316–317. URL: https://www2.scopus.com/inward/record.uri?eid=2-s2.0-0015885485&partnerID=40&md5=029d7413e38792bcbdbc1396d10eb22c.

Pirker, S., D. Kahrimanovic, and C. Goniva (2011). "Improving the applicability of discrete phase simulations by smoothening their exchange fields". In: *Applied Mathematical Modelling* 35.5, pp. 2479–2488. DOI: 10.1016/j.apm.2010.11.066.

Plenker, D. (2020). "Physical and numerical investigations of the dynamic interaction of granulates and fluid". PhD thesis. Hamburg: Hamburg University of Technology.

Puckett, J. G., F. Lechenault, and K. E. Daniels (2011). "Local origins of volume fraction fluctuations in dense granular materials". In: *Physical review. E, Statistical, nonlinear, and soft matter physics* 83.4 Pt 1, p. 041301. DOI: 10.1103/PhysRevE.83.041301.

Rapp, B. E. (2017). *Microfluidics: Modeling, mechanics, and mathematics*. Micro & nano technologies series. Kidlington, United Kingdom: William Andrew. URL: http://proquest.tech.safaribooksonline.de/9781455731510.

Reeks, M. W. and S. McKee (1984). "The dispersive effects of Basset history force on particle motion in a turbulent flow". In: *Physics of Fluids* 27, p. 1573.

Richardson, J. F. and W. N. Zaki (1997). "Sedimentation and fluidisation: Part I". In: *Chemical Engineering Research and Design* 75, S82–S100. DOI: 10.1016/S0263-8762(97)80006-8.

Roux, S. and F. Radjai (2010). "Texture-Dependent Rigid-Plastic Behavior". In: *Physics of Dry Granular Media*. Ed. by H. J. Herrmann, J.-P. Hovi, and S. Luding. Vol. 31. Dordrecht: Springer Netherlands, pp. 229–236. DOI: 10.1007/978-94-017-2653-5_13.

Rubinow, S. I. and J. B. Keller (1961). "The transverse force on spinning sphere moving in a viscous fluid". In: *Journal of Fluid Mechanics* 11(3), pp. 447–459.

Saffman, P. G. (1965). "The lift on a small spehere in a slow shear flow". In: *Journal of Fluid Mechanics* 22, pp. 385–400.

Schiller, L. and A. Naumann (1935). "A drag coefficient correlation". In: *Zeitschrift des Vereins Deutscher Ingenieure* 77, pp. 318–320.

Scholtès, L., P. Y. Hicher, and L. Sibille (2010). "Multiscale approaches to describe mechanical responses induced by particle removal in granular materials". In: *Comptes Rendus Mécanique* 338.10-11, pp. 627–638. DOI: 10.1016/j.crme.2010.10.003.

Schulze, D. (2008). *Powders and bulk solids: Behavior, characterization, storage and flow*. Berlin: Springer. URL: http://dx.doi.org/10.1007/978-3-540-73768-1.

Semar, O., K. J. Witt, and R. J. Fannin (2010). "Suffusion Evaluation-Comparison of Current Approaches". In: *International Conference on Scour and Erosion (ICSE-5)*, pp. 251–262. DOI: 10.1061/41147(392)24.

Shi, Y. F., Y. S. Yu, and L. T. Fan (1984). "Incipient fluidization condition for a tapered fluidized bed". In: *Industrial & Engineering Chemistry Fundamentals* 23.4, pp. 484–489. DOI: 10.1021/i100016a018.

Shire, T. and C. O'Sullivan (2013). "Micromechanical assessment of an internal stability criterion". In: *Acta Geotechnica* 8.1, pp. 81–90. DOI: 10.1007/s11440-012-0176-5. URL: https://link.springer.com/content/pdf/10.1007/s11440-012-0176-5.pdf.

Sommerfeld, M. (2017). "Numerical Methods for Dispersed Multiphase Flows". In: *Particles in Flows*. Ed. by T. Bodnár, G. P. Galdi, and Š. Nečasová. Vol. 30. Advances in

Mathematical Fluid Mechanics. Cham: Springer International Publishing, pp. 327–396. DOI: 10.1007/978-3-319-60282-0_6.

Stanier, S. A., J. Blaber, W. A. Take, and D. J. White (2016). "Improved image-based deformation measurement for geotechnical applications". In: *Canadian Geotechnical Journal* 53.5, pp. 727–739. DOI: 10.1139/cgj-2015-0253.

Statoil ASA, S. (Feb. 2018). *The world's first floating wind farm has already exceeded expectations.* https://www.equinor.com/en/news/15feb2018-world-class\protect\discretionary{\char\hyphenchar\font}{}{}performance.html. accessed: 2018-08-28. Statoil ASA, Stavanger.

Sun, R. and H. Xiao (2015). "Diffusion-Based Coarse Graining in Hybrid Continuum-Discrete Solvers: Applications in CFD-DEM". In: *International Journal of Multiphase Flow* 77, pp. 142–157.

"Zweidimensionale Potentialströmung" (2007). In: *Angewandte Strömungsmechanik*. Ed. by D. Surek and S. Stempin. Wiesbaden: B.G. Teubner Verlag / GWV Fachverlage GmbH Wiesbaden, pp. 221–242. DOI: 10.1007/978-3-8351-9094-8_8.

Sutton, M. A., S. R. McNeill, J. D. Helm, and Y. J. Chao (2000). "Advances in Two-Dimensional and Three-Dimensional Computer Vision". In: *Photomechanics, Topics in Applied Physics* 77, pp. 323–372. DOI: 10.1007/3-540-48800-6_10.

Tanaka, T., K. Yamagata, and Y. Tsuji (1990). "Experiment of fluid forces on a rotating sphere and spheroid". In: *Proceedings of the 2nd KSME-JSME Fluids Engineering Conference*. Vol. 1.

Tao, H. and J. Tao (2017). "Numerical Modeling and Analysis of Suffusion Patterns for Granular Soils". In: *Geotechnical Frontiers 2017*. Ed. by T. L. Brandon and R. J. Valentine. Geotechnical Special Publications. Reston: American Society of Civil Engineers, pp. 487–496. DOI: 10.1061/9780784480472.051.

Terzaghi, K. (1936). "Stress distribution in dry and in saturated sand above a yielding trapdoor". In: *International Conference of soil mechanics, Havard University, Camebridge, USA*, pp. 307–311.

Terzaghi, K. (1943). *Theoretical Soil Mechanics*. Hoboken, NJ, USA: John Wiley & Sons, Inc. DOI: 10.1002/9780470172766.

Terzaghi, K. (1956). "Varieties of Submarine Slope Failures". In: *Proceedings of the Eights Texas Conference on Soil Mechanics and Foundation Engineering*. Vol. 25.

Terzaghi, K. and R. B. Peck (1961). *Die Bodenmechanik in der Baupraxis*. Berlin, Heidelberg: Springer Berlin Heidelberg. DOI: 10.1007/978-3-642-92829-1.

Thielicke, W. and E. J. Stamhuis (2014). "PIVlab – Towards User-friendly, Affordable and Accurate Digital Particle Image Velocimetry in MATLAB". In: *Journal of Open Research Software* 2, p. 1202. DOI: 10.5334/jors.bl.

Tomac, I. and M. Gutierrez (2014). "Fluid lubrication effects on particle flow and transport in a channel". In: *Inernational Journal of Mulitphase Flow* 65, pp. 143–156.

Tomas, J. (2001). "Assessment of Mechanical Properties of Cohesive Particulate Solids. Part 1: Particle Contact Constitutive Model". In: *Particulate Science and Technology* 19.2, pp. 95–110. DOI: 10.1080/02726350152772056.

Torrey, V. H. (1995). "Flow slides in Mississippi riverbanks". In: *River, coastal, and shoreline protection*. Ed. by C. R. Thorne. Chichester and New York: J. Wiley, pp. 361–377.

Tsuji, Y., T. Kawaguchi, and T. Tanaka (1993). "Discrete particle simulation of two-dimensional fluidized bed". In: *Powder Technology* 77.1, pp. 79–87. DOI: 10.1016/0032-5910(93)85010-7.

van Buijtenen, M. S., N. G. Deen, S. Heinrich, S. Antonyuk, and J. A. M. Kuipers (2009). "A discrete element study of wet particle-particle interaction during granulation in a spout fluidized bed". In: *The Canadian Journal of Chemical Engineering* 87.2, pp. 308–317. DOI: 10.1002/cjce.20144.

van Buijtenen, M. S., W.-J. van Dijk, N. G. Deen, J. Kuipers, T. Leadbeater, and D. J. Parker (2011). "Numerical and experimental study on multiple-spout fluidized beds". In: *Chemical Engineering Science* 66.11, pp. 2368–2376. DOI: 10.1016/j.ces.2011.02.055.

van den Berg, J. H., A. van Gelder, and D. R. Mastbergen (2002). "The importance of breaching as a mechanism of subaqueous slope failure in fine sand". In: *Sedimentology* 49.1, pp. 81–95. DOI: 10.1046/j.1365-3091.2002.00433.x.

van Rhee, C. (1998). *The Breaching of Sand Investigated in Large-Scale Model Tests*. Virginia: American Society of Civil Engineers.

van Zyl, J. E., M. O. A. Alsaydalani, C. R. I. Clayton, T. Bird, and A. Dennis (2013). "Soil fluidisation outside leaks in water distribution pipes – preliminary observations". In: *Proceedings of the Institution of Civil Engineers - Water Management* 166.10, pp. 546–555. DOI: 10.1680/wama.11.00119.

Vardoulakis, I., M. Stavropoulou, and A. Skjaerstein (1998). "Porosity waves in a fluidized sand–column test". In: *Philosophical transactions. Series A, Mathematical, physical, and engineering sciences* 356.1747, pp. 2591–2608. DOI: 10.1098/rsta.1998.0288.

Vesic, A. S. (1969). *Breakout Resistance of Objects Embedded in Ocean Bottom*. Druham, North Carolina.

Wadell, H. (1935). "Volume, Shape, and Roundness of Quartz Particles". In: *The Journal of Geology* 43.3, pp. 250–280. DOI: 10.1086/624298.

Wang, Y., Z. Zou, H. Li, and Q. Zhu (2014). "A new drag model for TFM simulation of gas–solid bubbling fluidized beds with Geldart-B particles". In: *Particuology* 15, pp. 151–159. DOI: 10.1016/j.partic.2013.07.003.

Wen, C. Y. and Y. H. Yu (1966). "Mechanics of Fluidization". In: *Chemical Engineering Progress Symposium Series* 62, pp. 100–111.

White, D. J., W. A. Take, and M. D. Bolton (2003). "Soil deformation measurement using particle image velocimetry (PIV) and photogrammetry". In: *Géotechnique* 53.7, pp. 619–631. DOI: 10.1680/geot.2003.53.7.619.

Wood, D. M., K. Maeda, and E. Nukudani (2010). "Modelling mechanical consequences of erosion". In: *Géotechnique* 60.6, pp. 447–457. DOI: 10.1680/geot.2010.60.6.447.

Yang, Z. X., J. Yang, and L. Z. Wang (2012). "On the influence of inter-particle friction and dilatancy in granular materials: A numerical analysis". In: *Granular Matter* 14.3, pp. 433–447. DOI: 10.1007/s10035-012-0348-x.

Yerro, A., A. Rohe, and K. Soga (2017). "Modelling Internal Erosion with the Material Point Method". In: *Procedia Engineering* 175, pp. 365–372. DOI: 10.1016/j.proeng.2017.01.048.

Yu, A. B. and B. H. Xu (2003). "Particle-scale modelling of gas-solid flow in fluidisation". In: *Journal of Chemical Technology & Biotechnology* 78.2-3, pp. 111–121. DOI: 10.1002/jctb.788.

Zeghal, M. and U. El Shamy (2004). "A continuum-discrete hydromechanical analysis of granular deposit liquefaction". In: *International Journal for Numerical and Analytical Methods in Geomechanics* 28.14, pp. 1361–1383. DOI: 10.1002/nag.390.

Zhang, F., M. Li, M. Peng, C. Chen, and L. Zhang (2019). "Three-dimensional DEM modeling of the stress–strain behavior for the gap-graded soils subjected to internal erosion". In: *Acta Geotechnica* 14.2, pp. 487–503. DOI: 10.1007/s11440-018-0655-4. URL: https://link.springer.com/content/pdf/10.1007/s11440-018-0655-4.pdf.

Zhao, J. and T. Shan (2013). "Coupled CFD–DEM simulation of fluid–particle interaction in geomechanics". In: *Powder Technology* 239, pp. 248–258. DOI: 10.1016/j.powtec.2013.02.003.

Zhao, T., S. Utili, and G. B. Crosta (2016). "Rockslide and Impulse Wave Modelling in the Vajont Reservoir by DEM-CFD Analyses". In: *Rock Mechanics and Rock Engineering* 49.6, pp. 2437–2456. DOI: 10.1007/s00603-015-0731-0.

Zhou, Y. C., B. D. Wright, R. Y. Yang, B. H. Xu, and A. B. Yu (1999). "Rolling friction in the dynamic simulation of sandpile formation". In: *Physica A: Statistical Mechanics and its Applications* 269.2-4, pp. 536–553. DOI: 10.1016/S0378-4371(99)00183-1.

Zhu, H. P. and A. B. Yu (2002). "Averaging method of granular materials". In: *Physical review. E, Statistical, nonlinear, and soft matter physics* 66.2 Pt 1, p. 021302. DOI: 10.1103/PhysRevE.66.021302.

Zhu, H. P., Z. Y. Zhou, R. Y. Yang, and A. B. Yu (2007). "Discrete particle simulation of particulate systems: Theoretical developments". In: *Chemical Engineering Science* 62.13, pp. 3378–3396. DOI: 10.1016/j.ces.2006.12.089.

Ziems, J. (1969). *Beitrag zur Kontakterosion nichtbindiger Erdstoffe*. URL: https://books.google.de/books?id=mBgRtwAACAAJ.

Norms and standards

DIN 18126 (n.d.). *Baugrund, Untersuchung von Bodenproben - Bestimmung der Dichte nichtbindiger Böden bei lockerster und dichtester Lagerung*. Beuth Verlag.

Appendix A Notation

Nomenclature

Latin symbols

$\boldsymbol{F}_i^f$	Particle-fluid interaction force
$\boldsymbol{F}_i^g$	Gravitational force
$\boldsymbol{F}_n$	Normal contact force
$\boldsymbol{F}_t$	Tangential contact force
$\boldsymbol{F}_{ij}^c$	Contact force between particle i and j
$\boldsymbol{F}_{ik}^{nc}$	Non-contact force between particle i and k
$\boldsymbol{M}_{ij}$	Contact torque between particle i and j
$\boldsymbol{u}$	Fluid velocity
$\boldsymbol{v}_i$	Translational velocity of a particle i
$\boldsymbol{v}_n$	Relative normal velocity
$\boldsymbol{v}_t$	Relative tangential velocity
$\boldsymbol{x}_{p,n}$	Normal spatial overlap
$\boldsymbol{x}_{p,t}$	Tangential spatial overlap
a	Distance between particle surfaces
A_r	Archimedes number
C_D	Drag force coefficient
c_n	Normal damping coefficient
c_t	Tangential damping coefficient
c_v	consolidation coefficient
$C_{L,R}$	Lift coefficient

d_p Particle diameter

E^* Effective modulus of elasticity of contact partners

e_n Coefficient of restitution

e_n Restitution coefficient

E_s Stiffness modulus of soil

E_p Elastic modulus of partice

E_w Elastic modulus of wall

F_{Basset} Basset history force

F_{Mag} Magnus lift force

F_{Saffman} Saffman lift force

F_D Drag force

F_{D0} Drag force on a single particle

F_{D0} Drag force on isolated particle

F_{el} Elastic part of contact force

F_{vm} Virtual mass force

I_i Impulse of a particle i

K_f Permeability

k_n Normal spring stiffness

k_t Tangential spring stiffness

$k_{n,el}$ Contact stiffness in normal direction

K_{pf} Interaction force coefficient

m_i Mass of a particle i

n Void fraction

n Void fraction

p Fluid pressure

$p_{\max}$ Maximum contact pressure

p_{el} Elastic part of pressure distribution at particle contact

R^* Characteristic radius of the contact surface curvature

r_k Radius of contact area of a particle

$r_{k,el}$ Elastic parto of the radius of contact area of a particle

R_{pf} Particle-Fluid momentum exchange term

r_p Particle radius

Re_p Particle Reynolds number

s Elastic displacement in normal direction

t Time

t_p Particle response time

U Superficial fluid velocity

u_w Pore water pressure

u_{mf} Minimum fluidisation velocity

V_{cell} Volume of computational cell

v_{ini} Initial particle velocity (before impact)

v_{R} Particle velocity in restitution phase (after impact)

V_p Particle Volume

v_r Relative velocity between particle i and j

z Depth below surface

Greek letters

Δt Time interval

γ' Submerged unit weight

γ_w Specific weight of water

μ Friction coefficient

μ_f Fluid dynamic viscosity

μ_r Rolling friction coefficient

ν_f Kinematic fluid viscosity

ν_p Poisson ratio of particle

ν_w Poisson ratio of wall

Ω Spin parameter

ω_f Rotational speed of fluid

ω_p Rotational speed of particle

ϕ Solids fraction

ψ Dilation angle

ρ_f Fluid density

ρ_s Particle density

τ_f Fluid viscous stress tensor

φ Internal friction angle

φ_0 Angle of repose

φ_c Critical friction angle

φ_s Sphericity of particle

$\boldsymbol{\omega}_i$ Angular velocity of a particle i

Abbreviations

CFD Computational Fluid Dynamics

DEM Discrete Element Method

DIC Digital image correlation

DNS Direct Numerical Simulation

FVM Finite Volume Method

HMCM Hertz-Mindlin contact model

IBM Immersed Boundary Method

LBM Lattice-Boltzmann method

LSDM Linear Spring Dashpot Model

PIV Particle Image Velocimetry

RANS Reynolds averaged Navier-Stokes Equations

ROI Region of interest

STF Shear-thickening fluid

TFM Two-fluid method

VOF Volume of Fraction method

Physics Constants

g Gravitational Constant

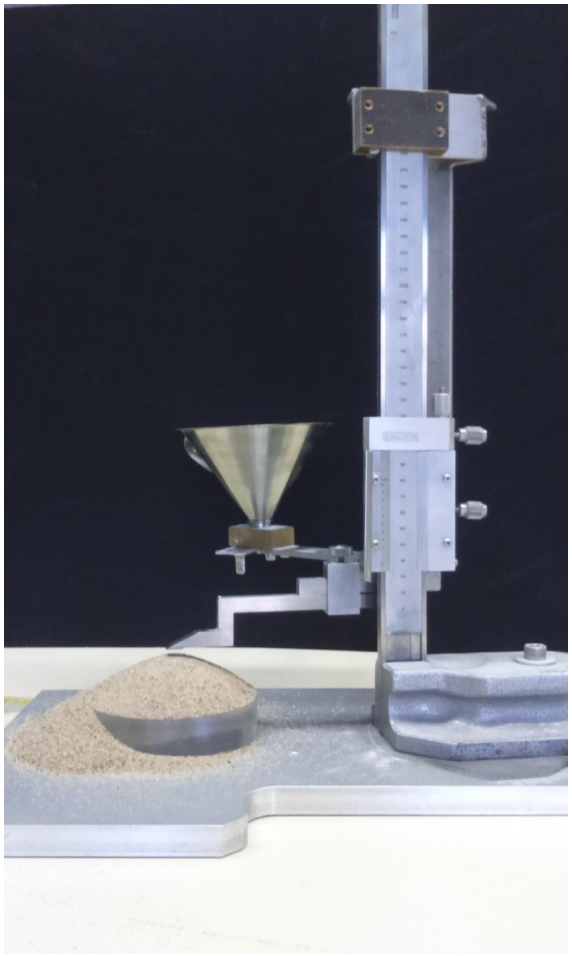
Appendix B Material tests

B.1 Shear cell test

Mittelwerte	SIGMA,pre,m Pa	TAU,pre,m Pa	TAU,pre,SD Pa	Anzahl der Punkte
	643	591,86	55,66	7
	1244	1033,14	34,94	7
	2244	1972,14	82,25	7
	3343	2912,14	142,90	7
	4543	3687,50	115,92	6

Reibungskoeffizient beim Anscheren		Kohäsion [Pa]	Reibungswinkel [°]
Mittelwert, ohne Kohäsion	0,84	0	40,01
Mittelwert, mit Kohäsion	0,81	85,55	39,11

Boschungswinkel =	**31,03 °**
h=30.08 mm	**Good Flowabilty**



PROTOCOL	-	TEST	WITH		RING	SHEAR	TESTER	RST-XS.s
Date:	7/13/2016,	Time:		12:13:03	PM			

YIELD	LOCUS	OF:	Sand_1mm_Cell_La_600Pa_01
ORDER:	1		

Prorating:	Yes		
Approximation:	Linear	regression	
N-RHOB-correction:	No		

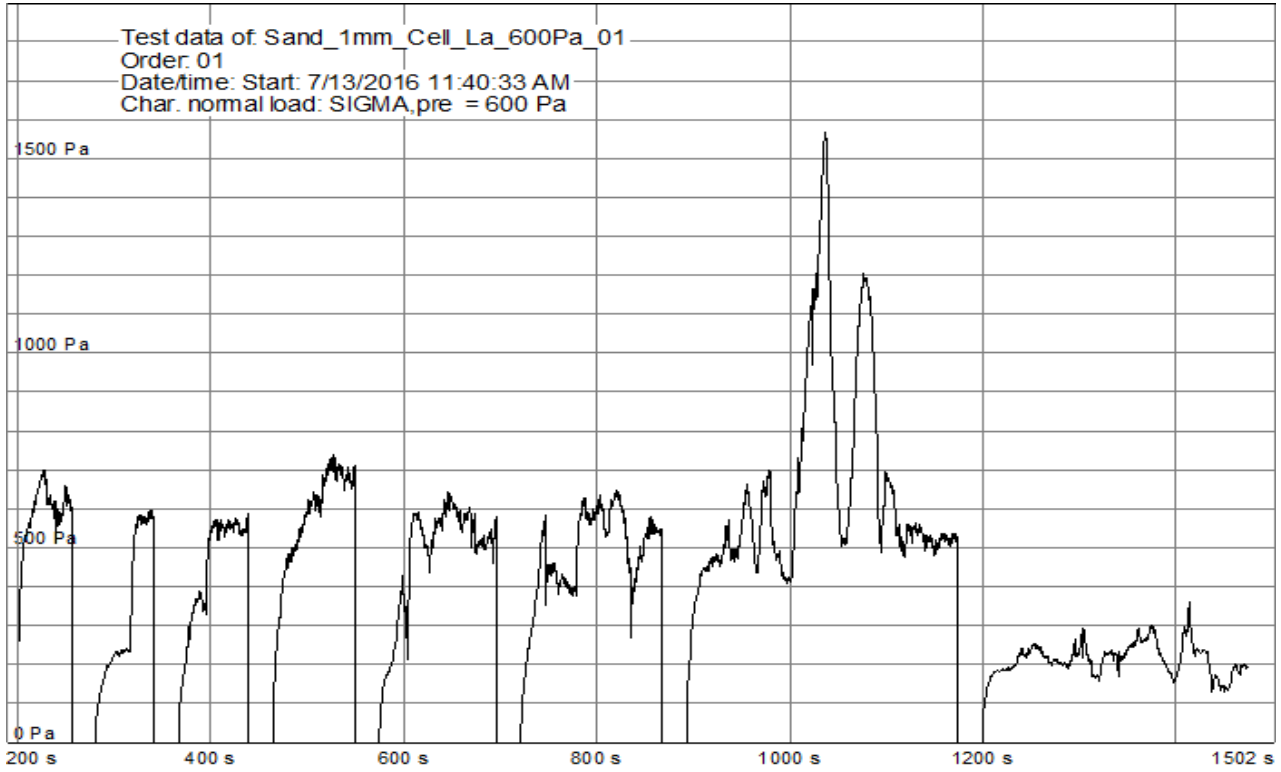
SIGMA,pre,m	=	643	Pa		
TAU,pre,m	=	**591,86**	Pa	**55,66**	
SIGMA1	=		Pa		
FC	=		Pa		
RHOB	=	1481	kg/m3		
PHIE	=				
PHILIN	=				
PHISF	=	**42,63**	0,92		
FFC	=				
FFRHO	=				
TAU,C	=		Pa		

No.		m [g]	Dh [mm]	RHOB [kg/m3]	TAU,pre	SIGMA,sh	TAU,sh,pr
1	2	319,3	-0,077	1478	605	194	234
2	2	319,3	-0,051	1480	581	359	394
3	2	319,3	-0,053	1480	587	524	645
4	2	319,3	-0,038	1481	700	194	357
5	2	319,3	-0,053	1480	600	359	606
6	2	319,3	-0,033	1482	540	524	1707
7	2	319,3	0,015	1486	530	194	400

Warning(s):

SLIP-STICK DETECTED!

****** END OF FILE ******



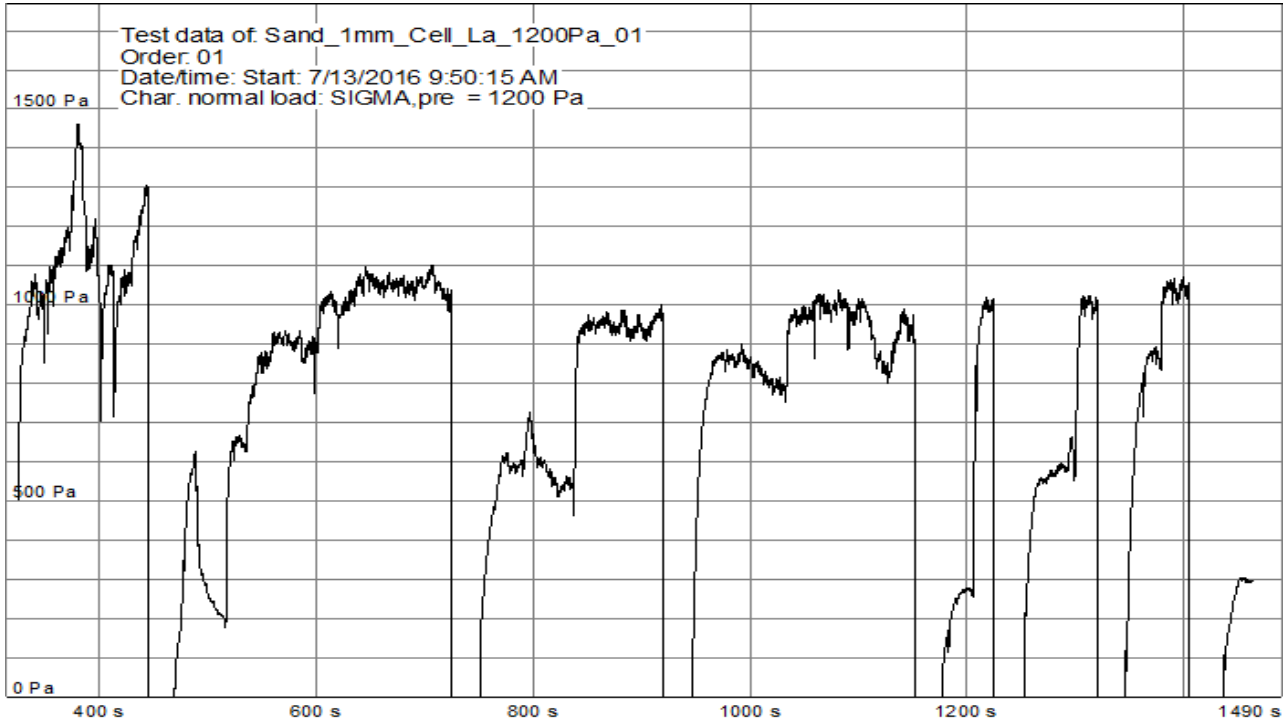
PROTOCOL	-	TEST	WITH		RING	SHEAR	TESTER	RST-XS.s
Date:	7/13/2016,	Time:		10:21:13	AM			
YIELD	LOCUS	OF:	Sand_1mm_Cell_La_1200Pa_01					
ORDER:		1						
Prorating:	Yes							
Approximation:	Linear	regression						
N-RHOB-correction:	No							
SIGMA,pre,m	=	1244	Pa					
TAU,pre,m	=	**1033,14286**	Pa		**34,945**			
SIGMA1	=		Pa					
FC	=		Pa					
RHOB	=		kg/m3					
PHIE	=							
PHILIN	=							
PHISF	=	**39,71**	0,83					
FFC	=							
FFRHO	=							
TAU,C	=		Pa					

No.	Shear	m [g]	Dh [mm]		RHOB [k	TAU,pre	SIGMA,sh	TAU,sh,pr
1	2	323,8		-0,533	1502	1100	284	552
2	2	323,8		-0,522	1503	1050	644	701
3	2	323,8		-0,476	1507	1000	1005	962
4	2	323,8		-0,464	1508	1020	284	299
5	2	323,8		-0,418	1512	1006	644	678
6	2	323,8		-0,414	1512	1012	1005	909
7	2	323,8		-0,386	1515	1044	285	301

Warning(s):

SLIP-STICK DETECTED!

****** END OF FILE ******



PROTOCOL	-	TEST	WITH		RING	SHEAR	TESTER	RST-XS.s
Date:	7/13/2016,	Time:		10:46:04	AM			

YIELD	LOCUS	OF:	Sand_1mm_Cell_La_2200Pa_01
ORDER:		1	

Prorating:	Yes
Approximation:	Linear regression
N-RHOB-correction:	No

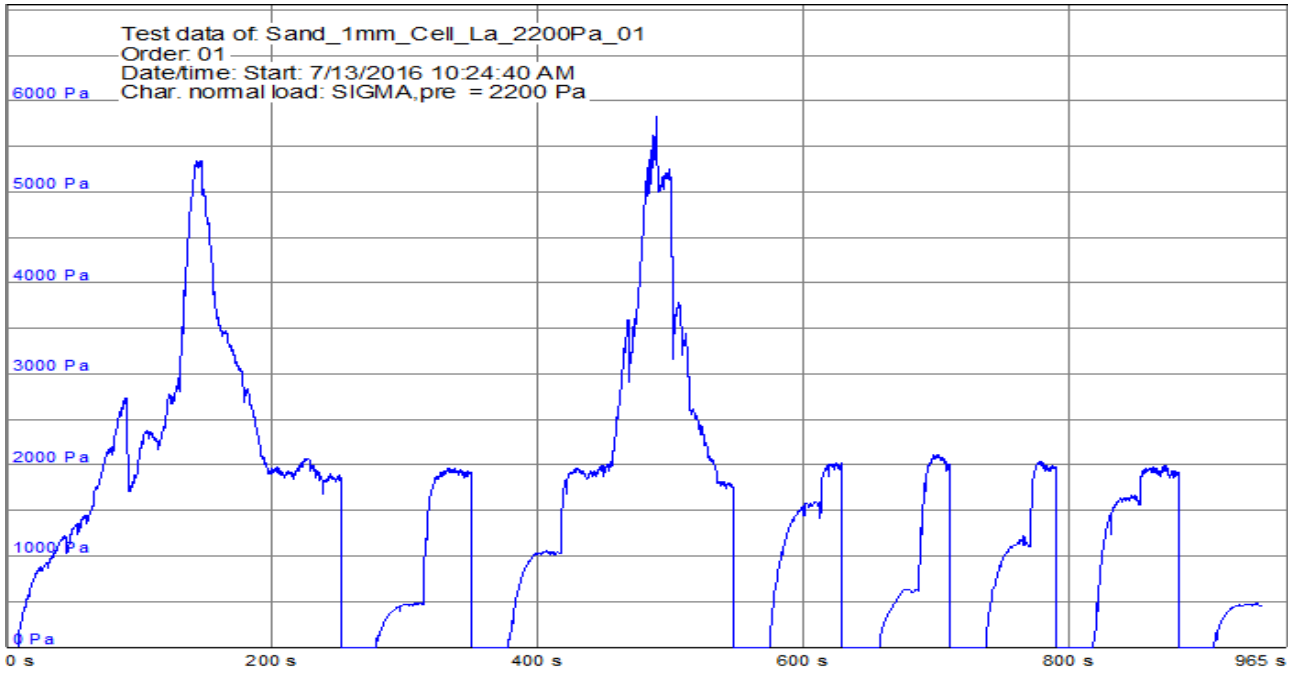
SIGMA,pre,m	=	2244	Pa	
TAU,pre,m	=	**1972,142857**	Pa	**82,253**
SIGMA1	=		Pa	
FC	=		Pa	
RHOB	=		kg/m3	
PHIE	=			
PHILIN	=			
PHISF	=	**41,31**	0,88	
FFC	=			
FFRHO	=			
TAU,C	=		Pa	

No.	Shear	m [g]	Dh [mm]		RHOB [k	TAU,pre	SIGMA,sh	TAU,sh,pr
1	2	320,9		-0,242	1486	1850	483	443
2	2	320,9		-0,217	1489	1900	1144	1256
3	2	320,9		-0,249	1486	1950	1803	1015
4	2	320,9		-0,203	1490	2025	483	708
5	2	320,9		-0,188	1491	2100	1144	1419
6	2	320,9		-0,178	1492	2000	1804	1946
7	2	320,9		-0,189	1491	1980	484	563

Warning(s):

SLIP-STICK DETECTED!
YIELD LOCUS CORRECTED.

****** END OF FILE ******



PROTOCOL	-	TEST	WITH		RING	SHEAR	TESTER	RST-XS.s
Date:	7/13/2016,	Time:		11:24:19	AM			

YIELD	LOCUS	OF:	Sand_1mm_Cell_La_3300Pa_01
ORDER:	1		

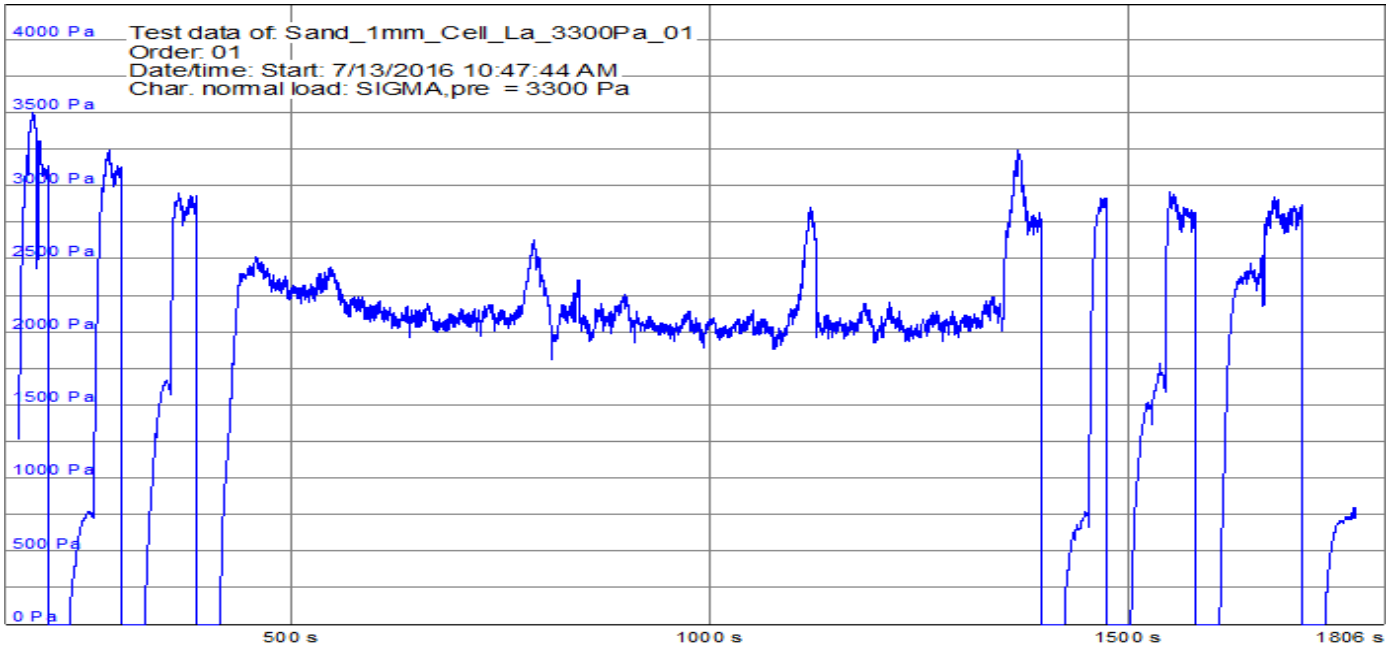
Prorating:	Yes		
Approximation:	Linear	regression	
N-RHOB-correction:	No		

SIGMA,pre,m	=	3343	Pa	
TAU,pre,m	=	**2912,14286**	Pa	**142,9025642**
SIGMA1	=		Pa	
FC	=		Pa	
RHOB	=		kg/m3	
PHIE	=			
PHILIN	=			
PHISF	=	**41,06**	0,87	
FFC	=			
FFRHO	=			
TAU,C	=		Pa	

No.	Shear	m [g]	Dh [mm]	RHOB [kg/m3]	TAU,pre	SIGMA,sh	TAU,sh,pr
1	2	320,7	-0,416	1468	3119	703	722
2	2	320,7	-0,401	1470	3106	1693	1556
3	2	320,7	-0,406	1469	2900	2683	2869
4	2	320,7	-0,534	1458	2800	702	808
5	2	320,7	-0,469	1464	2871	1693	1806
6	2	320,7	-0,475	1463	2789	2683	2632
7	2	320,7	-0,479	1463	2800	702	834

No warnings.

****** END OF FILE ******


Test data of: Sand_1mm_Cell_La_3300Pa_01
Order: 01
Date/time: Start: 7/13/2016 10:47:44 AM
Char. normal load: SIGMA,pre = 3300 Pa
4000 Pa
3500 Pa
3000 Pa
2500 Pa
2000 Pa
1500 Pa
1000 Pa
500 Pa
0 Pa
500 s
1000 s
1500 s
1806 s

PROTOCOL	-	TEST	WITH		RING	SHEAR	TESTER	RST-XS.s
Date:	7/13/2016,	Time:		12:35:01	PM			

YIELD	LOCUS	OF:	Sand_1mm_Cell_La_4500Pa_01
ORDER:		1	

Prorating:	Yes		
Approximation:	Linear	regression	
N-RHOB-correction:	No		

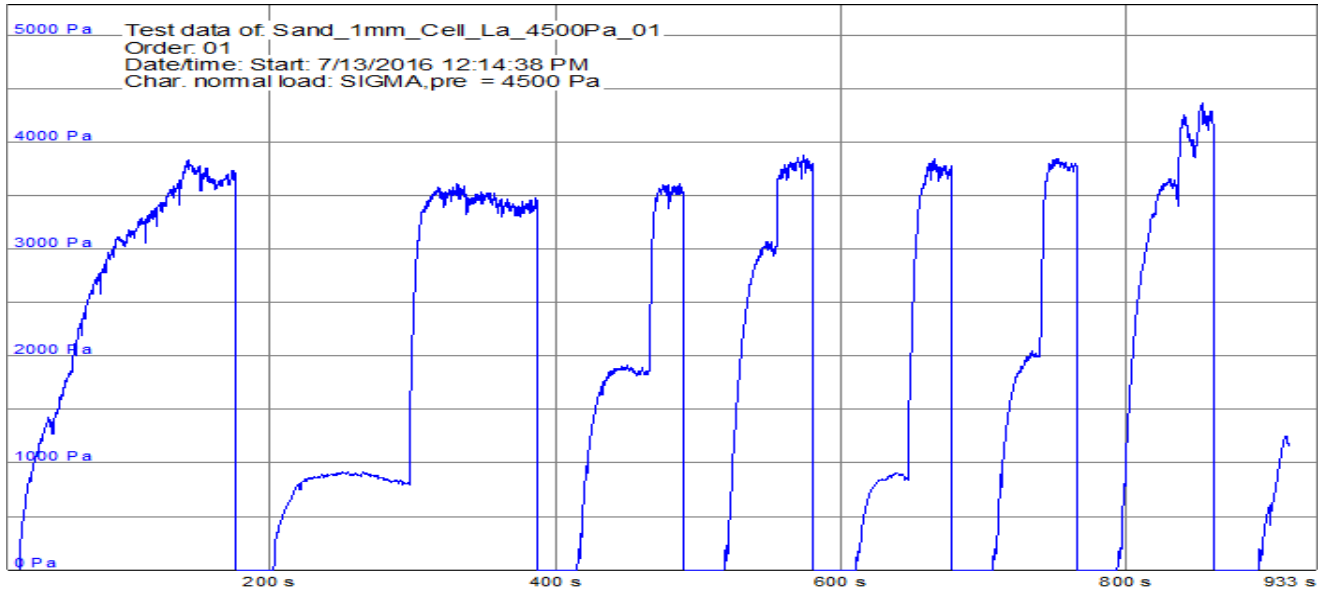
SIGMA,pre,m	=	4543	Pa		
TAU,pre,m	=	**3687,5**	Pa	**115,92**	
SIGMA1	=		Pa		
FC	=		Pa		
RHOB	=		kg/m3		
PHIE	=				
PHILIN	=				
PHISF	=	**39,07**		0,81	
FFC	=				
FFRHO	=				
TAU,C	=		Pa		

No.	Shear	m [g]	Dh [mm]		RHOB [k	TAU,pre	SIGMA,sh	TAU,sh,pr
1	2	318,3		-0,115	1461	3700	943	1018
2	2	318,3		-0,197	1454	3500	2292	2043
3	2	318,3		-0,163	1457	3600	3642	3211
4	2	318,3		-0,139	1459	3800	942	885
5	2	318,3		-0,129	1460	3750	2292	2021
6	2	318,3		-0,116	1461	3775	3642	3566
7	2	318,3		-0,118	1460			1110

Warning(s):

SLIP-STICK DETECTED!

****** END OF FILE ******

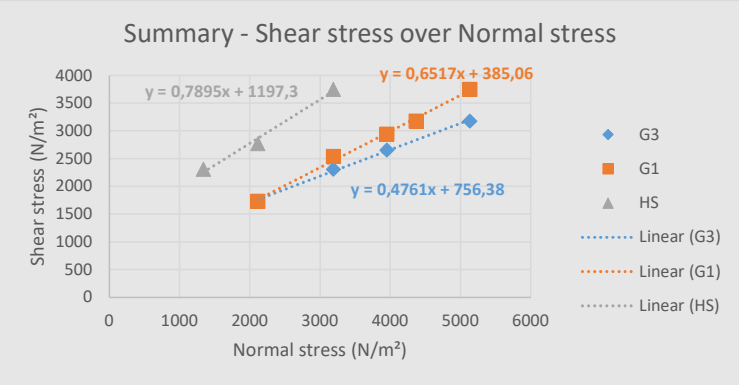


Summary

Normal weight (N)	Glass 3mm	Glass 1mm	Hamburger Sand
8,08	-	-	-
11,6	-	-	x
18,3	x	x	x
27,6	x	x	x
34,22	x	x	x
37,82	-	x	-
44,44	x	x	-

Normal weight (N)	Glass 3mm	Glass 1mm	Hamburger Sand
8,08	-	-	-
11,6	-	-	20
18,3	15	15	24
27,6	20	22	32,5
34,22	23	25,5	-
37,82	-	27,5	-
44,44	27,5	32,5	-

Diameter: 0,105 Height: 0,03 Add. Weigh 0,38966



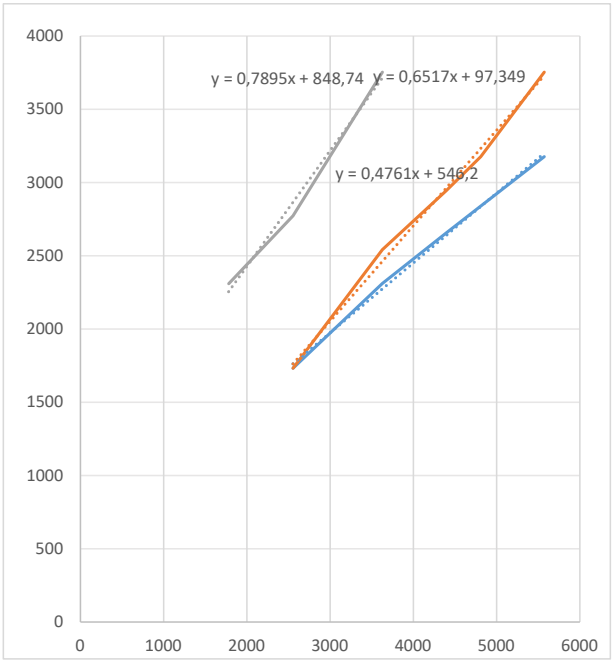
	Normal force (+part weight)	
8,08	11,902522	1374,581567
11,6	15,422522	1781,094328
18,3	22,122522	2554,854414
27,6	31,422522	3628,879609
34,22	38,042522	4393,400768
37,82	41,642522	4809,152456
44,44	48,262522	5573,673616

Details

Normal weight (N)	G3 - M1	G3 - M2	G3 - M3	G3 - M4	G3 - M5	G1 - M1	G1 - M2	G1 - M3	G1 - M4	G1 - M5
11,6	-	-	-	-	-	-	-	-	-	-
18,3	x	x	-	x	x	x	x	x	x	x
27,6		x	x	x	x	x	x	x	x	x
34,22	x	x	x	x	x	x	x	x	x	x
37,82	-	-	-	-	-	x	x	x	x	x
44,44	x	x	x	x	x	x	x	x	x	x

Normal weight (N)	Glass 3mm	Glass 1mm	Hamburger Sand
933,1315666	-	-	-
1339,644328	-	-	2309,7316
2113,404414	1732,2987	1732,2987	2771,677921
3187,429609	2309,7316	2540,7048	3753,313851
3951,950768	2656,19134	2944,9078	-
4367,702456	-	3175,881	-
5132,223616	3175,88095	3753,3139	-

Normal weight (N)	Glass 3mm	Glass 1mm	Hamburger Sand
8,08	-	-	-
11,6	-	-	1,724137931
18,3	0,81967213	0,8196721	1,31147541
27,6	0,72463768	0,7971014	1,177536232
34,22	0,67212157	0,7451783	
37,82		0,7271285	-
44,44	0,61881188	0,7313231	-



HS - M1	HS - M2	HS - M3	HS - M4	HS - M5
-	x	x	x	-
x	-	-	x	x
-	x	x	x	x
-	-	-	-	-
-	-	-	-	-
-	-	-	-	-

B.2 Triaxial test

X:\laborgutachten\intern-Labor_2016\i0616_Glaspartikel-3ax-D-ManuelaKanitz\[Triax-CU-Glaskugeln-3mm.xls]Anlage-Blatt1

TUHH
Technische Universität Hamburg-Harburg
Geotechnik und Baubetrieb
Univ.-Prof. Dr.-Ing. Jürgen Grabe

Harburger Schloßstr. 20
21079 Hamburg
Tel.: +49 (0)40 / 428 78-3782
Fax: +49 (0)40 / 428 78-4020
www.tu-harburg.de/gbt

Anlage
Blatt 1/6
Oktober 2016

TRIAXIALVERSUCH

DIN 18 137 - CU

Projekt Nr.: i0616
Glaskugeln 3 mm

Entnahmestelle: -
Entnahmetiefe: -
Bodenart: 3 mm Glaskugeln

Probenherstellung		1	2	3
Anfangsprobenhöhe h_0	[mm]	120,0	120,0	120,0
Anfangsprobendurchmesser d_0	[mm]	50,0	50,0	50,0
Anfangsprobenfeuchtmasse m_0	[g]	456,51	454,98	456,36
Trockenmasse der Probe m_d	[g]	375,72	375,72	375,72
Einbau Wassergehalt w	[%]	21,50	21,10	21,46
Einbaudichte ρ	[g/cm³]	1,938	1,931	1,937
Einbautrockendichte ρ_d	[g/cm³]	1,595	1,595	1,595
Porenanteil n	[-]	0,36	0,36	0,36
Porenzahl e	[-]	0,57	0,57	0,57
Sättigungsgrad S_r	[-]	0,95	0,93	0,95
Lagerungsdichte D	[-]	0,501	0,501	0,501
bezogene Lagerungsdichte I_D	[-]	0,519	0,519	0,519

Sättigung

Zelldruck σ_3	[kPa]	410,0	410,0	410,0
Sättigungsdruck u *(back pressure)*	[kPa]	400,0	400,0	400,0
Wassergehalt nach der Sättigung	[%]	22,71	22,71	22,71
Dichte	[g/cm³]	1,957	1,957	1,957

Konsolidation

Zelldruck σ_3 *(cell pressure)*	[kPa]	449,4	499,6	599,5
Porenwasserdruck u *(back pressure)*	[kPa]	400,0	400,0	400,0

Bearbeiter: ...ege.....

Geprüft von: .....gb.....

TUHH
Technische Universität Hamburg-Harburg
Geotechnik und Baubetrieb
Univ.-Prof. Dr.-Ing. Jürgen Grabe
Harburger Schloßstr. 20
21079 Hamburg
Tel.: +49 (0)40 / 428 78-3782
Fax: +49 (0)40 / 428 78-4020
www.tu-harburg.de/gbt

TRIAXIALVERSUCH

DIN 18 137 - CU

Projekt Nr.: i0616
Glaskugeln 3 mm

Entnahmestelle: -
Entnahmetiefe: -
Bodenart: 3 mm Glaskugeln

nach der Konsolidation, vor dem Abscheren		1	2	3
Volumen der Probe V_a	[cm³]	231,9	228,9	228,4
Probenhöhe h_a	[mm]	119,4	118,9	118,8
Wassergehalt nach der Konsolidation	[%]	21,72	20,91	20,80
Anfangsdichte	[g/cm³]	1,972	1,985	1,987
Anfangstrockendichte	[g/cm³]	1,620	1,642	1,645
Porenanteil n	[-]	0,352	0,343	0,342
Porenzahl e	[-]	0,543	0,523	0,520
Sättigungsgrad S_r	[-]	1,00	1,00	1,00
Lagerungsdichte D	[-]	0,73	0,92	0,95
bezogene Lagerungsdichte I_D	[-]	0,74	0,92	0,95

Abscheren

Zelldruck σ_3	[kPa]	449,4	499,6	599,5
Porenwasserdruck u *(back pressure)*	[kPa]	400,0	400,0	400,0
Schergeschwindigkeit	[mm/min]	0,050	0,050	0,050
Volumenänderung ΔV	[cm³]	0,0	0,0	0,0
Volumen der Probe nach dem Abscheren V_{end}	[cm³]	231,9	228,9	228,4
Feuchtmasse der Probe m_a	[g]	457,3	454,3	453,9
Trockenmasse der Probe m_d	[g]	375,7	375,7	375,7
Wassergehalt nach dem Abscheren	[%]	21,7	20,9	20,8
Dichte nach dem Abscheren	[g/cm³]	1,972	1,985	1,987
Trockendichte nach dem Abscheren	[g/cm³]	1,620	1,642	1,645
Porenanteil n	[-]	0,352	0,343	0,342
Porenzahl e	[-]	0,543	0,523	0,520
Sättigungsgrad S_r	[-]	1,00	1,00	1,00
Lagerungsdichte D	[%]	0,73	0,92	0,95
bezogene Lagerungsdichte I_D	[g/cm³]	0,74	0,92	0,95

Bearbeiter: .....

Geprüft von: .....

TUHH
Technische Universität Hamburg-Harburg
Geotechnik und Baubetrieb
Univ.-Prof. Dr.-Ing. Jürgen Grabe
Harburger Schloßstr. 20
21079 Hamburg
Tel.: +49 (0)40 / 428 78-3782
Fax: +49 (0)40 / 428 78-4020
www.tu-harburg.de/gbt

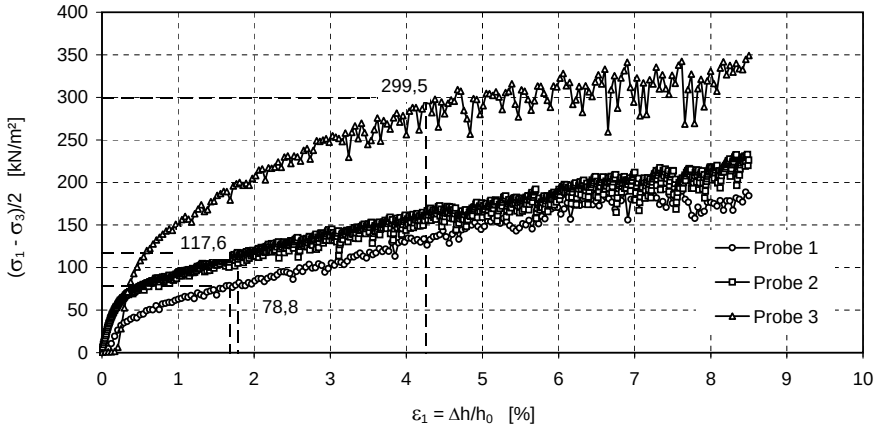
TRIAXIALVERSUCH

DIN 18 137 - CU

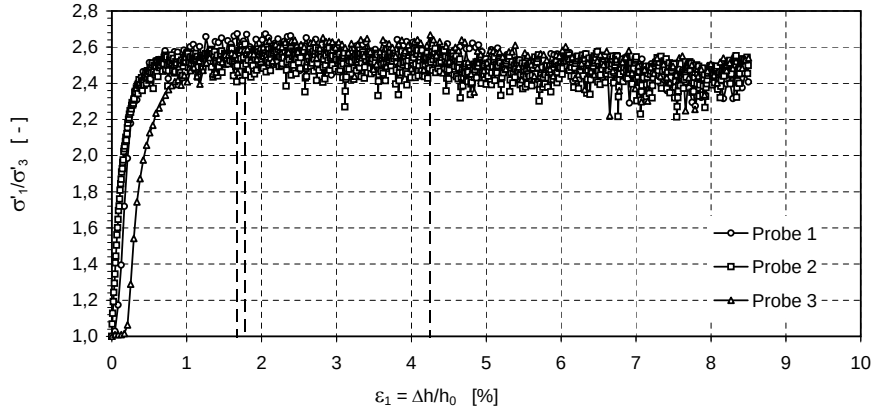
Projekt Nr.: i0616
Glaskugeln 3 mm

Entnahmestelle: -
Entnahmetiefe: -
Bodenart: 3 mm Glaskugeln

Stauchung - Spannung Diagramm



Stauchung - Hauptspannungsverhältnis Diagramm



Bearbeiter: .....

Geprüft von: .....

TUHH
Technische Universität Hamburg-Harburg
Geotechnik und Baubetrieb
Univ.-Prof. Dr.-Ing. Jürgen Grabe
Harburger Schloßstr. 20
21079 Hamburg
Tel.: +49 (0)40 / 428 78-3782
Fax: +49 (0)40 / 428 78-4020
www.tu-harburg.de/gbt

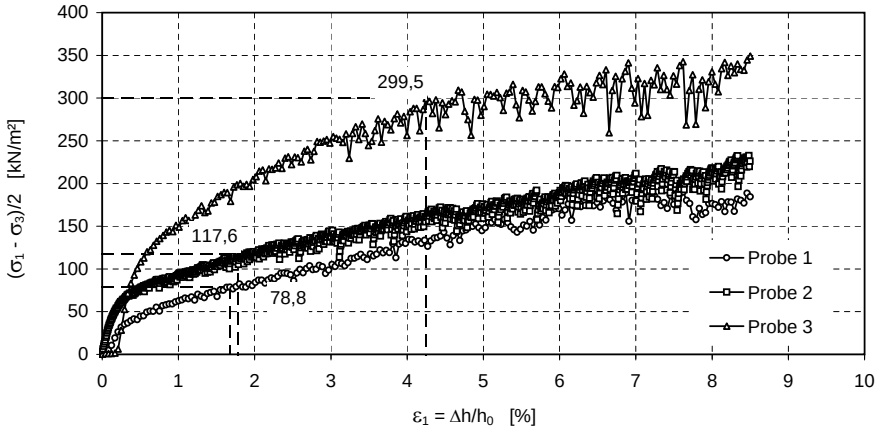
TRIAXIALVERSUCH

DIN 18 137 - CU

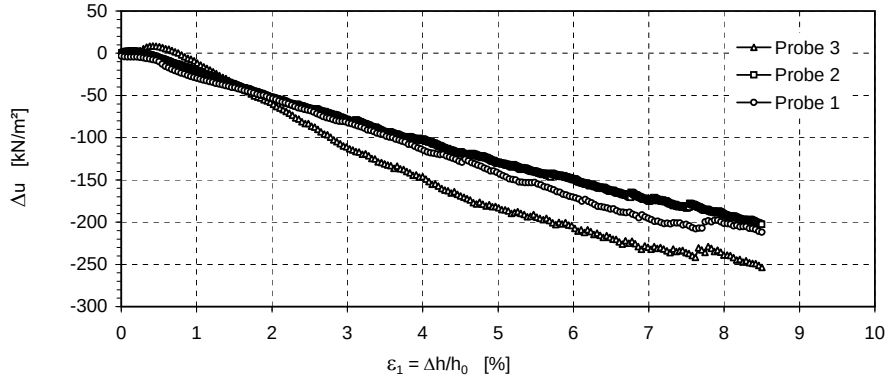
Projekt Nr.: i0616
Glaskugeln 3 mm

Entnahmestelle: -
Entnahmetiefe: -
Bodenart: 3 mm Glaskugeln

Stauchung - Spannung Diagramm



Stauchung - Porenwasserdifferenzdruck Diagramm



Bearbeiter: .....

Geprüft von: .....

TUHH
Technische Universität Hamburg-Harburg
Geotechnik und Baubetrieb
Univ.-Prof. Dr.-Ing. Jürgen Grabe
Harburger Schloßstr. 20
21079 Hamburg
Tel.: +49 (0)40 / 428 78-3782
Fax: +49 (0)40 / 428 78-4020
www.tu-harburg.de/gbt

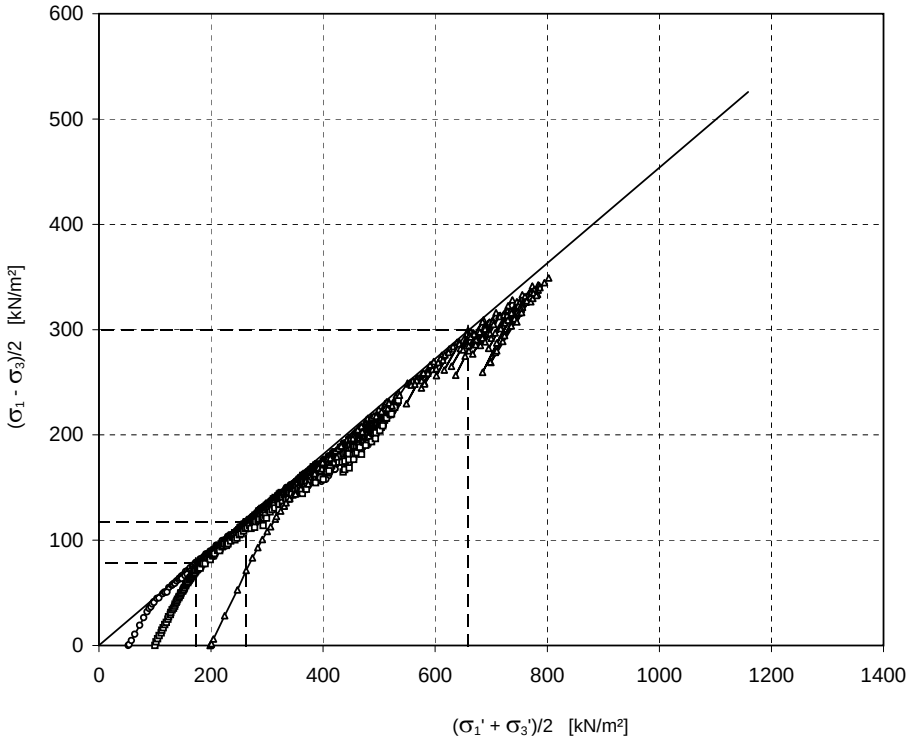
TRIAXIALVERSUCH

DIN 18 137 - CU

Projekt Nr.: i0616
Glaskugeln 3 mm

Entnahmestelle: -
Entnahmetiefe: -
Bodenart: 3 mm Glaskugeln

Effektive Spannungspfade und die Bruchgerade



tg α' - Neigung der Bruchgerade = 0,45377

b' - Achsenabschnitt der Bruchgerade = 0,0

$\tan \alpha' = \sin \varphi'$ $\quad b' = c' \cos \varphi'$

effektiver Reibungswinkel φ' = 27 °

effektive Kohäsion c' = 0 kN/m²

Bearbeiter: .....

Geprüft von: .....

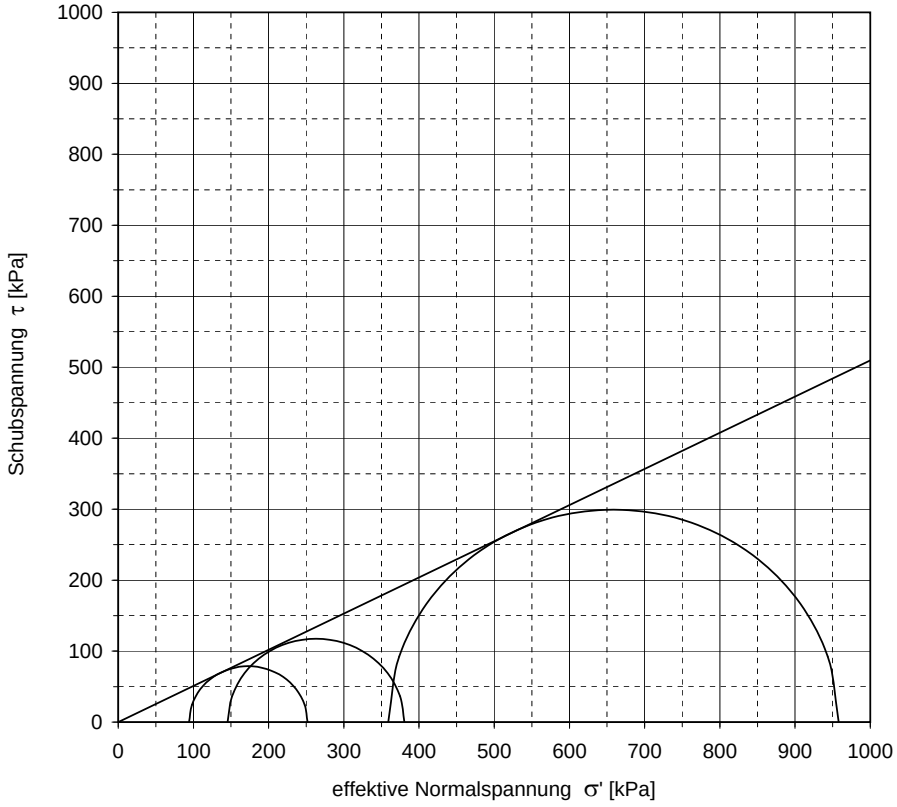
TUHH
Technische Universität Hamburg-Harburg
Geotechnik und Baubetrieb
Univ.-Prof. Dr.-Ing. Jürgen Grabe
Harburger Schloßstr. 20
21079 Hamburg
Tel.: +49 (0)40 / 428 78-3782
Fax: +49 (0)40 / 428 78-4020
www.tu-harburg.de/gbt

TRIAXIALVERSUCH

DIN 18 137 - CU

Projekt Nr.: i0616	Entnahmestelle: -
Glaskugeln 3 mm	Entnahmetiefe: -
	Bodenart: 3 mm Glaskugeln

Spannungskreise im Grenzzustand und die gerade Umhüllende
als Grenzbedingung nach Mohr-Coulomb



effektiver Reibungswinkel φ' = 27 °

effektive Kohäsion c' = 0 kN/m²

Bearbeiter: .....

Geprüft von: .....

B.3 Loosest and densest packing

TUHH
Technische Universität Hamburg
Geotechnik und Baubetrieb
Univ.-Prof. Dr.-Ing. Jürgen Grabe

Harburger Schloßstr. 20
21079 Hamburg
Tel.: +49 (0)40 / 428 78-3782
Fax: +49 (0)40 / 428 78-4020
www.tuhh.de/gbt

Anlage
03.08. 2016

Bestimmung der Dichte nichtbindiger Böden
bei lockerster und dichtester Lagerung
DIN 18126

Projekt Nr.: i0616
Silico Glaskugeln 3 mm

Entnahmestelle: Silico Glaskugeln 3 mm
Entnahmetiefe: -
Entnahmeart : GP
Bodenart: -

Korndichte ρ_S = 2,5 g/cm³ nach Herstellerangabe

Porenanteil in natürlicher Lagerung n = _____ %

Porenanzahl in natürlicher Lagerung e = _____

Ungleichförmigkeitszahl U = _____

Größtkorn *max* d = _____ mm

Bestimmung der Dichte in **lockerster Lagerung**

		1	2	
Versuchszylinder	V_Z = 942,48 cm³	1468,61	1434,14	g

		3	4	5	
Probenmasse		1472,61	1432,66	1440,08	g
	Mittelwert :	1449,62			g

min Trockendichte $min\ \rho_d = min\ m_d / V_Z$ = **1,538** g/cm³

max Porenanteil $max\ n = 1 - (min\ \rho_d / \rho_s)$ = **0,385**

max Porenzahl $max\ e = (\rho_s / min\ \rho_d) - 1$ = **0,625**

Bestimmung der Dichte in **dichtester Lagerung**

Versuchszylinder h = 12,0 cm A = 78,5 cm² Platte h_P = 4,0 cm

		1	2	
Setzung	x_1 =	31,2		mm
	x_2 =	31,9		mm
	x_3 =	32,2		mm
	Mittelwert s_m =	31,77		mm
Volumen	$minV = A*(h - h_P + s_m)$ =	877,8		cm³

max Trockendichte $max\ \rho_d = m_d / minV$ = **1,651** g/cm³

min Porenanteil $min\ n = 1 - (max\ \rho_d / \rho_s)$ = **0,339**

min Porenzahl $min\ e = (\rho_s / max\ \rho_d) - 1$ = **0,514**

Abgeleitete Größen

Lagerungsdichte $D = (max\ n - n) / (max\ n - min\ n)$ =

Bezogene Lagerungsdichte $I_D = (max\ e - e) / (max\ e - min\ e)$ =

Verdichtungsfähigkeit $I_f = (max\ e - min\ e) / min\ e$ = 0,22

TUHH
Technische Universität Hamburg-Harburg
Geotechnik und Baubetrieb
Univ.-Prof. Dr.-Ing. Jürgen Grabe

Harburger Schloßstr. 20
21079 Hamburg
Tel.: +49 (0)40 / 428 78-3782
Fax: +49 (0)40 / 428 78-4020
www.tu-harburg.de/gbt

Anlage
Dezember 2016

Bestimmung der Dichte nichtbindiger Böden bei lockerster und dichtester Lagerung DIN 18126

Projekt Nr.:

Entnahmestelle:
Entnahmetiefe: -
Entnahmeart :
Bodenart: Glasperlen 1mm

Korndichte ρ_S = 2,65 g/cm³

Porenanteil in natürlicher Lagerung	n =		%
Porenanzahl in natürlicher Lagerung	e =		
Ungleichförmigkeitszahl	U =		
Größtkorn	*max* d =	<2	mm

Bestimmung der Dichte in **lockerster Lagerung**

Versuchszylinder V_Z = 443,43 cm³ m_Z =

Probenmasse	min m_{d1} =		656,6	g
	min m_{d2} =		657,1	g
	min m_{d3} =		657,9	g
	min m_{d4} =		656,4	g
	min m_{d5} =		656,9	g
	Mittelwert :		656,98	g

min Trockendichte	$min\ \rho_d = min\ m_d / V_Z$ =	1,482	g/cm³
max Porenanteil	$max\ n = 1 - (min\ \rho_d / \rho_s)$ =	0,441	
max Porenzahl	$max\ e = (\rho_s / min\ \rho_d) - 1$ =	0,789	

Bestimmung der Dichte in **dichtester Lagerung**

Versuchszylinder h = 11,25 cm A = 39,6 cm² Platte h_P = 1,50 cm

Probenmasse	m_d =	656,9	g
Setzung	s_1 =	6,80	mm
	s_2 =	6,70	mm
	s_3 =	6,60	mm
	Mittelwert s_m =	6,70	mm
Volumen	minV = A*(h–h_P–s_m) =	412,55	cm³

max Trockendichte	$max\ \rho_d = m_d / minV$ =	1,592	g/cm³
min Porenanteil	$min\ n = 1 - (max\ \rho_d / \rho_s)$ =	0,399	
min Porenzahl	$min\ e = (\rho_s / max\ \rho_d) - 1$ =	0,664	

Abgeleitete Größen

Lagerungsdichte	D = (max n – n) / (max n – min n) =	
Bezogene Lagerungsdichte	I_D = (max e – e) / (max e – min e) =	
Verdichtungsfähigkeit	I_f = (max e – min e) / min e =	0,19

TUHH
Technische Universität Hamburg-Harburg
Geotechnik und Baubetrieb
Univ.-Prof. Dr.-Ing. Jürgen Grabe

Harburger Schloßstr. 20
21079 Hamburg
Tel.: +49 (0)40 / 428 78-3782
Fax: +49 (0)40 / 428 78-4020
www.tu-harburg.de/gbt

Anlage
März 2013

Bestimmung der Dichte nichtbindiger Böden bei lockerster und dichtester Lagerung DIN 18126

Projekt Nr.: Modellboden
HH-01 Sand

Entnahmestelle:
Entnahmetiefe:
Entnahmeart : GP
Bodenart: gS, ms

Korndichte ρ_S = 2,639 g/cm³

Porenanteil in natürlicher Lagerung	n =		%
Porenanzahl in natürlicher Lagerung	e =		
Ungleichförmigkeitszahl	U =		
Größtkorn	*max* d =	<4	mm

Bestimmung der Dichte in **lockerster Lagerung**

Versuchszylinder V_Z = 438,45 cm³ m_Z =

Probenmasse	min m_{d1} =		640,67	g
	min m_{d2} =		641,14	g
	min m_{d3} =		640,26	g
	min m_{d4} =		641,48	g
	min m_{d5} =		640,92	g
	Mittelwert :		640,89	g

min Trockendichte	$min\ \rho_d = min\ m_d / V_Z$ =	1,462	g/cm³
max Porenvolumen	$max\ n = 1 - (min\ \rho_d / \rho_s)$ =	0,446	
max Porenzahl	$max\ e = (\rho_s / min\ \rho_d) - 1$ =	0,805	

Bestimmung der Dichte in **dichtester Lagerung**

Versuchszylinder h = 11,15 cm A = 39,2 cm² Platte h_P = 1,50 cm

Probenmasse	m_d =	640,12	g
Setzung	s_1 =	2,40	mm
	s_2 =	1,90	mm
	s_3 =	2,80	mm
	Mittelwert s_m =	2,37	mm
Volumen	minV = A*(h–h_p–s_m) =	368,71	cm³
Trockendichte	ρ_d =	1,736	g/cm³

max Trockendichte	$max\ \rho_d = m_d / minV$ =	1,736	g/cm³
min Porenvolumen	$min\ n = 1 - (max\ \rho_d / \rho_s)$ =	0,342	
min Porenzahl	$min\ e = (\rho_s / max\ \rho_d) - 1$ =	0,520	

Abgeleitete Größen

Lagerungsdichte	D = (max n – n) / (max n – min n) =	
Bezogene Lagerungsdichte	I_D = (max e – e) / (max e – min e) =	
Verdichtungsfähigkeit	I_f = (max e – min e) / min e =	0,55

B.4 Permeability

TUHH
Technische Universität Hamburg-Harburg
Geotechnik und Baubetrieb
Univ.-Prof. Dr.-Ing. Jürgen Grabe
Harburger Schloßstr. 20
21079 Hamburg
Tel.: +49 (0)40 / 428 78-3782
Fax: +49 (0)40 / 428 78-4020
www.tu-harburg.de/gbt

Anlage

März 2018

DURCHLÄSSIGKEITSVERSUCH

DIN 18 130 - ZY - MS - MZ - 3

Projekt Nr.
Vincent

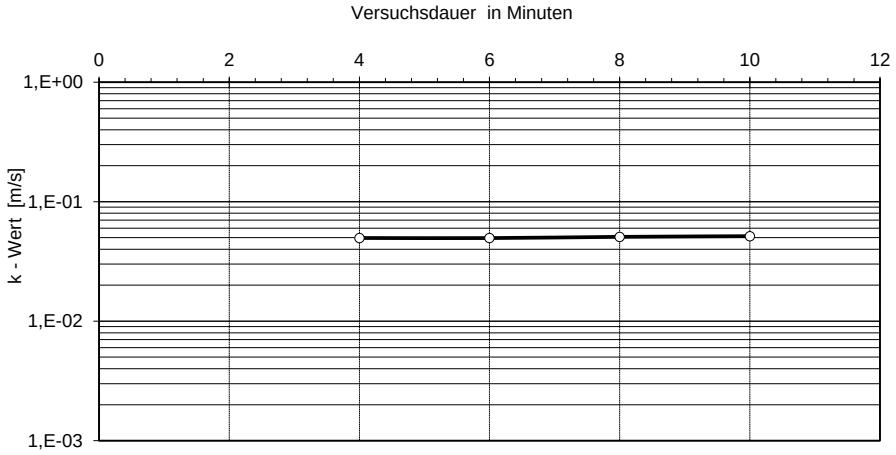
Länge der Probe	14,0	cm
Durchmesser	8,0	cm
Querschnittsfläche	50,27	cm²

Entnahmestelle : Eimer
Entnahmetiefe: -
Bodenart: Glasperlen 3mm

Einbaudichte ρ_d 0,000 g/cm³

Versuchsart: konstantes hydraulisches Gefälle
Durchströmung von unten nach oben

hydraulische Druckhöhe	0,0020	m WS
Temperatur	19,1	°C



Zeitspanne [Min.]	Volumen des Wassers [cm³]	Durchfluß [m³/s]	Durchlässigkeitsbeiwert $k_{10°C}$ [m/s]
4,0	1085,7	4,52E-06	4,97E-02
2,0	542,1	4,52E-06	4,96E-02
2,0	555,1	4,63E-06	5,08E-02
2,0	562,3	4,69E-06	5,14E-02

Durchlässigkeitsbeiwert $k_{10°C}$

Mittelwert aus 4 Versuchen: 5,0E-02 m/s

Bearbeiter: .....

Geprüft von: .....

C:\Users\Manue\AppData\Local\Packages\microsoft.windowscommunicationsapps_8wekyb3d8bbwe\LocalState\Files\S0\19569\Attachments\[k-we

TUHH
Technische Universität Hamburg-Harburg
Geotechnik und Baubetrieb
Univ.-Prof. Dr.-Ing. Jürgen Grabe

Harburger Schloßstr. 20
21079 Hamburg
Tel.: +49 (0)40 / 428 78-3782
Fax: +49 (0)40 / 428 78-4020
www.tu-harburg.de/gbt

Anlage

Mai 2015

DURCHLÄSSIGKEITSVERSUCH

DIN 18 130 - ZY - MS - MZ - 3

Projekt Nr.
Lisa

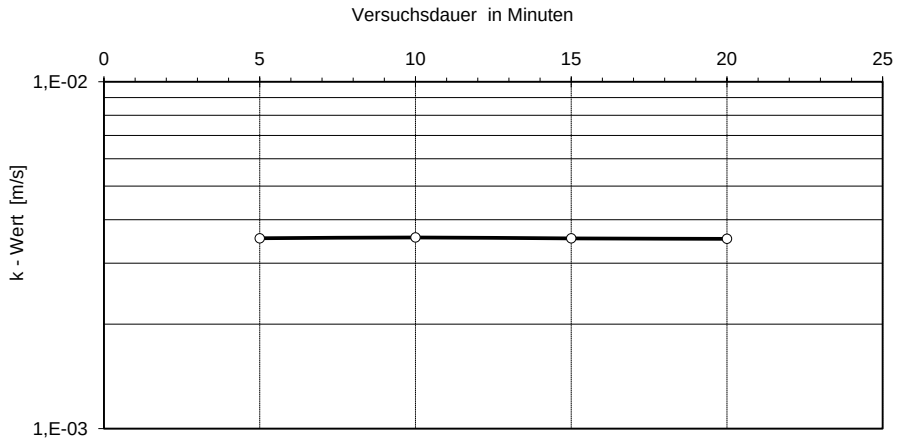
Länge der Probe	14,0	cm
Durchmesser	8,0	cm
Querschnittsfläche	50,27	cm²

Entnahmestelle : Eimer
Entnahmetiefe: -
Bodenart: Glasperlen 1mm

Einbaudichte ρ_d 1,528 g/cm³

Versuchsart: konstantes hydraulisches Gefälle
Durchströmung von unten nach oben

hydraulische Druckhöhe	0,0000	m WS
Temperatur	18,0	°C



Zeitspanne [Min.]	Volumen des Wassers [cm³]	Durchfluß [m³/s]	Durchlässigkeitsbeiwert $k_{10°C}$ [m/s]
5,0	1439,5	4,80E-06	3,54E-03
5,0	1446,6	4,82E-06	3,56E-03
5,0	1438,0	4,79E-06	3,53E-03
5,0	1433,7	4,78E-06	3,52E-03

Durchlässigkeitsbeiwert $k_{10°C}$
Mittelwert aus 4 Versuchen 3,5E-03 m/s

Bearbeiter: .....
Geprüft von: .....

TUHH
Technische Universität Hamburg-Harburg
Geotechnik und Baubetrieb
Univ.-Prof. Dr.-Ing. Jürgen Grabe

Harburger Schloßstr. 20
21079 Hamburg
Tel.: +49 (0)40 / 428 78-3782
Fax: +49 (0)40 / 428 78-4020
www.tu-harburg.de/gbt

Anlage

November 2013

DURCHLÄSSIGKEITSVERSUCH

DIN 18 130 - ZY - MS - MZ - 3

Projekt Nr. XXX
Modellboden

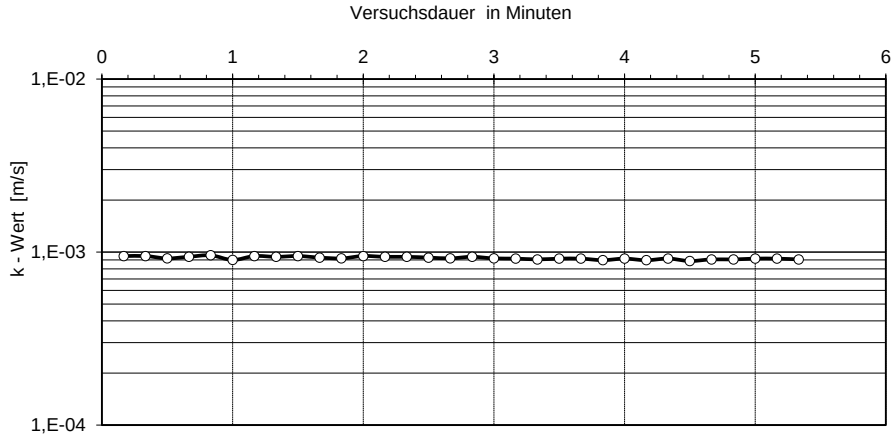
Länge der Probe	14,0	cm
Durchmesser	8,0	cm
Querschnittsfläche	50,27	cm²

Entnahmestelle :
Entnahmetiefe:
Bodenart: HH-01 Sand (gS, ms)

Einbaudichte ρ_d 1,565 g/cm³

Versuchsart: konstantes hydraulisches Gefälle
Durchströmung von unten nach oben

hydraulische Druckhöhe	0,42	m
Temperatur	10,0	°C



Zeitspanne [Min.]	Volumen des Wassers [cm³]	Durchfluß [m³/s]	Durchlässigkeitsbeiwert $k_{10°C}$ [m/s]

Durchlässigkeitsbeiwert $k_{10°C}$
Mittelwert, gesamte Messung: 9,24E-04 m/s

Bearbeiter: .....
Geprüft von: .....

TUHH
Technische Universität Hamburg-Harburg
Geotechnik und Baubetrieb
Univ.-Prof. Dr.-Ing. Jürgen Grabe

Harburger Schloßstr. 20
21079 Hamburg
Tel.: +49 (0)40 / 428 78-3782
Fax: +49 (0)40 / 428 78-4020
www.tu-harburg.de/gbt

Anlage

November 2013

DURCHLÄSSIGKEITSVERSUCH

DIN 18 130 - ZY - MS - MZ - 3

Projekt Nr. XXX
Modellboden

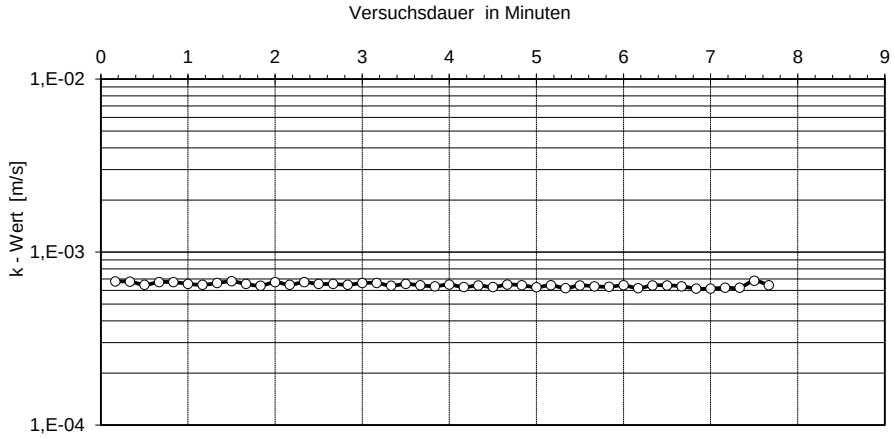
Länge der Probe	14,0	cm
Durchmesser	8,0	cm
Querschnittsfläche	50,27	cm²

Entnahmestelle :
Entnahmetiefe:
Bodenart: HH-01 Sand (gS, ms)

Einbaudichte ρ_d 1,595 g/cm³

Versuchsart: konstantes hydraulisches Gefälle
Durchströmung von unten nach oben

hydraulische Druckhöhe	0,52	m
Temperatur	10,0	°C



Zeitspanne [Min.]	Volumen des Wassers [cm³]	Durchfluß [m³/s]	Durchlässigkeitsbeiwert $k_{10°C}$ [m/s]

Durchlässigkeitsbeiwert $k_{10°C}$
Mittelwert, gesamte Messung: 6,46E-04 m/s

Bearbeiter: .....
Geprüft von: .....

Appendix C Cohesion model implementation in LIGGGHTS®

```
/* ----------------------------------------------------------------------
   This is the

   LIGGGHTS

   DEM simulation engine, released by
   DCS Computing Gmbh, Linz, Austria
   http://www.dcs-computing.com, office@dcs-computing.com

   LIGGGHTS is part of CFDEMproject:
   http://www.liggghts.com | http://www.cfdem.com

   Core developer and main author:
   Christoph Kloss, christoph.kloss@dcs-computing.com

   LIGGGHTS is open-source, distributed under the terms of the GNU Public
   License, version 2 or later. It is distributed in the hope that it will
   be useful, but WITHOUT ANY WARRANTY; without even the implied warranty
   of MERCHANTABILITY or FITNESS FOR A PARTICULAR PURPOSE. You should have
   received a copy of the GNU General Public License along with LIGGGHTS.
   If not, see http://www.gnu.org/licenses . See also top-level README
   and LICENSE files.

   LIGGGHTS and CFDEM are registered trade marks of DCS Computing GmbH,
   the producer of the LIGGGHTS software and the CFDEMcoupling software
   See http://www.cfdem.com/terms-trademark-policy for details.

-------------------------------------------------------------------------
   Contributing author and copyright for this file :

   Christoph Kloss (DCS Computing GmbH, Linz)
   Christoph Kloss (JKU Linz)
```

```
33      Richard Berger (JKU Linz)
34
35      Copyright 2012-     DCS Computing GmbH, Linz
36      Copyright 2009-2012 JKU Linz
37  ------------------------------------------------------------------------- */
38
39
40  #ifdef COHESION_MODEL
41  COHESION_MODEL(COHESION_DILATANCY,dilatancy,18)
42  #else
43
44  #ifndef COHESION_MODEL_DILATANCY_H_
45  #define COHESION_MODEL_DILATANCY_H_
46
47  #include "contact_models.h"
48  #include "cohesion_model_base.h"
49  #include <cmath>
50  #include <ctime>
51  #include "global_properties.h" // added by alice
52  #include "fix_property_atom.h" // added by alice
53  #include "neighbor.h"          // added by alice
54  #include "update.h"            // added by manuela
55  #include "atom.h"              // added by manuela
56  #include "neigh_list.h"
57
58  namespace MODEL_PARAMS
59  {
60
61      inline static ScalarProperty* createDilatancyMultiplier(PropertyRegistry &
            registry, const char * caller, bool sanity_checks) // added by manuela:
            multiplier factor for calibration purpose
62      {
63        ScalarProperty* DilatancyFactor = MODEL_PARAMS::createScalarProperty(
              registry, "dilatancyfactor", caller);
64        return DilatancyFactor;
65      }
66
67     inline static ScalarProperty* createMinimumVoidfraction(PropertyRegistry &
          registry, const char * caller, bool sanity_checks) // added by manuela:
          minimum void fraction
68      {
69        ScalarProperty* nMin = MODEL_PARAMS::createScalarProperty(registry, "
              nmin", caller);
70        return nMin;
71      }
```

```
72
73 }
74
75 namespace LIGGGHTS {
76 namespace ContactModels {
77   using namespace std;
78   using namespace LAMMPS_NS;
79
80   template<>
81   class CohesionModel<COHESION_DILATANCY> : public CohesionModelBase {
82   public:
83     CohesionModel(LAMMPS * lmp, IContactHistorySetup * hsetup, class
          ContactModelBase * c) :
84         CohesionModelBase(lmp, hsetup, c),
85         DilatancyFactor(0),
86       nMin(0),
87         fix_dissipated_(NULL),
88         dissipatedflag_(false),
89         dissipation_history_offset_(-1)
90     {
91       /*NL*/ if(comm->me == 0) fprintf(screen, "COHESION/DILATANCY loaded\
             n");
92     }
93
94     void registerSettings(Settings &settings)
95     {
96         settings.registerOnOff("computeDissipatedEnergy", dissipatedflag_, false);
97     }
98
99     inline void postSettings(IContactHistorySetup * hsetup, ContactModelBase *cmb)
100    {
101        if (dissipatedflag_)
102        {
103            if (cmb->is_wall())
104            {
105                fix_dissipated_ = static_cast<FixPropertyAtom*>(modify->
                       find_fix_property("dissipated_energy_wall", "property/atom", "
                       vector", 0, 0, "dissipated energy"));
106                dissipation_history_offset_ = cmb->get_history_offset("
                       dissipation_force");
107                if (!dissipation_history_offset_)
108                    error->one(FLERR, "Internal error: Could not find dissipation
                           history offset");
109            }
110            else
```

```
111                 fix_dissipated_ = static_cast<FixPropertyAtom*>(modify->
                        find_fix_property("dissipated_energy", "property/atom", "vector",
                        0, 0, "dissipated energy"));
112             if (!fix_dissipated_)
113                 error->one(FLERR, "Surface model has not registered
                        dissipated_energy fix");
114         }
115
116     }
117
118     void connectToProperties(PropertyRegistry & registry)
119     {
120         registry.registerProperty("dilatancyfactor", &MODEL_PARAMS::
                createDilatancyMultiplier); // added by manuela
121         registry.connect("dilatancyfactor", DilatancyFactor,"cohesion_model dilatancy
                "); // added by manuela
122       registry.registerProperty("nmin", &MODEL_PARAMS::
              createMinimumVoidfraction); // added by manuela
123         registry.connect("nmin", nMin,"cohesion_model dilatancy"); // added by
                manuela
124
125         //NP modified C.K.
126         // error checks on coarsegraining
127         if(force->cg_active())
128             error->cg(FLERR,"cohesion model dilatancy");
129
130         //set neighbor contact_distance_factor here
131         /*NL*/ //fprintf(screen,"COHESION_BOND: cdf_all = %g\n",cdf_all);
132         // deterimine min & max rad
133
134         //set neighbor contact_distance_factor here
135         // worst case is for equal size particles
136         // bigger particle ratio leads to smaller cdf
137         // max distance as defined by deltaC leads to: maxDistance = ri + 2*rij + rj
138         // rij = [0.5, 1] * min(ri,rj)
139         // cdf = maxDistance / (ri+rj)
140         // worst case: for ri == rj, cdf = 1.5
141         //neighbor->register_contact_dist_factor(1.1*2); // 1.1 for safety reasons
142         /*const double minrad = registry.min_radius();
143         const double maxrad = registry.max_radius();
144
145       //set neighbor contact_distance_factor here
146         /*NL*/ //fprintf(screen,"COHESION_BOND: cdf_all = %g\n",cdf_all);
147         // deterimine min & max rad
148         const double minrad = registry.min_radius();
```

```
149         const double maxrad = registry.max_radius();
150
151         double cdf_all = 2.0*maxrad/2/minrad;
152         const char* neigharg[2];
153         neigharg[0] = "contact_distance_factor";
154         char arg2[30];
155         sprintf(arg2,"%e",cdf_all);
156         neigharg[1] = arg2;
157         neighbor->modify_params(2,const_cast<char**>(neigharg));
158     }
159
160     void surfacesIntersect(SurfacesIntersectData &sidata, ForceData & i_forces,
            ForceData & j_forces)
161     {
162         if(sidata.contact_flags) *sidata.contact_flags &= ~
                CONTACT_COHESION_MODEL;
163     }
164
165     inline void endSurfacesIntersect(SurfacesIntersectData &sidata, ForceData&,
            ForceData&) {}
166     void beginPass(SurfacesIntersectData&, ForceData&, ForceData&){}
167     void endPass(SurfacesIntersectData&, ForceData&, ForceData&){}
168
169     void surfacesClose(SurfacesCloseData& scdata, ForceData & i_forces, ForceData &
            j_forces)
170     {
171
172         //r is the distance between the sphere's centers
173         const double r = sqrt(scdata.rsq); // distance between the sphere centers
174         const double ri = scdata.radi; // radius of sphere i
175         const double rj = scdata.radj; // radius of sphere j
176         double **x = atom->x;
177
178         // added by alice:
179         const double h = scdata.is_wall ? r - ri : r - (ri + rj); // distance between
                the particle surfaces
180
181         const double rij = scdata.is_wall ? ri*0.5 : (ri*rj)/(ri+rj); // effective
                radius
182         const double deltaC = 4*rij; // cutoff-distance until which force is active
183         const double minDist = 1e-4*(1.*rij); // minimal distance in which force is
                considered
184
185       //relative translational velocity
186         int i = scdata.i;
```

```
187         int j = scdata.j;
188
189         const double vr1 = scdata.v_i[0] - scdata.v_j[0];
190         const double vr2 = scdata.v_i[1] - scdata.v_j[1];
191         const double vr3 = scdata.v_i[2] - scdata.v_j[2];
192         const double vr = sqrt(vr1*vr1+vr2*vr2+vr3*vr3);
193
194        // added by manuela:
195         const double Xi = DilatancyFactor; // reading the dilatancy factor from the
               input file
196       const double n = nMin; // reading minimum void fraction from the input file
197
198         // calculate vn and vt since not in struct
199         const double rinv = 1.0 / r;
200         const double dx = abs(x[i][0]-x[j][0]);
201         const double dy = abs(x[i][1]-x[j][1]);
202         const double dz = abs(x[i][2]-x[j][2]);
203         const double enx = dx * rinv;
204         const double eny = dy * rinv;
205         const double enz = dz * rinv;
206         const double vi1 = enx*scdata.v_i[0];
207         const double vi2 = eny*scdata.v_i[1];
208         const double vi3 = enz*scdata.v_i[2];
209
210         //fprintf(screen,"timestep = %g\n",dt);
211
212        // normal component
213         const double vn = vr1 * enx + vr2 * eny + vr3 * enz;
214         const double vn1 = vn * enx;
215         const double vn2 = vn * eny;
216         const double vn3 = vn * enz;
217
218         // added by manuela:
219         if(h > deltaC || h < minDist || vr > 0.25)                    // criterion for
               deactivation of model
220         {
221
222         //fprintf(screen, "Out of reach\n");
223             if(scdata.contact_flags)
224                 *scdata.contact_flags &= ~CONTACT_COHESION_MODEL;
225
226             return;
227         }
228
229       // computing force acting on particle
```

```
230         const double mult_n = -6*M_PI*mu*rij*pow(n,-Xi)/(1-n);
231         const double fx = mult_n*vn1;
232         const double fy = mult_n*vn2;
233         const double fz = mult_n*vn3;
234
235         //fprintf(screen,"x_Force = %g\nmult = %g\n ddx = %g\n",fx,mult,ddx);
236
237         scdata.has_force_update = true;
238         if(scdata.contact_flags)
239             *scdata.contact_flags |= CONTACT_COHESION_MODEL;
240
241         // compute dissipated energy from this model
242         if(h>minDist || h<deltaC)
243        if (dissipatedflag_)
244         {
245             double * const * const dissipated = fix_dissipated_->array_atom;
246
247             double * const dissipated_i = dissipated[scdata.i];
248             dissipated_i[0] -= fx;
249             dissipated_i[1] -= fy;
250             dissipated_i[2] -= fz;
251             if (scdata.j < atom->nlocal && !scdata.is_wall)
252             {
253                 double * const dissipated_j = dissipated[scdata.j];
254                 dissipated_j[0] += fx;
255                 dissipated_j[1] += fy;
256                 dissipated_j[2] += fz;
257             }
258             else if (scdata.is_wall)
259             {
260                 double * const diss_force = &scdata.contact_history[
                        dissipation_history_offset_];
261                 diss_force[0] += fx;
262                 diss_force[1] += fy;
263                 diss_force[2] += fz;
264             }
265         }
266
267         if(scdata.is_wall) {
268           i_forces.delta_F[0] += fx;
269           i_forces.delta_F[1] += fy;
270           i_forces.delta_F[2] += fz;
271
272         } else {
273           i_forces.delta_F[0] += fx;
```

```
274             i_forces.delta_F[1] += fy;
275             i_forces.delta_F[2] += fz;
276
277
278             j_forces.delta_F[0] -= fx;
279             j_forces.delta_F[1] -= fy;
280             j_forces.delta_F[2] -= fz;
281
282         }
283
284     }
285
286   private:
287     double DilatancyFactor;
288    double nMin;
289     class FixPropertyAtom *fix_dissipated_;
290     bool dissipatedflag_;
291     int dissipation_history_offset_;
292   };
293 }
294 }
295
296 #endif // COHESION_MODEL_DILATANCY_H_
297 #endif
```